An experimental and numerical approach for tuning the cathode for high performance IT-SOFC

Ozden Celikbilek

Communauté
UNIVERSITÉ Grenoble Alpes

THÈSE

Pour obtenir le grade de

DOCTEUR DE LA COMMUNAUTÉ UNIVERSITÉ GRENOBLE ALPES

Spécialité : **Matériaux, Mécanique, Génie Civil, Electrochimie**
Arrêté ministériel : 25 mai 2016

Présentée par

Özden ÇELİKBİLEK

Thèse dirigée par **Elisabeth DJURADO** et
codirigée par **Christophe L. MARTIN** et
David JAUFFRÈS et **Mónica BURRIEL**

préparée au sein du **Laboratoire d'Electrochimie et de Physico-chimie des Matériaux et des Interfaces (LEPMI)** et **au Laboratoire Science et Ingénierie des Matériaux et Procédés (SIMaP)** dans **l'École Doctorale IMEP2/ Ingénierie - Matériaux, Mécanique, Environnement, Energétique, Procédés, Production**

Optimisation de la cathode pour pile à combustible à oxyde électrolyte solide : approches expérimentale et numérique

Thèse soutenue publiquement le **9 Décembre 2016**
devant le jury composé de :

Mme, Marie-Cécile PERA
Professeur, Université de Franche-Comté, Président du Jury
M. Stephen SKINNER
Professeur, Imperial College London, Rapporteur
M. Olivier JOUBERT
Professeur, Ecole Polytechnique de l'Université de Nantes, Rapporteur
M. Norbert H. MENZLER
Docteur, Forschungszentrum Jülich, Membre
M. David JAUFFRÈS
Maître de conférence, Université Grenoble Alpes, Co-encadrant
Mme Mónica BURRIEL
Chargée de Recherche, CNRS, Université Grenoble Alpes, Co-encadrant
M. Christophe L. MARTIN
Directeur de Recherche, CNRS, Université Grenoble Alpes, Co-directeur
Mme Elisabeth DJURADO
Professeur, Université Grenoble Alpes, Directeur

ACKNOWLEDGEMENTS

For the three years that I have spent in Laboratoire d'Electrochimie et de Physico-chimie des Matériaux et Interfaces (LEPMI) et Laboratoire de Science et Ingénierie des Matériaux et Procédés (SIMAP) in Université de Grenoble Alpes, I would like to thank all those who contributed to the successful completion of my PhD.

I would like to start by thanking all the jury members who accepted to be in my doctoral defense. I appreciate the time and efforts, especially by the referees Prof. Olivier Joubert and Prof. Stephen Skinner, in reviewing my manuscript. I would like to thank the president of the jury Prof. Marie Cecile Pera, the examiner Dr. Norbert Menzler and the invited member and external collaborator of this work Dr. Julian Dailly for having spent long hours reading my manuscript and for a very fruitful discussion about my work during the defense.

This work would not come out without the collaboration of my thesis supervisors Prof. Elisabeth Djurado and Dr. Christophe Martin. The combination of their expertise in two widely different fields of material science enabled me to present a unique work in our field. I would also like to thank both of them for their constant encouragement for my professional and personal development. Next, I would like to thank my two co-supervisors: Dr. Mónica Burriel for following my work throughout my PhD and for having fruitful discussions and Dr. David Jauffrès for his involvement in my thesis and correcting every bit of my manuscript. I consider myself lucky to have worked with him. From each and every one of them, I have learnt a great deal about becoming a good scientist.

I would like to express my deep gratitude to Prof. Elisabeth Siebert. I am grateful for her patience for my endless questions and her kindness towards me. I also would like to thank Prof. Laurent Dessemond. Without his valuable contributions, this thesis would not have been complete.

This work had been possible by the major funding of the Centre of Excellence of Multifunctional Architectured Materials (CEMAM) and I gratefully appreciate it.

I would like to acknowledge the members of the ‘Consortium des Moyens Technologiques Communs’ (CMTC) for allowing me to carry out a large number of characterizations on my

samples. I would like to thank Stéphane Coindeau, Thierry Encinas and Hervé Roussel, the XRD experts, for their immediate availability and for the many helpful discussions. Special thanks to Rachel Martin for the magnificent SEM images she has taken for me and our lovely conversations. I acknowledge Joelle Calabro for her meticulous work in preparing many of my samples and lastly, Frédéric Charlot with whom I worked for the most significant part of my work, the FIB/SEM characterization.

A great part of my work was supported by the platform 'Matériaux Electrochimiques pour l'Energie' (M2E). I would sincerely like to thank Etienne Omnes-Sabardak, Sandrine Boudin, Michel Dessarts and Cesar M. Steil for their valuable contribution in the preparation of the electrolyte support and screen printing instrument.

I would thank the two laboratories LEPMI and SIMAP who have welcomed me three years, in particular, MIEL and GPM2 teams. Thanks to the administration, Prof. Jean Claude Leprêtre, Fannie Alloin, Claire Girardi, Yasmine Bouhadjar, Claire Benoit, Nabil Smaili, Linda Vivenzio and Elisabeth Lussi (GPM2). For all the other technical work, I would like to thank Vincent Martin, Claude Roux, Laure Cointeaux, and Olivier Szydlo.

A big thanks to those with whom I shared unforgettable moments; long lunch breaks, coffee breaks, evenings out, hikings and weekend ski events; Marie Lachal, Emmanuelle Bichaud, Marc Zimmermann, Hana el-Khal, Shayenne Nobrega, Cheah Seng Kian, Phillipe Dumaz, Guilliaume Constantin, Lucien Duclos, Lavinia Astratine, Olesia Danyliv, Vlad Tezyk, Rakesh Sharma, and all the others.

My crazy friends from the European Master Program; Che-Hung Lin, Ana Carolina Lopez Selvati and Saumya Mukherjee. I would like to thank them individually for always being there for me, for still meeting up time to time and cherish the jokes about our North Korean bloods.

Again last but not least, my college friends from Turkey; Esra Eroğlu, Şeyma Ekiz, Çağatay Dengiz and Murat Kadir Deliömeroğlu. No matter how long the distance is or the time difference between us, we end up chatting on a daily basis. I am grateful to have you as my *kankies for life*.

Before the end, I would like to thank Fabio Agnese. I would be somewhere else living another life if it wasn't for you; and I would probably be missing out on this amazing life I had with you. I also would like to thank your lovely parents with whom I always felt welcomed in your family.

Finally, I would like to dedicate this manuscript to my family, especially my parents. I had unconditional love and support throughout my life and I cannot thank them enough.

RÉSUMÉ (FRANÇAIS)

Comprendre, contrôler et optimiser la réaction de réduction de l'oxygène à la cathode devient une nécessité pour améliorer les dispositifs de conversion d'énergie de haute performance tels que les piles à combustible à oxyde électrolyte solide (SOFC). Des films poreux à conduction mixte, ionique et électronique (MIEC) et leurs composites comprenant un conducteur ionique offrent des propriétés uniques. Cependant, la corrélation des propriétés intrinsèques des composants d'électrodes aux caractéristiques microstructurales reste une tâche difficile. Dans le cadre de cette thèse, la couche fonctionnelle de cathode de $La_{0.6}Sr_{0.4}Co_{0.2}Fe_{0.8}O_{3-\delta}$ (LSCF) pure et du composite LSCF/$Ce_{0.9}Gd_{0.1}O_{2-\delta}$ (CGO) a été élaborée par la technique d'atomisation électrostatique. Une microstructure à porosité hiérarchique a été obtenue dans un domaine nanométrique à micrométrique. Les films ont été recouverts d'un collecteur de courant (CCL), LSCF, par sérigraphie. Une étude paramétrique a été réalisée expérimentalement pour optimiser la double couche en termes de température de frittage, de composition et d'épaisseur des couches de CFL et CCL. En se basant sur ces résultats, un modèle éléments finis 3D a été développé en utilisant les paramètres microstructuraux déterminés par tomographie de FIB-MEB dans une géométrie simple, similaire à des caractéristiques colonnaires. Sur la base de ce modèle, un guide de conception du matériau d'électrode a été proposé reliant des performances électrochimiques optimisées à la microstructure et aux propriétés du massif. Une cellule complète de SOFC intégrant la cathode optimisée double couche de LSCF a été testée dans des conditions réelles d'exploitation et sa durabilité a été suivie pendant 700h.

ABSTRACT (ENGLISH)

Understanding, controlling and optimizing the mechanism of oxygen reduction reaction at the cathode need to be addressed for high performance energy conversion devices such as solid oxide fuel cells (SOFCs). Structured porous films of mixed ionic electronic conductors (MIECs) and their composites with addition of a pure ionic conductor offer unique properties. However, correlating the intrinsic properties of electrode components and microstructural features to performance remains a challenging task. In this PhD thesis, cathode functional layers (CFL) of $La_{0.6}Sr_{0.4}Co_{0.2}Fe_{0.8}O_{3-\delta}$ (LSCF) and LSCF/$Ce_{0.9}Gd_{0.1}O_{2-\delta}$ (CGO) composite cathodes with hierarchical porosity from nano- to micro-range are fabricated by electrostatic spray deposition technique. The films were topped with LSCF as a current collecting layer (CCL) by screen printing technique. A parametric optimization study was conducted experimentally in terms of sintering temperature, composition, and thickness of CFL and CCL layers. The experimental results were supported by a numerical 3D Finite Element Model (FEM). Microstructural parameters determined by FIB-SEM tomography were used in a simple geometry similar to experimentally observed columnar features. In this work, experimental results and modelling were combined to provide design guidelines relating optimized electrochemical performances to the microstructure and bulk material properties. A complete fuel cell with optimized cathode film was tested in long term degradation in real SOFC operational conditions.

CONTENTS

INTRODUCTION

The combustion engines have been proven to be effective means of generating mechanical work from a fossil fuel source. Gasoline or diesel engine powered automobiles are the simplest examples that billions of people use on daily basis. However, some concerns have been raised both on the continuity of fossil fuels and the environmental effects caused by the combustion of these fuels. Therefore, efficient and sustainable energy has been the main research interest over the last decades in order to be less dependent on fossil fuels. Hydrogen or methane is considered as efficient and convenient energy carriers for sustainable energy. For conversion of these fuels to electrical energy, electrochemical devices such as solid oxide fuel cells (SOFC) are necessary. Fuel cells are devices that can directly convert chemical energy from a fuel into electrical energy through an electrochemical reaction. A fuel (e.g. hydrogen, methane) and an oxidant (e.g. air) meet to produce electrical energy and water (in the case of hydrogen and air). They offer significant increase in the conversion efficiency of about 60% (Figure 1) and cogeneration efficiency up to 80-90% [1]. Therefore, they grabbed a lot of attention as clean and efficient energy conversion devices for the future.

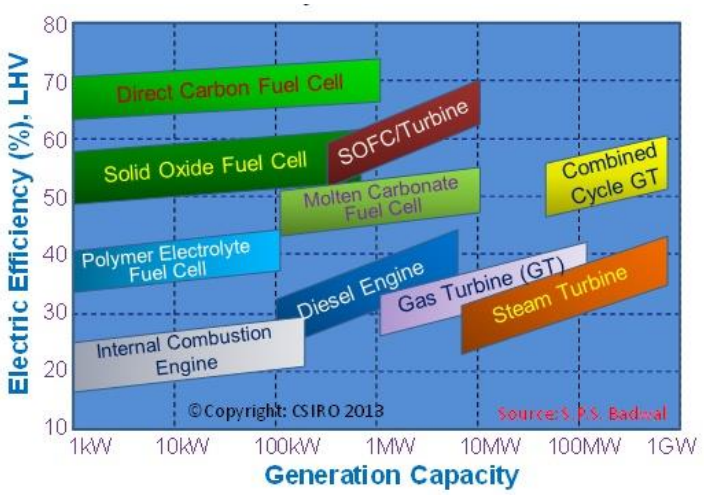

Figure 1 The electric efficiency versus power plant size for different power generation technologies. Retrieved from https://csiropedia.csiro.au/ceramic-fuel-cells/

Putting aside the issues concerning lack of infrastructure for hydrogen fuel manufacture, transport and storage, there are other issues regarding the efficiency and the cost of making the cells. Fuel cell manufacture costs can be brought down significantly by replacing the expensive components of a cell by their cheaper counterparts and by different manufacturing techniques.

In order to attain reasonable power density, typical operating temperatures of current thick-film (1-50 μm) SOFCs are in the high temperature regime of 800-1000 °C. High operating temperatures bring about material compatibility and sealing issues. Therefore, current research is focused towards lowering down the operating temperatures in the intermediate range (400-700 °C). Since the system kinetics are known to be thermally activated, lowering the temperatures introduce severe problems concerning the overall efficiency. The most significant obstacle is that fully compatible material components in a high temperature SOFC (HT-SOFC) are not operational in an intermediate temperatures SOFC (IT-SOFC). Consequently, alternative material components and fabrication methods have become the main focus. Among the components, the cathode material is known to limit the overall performance at intermediate temperatures. Therefore, the development and fabrication of new materials with good ionic/electronic conductivity, high electrochemical activity and high surface exchange properties at intermediate operating temperatures are necessary. The composite of mixed ionic and electronic conductors (MIEC) with ionic conductors (IC) are preferred over pure components in order to increase the effective ionic conductivity of the film at intermediate

temperature ranges. New strategies for rational design of microstructures with hierarchical features through a facile and low-cost approach are also necessary.

Objective of the thesis

The performance of an SOFC depends on several combined factors in each cell compartments (i.e. anode, cathode and electrolyte). Most of the presented work concerns the cathode, as the polarization resistance of this layer becomes significant for intermediate temperature operations. The cathode reaction kinetics and influence of microstructure of state-of-the-art cathode material (La,Sr)(CoFe)$O_{3-\delta}$ (LSCF) have been extensively studied through comparative experimental works and numerical simulations in the literature. Earlier in our group, reaction kinetics of LSCF deposited by electrostatic spray deposition (ESD) technique was studied in three different microstructures. Thanks to nanostructured microstructure features, one of the lowest resistance values compared to literature was achieved. As a continuation, this thesis focuses on the micro- to nano-scale changes in the cathode microstructure through the variation on the deposition parameters, film composition (composite LSCF/$Ce_{1-x}Gd_xO_{2-\delta}$), and the sintering temperature. The objective of this thesis is to experimentally monitor the microstructure/performance relationship and to provide general design guidelines using a model system comparable to experimental conditions. A numerical model with finite element method (FEM) is chosen since it can provide an efficient technical approach and information that are not possible to get with analytic models. However, FEM models are usually costly in terms of computation time, especially for the calculations of three-dimensional microstructures that combine micro- and nano-sized features similar to the ESD cathodes. Therefore, an original strategy combining homogenization approach and finite element method is proposed.

Chapter 1 introduces the state-of-the-art SOFC systems. The operating principles and kinetics in the cathode, the other SOFC components, and degradation mechanisms in each compartment are reviewed. The microstructural factors affecting the cathode performances are discussed.

Chapter 2 is devoted to the technical information on the fabrication and characterization of pure LSCF and LSCF/CGO cathode films for the applications in IT-SOFCs. The parameters for successive depositions of electrostatic spray deposition (ESD) and screen printing (SP) techniques to obtain double layer films are given. The widely used fundamental characterization techniques such as scanning electron microscope (SEM), transmission

electron microscope (TEM) and x-ray diffraction (XRD) are outlined. 3D microstructural characterization by 3D FIB/SEM tomography (focused ion beam/scanning electron microscope) and image analysis are elaborately explained. A detailed description of the electrochemical characterization by electrochemical impedance spectroscopy (EIS) is presented.

Chapter 3 starts with a comparison of cathode resistance of LSCF in two type of microstructures. The microstructures are controlled by varying ESD deposition parameters. Then, various LSCF/CGO compositions are studied by SEM, TEM, XRD, and EIS to see the effect of microstructure evolution on the electrode performance. Only pure LSCF and 60:40 vol. % LSCF/CGO are chosen for the reconstruction by FIB/SEM tomography. The same composite composition (60:40) is selected to study the effect of sintering temperature on the electrode performance. The grain growths are monitored by SEM and XRD, and possible consequences are discussed with respect to initial ESD deposition parameters and electrode polarization resistances.

Chapter 4 focuses on the optimization of the double layer cathode films of pure LSCF deposited by ESD technique as cathode functional layer (CFL) topped by LSCF deposited by SP technique as current collecting layer (CCL). The thicknesses of CFL and CCL are varied and current constriction effects are monitored by electrochemical impedance spectroscopy. Finally, the optimized double layer LSCF films are deposited on anode-supported fuel cells. The performances and long term durability of the complete cells are tested at 675 °C.

Chapter 5 presents two 3D FEM models taking into account of the hierarchical nature of ESD cathode microstructure. The procedures, assumptions and equations are introduced. Model 1 is based on cubic particles that was previously reported in the literature for homogeneous pure LSCF microstructures. The model equations are taken from the references and adapted to our 60:40 LSCF/CGO composite columnar-type microstructure. Following model 1, a new 3D FEM model is proposed (model 2). It still takes into account the hierarchical nature of the microstructure but also enables simulations of larger micro- features that is usually very demanding in terms of computation. The real microstructural parameters obtained from FIB/SEM tomography are included in model 2 and the results are discussed in relation with the experimental data. Finally a general conclusion with new perspectives are given.

1 FUNDAMENTALS OF SOFC

Chapter 1 introduces the state-of-the-art SOFC systems. The operating principles and kinetics in the cathode, the other SOFC components, and degradation mechanisms in each compartment are reviewed. The microstructural factors affecting the cathode performances are discussed.

1.1 Fundamentals of SOFC

Fuels cells are electrochemical devices that can directly convert the energy stored within the chemical bonds of a fuel into electrical energy and heat. The main difference between a fuel cell and heat engine is that in heat engines chemical energy is first converted into mechanical energy and then into electrical energy which in turn result in loss of energy. On the contrary, the working principle to generate electricity through electrochemical reactions is similar to batteries; however, a fuel cell produces electricity as long as it has a fuel supply, while the battery must be recharged after being used up. The operation of a fuel cell or any other combustion cell is simply the combustion of a mole of hydrogen gas (fuel) and half a mole of oxygen gas (oxidant) producing a mole of water.

$$H_2 + \frac{1}{2}O_2 \rightarrow H_2O \qquad 1\text{-}1$$

This is a reaction involving bond splitting of one mole of H-H bonds and half a mole of O-O bonds to form two O-H bonds. Energy is provided by the combination of atoms and decrease of the entropy. The excess energy is released as heat. In a combustion engine, this heat is converted into mechanical energy and then into electrical energy, which brings about loss of energy in each stage. On the other hand, an electrochemical fuel cell benefits from spatial separation of hydrogen in the anode and oxygen in the cathode compartments (Figure 1-1). The two half reactions are combined by the electron transfer. Therefore, since the electrons move from the fuel species to the oxidant species, they represent an electrical current. The two electrochemical half reactions are:

the oxidation reaction at the anode:

$$H_2 + O^{2-} \rightarrow H_2O + 2e^- \qquad 1\text{-}2$$

the reduction reaction at the cathode:

$$\frac{1}{2}O_2 + 2e^- \rightarrow O^{2-} \qquad 1\text{-}3$$

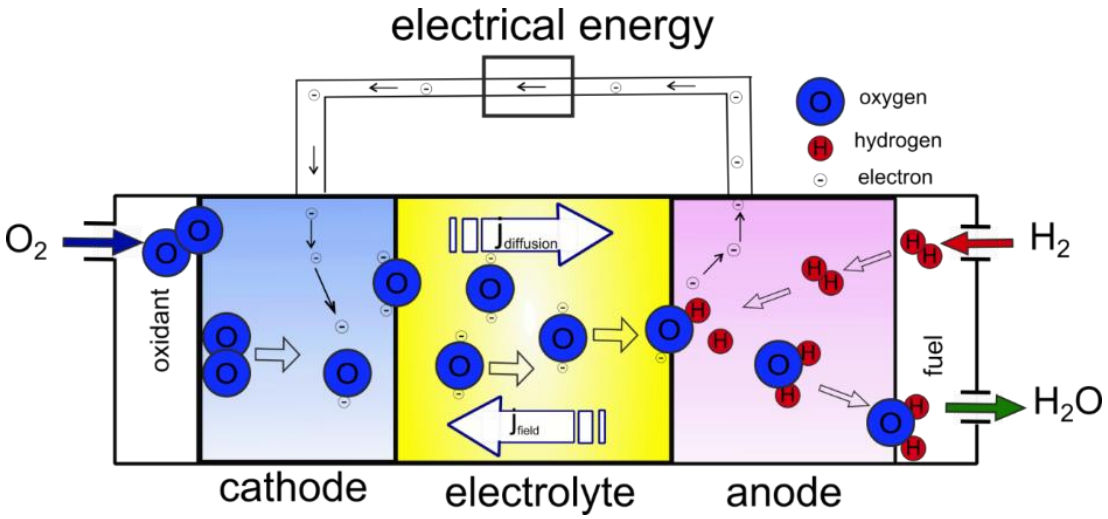

Figure 1-1 The working principles of SOFC

As shown in Eq. 1-4 and Eq. 1-5, chemical energy is formed from chemical reaction between the oxidizing gas (oxygen, O_2) on the cathode side and the fuel gas (in this case hydrogen, H_2) on the anode side. The resulting reaction products (in this case water vapor, H_2O) are carried out from the anode side. The dense electrolyte separates the two compartments. This results in an oxygen partial pressure gradient between the cathode side and the anode side, which is maintained by the continuous feeding and removal of the gases. Because of the gradients, oxygen ions are transported from the cathode side to the anode side. On the cathode side, the oxygen ions are provided from the oxygen molecules in the gas phase, while the electrons are received from the anode side by the external circuit. On the anode side, the oxygen ions react with hydrogen to give water vapor and return in the gas phase.

$$\frac{1}{2}\,O_2 + V_O^{\cdot\cdot} + 2\,e^- \rightarrow O_O^x \qquad 1\text{-}4$$

$$H_2 + O_O^x \rightarrow H_2O + 2\,e^- + V_O^{\cdot\cdot} \qquad 1\text{-}5$$

The transport of oxygen ions is accompanied by a depletion of electrons on the cathode side and an accumulation on the anode side, where an ideal electrolyte has only the conductivity for oxygen ions. Accordingly, a potential difference is created between the electrodes. The

potential differences can be balanced through the external circuit, thereby providing the electrical energy for the consumer.

In the case of an open circuit, an equilibrium situation will be reached after a relaxation period. The potential gradient, which at first causes oxygen ions to move from cathode to anode side, is balanced by an electrical gradient opposite to the direction of the diffusion force. In this situation the Nernst-voltage E_{Nernst} arises between cathode and anode as shown in the following equation:

$$E_{Nernst} = E_0 - \frac{RT}{nF}\left(\frac{P_{H2O}}{P_{O2}^{1/2} P_{H2}}\right) \qquad 1\text{-}6$$

where E_0 the standard cell potential, R the gas constant, F the Faraday constant, n the number of electrons involved, T the temperature, p the partial pressure of reactants and products. In typical operation temperatures (800 °C) of a SOFC operated on hydrogen and air values around 1.1 V is obtained as Nernst voltage.

1.2 Electrochemical Processes at MIEC Cathodes

The proposed reactive pathway is decomposed into a succession of steps that combines a “bulk” and a “surface” path (Figure 1-2). Both pathways are joined in a common reaction corresponding to the oxygen desorption/adsorption that produces/consumes gaseous oxygen molecules in the electrode porosities. They are in competition and occur parallel to each other. The slowest process in such a situation is referred to as rate determining step. However, the knowledge about this reaction is still limited, even though considerable research have been made over the years.

The oxygen surface exchange reactions involving are suggested to comprise adsorption of O_2 on the cathode surface and its dissociation into two oxygen atoms. Oxygen is then incorporated as an oxygen ion (O^{2-}) into a vacancy ($V_O^{\bullet\bullet}$) in the vicinity of the surface (s_{MIEC}) with a number of steps. These steps are summarized in 4 steps from Eq. 1.7 to Eq. 1.10. The charge transfer steps includes adsorption of gaseous O_2 onto an open surface vacancy, dissociation of O_2 by the occupation of a neighboring surface vacancy, and incorporation of the surface oxygen into the bulk [2]:

$$R1: \quad O_{2(gas)} + 2s_{MIEC} \leftrightarrow 2O - s_{MIEC} \qquad 1\text{-}7$$

$$R2: \quad 2O - s_{MIEC} + 2V_{O\,(surface)}^{\cdot\cdot} + 4e^{-} \leftrightarrow 2O_{O\ (MIEC)}^{x} + 2s_{MIEC} \qquad 1\text{-}8$$

$$R3: \quad 2O - s_{MIEC} + 2V_{O\,(CGO)}^{\cdot\cdot} + 4e^{-} \leftrightarrow 2O_{O\ (CGO)}^{x} + 2s_{MIEC} \qquad 1\text{-}9$$

$$R4: \quad 2O_{O\ (MIEC)}^{x} + 2V_{O\,(CGO)}^{\cdot\cdot} \leftrightarrow 2O_{O\ (CGO)}^{x} + 2V_{O\,(MIEC)}^{\cdot\cdot} \qquad 1\text{-}10$$

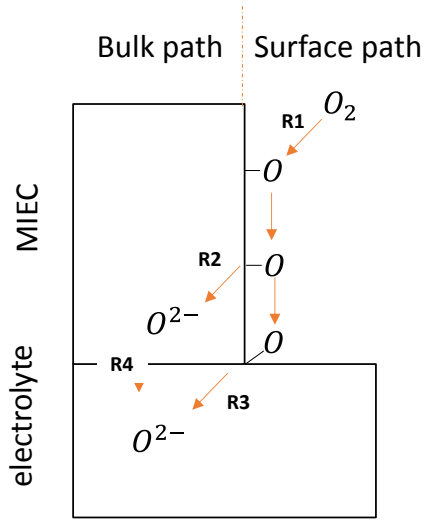

Figure 1-2 Schematic diagram illustrating the possible oxygen reduction reaction pathways in a dense MIEC cathode. Bulk and surface pathways are in competition as they occur parallel to each other. Oxygen incorporation at the side walls is also shown. Reproduced from ref. [2].

1.3 Power Losses in SOFCs

The performance of a fuel cell can be depicted from an I-V curve as shown in Figure 1-3. The current is normalized to the area of the fuel cell (A cm^{-2}) in order to be comparable with other systems. The voltage output of a real fuel cell is less than the thermodynamically predicted voltage output due to irreversible kinetic losses. The more current drawn from the system, the greater is the voltage drop from the ideal voltage. Three major losses account for the difference between the two curves, namely; ohmic, activation and concentration polarizations.

The overall cell voltage can be calculated using the following equation:

$$U_C(j) = U_N(j) - \eta_{ohm}(j) - \eta^c_{conc} - \eta^a_{conc} - \eta^c_{act} - \eta^a_{act} \qquad 1\text{-}11$$

U_C : Real output voltage of the fuel cell

U_N: Thermodynamically predicted voltage output of the fuel cell from Eq. 1.4

η_{ohm} : Ohmic losses based on total fuel cell current including fuel crossover loss

η_{act} : Activation losses based on total fuel cell current. Superscript [a] and [c] refer to anode and cathode, respectively.

η_{conc} : Concentration losses based on total fuel cell current. Superscript [a] and [c] refer to anode and cathode, respectively.

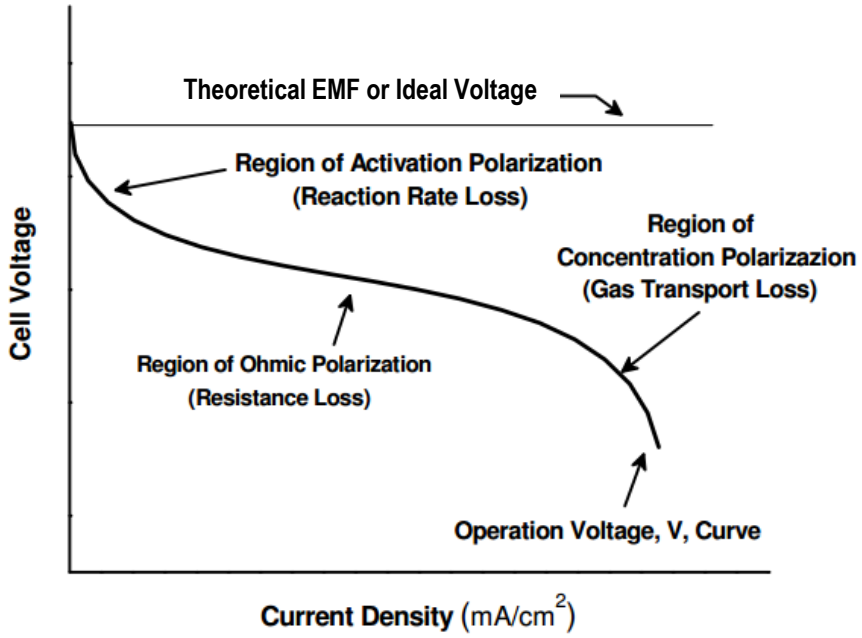

Figure 1-3 Ideal vs. actual fuel cell I-V curves.

Ohmic losses, η_{ohm}, occur during the electronic or ionic transport through the electrodes and the electrolyte, since every component has a finite conductivity. The overall ohmic resistance is the sum of each individual ohmic contribution R_s. According to Ohm's law, the ohmic overpotential linearly increases with the current density j.

$$\eta_{ohm} = j \cdot \sum_s R_s = j \cdot R_{ohm} \qquad 1\text{-}12$$

Concentration polarization, η_{conc}, is another significant loss, which originates from the transport of gaseous species through the porous electrodes by bulk diffusion and Knudsen diffusion. From the Nernst equation (Eq. 1.6), it is clear that decreasing the partial pressure of reactants causes a voltage drop. Electrode microstructures, pore sizes and pore morphology (tortuosity) are shown to influence the transport of gaseous species. Smaller electrode thicknesses are suggested to avoid concentration polarization losses [3].

Activation polarization, η_{act}, describes the electrochemical loss mechanisms taking place mainly at the three-phase boundary (TPB) where ionic-conducting, electronic-conducting and gas phases meet. An activation energy is necessary in order to overcome the energy barrier that prevents a spontaneous reaction. The higher the temperature, the higher the probability for reactants to gain the necessary activation energy, therefore the overpotential is reduced. A commonly used equation for describing the influence of activation overpotential on current density is the well-known Butler-Volmer equation:

$$j = j_o\left[\exp(\frac{\alpha_a nF\eta}{RT}) - \exp(\frac{\alpha_c nF\eta}{RT})\right] \qquad 1\text{-}13$$

where j_o is the exchange current density, n is the number of electrons involved in each electrode reaction, α_a and α_c are the anodic and cathodic charge transfer coefficients, and η is the activation overpotential of the electrode.

1.4 Triple Phase Boundary

In a system where the cathode is purely electronic while the electrolyte is ionic conductor (e.g. LSM), the electrode reactions are bound to happen on the triple phase boundary points (TPB) as illustrated in Figure 1-4a. In this case, the presence of all three phases is essential to support the oxygen reduction reactions. In composite electrodes comprising electronic and ionic conductivity such as LSM/YSZ or a mixed ionic-electronic conductor (MIEC) such as LSCF, the process of charge transfer extended at the electrode/electrolyte interface, beyond the triple

phase boundary (TPB) points as depicted in Figure 1-4b. This means that the microstructural requirements can be less stringent; however in the case of LSM/YSZ, percolation of each phase between the electrolyte and current collector remains a pre-requisite for electrochemical activity. In this case an 'active two phase boundary' defines the solid/pore interface.

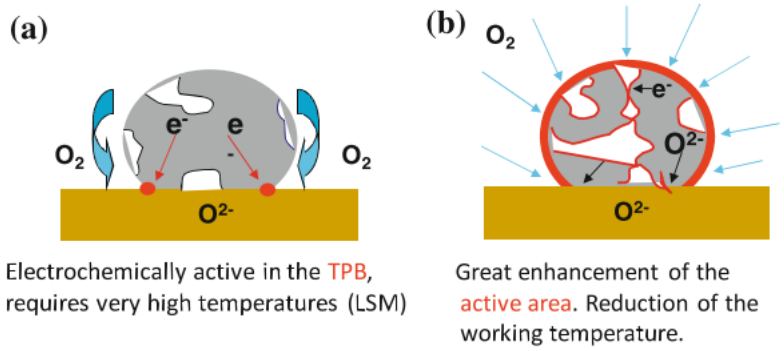

Figure 1-4 a) Electrode reaction sites restricted in TPB regions in electronic conducting cathode. b) Electrode reactions sites are extended to the whole volume of the electrode in a MIEC cathode. Reprinted from ref. [4].

In view of the connectivity of the phases by the percolation theory, some active and inert TPBs must be considered. A connected pathway of ionic conductor is required to deliver oxide ions from electrode to the electrolyte. Similarly, a continuous pore network is essential to deliver gas species to the surface of the electrode. Therefore, an isolated pore will not contribute to the gas transport, thus reducing the overall porosity and active surface area.

In the case of composite electrodes comprising a MIEC and an ionic conductor (e.g. LSCF/CGO) the percolation of the CGO phase will be crucial when the ionic conductivity of the MIEC falls down in a great extent at low temperatures and when it behaves as a pure electronic conductor. In such a case, active and inert TPBs determine the overall performance. As an example, TPB1 can be considered theoretically active as there is a contiguous ionic, electronic and pore network. However, TPB2 and TPB3 are inactive because of a lack of connectivity in the electronic and ionic phases, respectively (Figure 1-5).

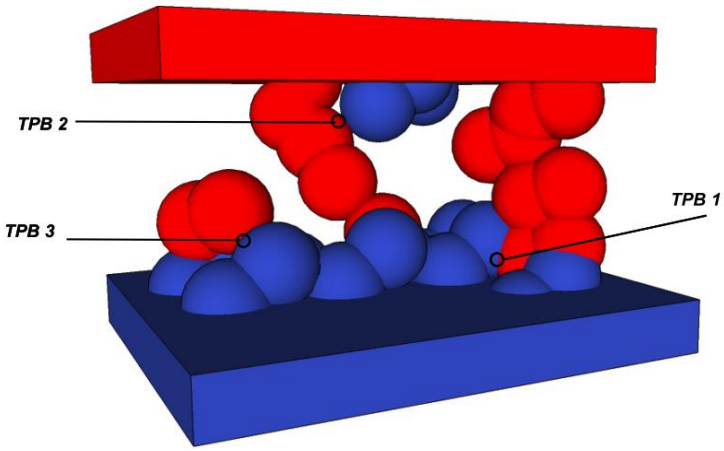

Figure 1-5 Representative composite cathode, blue is ionic conducting phase, red is electronic conducting phase. Reprinted from ref. [5].

In summary, most of the power losses in a SOFC cell originate from the electrode and the electrolyte. The rate of electrode kinetics and charge transfer properties in the solid state depend on the physical and chemical properties of the SOFC elements. Furthermore, since the individual losses scale with the relevant geometrical parameters, the geometry of electrode (microstructure) and the electrolyte (thickness) are decisive in SOFC performance. Accordingly, the main focus of the development of SOFCs is directed on the reduction of polarization and ohmic losses through the material choice and the microstructural design. A fine microstructure would increase the active sites for oxygen reduction reactions (ORR) and facilitates the electrode kinetics. Particularly, the amount and the scale of the porosity have great significance in rate determining steps. An open porosity helps bringing the oxygen to the active sites. At the same time, porosity in the nano-scale increases the surface area, thus enabling more oxygen exchange at the surface. The electrochemically active zone in a cathode material is restricted from some hundreds of nanometers to a few micrometers. This could be further exploited by engineering the structure of the pores; nano-scale porosity near the electrode/electrolyte interface and micro-scale porosity above the active length to convey the bulk diffusion of oxygen. Hierarchically structured porous materials are increasingly being recognized by their high performance in many applications for energy conversion and storage devices [6,7]. It has been shown that while macro-pores facilitates mass transport, nano porous network enhances electrochemical reactions in the SOFC electrodes [8]. Nevertheless, hierarchical porosity should be well tailored according to the percolation of electronic and ionic phases. All these factors play a key role on the polarization resistance of SOFC electrodes [9–

11]. In the following, after a quick review on the state-of-the-art electrolyte and anode materials, more detailed information on the cathode materials are given.

1.5 State-of-the-art SOFC components

Numerous materials and material combinations have been considered since the SOFC research has emerged. Nevertheless, only a few candidates take the lead for SOFC components. Common materials for electrolytes and anodes are presented in the following sections. According to the focus of this work, detailed information will be given on the cathode materials, in particular $La_{0.6}Sr_{0.4}Co_{0.2}Fe_{0.8}O_{3-\delta}$ will be discussed.

1.5.1 Electrolyte materials

The main task of the solid electrolyte is to separate the cathode and the anode gas space and connect them by only ion conduction. The membrane must therefore be gas-tight and have high ionic conductivity (σ_{ic}) and low electronic conductivity (σ_{ec}). Doped zirconium oxide (ZrO_2) has established itself as one of the most preferred electrolyte material as it best meets the requirements. The high ionic conductivity of the material results from the substitution of Zr^{+4} cation by a trivalent cation from transition group metals. Typically, yttrium or scandium are used, although other cations such as the alkaline earth metals, calcium or magnesium (low ionic conductivity) or the rare earth samarium, neodymium, dysprosium or gadolinium, would also be possible [12]. The oxygen vacancies are formed by this substitution in the crystal lattice, thus leading to an improvement in the ionic conductivity, which is based on a hopping mechanism [13]. This process is thermally activated, so that high temperatures up to 1000 °C are required for high ionic conductivity. Most commonly yttrium is used as a doping element with 8 mol. % Y_2O_3 in ZrO_2 (8YSZ). With this doping amount the fluorite phase is stabilized in the cubic phase up to the melting point above 2500 °C [12]. The linear thermal expansion coefficient of 8YSZ in the temperature range of 30 to 800 °C is $\alpha_{8YSZ} = 10.5 \cdot 10^{-6}\ K^{-1}$ [14]. Besides 8YSZ, 3YSZ (3 mol. % Y_2O_3 in ZrO_2) has also been extensively studied in the past. It is mechanically much more stable (higher tensile strength, elastic) than 8YSZ, but has a significantly lower ionic conductivity [12,15]. The highest ionic conductivity of doped zirconia is achieved with a doping of 10 mol. % Sc_2O_3. This is attributed to the lower distortion of

crystal lattice (ionic radii of Sc^{+3} is close to Zr^{+4}), leading to a smaller energy for defect association, which increases mobility and thus conductivity [16,17] (Figure 1-6).

In addition to the zirconium oxide-based electrolyte materials, there are other interesting alternatives to YSZ, especially for lower operating temperatures, such as ceria-based or lanthanum gallate-based materials [4,16]. The most common doping of ceria-based electrolyte materials are gadolinium (CGO), samarium (SDC) and yttrium (YDC), wherein cerium oxide doped with gadolinium and samarium ions have the highest ionic conductivity due to similar ionic radii of Gd^{3+} and Sm^{3+} to that of Ce^{4+}. For CGO, there are often inconsistent experimental reports for the optimal doping concentration of gadolinium that exhibits the maximum conductivity. For instance, 10 mol. % [18], 15 mol. % [19] or 20 mol. % [20] have been reported as optimum. Some authors suggested that the peak concentrations were temperature dependent. For example, shifts from 15 to 21 % mole fraction of the dopant with a temperature increase from 500 to 800 °C [21], from 20 to 24 % mole fraction with a temperature increase from 700 to 800 °C [22], and from 15 % mole fraction of the dopant below 400 °C to 20 % above 400 °C [20] have been reported. The scatter in the data can be mainly attributed to the sample preparation, e.g. fabrication technique, sintering temperature, the amount of impurities in the starting powders. Steele reported a considerable grain boundary resistivity in the presence of SiO_2 in ceria-based materials [23]. He described SiO_2 as an omnipresent impurity in minerals, which can also easily be introduced from the furnace refractories during sintering procedure. Kharton *et al*. reported the best stability for 10 mol.% Gd doped ceria ($Ce_{0.9}Gd_{0.1}O_{2-\delta}$) in reducing atmospheres and at temperatures below 1000 K, which makes $Ce_{0.9}Gd_{0.1}O_{2-\delta}$ the most appropriate electrolyte material for IT-SOFCs [24]. The linear thermal expansion coefficient of $Ce_{0.9}Gd_{0.1}O_{2-\delta}$ in the temperature range of 30 to 800 °C is $\alpha_{CGO} = 13.4 \cdot 10^{-6}\ K^{-1}$ [24]. In comparison to zirconium oxide-based electrolytes, doped ceria electrolytes have the advantage of being chemically stable with highly active cathode materials such as $(La,Sr)CoO_{3-\delta}$ (LSC), $(La,Sr)(Co,Fe)O_{3-\delta}$ (LSCF), and $La(Ni,Fe)O_{3-\delta}$ (LNF). Therefore, they are used as barrier layer between otherwise incompatible combinations of 8YSZ and the aforementioned electrodes [25,26].

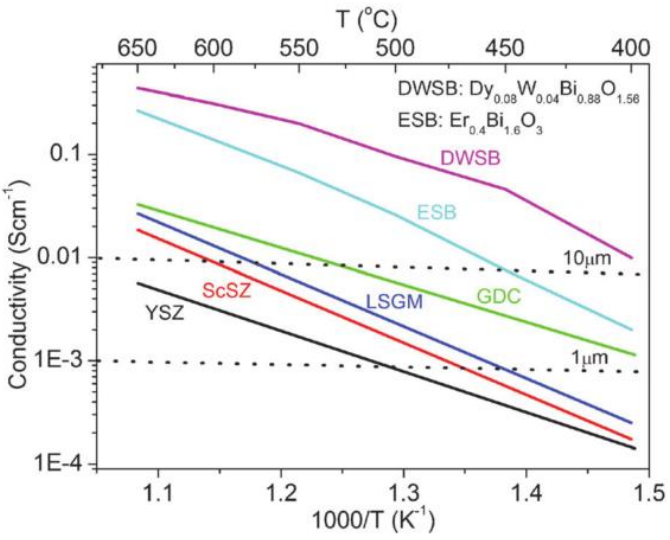

Figure 1-6 Temperature-dependent ionic conductivity of solid electrolyte materials. The two lateral lines represent the theoretical ionic conductivity for 1 and 10 μm thick electrolytes. Reprinted from [27].

Unfortunately, ceria undergoes partial reduction to Ce^{3+} in a reducing atmosphere, such as the one existing at the anode [28,29]. The electrolyte becomes mixed conductor, resulting in an internal short circuit of the cell. Studies on $Ce_{0.9}Gd_{0.1}O_{1.95}$ have shown that this is particularly pronounced at temperatures greater than 600 °C [30]. However, this may be acceptable for applications at lower temperatures [30]. Nevertheless, the electronic conductivity cannot be completely eliminated even by a thin, electron-blocking intermediate layer of doped zirconia [31,32].

The lanthanum gallate perovskites, especially doped with strontium and magnesium, $La_{1-x}Sr_xGa_{1-y}Mg_yO_{3-\delta}$ with x, y = 0.1-0.2 (LSGM), possess the highest ionic conductivity at temperatures greater than 650 °C compared to the previously mentioned materials (see the trend in Figure 1-6). Furthermore, the linear thermal expansion coefficient of LSGM in the temperature range of 30-800 °C is in the range of α_{LSGM} = 10.4 -10.9·10^{-6} K^{-1} [14]. However, this material show several chemical instabilities, e.g. Ga evaporation during sintering [33], formation of a poorly conducting second phase in combination with nickel-containing anodes, degradation during long-term exposure in reducing environments (gallium oxide depletion) [34], which make them dubious candidates for further application in SOFCs.

For an electrolyte resistance less than 0.1 Ω cm^2 (consistent with a desired power density greater than 1 W cm^{-2}) and a typical electrolyte thickness of ~ 10 μm, the conductivity of the

electrolyte should be greater than 0.01 S cm^{-1}. Following Figure 1-6, the operating conditions of YSZ should be higher than 700 °C. Otherwise, reducing the thickness of the YSZ to 1 μm, allows the operating temperature to be lowered to 600 °C. Apart from that, higher conductivity electrolyte materials such as ScSZ, CGO or LSGM or the combination of two ionically conducting bi-layered electrolytes can be used for intermediate to low temperature SOFCs.

1.5.2 Anode materials

At the anode, the fuel gas reacts with oxygen ions coming from the electrolyte at the TPB, giving two electrons per oxygen ion. In the case of hydrogen (H_2) as fuel gas, water vapor is produced (Eq. 1-1).

In principle, the following requirements should be fulfilled: The anode must have high electrical conductivity, high catalytic activity and high number of reaction sites (TPB). It should also be sufficiently porous in order to ensure the supply and removal of the fuel gas and the reaction products. Furthermore, it must be chemically stable and chemically compatible with the electrolyte material. These requirement profiles are best met in a combination of nickel and YSZ [35]. This composite anode shows a percolation threshold in the conductivity vs. the amount of Ni curve. The percolation of the two conducting phases, Ni the electronic conductor and YSZ the ionic conductor, is required to ensure a well-functioning anode [36]. Pure metallic nickel has a very high thermal expansion coefficient (TEC) ($16.9 \cdot 10^{-6}\,K^{-1}$), compared to 8YSZ ($10.5 \cdot 10^{-6}\,K^{-1}$). When both are mixed, they form a Ni-YSZ cermet which has a reduced TEC ($12.7 \cdot 10^{-6}\,K^{-1}$, for 40 vol. % of Ni + 60 vol. % YSZ).

Although, the potential of Ni-YSZ cermet as anode material is beyond doubt, there are still some problems such as agglomeration of nickel, sulphur poisoning and carbon deposition when natural gas is used as the fuel. Issues similar to electrolyte materials may come up, regarding the expansion of its volume upon redox cycling which may even cause cracking of the anode (cermet) and/or thin electrolyte coating. This may lead to gradual degradation in output power.

1.6 Cathode Materials

Cathode polarization resistance R_{pol} is a dominant cell loss mechanism with relatively high activation energy associated with oxygen reduction especially at low temperatures. A good candidate should possess sufficient electronic conductivity to minimize ohmic losses. A thermal expansion coefficient matching reasonably well with the electrolyte material is also desirable to avoid thermo-mechanical stresses. Phase stability with the electrolyte is another issue to be concerned about for long-term usage.

Three main families of perovskite based MIEC cathodes have been extensively studied for IT-SOFCs: the cubic type perovskites (ABO_3), the layered perovskites ($AA'B_2O_6$) and the Ruddlesden-Popper ($A_{n+1}B_nO_{3n+1}$) phases. Since a cubic type perovskite is used in this thesis, only the crystal structure of ABO_3 type perovskite is shown in Figure 1-7. These materials possess an oxygen 6-fold coordinated transition metal scaffold (BO_6) where alkaline earth or lanthanides ions (A) are located on the vertices of the cube containing the octahedral. The alkaline earth (Ca, Sr, Ba) and/or lanthanide (Ln = La, Pr, Nd, etc.) cations are randomly distributed on A-sites and O-vacancy defects are also randomly distributed on the O-sub-lattice [37].

Among the many possible combinations, the $La_{1-x}Sr_xCo_{1-y}Fe_yO_{3-\delta}$ family of compounds have been widely studied and applied to SOFCs as electrode components. The cubic perovskite structure is stable over the full composition space because of the similar ionic radii (Sr^{2+} (XII) = 1.44 and La^{3+} (XII) =1.36, $Co^{3+/4+}$ (VI) = 0.53-0.61 and $Fe^{3+/4+}$ (VI) = 0.55–0.645 Å). In general, these compounds have high electrical (100–1000 S cm^{-1}) and ionic conductivity (0.001–0.1 S cm^{-1}) at 600 °C. The compositions in both A-site and B-site were explored to find an optima in MIEC properties. The $x > 0.2$ of Sr in the A-site results in increased TEC [38]. The electrical conductivity increases for $x < 0.4$ and decreases for $x > 0.4$ for Co-rich compounds [38,39], while compounds with rich Fe content in the B-site decrease the TEC [39]. $La_{0.6}Sr_{0.4}Co_{0.2}Fe_{0.8}O_{3-\delta}$ is therefore the best compromise between high TEC values and low conductivity. It has a rhombohedral structure at room temperature [38].

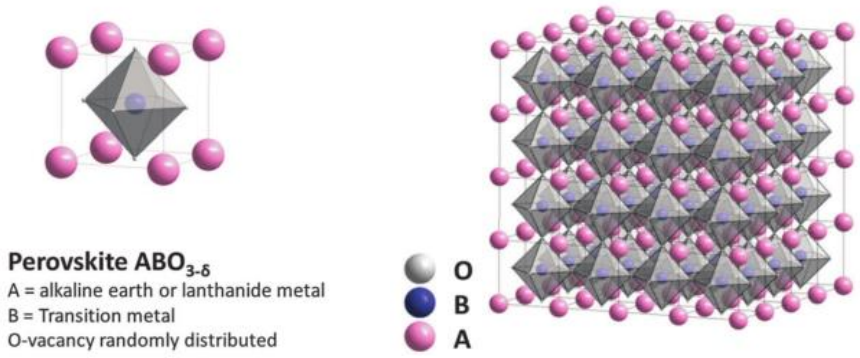

Figure 1-7 Crystal structures of perovskite MIEC materials. Reprinted from ref. [40].

1.7 Microstructural factors affecting the cathode performance

The influence of electrode microstructure on SOFC performance has been widely demonstrated affecting the electrochemical, transport and mechanical properties of the cell. This has motivated significant efforts to design and model high performance electrodes.

This section describes performance-related microstructure properties in single-phase and composite LSCF cathodes. The Adler–Lane–Steele (ALS) model provides a good illustration of how these basic oxygen transport properties and microstructure properties determine the area specific resistance *ASR* of a porous single phase MIEC electrode. It is based on semi-infinite porous cathodes which uses volume-averaged geometrical parameters, linear irreversible thermodynamics in reaction rates and neglects gas transport losses. Some information on the real geometrical parameters are required, all of which can be obtained from 3D reconstructed synchrotron tomography [41,42] or FIB/SEM data [43,44]. The model gives:

$$ASR = \left(\frac{RT}{4F^2}\right)\left(\sqrt{\frac{\tau}{(1-\varepsilon)aD_o k_o C_o^2}}\right) \qquad 1\text{-}14$$

where R the gas constant, T the temperature, F Faraday's constant, c_o the concentration of oxygen lattice sites in equilibrium, τ the solid-phase tortuosity, ε the fractional porosity, a the specific surface area and Do, ko the oxygen transport parameters.

1.7.1 Influence of particle size

The processing is shown to have great influence on the electrochemical performance [45,46]. Sintering is a matter of processing and it affects long term operation of SOFC cathodes. During fabrication, optimization of the sintering temperature aims to regulate the particle size to maximize the tpb density for an enhanced electrochemical performance, while maintaining desirable mechanical and mass transport properties.

Eq. 1.14 illustrates the important role of nano-scale microstructures (small particle size) leading to high characteristic surface areas. Using the same equation, an estimate of *ASR* for a broad range of transport parameters and particle sizes is made (Figure 1-8, [40]) Specific surface area is an estimate depending on the particle size. At 600 °C, a reduction in *ASR* by factor of ~ 30 is anticipated when the particle size is reduced from 1 μm to 1 nm.

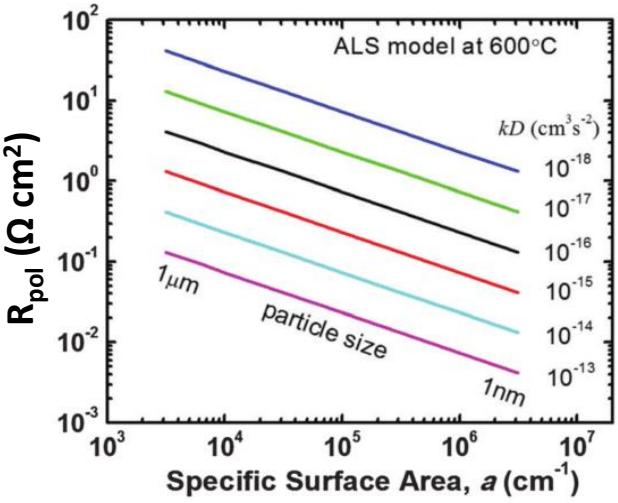

Figure 1-8 Cathode polarization resistance calculated by ALS model at 600 °C for *kD* values ranging between 10^{-13}-10^{-18} cm^3s^{-2} at pO_2 = 0.209 atm. Reprinted from ref. [40]

Völker *et al*. conducted a parametric study on the influence of particle size (50 nm to 1000 nm) in LSM/YSZ cathode by their one-dimensional percolation micro-model [47]. As an output of the model, they reported the power density of identical volume fractions of monodisperse cathode particles. The cathode showed the peak performance when the particle radii was150 nm. In the following, they showed the influence of particle size for different volume fractions of electronic phase. A constant volume fraction of 0.415 yielded the highest power density within the range of 200 nm to 1000 nm, dropping to smaller volume fractions only for particles

smaller than this range. It is important to note that the particle size ratios of ionic to electronic conductor influences the volume fractions. Considering $R = {}^{r_{ic}}/_{r_{ec}}$ (r_{ic} and r_{ec} are the particle sizes of ionic and electronic conductors, respectively), Völker *et al*. reported that for r_{ec} < 200 nm, a particle size ratio of R > 1 leads to an increase of the maximum achievable power density. For example, for r_{ec} = 75 nm, the highest power density was achieved for a size ratio of R = 4.7 and an electric particle volume fraction of 0.16.

1.7.2 Influence of pore phase

The influence of pore size is one of the key parameters used to evaluate different mass transport models. This is because an appropriate mass transport model for large pore sizes may be not suitable for small pore sizes. The diffusion process within a pore can be typically divided into two diffusion mechanisms: molecular diffusion and Knudsen diffusion. Molecular diffusion is dominant for large pore sizes and high system pressures, while Knudsen diffusion becomes significant when the mean-free path of the molecular species is much larger than the pore size. Suwanwarangkul *et al*. studied the relationship between pore size and the concentration overpotential [48] by comparing Fick's dusty-gas and Stefan-Maxwell models. They came to a conclusion that the dusty-gas model is suited best for simulating the gas transport of a binary gas mixture.

In a numerical model generating composite electrodes, Kenney *et al*. [49] showed that pore size depends on the composition of the microstructure. For example in LSM/YSZ composite cathode, the pore size tend to increase as the LSM volume fraction increases since the LSM particles are larger than the YSZ particles. On the other hand, for the mono-sized particle case, pore size remains constant throughout the entire range of LSM volume fraction.

1.7.3 Influence of ionically conducting second material in MIEC electrodes

In terms of influence of microstructure, Mortensen *et al*. took a similar approach to the ALS model and defined a 1D analytical expression describing the impedance of porous MIEC:CGO composite electrodes [50]. Their model includes vacancy transport coefficient, $\widetilde{D}_v$ in both the MIEC and the CGO (IC), and oxygen exchange at the MIEC/gas surface.

$$\widetilde{D}_v = \frac{\Phi_{IC} \cdot c_{v,IC}}{\tau_{IC} \cdot c_{v,MIEC}} D_{v,IC} + \frac{\Phi_{MIEC}}{\tau_{MIEC}} D_{v,MIEC} \qquad 1\text{-}15$$

where Φ represents the volume fractions of a phase, τ is the tortuosity and c_v is the oxygen vacancy concentration. They found that *ASR* could be decreased in the cases where the vacancy transport coefficient of ionically conducting phase was larger than the MIEC phase. The model has been successfully fitted to the impedance spectra of $(La_{0.6}Sr_{0.4})_{0.99}CoO_{3-\delta}$– $Ce_{0.9}Gd_{0.1}O_{2-\delta}$ composite films. As in the case of pure MIEC electrodes, increasing the MIEC surface area in the composite reduces the *ASR*.

Although the electronic conductivity of LSCF(6428) is high enough (330 S cm^{-1} at 650 °C [38]), its oxygen ion conductivity is quite low (0.007 S cm^{-1} at 650 °C [51]). It has been demonstrated that the addition of a second phase with high ionic conductivity in the MIEC matrix, typically the same as the electrolyte material, allows the electrode performance to be dramatically improved [52–58]. Typically, $Ce_{0.9}Gd_{0.1}O_{1.95}$ (σ_{CGO} = 0.025 S cm^{-1} at 650 °C) is used as the secondary cathode component, for its good chemical compatibility with LSCF, its availability and affordability. Dusastre *et al*. reported a fourfold performance improvement by the introduction of 36 vol. % CGO in LSCF [52] and Murray *et al*. measured a tenfold decrease in cathode polarization resistance with 50 wt. % CGO [54]. Similarly, with a 60 wt. % CGO composite Leng *et al*. recorded a cathode polarization resistance of 0.17 Ω cm^2 at 600 °C, about seven times lower than pure LSCF [57]. All these studies point to the conclusion that CGO addition leads to a lowering of the area specific resistance (ASR). Dusastre *et al*. were the first to correlate the optimal CGO content to the porosity levels in LSCF [52]. Figure 1-9 illustrates the effective conductivity values for given amount of CGO and porosity in LSCF film. A sudden jump in σ^{eff} implies that the percolation limit is reached at that value. For example, in a dense LSCF/CGO film (0 % porosity), at least 36 vol. % CGO should be added in LSCF to improve the cathode ionic conductivity. Increasing the porosity, increases the necessary amount of CGO for a percolating network. Nevertheless, it is also important not to disrupt the percolation network of the MIEC phase (electronic percolation).

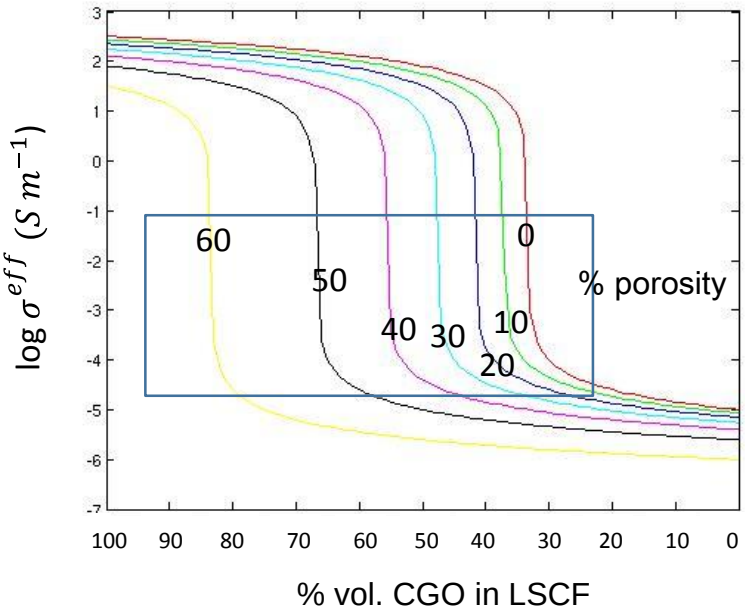

Figure 1-9 Effective conductivity of LSCF/CGO composite films at 500 °C calculated by effective medium theory. Readapted according to ref [52].

1.7.4 Hierarchical cathode microstructures

Typical SOFC electrodes deposited by screen-printing or tape-casting techniques suffer from lack of microstructural control at different length scales [59,60]. The resulting microstructures have highly tortuous gas and percolation pathways which hinder gas flow and lead to reduced efficiencies [61,62]. At this point, there is widespread interest in the development of hierarchically porous materials, which integrate multiple levels of porosity (micro- to nano-) in its microstructure. Owing to their outstanding properties such as high surface area, excellent accessibility to active sites, and enhanced mass transport and diffusion, they can facilitate charge transfer through the electrode/electrolyte interface, reduce the ion diffusion pathway, and accommodate volume changes during cycling [63]. In the following, some examples of innovative techniques for depositing hierarchical microstructures is given.

Freeze-casting is a technique that generates highly anisotropic pore structures in different length-scales. Lichtner *et al*. manufactured LSM/YSZ composite cathodes with this technique [64]. Figure 1-10 shows the microstructure with aligned pore channels of ~50 μm (in width), which improve the gas penetration and provide enhanced mechanical properties.

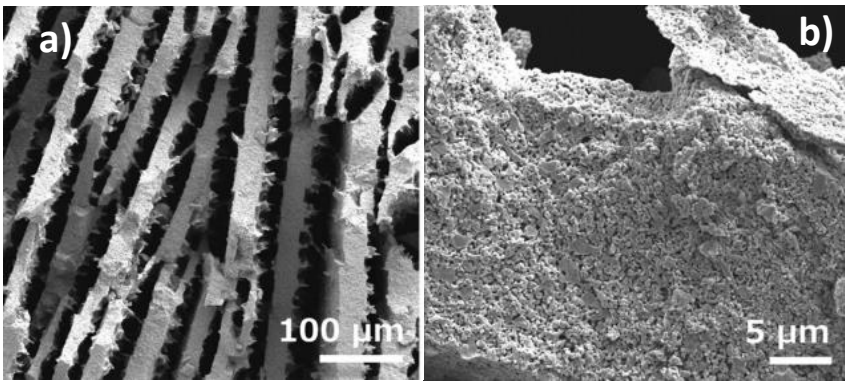

Figure 1-10 Top view SEM images of freeze cast LSM/YSZ composite cathode with a) micro-porosity b) nano-porosity. Reprinted from ref. [64]

Li *et al*. [65] and Droushiotis *et al*. [66] showed the micro-tubular SOFC design deposited by co-extrusion technique. The hierarchical nature of the electrode microstructures consist of vertically oriented micrometer-sized porosity of ~500 µm, as illustrated in Figure 1-11.

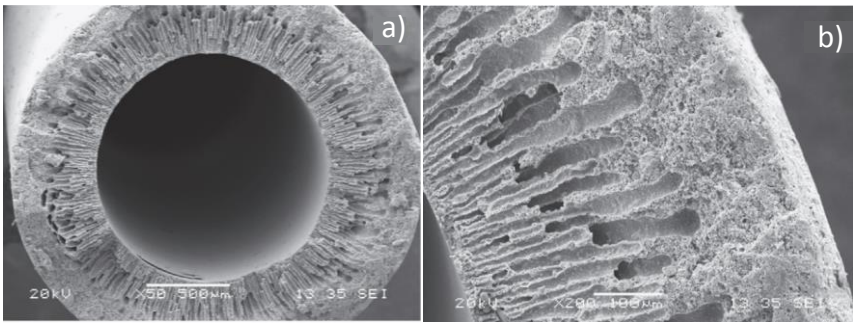

Figure 1-11 SEM images of micro-tubular SOFC: a) whole tube, b) zoom in to the tube wall. Reprinted from ref. [65].

Finally, Lejeune *et al*. showed the fabrication of different kinds of 3D ceramic pillar array structures by ink-jet printing process [67]. Figure 1-12 illustrates the highly ordered ceramic structures grown on ceramic supports. Recently, Yu *et al*. reported a porous silver thin film cathode fabricated by inkjet printing process for low-temperature solid oxide fuel cell applications [68]. Although, the method is still in its infancy, it shows the feasibility for such applications. The electrochemical performance of the inkjet-printed silver cathode was compared with those fabricated by typical sputtering methods. They reported that inkjet-printed silver cathodes showed lower electrochemical impedance due to their porous structure, which facilitated oxygen gaseous diffusion and oxygen surface adsorption−dissociation reactions.

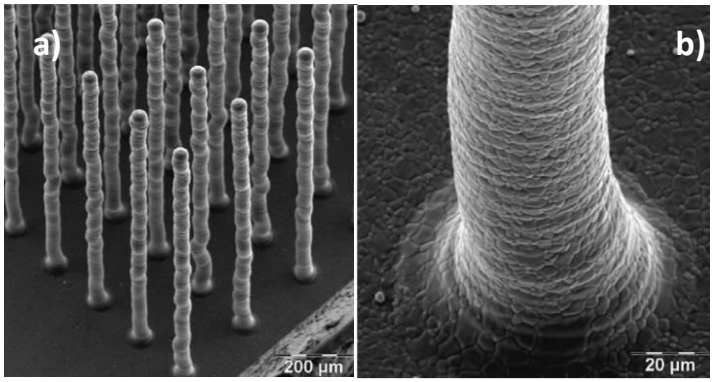

Figure 1-12 SEM images of sintered TiO_2 micro-pillars, fabricated on TiO_2 green tape. Reprinted from ref. [67].

The next paragraph is entirely devoted to the electrostatic spray deposition, which is the fabrication technique that is used in this thesis for processing hierarchical microstructures in finer scale. The highlights of the two previous PhD projects are also briefly introduced.

Electrostatic spray deposition (ESD) is a unique and a versatile thin film fabrication method which provides several advantages of simple and low–cost setup, non–vacuum, low deposition temperature, as well as good control of the composition and morphology. Although reports from many laboratories in different fields exist [69–74], it has been mostly and extensively studied by Prof. Schoonman (Delft University of Technology) and Prof. Djurado (Université Grenoble Alpes) groups for various components in energy devices such as batteries [75,76] and fuel cells [77–80]. The resulting electrodes could be dense, porous, thick-film and thin-film, all of which can be controlled by varying deposition conditions [81] (Figure 1-13). It is believed that controlling the electrode microstructures is an effective way to optimize electrochemical performance. For example, the 3D cauliflower–like films with high surface area and high porosity are found beneficial for improving reaction kinetics [82,83].

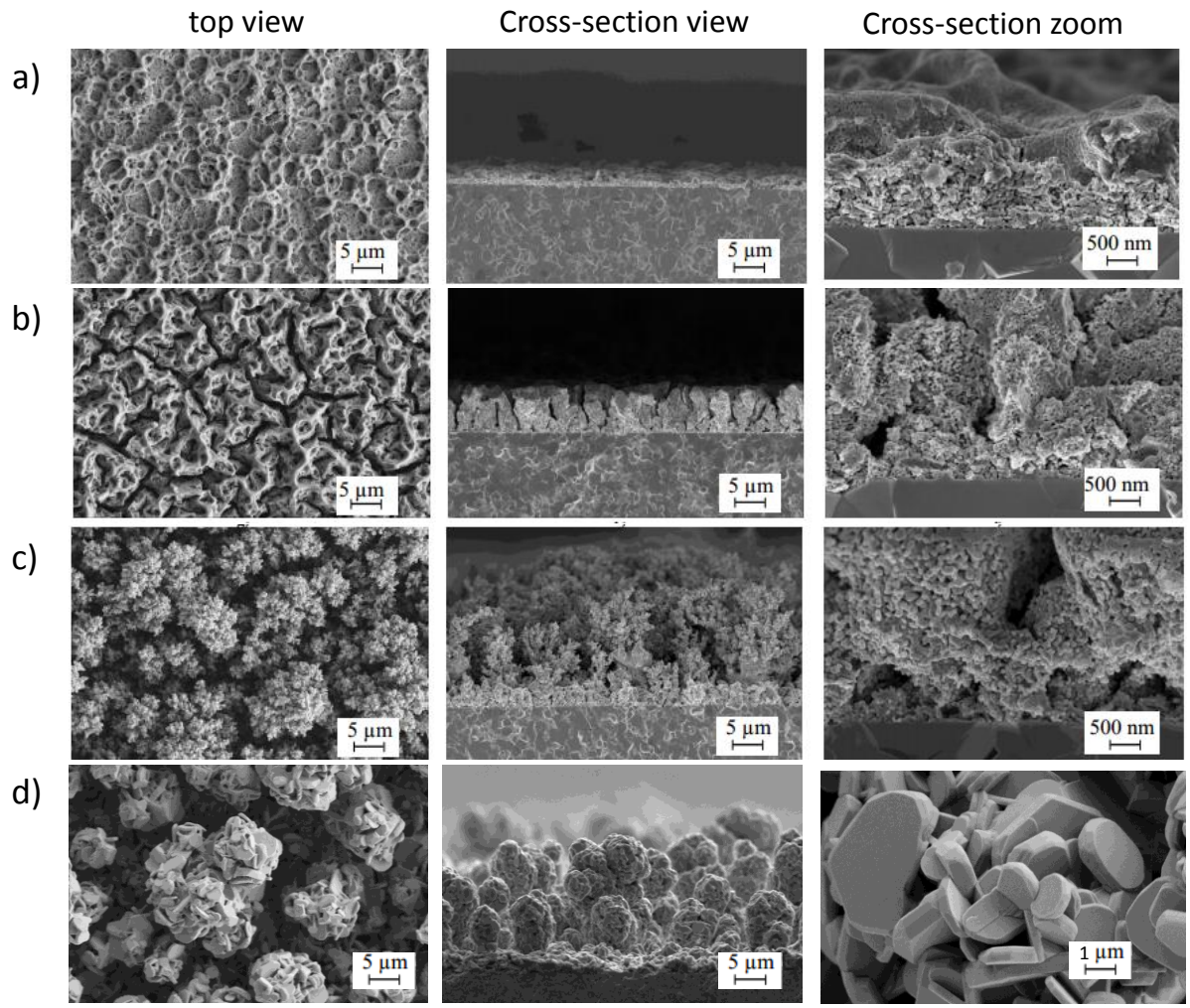

Figure 1-13 The microstructures that can be obtained by ESD, a) dense b) columnar and c) coral [83] and d) coral-type microstructure with plate-like grains [84].

Previously in our group, cathode films deposited by ESD for applications in IT-SOFCs were studied by Daniel Marinha [85] and Jaroslaw Sar [86]. Marinha *et al.* studied the performance of LSCF films sintered at 900 °C for 2 h in ambient air on dense CGO electrolyte in terms of cathode area specific resistance (ASR) from 400 to 600 °C in OCV [83]. The oxygen reduction reaction mechanisms in LSCF films have been studied for three distinct morphologies (dense, columnar and coral-type, Figure 1-13a, 13b, 13c) as a function of oxygen partial pressure and temperature. Up to three elementary steps were identified by equivalent circuit fitting: charge transfer process at the LSCF/CGO interface, a diffusion process within the volume of LSCF and oxygen transfer at the LSCF/gas interface. Among the three microstructures, the coral one with higher electrode-pore surface area was found to show the peak performance with 0.82 Ω

cm^2 at 600 °C, using Pt grid as CCL. Following this work, Sar *et al.* fabricated LSCF/CGO composite films in coral-type microstructures sintered at 900 °C for 2 h in ambient air on YSZ electrolyte to study the electrode performance of composite films [87]. The presence of the CGO phase in the cathode becomes increasingly important to retain electrochemical performance at low temperatures, due to limitations of ionic transport in LSCF [53]. A thin dense layer of CGO film (~ 100 nm) was deposited on YSZ electrolyte prior to the deposition of composite films (5-10 μm) to avoid the formation of insulating phases like $La_2Zr_2O_7$ and $SrZrO_3$. The composition of the films in a given thickness was altered by graded or homogeneous spraying of the same amount of salt solutions of LSCF and CGO. Although a decrease in ASR was experimentally and theoretically demonstrated in graded composite films [10,88,89], Sar reported quite similar values in both compositions. However, the ASR of the composite were about 80-fold higher (66 Ω cm^2) at 600 °C than pure LSCF of the same morphology reported by Marinha *et al*. [87]. They concluded that addition of CGO did not improve the electrode performance. Although FIB/SEM or synchrotron tomography did not provide resolution of the two phases, they speculated on the insufficient percolation of LSCF and CGO phases. However, this conclusion remained no more than a mere speculation. Another point to keep in mind is that Sar *et al*. used YSZ electrolytes as support material (CGO by Marinha *et al*.) which might have influenced the total resistance. It was shown that the performance can be significantly affected by the electrolyte material, aside from the nature of the electrode/electrolyte interface and the bulk properties of the electrode material [90]. Later on, both authors deposited a second layer of LSCF (~ 20-30 μm) as current collecting layer (CCL) by screen printing above the cathode functional layer (CFL). They reported a decrease in ASR value by at least a factor of 20 at 600 °C. With this double layer cathode configuration, Marinha *et al.* achieved an ASR value of as low as 0.13 Ω cm^2 at 600 °C in a columnar-type film [91]. The lowest ASR value that Sar *et al*. obtained with double layer composite film was 0.6 Ω cm^2 at 600 °C [86].

1.8 Modelling of SOFC cathodes

Beside 1D models already presented, 2D and 3D numerical simulations of electrochemical behavior in an SOFC can be achieved by implementing charge, mass and energy balances on the microstructural framework. The first attempts of numerical models used microstructural analogues of electrodes, while more recent studies use directly tomography data. In the first

part, the modelling of SOFC cathodes is reviewed and then the finite element method (the method used in this thesis) is briefly introduced.

1.8.1 State of the Art

Models were conducted in one dimensional [92–94] two-dimensional [95,96] three-dimensional [97–100] or by Monte Carlo type techniques to randomly distribute particles of each phase with a probability assigned according to the expected volume fraction of the final electrode [101].

Several theoretical [92,102–111] studies have been dedicated on one-dimensional model to investigate the electrochemical mechanism of MIEC cathodes. All these extensive studies have led scientists to a global reactive pathway that cathodic polarization is mainly controlled by the oxygen incorporation step from the MIEC surface into the material followed by a solid state diffusion up to the cathode/electrolyte interface (where oxygen is transferred into the electrolyte).

Three-dimensional model geometries can be used to develop microkinetic models that employ a model geometry similar to actual microstructure. Schneider *et al*. used 3D discrete element method to model the performance of SOFC electrodes [10,112]. The electrodes consist of sintered mixtures of mono-sized particles of electronic and ionic conducting phases. The particle packing is created from 40 000 homogeneously mixed, randomly orientated, spherical and mono-sized particles. The packing is created numerically and densified by using the discrete element method. The model is discretized into a resistance network and solved using Kirchhoff's Law. Potential and current distributions may then be calculated and the effects of electrode composition, thickness and density are investigated. Chen *et al*. have reported techniques for extraction of geometrical and effective physical parameters from simulated microstructures based on percolation theory [113]. A sequence of papers from Ivers-Tiffée group in Karlsruhe Institute of Technology (KIT) are based on a 3-dimensional cube model solved by finite element method [100,114]. The MIEC structure is artificially generated by randomly distributed LSCF particles and porosity in a relatively narrow column. The results in terms of ASR and impedance spectra agreed well with the 1D ALS model predictions. The group then combined real electrode microstructure with their FEM model [115,116]. Indeed,

Rüger *et al*. were among the first to explore the potential of tomography data in a finite element simulation to predict ionic concentration gradients in the cathode material [116].

1.8.2 An Introduction to the Finite Element Method

The complex physical problems are expressed in terms of *partial differential equations* (PDEs). For the vast majority of geometries and problems, where these PDEs cannot be solved analytically, numerical methods like the finite element method (FEM) can be used. However, due to the discretization of the problem, the solution provided by the FEM is only an approximation of the real solution to the PDEs.

As an example, a function u can be approximated by a function u_h using linear combinations of base functions according to the following expressions:

$$u \approx u_h \qquad 1\text{-}16$$

and,

$$u_h = \sum_i u_i \, \psi_i \qquad 1\text{-}17$$

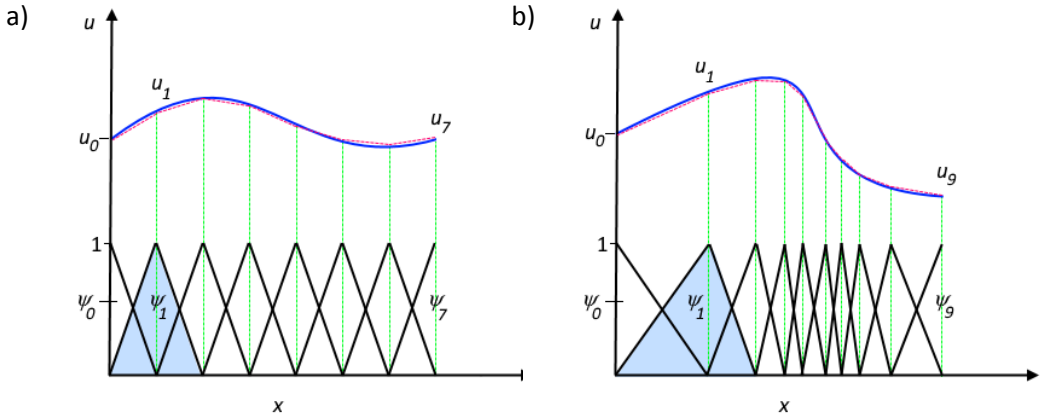

Figure 1-14 The function u (solid blue line) is approximated with u_h (dashed red line), which is a linear combination of linear basis functions (ψ_i is represented by the solid black lines). The coefficients are denoted by a) u_0 through u_7 b) u_o through u_9 . Adapted from *https://www.comsol.com/multiphysics/finite-element-method*

Here, ψ_i denotes the base functions used for the discretization and u_i denotes the coefficients of the functions that approximate u with u_h. Figure 1-14 illustrates this principle for a 1D problem using linear functions. In this particular example, seven uniformly distributed elements along the *x*-axis, where the function u is defined (Figure 1-14a) while smaller elements are defined in a region where the gradient of u is large (Figure 1-14b). Depending on the problem, other functions may be chosen instead of linear functions.

1.9 Degradation problems and long term stability

Although research efforts were primarily focused on increasing the efficiency of the SOFCs, increasing number of studies have also been conducted to analyze the degradation mechanisms. A good compilation on general aspects of chemical reactions and related phenomena that lead to the mechanical instability of the cell or degradation of the electric power has been thoroughly reported by Yokokawa *et al*. [117]. In the following, the degradation mechanisms of the individual cell components were described and discussed. The ageing processes with emphasis on the material systems were explained.

1.9.1 Degradation in electrolytes

The degradation of the electrolyte can be described with reference to the speed of decreasing ionic conductivity. Although the degradation behavior of doped zirconium oxide is relatively simple, there are many long-term studies in the literature [12,118–120]. In principle, it can be said that the change in conductivity over time depends on the temperature and the dopant concentration. Furthermore, the precipitation of impurities in the grain boundaries [121,122], the segregation of dopant cations in the grain and the grain boundaries [123], the precipitation of tetragonal phases [124] were proposed to be reasons of the decreasing conductivity.

Contrary to the many studies on YSZ, few degradation studies are found on the Gd doped ceria so far. Zhang *et al*. [125,126] investigated the aging effects in various compositions of $Ce_{1-x}Gd_xO_{2-\delta}$ ($0.05 \leq x \leq 0.4$). It was found that the aging of the material was dependent on the Gd content. The compositions with $x \leq 0.2$ after aging at 1000 °C for 8 days show an increase in the grain boundary conductivity, while compositions with $x \geq 0.2$ show a decrease in conductivity values both in the grains and the grain boundaries. As aging mechanism, the formation of micro-domains was proposed, which develop from a critical doping concentration

at x = 0.2. In another study, it was shown that the reduction of Ce^{4+} ion under fuel conditions led to an increase in volume, which eventually may lead to mechanical stresses to cracking or delamination of individual layers [29,127].

Another degradation phenomenon, which is primarily relevant in multilayer electrolyte structures such as Gd-doped ceria (CGO) on 8YSZ electrolyte, may occur depending on the interactions between the two layers and contribute greatly to the electrolyte resistance. State-of-the-art CGO interlayers are usually screen printed on the electrolyte 8YSZ and sintered at elevated temperatures. The sintering step leads to inter-diffusion of elements between YSZ and CGO and the formation of YSZ / CGO mixed phases, which have a much lower conductivity [128]. Despite a relatively high sintering temperature, the porosity and the impurity phases in the CGO layer can influence the conductivity of the electrolyte material and thus contribute to degradation. According to ZrO_2-CeO_2 phase diagram, a continuous cubic fluorite solid solution forms in between the two pure constituents [129].

1.9.2 Degradation in anodes

The agglomeration of nickel particles is one of the typical degradation phenomena in Ni / 8YSZ anodes. Here, the Ni particles agglomerate and the connected Ni network is disrupted [130–133]. Other phenomena are changing the Ni-morphology, the collapse of the ceramic network, the change in the anode porosity, delamination [117], and sulfur poisoning [134,135]. The following degradation mechanisms were specified by Yokokawa [117]: (i) material transport mechanisms (ii) deactivation (iii) thermomechanical mechanisms. The two main material transport phenomena are the change in the Ni-morphology, and the increase of the Ni particle size. This is due to the tendency of nickel, to minimize its surface energy under operating conditions. This mechanism is strongly dependent on the temperature and the water vapor pressure. Ni surface is associated with the number of catalytically active regions and thus a decrease in Ni surface results in an increased polarization resistance [117]. In operation of a SOFC, redox or thermal cycles are critical parameters as well. In this case, the change of Ni particle size in the redox cycles from Ni to NiO and back to Ni leads to irreversible changes in the microstructure [136,137] and may lead to the breaking of the cell.

1.9.3 Degradation in cathodes

Yokokawa *et al.* [117] proposed the following cathode degradations mechanisms depending on the cathode material in aging studies. All effects are influenced by operating parameters of the cell, such as temperature, current density, overvoltage, oxygen and water partial pressures (humidity) in the air: (i) Coarsening of the microstructure due to sintering; (ii) Decomposition of the cathode material; (iii) Chemical reaction with electrolyte to form insulating phases at interfaces; (iv) Spallation of the cathode; (v) Poisoning of the cathode (e.g. by chromium species).

As a result of these effects, the electronic or ionic conductivity, as well as the electro-catalytic activity of the cathode material, the electrochemically active surface area, and/or the porosity will decrease, which will results in a decreased performance of the cell.

While the ALS model suggests that increasing surface area will lead to improved electrodes, small particle sizes suffer from particle coarsening. A coarser structure improves ionic and electronic conductivity and gas permeability of the cathode, while a finer structure offers higher specific surface area and therefore to a greater number of reaction sites [138]. These effects have been observed by Shah *et al.*, for example, in recent studies of nano-scale $La_{0.6}Sr_{0.4}Co_{0.2}Fe_{0.8}O_{3-\delta}$ (LSCF) electrodes infiltrated into gadolinium-doped ceria (CGO) scaffolds [139]. They used a standard power-law coarsening model to calculate the degradation rate as a function of LSCF particle size. For a given target resistance, based on the increase in surface resistance of LSCF with decreasing T, smaller particle sizes are necessary to achieve the required R_{pol}. According to the model, in order to obtain a target resistance of 0.2 Ω cm^2, the particle size should be 2.8 nm, 38 nm and 240 nm at 500, 600 and 700 °C, respectively [140]. They found that the rate of degradation was very high at 500 °C, moderate at 600 °C and quite low at 700 °C. At high temperatures, the particle sizes are large enough that degradation could be negligible. Wang *et al.* [58] studied the degradation of LSCF/CGO composite films on YSZ electrolyte in symmetric cells at 800 ˚C for 180 h. Their results showed modest increase of the R_{pol} and no obvious increase of R_s. They have not reported any reaction product at the electrode−electrolyte interface. The authors attributed the degradation to the densification of the LSCF/CGO cathode during heat treatment rather than reactions with YSZ.

The other degradation phenomenon results from the tendency of Sr to diffuse readily from the bulk of the cathode to the surface. Sr segregation (Sr-enrichment at the cathode / electrolyte and cathode / current collector interfaces) in the anode supported cells with $La_{0.6}Sr_{0.4}Co_{0.2}Fe_{0.8}O_{3-\delta}$ cathode was observed by Simner *et al.* at 750 °C after 500 h [141]. A

non-linear degradation is determined with 0.26 % h^{-1} in the first 50 h and to 0.047 % h^{-1} in the remaining 450 h, suggesting two different degradation mechanisms. In another study, Gong *et al*. applied a thin-layer ZrO_2 coating on MIEC nano-particles using atomic-layer deposition to reduce the degradation rate [142]. The coating was found useful in suppression of Sr enrichment on the surface.

Sr also reacts with YSZ (electrolyte) and forms insulating Sr zirconate phases. When a CGO barrier layer is introduced between LSCF and YSZ, Sr may still diffuse through CGO and reach the surface of the YSZ. This can happen especially during high sintering temperatures when the diffusion kinetics are fast. The cation diffusion in the CGO layer deposited by two different techniques, screen printing and magnetron sputtering, were investigated by Jordan *et al.* [25]. The formation of $SrZrO_3$ was observed at the interface in both techniques, with in a minor degree by magnetron sputtering. The samples yielded lower durability with a poor adhesion of CGO on the YSZ electrolyte. Other techniques such as screen printed and PVD (physical vapor deposition) [143], sprayed and PLD (pulse laser deposition) [144] were employed to deposit dense CGO layers. In any case, Sr (and other metal ion) migration through the barrier layer was observed to proceed via grain boundaries.

The interaction between LSCF and CGO has been studied for a possible degradation mechanism. Inter-diffusion of elements were suggested due to mutual solubility between LSCF and CGO. Du *et al*. reported a La solubility of around 40 mol.% in CeO_2 at 700 °C [145]. Martínez-Amesti *et al*. [146] examined the solid-state reaction and inter-diffusion phenomena between doped ceria and perovskite LSF. In XRD, no extra peaks were found, but a significant shift in the peak position for LSF was observed, which was attributed to the diffusion of Ce into LSF lattice. Kiebach *et al*. studied degradation phenomena during sintering and cell operation in LSCF/CGO composite film on YSZ/CGO bilayer electrolyte [147]. They concluded that phase separation and inter-diffusion across interfaces happened mainly during sintering and to a very little degree during operation. A similar conclusion has been reached by Tonus *et al*. with LSCF (6428) and $Ce_{0.9}Pr_{0.1}O_{2-\delta}$ by studying the crystallographic structure evolution and degradation by in-situ neutron diffraction [148]. Nevertheless, the inter-diffusion between LSCF and CGO did not appear to affect the oxygen exchange properties and electrical conductivity [149].

In a recent work from Ni *et al*., Cr poisoning was investigated on symmetrical cells of LSCF(6428) at the micro- and nano-scale using impedance spectroscopy and transmission

electron microscopy [150]. While no significant microstructural change was detected, the samples poisoned by Cr showed up to 2 orders of magnitude reduction in conductivity, oxygen surface exchange rate, and diffusivity due to the formation of nanometer size $SrCrO_4$ (poor electronic conductor) and grain boundary segregation of Cr at the nano-scale. On the contrary, Chen *et al*. showed that at the micro-scale Cr deposition on the electrode surface reduced the linear porosity of the electrode from 25 % to 2 % at the surface during the polarization test at 900 °C in the presence of a Fe-Cr metallic interconnect [151].

2 FABRICATION AND CHARACTERIZATION METHODS

Chapter 2 is devoted to the technical information on the fabrication and characterization of pure LSCF and LSCF/CGO composite cathode films for IT-SOFC applications. The parameters for successive depositions of electrostatic spray deposition (ESD) and screen printing (SP) techniques to obtain double layer films are given. The widely used fundamental characterization techniques such as scanning electron microscope (SEM), transmission electron microscope (TEM) and x-ray diffraction (XRD) techniques are outlined. 3D microstructural characterization by 3D FIB/SEM tomography (focused ion beam/scanning electron microscope) and image analysis are elaborately explained. A detailed description of electrochemical characterization by electrochemical impedance spectroscopy (EIS) is presented.

2.1 Fabrication of the cell constituents

2.1.1 Fabrication of the electrolyte

1 mm thick, 1.8 mm large, dense $Ce_{0.9}Gd_{0.1}O_{2-\delta}$ (CGO) substrates were prepared by isostatically pressing CGO powder (Praxair, 99.9%, 20.5 m^2/g) at 300 MPa, followed by sintering at 1200 °C for 2 h in air. The substrates were grinded and polished to obtain a flat and uniform surface.

2.1.2 Fabrication of the cathode films

The double layer cathode films were obtained using electrostatic spray deposition (ESD) and screen-printing (SP) in sequence.

2.1.2.1 Electrostatic Spray Deposition (ESD)

The electrostatic spray deposition (ESD) is a deposition technique in which a precursor solution is contained in a syringe and injected through a needle with controlled flow rate. The solution is then atomized as an aerosol by applying an electric field between the needle and the substrate. The electric field generates the aerosol and transports it to the substrate on which the droplets spread, dry and decompose to form the film. The microstructure is thus highly dependent on the size of the droplets in the spray. The droplet size may be mono-dispersed and controlled by the deposition parameters such as solution flow rate, the distance between the substrate and the needle or the substrate temperature. ESD is of major interest based on ease of implementation and low cost of the device that requires no vacuum generation. It allows good control of the stoichiometry of the mixture of precursor salts. In addition, the films adhere well on the substrate. To prepare the precursor solution, the salts are mixed in selected proportions in a liquid solvent. ESD allows the use of a large number of precursor salts, the most common being the nitrates and chlorides but also of organometallic and even non-metallic compounds. In general, the precursor salt solutions are prepared taking into account the solvent. The solutions must decompose at the temperature of deposition. The choice of solvent is important because it influences the quality of the aerosol and the size of the droplets. In this connection, a surface tension and a relatively low viscosity are required to obtain a stable spray. The conductivity of

the solutions can vary between 10^{-8} to 10^{-1} S.cm^{-1}. The boiling temperature of the solutions containing the precursors is another fundamental characteristic that also control the morphology of deposits. Ethanol, with a boiling temperature of 78 °C is commonly used in combination with butyl carbitol whose boiling temperature is at 231 °C. By mixing the solvents in different proportions, an intermediate boiling point between these extremes can be obtained.

A diagram of the ESD device is shown in Figure 2-1a**.** The experimental setup involves a syringe-pump connected to a hypodermic needle that controls the solution flow. The substrate is placed above the needle facing the hotplate on one side. A circular mask is used to define the deposition area. The substrate temperature is measured with a type K thermocouple. The deposition process can be separated into five steps as illustrated in Figure 2-1b. Step 1 consists of atomization of the solution precursors. The principle is based on the deformation of the surface of liquid ϒ, under an applied electric field between the positively polarized tip of the syringe needle and the substrate connected to the ground. In an electric field, the ions migrate to the surface of the solution, which causes surface to charge. Finally, the hydrodynamic forces associated with the liquid and the electrical forces created by the electric field oppose each other. This leads to surface instability and distortion of the droplet that is to be atomized at the tip of the needle, which forms a stable shape called Taylor cone. Step 2 consists of transport of the aerosol. The positively charged droplets in the aerosol are attracted by the substrate that is connected to the ground. Evaporation occurs during transport which depends not only on the initial droplet size but also the distance of the substrate temperature and flow rate of the solution precursors. Indeed, the droplet size plays a vital role in the spread of the droplets on the substrate and therefore on the morphology of the layer. Steps 3 and 4 consist of the impact of droplets onto the substrate followed by spreading and drying, respectively. Step 5 illustrates the surface diffusion and decomposition/reaction of the precursor salts. What is deposited on the substrate may be a droplet or a particle depending on the process parameters and the physicochemical properties of the solution of precursors. The substrate temperature is set so as to ensure complete evaporation of the solvent. The microstructure of the deposited layer depends on the physicochemical properties of the solution of precursors and deposition conditions. A main benefit of ESD is the high degree of control of these settings for a variety of microstructures.

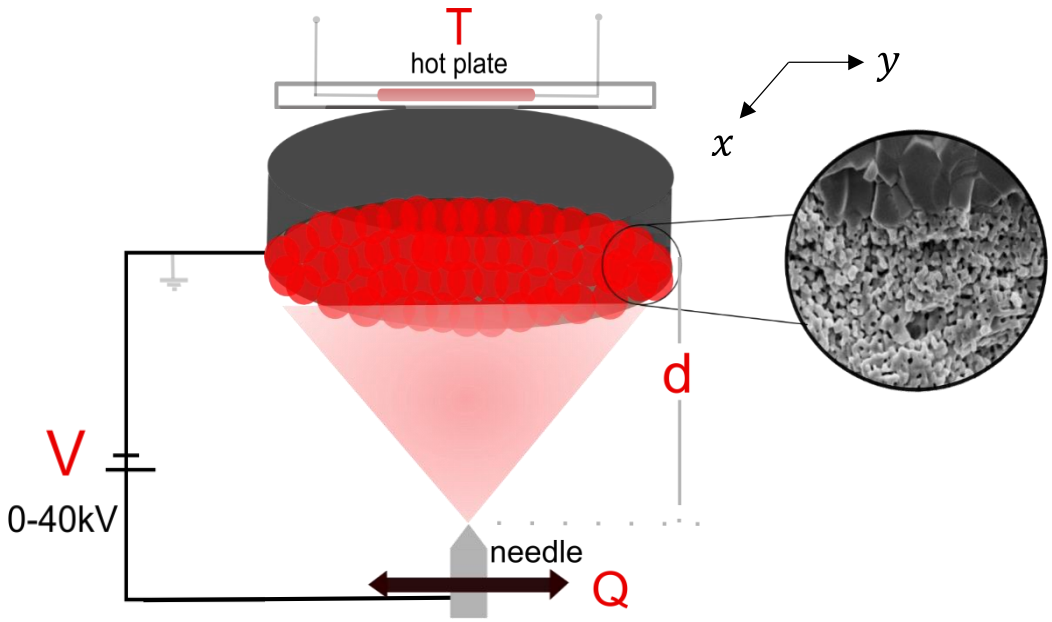

Figure 2-1 The scheme of electrostatic spray deposition (ESD); the microstructure is controlled by combined influences of Q (flow rate), d (distance between needle and substrate), T (temperature of hot-plate), V (voltage to create the spray) and the solvents in the solution [152]. The substrate holder is moved in *x-y* direction within a certain speed for more homogeneous deposition.

2.1.2.2 Microstructural Control by ESD

The formation mechanism of a layer and its microstructure mainly depends on the size of the droplets impacting the substrate and the temperature of the latter. Depending on the deposition parameters, the droplet size can vary from ~ 10 nm to 100 µm. Gañan-Calvo et al. [152] presented an equation where the droplets size (d) is correlated to the solution density (ρ), vacuum permeability (ε_0 = 8.85 x 10^{-12} F m^{-1}), flow rate (Q), solution surface tension (ϒ) and solution electrical conductivity (σ), as the following:

$$d_s \sim \left(\frac{\rho \varepsilon_o Q^3}{\Upsilon \sigma}\right)^{1/6} \qquad 2\text{-}1$$

The boiling point of the solvent is an important parameter that influences the quality of the aerosol and the droplet size. The solvent evaporation during flight can be regulated by a careful

choice of the boiling point of the solvent mixture, the temperature of the substrate and the needle-substrate distance, all of which can alter the flight time. In summary, it is the size of the droplet at the impact on the substrate and the combined effects of the spreading and drying speeds that determine the morphology of the layer. Two separate cases can be considered as shown in Figure 2-2.

- The droplets retain enough liquid to simultaneous spreading and drying on the substrate surface leading to the formation of dense or columnar type films (Figure 2-2a).
- The droplets dry completely during flight, followed by the formation of solid particles that forms with the collision on the substrate and accumulation, giving rise to a coral-type highly porous microstructure (Figure 2-2b).

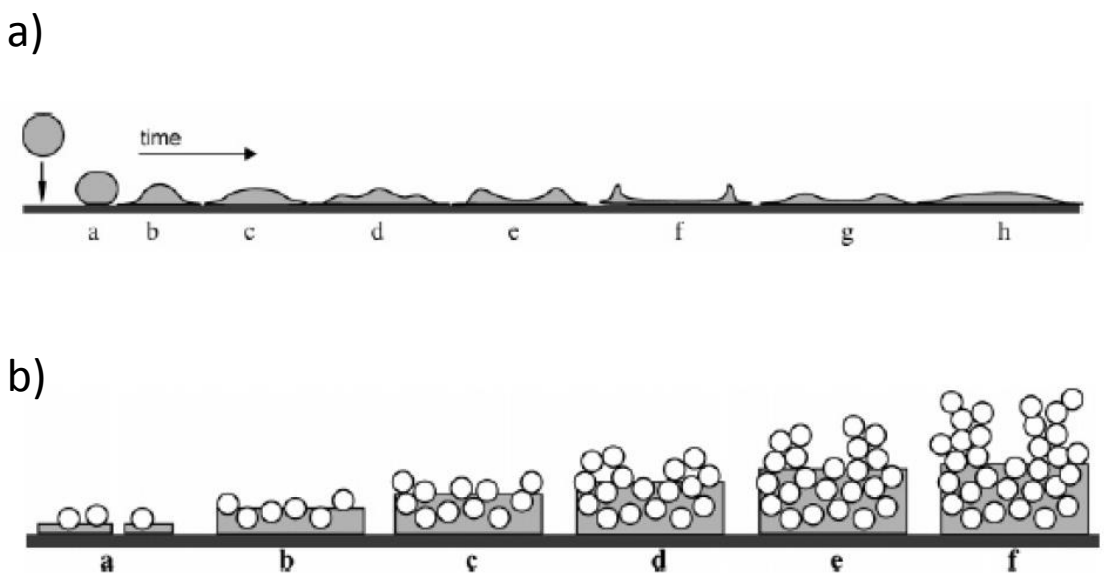

Figure 2-2 a) Spreading of droplets on the substrate b) Steps of film growth

Concerning ESD coatings, we have used the following optimized parameters as determined by Marinha [153]. A precursor salts solution for $La_{0.6}Sr_{0.4}Co_{0.2}Fe_{0.8}O_{3-\delta}$ (LSCF) was prepared by dissolving $La(NO_3)_3.6H_2O$ (Prolabo, 99.99%), $SrCl_2.6H_2O$ (Strem Chemicals, 99%), $Co(NO_3)_2.6H_2O$ (Sigma-Aldrich, 99.999%) and $Fe(NO_3)_2.9H_2O$ (Sigma-Aldrich, 99.99%) salts in adequate amounts to ensure the desired stoichiometry. These salts were mixed in absolute ethanol (C_2H_5OH, 99.9%; Prolabo) and butyl carbitol ($CH_3(CH_2)_3OCH_2CH_2OCH_2CH_2OH$, 99+%; Acros Organics 99+%) with a 1:2 volume ratio

and a total salt concentration of 0.02 mol L^{-1} for the columnar microstructures. Similarly, 5:1 distilled water/ethanol ratio have been used to deposit coral-type microstructures. The CGO solution was prepared by mixing powders of cerium nitrate hexahydrate ($Ce(NO_3)_3.6H_2O$, Rectapur Prolabo, 99.5 %) and gadolinium nitrate ($Gd(NO_3)_3.6H_2O$, Aldrich, 99.99 %). These precursors were also mixed in ethanol and butyl carbitol with a 1:4 volume ratio and a total salt concentration of 0.02 mol. L^{-1}. 100 vol. % LSCF, 75:25, 60:40 and 40:60 vol. % LSCF/CGO solutions (referred to as 100 LSCF, 75:25 LSCF/CGO, 60:40 LSCF/CGO and 40:60 LSCF/CGO, respectively) were deposited on CGO substrates using a vertical ESD setup (Figure 2-1a). The deposition was operated by controlling the substrate holder motion in x and y directions with a 1 mm s^{-1} speed. The film deposition parameters are given in Table 2-1. The solutions were atomized using a high voltage (5-6 kV columnar, 12-13 kV coral), which maintains a cone-jet atomization regime for 3 h, substrate temperatures at 300 °C (columnar) and 350 °C (coral), nozzle to substrate distances of 15 mm (columnar) and 50 mm (coral) and flow rate of 1.5 mL h^{-1} (columnar and coral). All samples were sintered at 800 °C for 2 h with a 2 °C min^{-1} heating rate and a 3 °C min^{-1} cooling rate.

Table 2-1 The ESD deposition parameters for CFL films with columnar and coral microstructures. E refers to ethanol, B butyl carbitol and W distilled water. §: σ = 60 µS/cm, γ = 0.027 N/m, boiling point: 180 °C; ¥: σ = 7500 µS/cm, γ = 0.064 N/m, boiling point: 96 °C; φ: σ = 10 µS/cm, γ = 0.028 N/m, boiling point: 200 °C [154].

Film microstructures	solvents used for LSCF	solvents used for CGO	Q, ml/h	t, h	Voltage kV	T, °C	d, mm
columnar	1:2 E/B§	1:4 E/Bφ	1.5	1h45’	5-6	300	15
coral	1:5 E/W¥	1:4 E/B	1.5	3	12-13	350	50

2.1.2.3 Screen Printing (SP)

The second layer is deposited on top of ESD coatings by screen printing technique (Figure 2-3). The support is placed onto the printing table. A printing screen of very fine mesh is mounted within a frame and placed 1 cm above the surface of the support (electrolyte). The frame is covered with a polymeric resin which leaves only some areas open where the paste can go through. The ink containing the powder is spread by the squeegee tool which forces the ink

through the screen and onto the ESD coatings. This process is controlled by the speed and pressure of squeegee, the distance between the substrate and the screen and finally the viscosity of the ink.

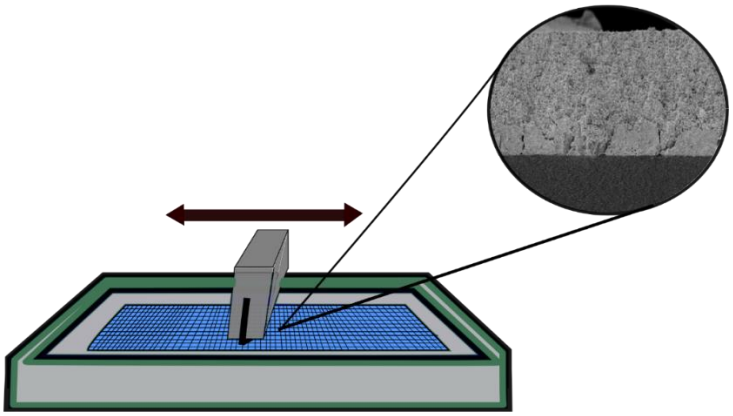

Figure 2-3 The scheme of SP; the support is placed 1 cm below the screen (grid) and the squeegee spreads the ink on the grid by applying 1 kg force.

The ink made up of $La_{0.62}Sr_{0.38}Co_{0.19}Fe_{0.8}O_{3-\delta}$ powder is provided from Marion Tech. d50 = 0.27 μm. A commercial solvent '*Produkt KD2921'* supplied from ZSCHIMMER & SCHWARZ was mixed with LSCF powder 50/50 wt. % and stirred mechanically using rotating three cylinders. The distance between two cylinders are tightened slowly after each 5 minutes during half an hour. The thickness of this layer was controlled with one or several successive depositions with intermediate drying steps at 100 °C. In the rest of the thesis, an ESD deposited film will be referred to as a cathode functional layer, simply CFL, and screen printed layer above ESD film as current collecting layer, simply CCL. A 0.5 °C min^{-1} ramp from room temperature to 160 °C for 5 h then to 350 °C for another 5 h was used to burn out binders and ink solvents. Finally, the temperature was increased to 700 °C with 2 °C min^{-1} rate, followed by a fast cooling down to room temperature at 10 °C min^{-1} rate. Although well below the sintering temperature, a 700 °C temperature was found high enough to generate some necking between particles.

2.2 Film Characterization Techniques

2.2.1 Scanning Electron Microscopy (SEM)

The morphology of the films was investigated by SEM with a field emission gun, FEG-SEM, (ZEISS Ultra 55) operating at a 3 kV voltage and a 7 mm working distance. The samples were coated with Pd to avoid electrons charging. The local chemical composition of the samples was analyzed by energy-dispersive X-ray spectrometry (EDXS) with typical accelerating voltages of 15 to 25 kV using a Philips XL30 microscope.

2.2.2 Powder X-ray Diffraction (PXRD)

X-ray powder diffraction (XRD) was performed using a Bruker D8 Advance diffractometer equipped with Lynx Eye detector with a Ge (111) Johansson type monochromator using Cu $K\alpha_1$ radiation with $\lambda = 1.54056$ Å. The data were collected in the Bragg–Brentano geometry in 2θ range from 20 ° to 130 ° with a 0.011 ° step width and a 1 s step time. The phase identification was carried out using the International Centre for Diffraction Data database (ICDD). The positions of the X-ray diffraction peaks as well as the cell parameters were obtained by refinement using Fullprof Suite software [155].

2.2.3 Transmission Electron Microscopy (TEM)

High Resolution TEM (HRTEM) was performed on a JEOL 2010 LaB_6 (JEOL, Japan) transmission electron microscope with a 200 kV accelerating voltage and a 0.19 nm resolution.

2.2.4 Focused Ion Beam Scanning Electron Microscope (FIB/SEM) tomography

2.2.4.1 The principles and the set-up

By combining FIB milling capabilities and SEM imaging capabilities a three-dimensional image of a microstructure can be obtained at high resolution (10 nm at best). Figure 2-4a schematically shows a typical setting for FIB-SEM. In this system, the two beams have a

coincident angle of 54˚. Imaging was performed using a dual column focus ion beam (FIB) (Ga) field emission gun scanning electron microscopy FEG-SEM NVISION 40 from Carl ZEISS. A low viscosity resin was vacuum-infiltrated into the samples. This step is repeated after cutting the samples in the middle so that the resin penetrates into the nano-pores of the cross-section. Carbon was deposited on the surface of the target volume to provide support, to prevent the charging up and to facilitate the image reconstruction (Figure 2-4b). Reference marks were created on the carbon layer by FIB (Figure 2-4c). During image acquisition, thermal drift is difficult to avoid. These marks help the alignment process of SEM images. They can also be useful to double-check the milling distance. The front part of the target volume was removed in the z direction by FIB milling, so that the surface in x-y direction was exposed for SEM imaging. Figure 2-4c shows the SEM image of a sample electrode after appropriate sample preparation. A sequence of slices was obtained after using a 30 kV 0.700 nA ion beam energy. Images were collected using backscattered electrons detector (BSE) with the accelerating electron voltage of 1.5 kV.

Separation of material and the pore phase was carried out for each SEM image. The pore phase filled with epoxy resin is easily distinguished because it appears black in the images (Figure 2-4d). However, the images of the ESD composite did not give good contrast gradient between LSCF and CGO phases due to the resolution limit being close to the very small grain sizes. Moreover, the CCL and CFL layers were distinguished thanks to different porosity and grain size amounts.

2.2.4.2 Image analysis and data processing

Data processing was carried out according to the following protocol:

(i) alignment of the consecutives slices (image registration),
(ii) segmentation and recognition of each phase by thresholding of the grey levels
(iii) 3D image visualization and quantitative analysis

Images with 15 nm pixel^{-1} in x–y–z resolution were obtained. Post-processing and 3D visualization were performed by ImageJ and GeoDict softwares [156]. Approximately 400 image slices were aligned with reference to sample edges using StackReg plugin within ImageJ.

For the calculation of microstructural parameters two representative volume element (RVE) of approximately 125 and 45 μm^3 are further extracted within the columns, excluding the macro-pore channels. These two RVEs were segmented using three different threshold values (min acceptable, most trusted and max acceptable) in order to assess the uncertainty on the microstructural parameters as proposed by Joos *et al*. [157]. The amount of porosity was obtained based on the following assumption for connectivity: a pore is considered open if it is connected by one of the 5 faces of the selected volume. The 6th face (bottom) is considered closed to gas as it is in contact with the dense electrolyte. The specific surface area of open pores is then computed using a marching cube algorithm. Pore size distribution is computed using morphological operations [158]. Tortuosity factor, τ, of the solid phase is deduced from the effective diffusion coefficient D_{eff}^{k} obtained by solving the Laplace equation [64,159]. Tortuosity factor τ_k in direction $k = x, y, z$ was calculated by:

$$\tau_k = \varphi \cdot \frac{D_{bulk}}{D_{eff}^{k}} \qquad 2\text{-}2$$

where D_{bulk} denotes the bulk diffusion and φ represents the volume fraction of the solid phase. With this definition, the tortuosity factor may be less than unity.

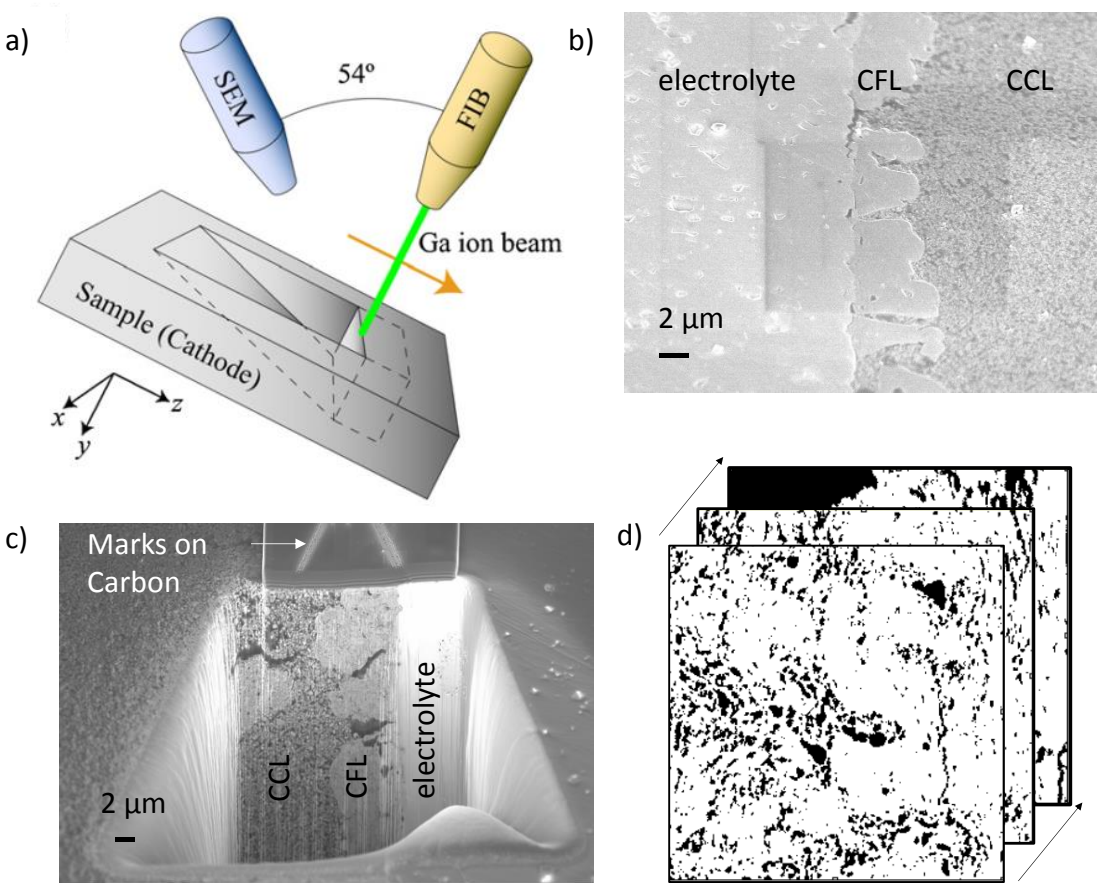

Figure 2-4 a) Schematic diagram of FIB-SEM setting adapted from [160] b) and c) the reference marks of carbon deposition on the cross-section and FIB milling under it. d) Segmented stack of images of CFL.

2.3 Electrochemical Impedance Spectroscopy (EIS)

The complex impedance spectroscopy measures the response of an electrochemical system to a small ac perturbation. A small ac-perturbation (e.g. ac voltage) is applied to the cell and the response is measured (e.g. ac current). The amplitude of the current is a function of the complex impedance (Z) of the system:

$$Z(\omega) = \frac{V_o \cdot e^{j\omega t}}{I_o \cdot j(\omega t - \theta)} = \frac{V_o}{I_o} \frac{e^{j\omega t}}{e^{j(\omega t - \theta)}} \qquad 2\text{-}3$$

$$Z_o(cos\theta + jsin\theta) = Z' + jZ'' \qquad 2\text{-}4$$

with *Z(ω)* is the complex impedance, Z' is the real part of the impedance (resistance) and Z'' is the imaginary part of the impedance (reactance), while θ refers to the phase shift. In Eq.2-3**,** $V_O \cdot e^{j\omega t}$ gives the applied ac voltage with ω the angular frequency, $\omega = 2\pi f$. The current response is then; $I_o \cdot e^{j(\omega t-\theta)}$.

For a resistance: $Z_R(\omega) = R$

For a capacitor: $Z_C(\omega) = \frac{1}{jC\omega} = \frac{1}{C\omega} \cdot e^{-j\frac{\pi}{2}}$

For an inductance: $Z_L(\omega) = jL\omega = L\omega \cdot e^{j\frac{\pi}{2}}$

The resistance thus has only a real component, while capacitance and inductance have only imaginary components. By combining these three elements in series, $Z_{tot}(\omega) = \sum_i Z_i$ or in parallel, $\frac{1}{Z_{tot}(\omega)} = \sum_i \frac{1}{Z_i}$ the expression for the complex impedance of any electrical circuit can be obtained.

For each frequency, the impedance of the system is measured. The imaginary and real part are represented in the x-y plane, and this diagram is called the Nyquist plot. An example is given for a parallel RC circuit in Figure 2-5.

The RC circuit impedance is in the form of a half-circle centered on the real axis. The values on this spectrum are:

- the resistance of the system corresponding to the intersection of the circle with the real axis:

$$\lim_{w\to\infty}[Re\{Z_\omega\}] = 0 \; and \; \lim_{w\to 0}[Re\{Z_\omega\}] = R \qquad 2\text{-}5$$

- the modulus | Z | of the complex impedance is the vector connecting the origin to any point of the circle,

$$|Z| = \sqrt{(A^2 + B^2)} \; with \; A = |Z| \, cos(\theta) \; and \; B = |Z| \, sin(\theta) \qquad 2\text{-}6$$

- the variable of the complex corresponding to the θ angle between this vector and the real axis:

$$\theta = arctan(B/A) \qquad 2\text{-}7$$

- the relaxation frequency f_0 is the frequency at the minimum of the imaginary part of the impedance, which is characteristic of the circuit:

$$f_o = \frac{1}{2\pi RC} \qquad 2\text{-}8$$

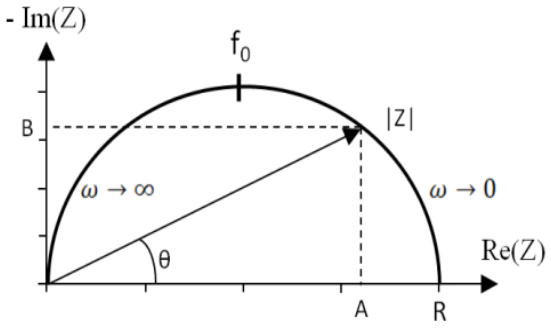

Figure 2-5 Representation of a Nyquist plot of an RC element. Adapted from ref. [161]

Thus, from the Nyquist diagram, one can determine the resistance *R*, the relaxation frequency f_0 at the top of the semicircle, and deduce the capacitance *C* of the circuit.

Figure 2-6 shows the response of the current of a purely resistive, purely capacitive and purely inductive circuit. Voltage and current in a purely resistive circuit are in phase with each other. For a capacitor, the peak values of current occur a quarter of a cycle (90˚) before those of the voltage and for an inductor, a quarter of a cycle (90˚) after those of the voltage.

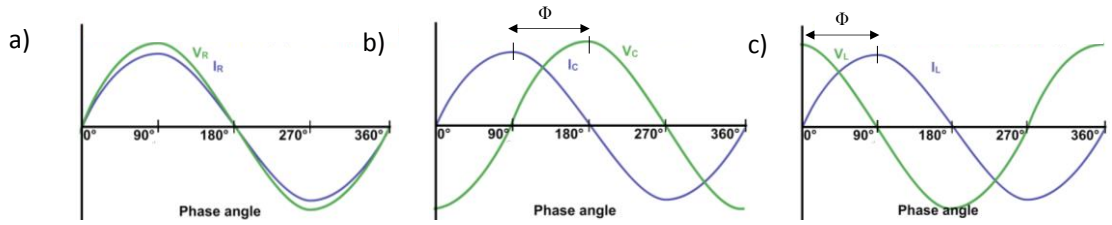

Figure 2-6 Schematic diagrams showing sinusoidal perturbation voltage and the corresponding current response (Φ represents a phase difference) of a) purely resistive b) purely capacitive c) purely inductive circuits

Since the frequency domain is not visible in the Nyquist plot, it is often convenient to use other complementary representations, such as Bode plots to study frequency-dependent processes. The two representations, Nyquist and Bode, are shown in Figure 2-7 for two RC circuits connected in series.

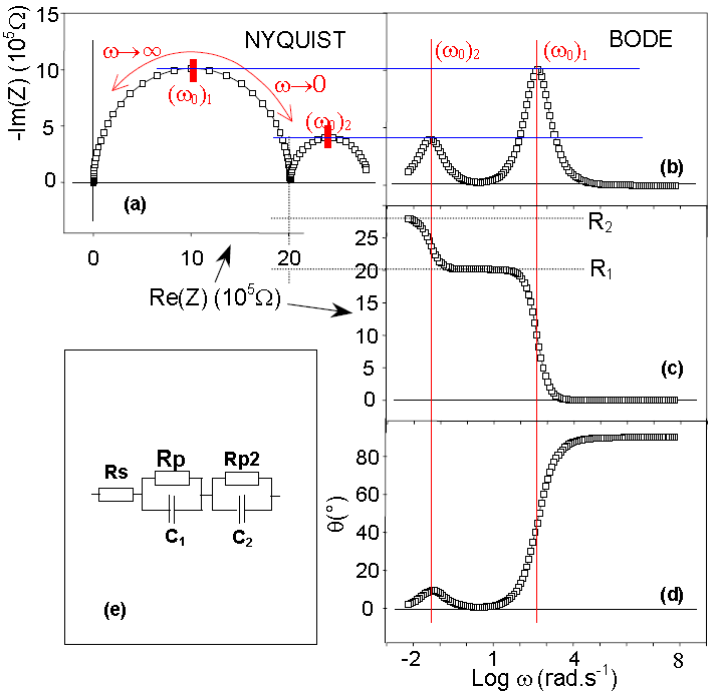

Figure 2-7 Representation in the a) Nyquist plot and b-d) Bode plots of the impedance of a circuit e) (R1//C1) - (R2//C2). Adapted from ref. [161]

2.3.1 RC and RQ circuits

One of the important equivalent circuit element for the description of electrochemical reactions is the RQ-element. It is composed of a resistor and a capacitive constant phase element (CPE).

In the case of non-ideal, real electrodes a constant phase element Q is most often used as a capacitive element (in a unit of capacity, F cm^{-2}), which shows the deviation from the ideal behavior of a capacitor.

The impedance of an RC-element;

$$Z_{RC}(\omega) = \frac{R}{1+j\omega\tau} \text{ with } \tau_{RC} = \frac{1}{\omega} = RC \qquad 2\text{-}9$$

The impedance of an RQ-element;

$$Z_{RQ}(\omega) = \frac{R_{RQ}}{1+(j\omega\tau)^{p}} \text{ with } \tau_{RQ} = (RQ)^{1/p} \qquad 2\text{-}10$$

where 0 < p < 1. The smaller the value of p, the more is the flattened semicircle in the Nyquist representation of the impedance (Figure 2-8). For the limiting case of p = 1, the term is identical to the impedance of a parallel circuit of a resistor RC.

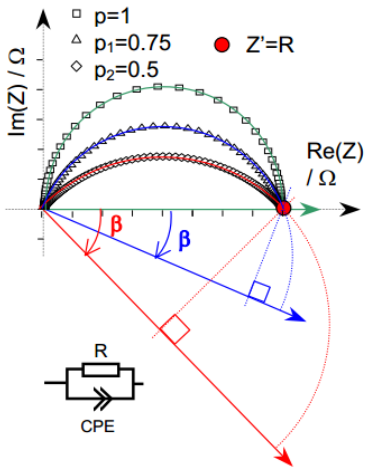

Figure 2-8 The representation of RQ circuit as a function of p parameter. Adapted from ref. [161].

2.3.2 Gerischer Impedance

Adler *et al*. [92] gave an analytical expression for the impedance of a semi-infinite porous SOFC mixed cathode material. This equation mathematically corresponds to the impedance of a Gerischer element. The impedance of the Gerischer element is given by:

$$Z(\omega) = \frac{R_{chem}}{\sqrt{1+j\omega t_{chem}}} \qquad 2\text{-}11$$

Here R_{chem} and t_{chem} are the characteristic resistance and the time constant of the cathode, respectively. They are linked with the microstructure of the cathode, the ionic conductivity, the surface exchange and thermodynamic properties of the cathode material as following:

$$R_{chem} = \frac{RT}{4F^2}\sqrt{\frac{\tau}{(1-\varepsilon)aD_o k_o C_o^2}} \qquad 2\text{-}12$$

$$t_{chem} = \frac{c_v}{c_o}\frac{1}{a\,\gamma}\frac{1}{k_o} \qquad 2\text{-}13$$

Here ε describes the porosity, a electrochemically active surface (cm^{-1}), τ tortuosity, c_o molar concentration of oxygen ions in equilibrium (mol cm^{-3}), c_v concentration of oxygen vacancy concentration in MIEC lattice (mol cm^{-3}), D_o, k_o the oxygen transport parameters and γ thermodynamic factor.

Figure 2-9 shows the impedance of a Gerischer element in the Nyquist presentation. Characteristic of this plot is a straight line at high frequencies with a phase angle of 45°. This part of the plot originates from the semi-infinite chemical diffusion of the oxygen ions in the solid [100]. At low frequencies, it looks like the characteristics of an RC-element.

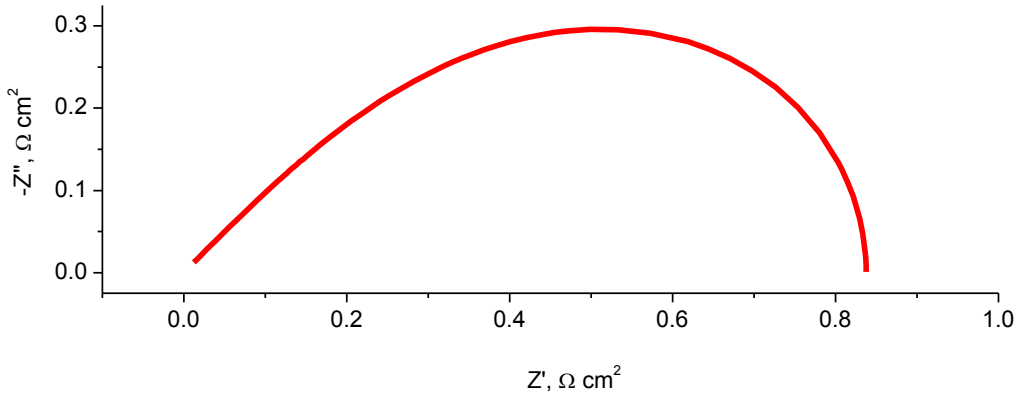

Figure 2-9 Simulated Nyquist plot of a Gerischer element with R_{chem} = 0.84 Ω cm^2 and t_{chem} = 0.0033 s.

The key assumptions of the ALS model are:

1) The only contribution to polarization resistance is the diffusion of oxygen species in the solid and exchange of O_2 at the solid/gas interface.
2) The porous electrode is treated as a superposition of two continuous phases, solid and gas.
3) An active or utilization layer thickness is larger than the constituent particles.
4) The total electrode thickness is much larger than the active layer thickness.

Deviations from these assumptions (e.g. utilization lengths approaching the size of the particles at higher frequencies or utilization length approaching the total thickness of the cathode) may account for non-ideal (n < 1) exponents in the Gerischer impedance. In this work, the first case is more relevant since the utilization length has the same order of magnitude as the particle sizes.

Figure 2-10 illustrates the impedance models used to fit all of the impedance diagrams of the symmetrical cells in the thesis. *L* represents inductance of the wires, R_s is the series resistance of the electrolyte and the *R//CPE*s correspond to the electrode reactions. This model was fitted to all data above 550 °C. All the rest below this temperature was fitted with R_s and a fractal Gerischer impedance, G_f, in parallel with a capacitance, *C*. The information on the fractal Gerischer impedance can be found in Appendix B.

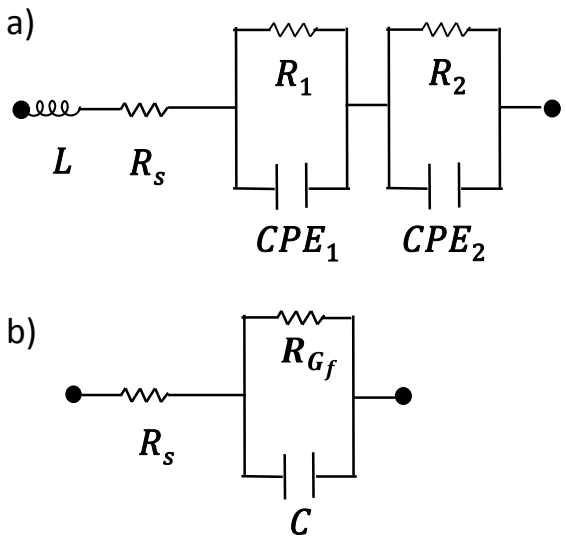

Figure 2-10 The impedance model used to fit the diagrams a) 550-650 °C b) 400-500 °C.

The capacitance at higher temperatures (550-650 °C) were calculated using the expression:

$$C = R^{\frac{1-p}{p}} \cdot Q^{\frac{1}{p}} \qquad 2\text{-}14$$

Where *R* is the resistance, *Q* is the admittance of the constant phase element (CPE) and *p* is the exponent to which the CPE is raised.

2.4 Materials and cell preparation for symmetrical cells

Electrochemical characterization of all films was performed by means of impedance spectroscopy on a symmetrical cell setup (Figure 2-11). Electrochemical impedance spectroscopy (EIS) measurements were carried out in stagnant ambient air at 50 °C temperature steps from 400 to 650 °C. Autolab frequency response analyzer operating in a frequency range of $0.05 \leq f \leq 10^4$ Hz is used. The amplitude of the measuring signal was adjusted to 20 mV and the measurements were performed in open circuit voltage (OCV). The deposited films were contacted with Pt grids (Heraeus, 3600 meshes.cm^{-2}) and then sandwiched between Al_2O_3

blocks with gas channels, which were pressed to ensure maximum contact points. All impedance diagrams were fitted with electrical equivalent circuits using the EC-Lab® software (V10.44). The magnitude of the total area specific polarization resistance, ASR_{pol}, was determined from the difference between the low frequency and high frequency intercepts of the electrode characteristics on the real axis in the impedance plane. Since the measurements were performed on symmetrical cells, the obtained ASR value was divided by two and then multiplied by the surface area of the electrode films.

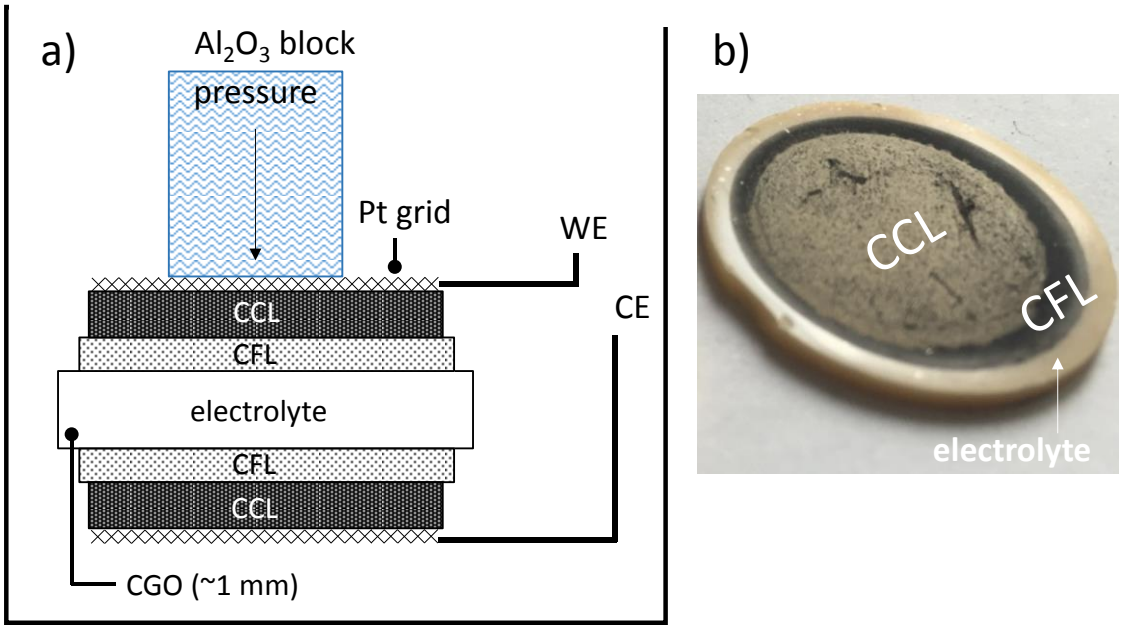

Figure 2-11 a) The schematics of the impedance cell configuration for a symmetrical 2-electrode sample. b) The symmetrical sample showing the double-layer electrode deposition and the electrolyte

Reproducibility of the ASR measurements was confirmed by two tests. In the first test, the ASR was measured from 650 °C - 400 °C - 650 °C cycles (Figure 2-12a). In the second test, the ASR was measured for two identical symmetrical cells between 400 °C and 650 °C (Figure 2-12b). Both tests show good agreement in results.

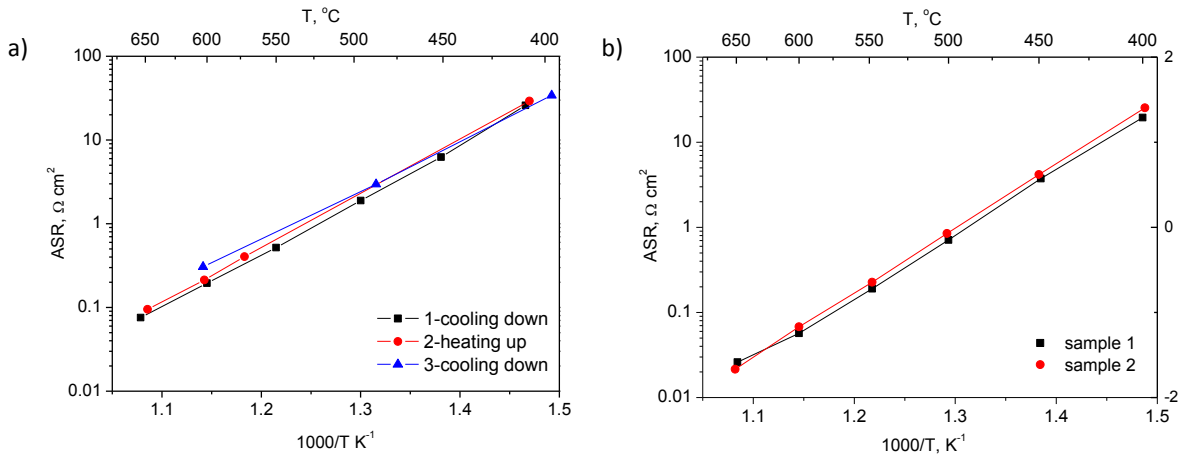

Figure 2-12 a) Arrhenius plot of ASR when cooling down and heating up b) Reproducibility of pure LSCF symmetrical cells

2.5 Materials and cell preparation for anode supported cell

Commercially available (H.C Stark, Germany) anode supported half fuel cells of 4 cm in diameter (Courtesy J. Laurencin from CEA-LITEN), were used for the performance study in anode-supported full fuel cell. The materials, architecture, and typical dimensions of the full cells are illustrated in Figure 2-13a. The LSCF CFL-CCL double layer films were deposited in the cathode compartment. The anode layer is composed of anode functional layer of NiO-8YSZ (56 vol. % NiO and 24 vol.% zirconia stabilized with 8 mol. % of Y_2O_3 and 20 vol.% porosity [162]), current collecting support layer of NiO-3YSZ and a thin layer of pure Ni to improve the electrical contact with the metallic interconnect. 3YSZ is preferred over 8YSZ from a mechanical point of view [15].

A sequential deposition and sintering of barrier layer, CFL and CCL layers were performed. A 4 µm-thick, dense CGO barrier layer was deposited on YSZ by ESD technique prior to CFL in order to prevent the formation of insulating phases, e.g. $La_2Zr_2O_7$ and $SrZrO_3$, between LSCF and YSZ [163]. The ESD deposition parameters for the barrier layer were taken from Constantin *et al.* [78]. This layer was sintered at 900 °C for 2 h in air. Then, LSCF film of columnar microstructure as CFL was deposited by ESD as described previously for 3h. In order to keep a similar microstructure compared to CGO electrolyte supported cells, the speed of spray scanning in *x-y* direction was increased by 4, since the surface of commercial anode

supported cells was 4 cm in diameter, about 2.5 times larger than previously described symmetric cells. After sintering of this layer at 800 °C for 2 h in air, 30 µm CCL was deposited by SP technique and heat treated at 700 °C to remove the solvents and binders.

The electrochemical measurements on the two full cells were performed by Dr. Julian Dailly in the European Institute for Energy Research, (EIFER) the joint research center of Karlsruhe Institute of Technology and EDF.

Two samples were studied for electrochemical measurements. After heating to 675 °C, the reduction of the anode of both samples was carried out gradually switching from N_2 (2 L h^{-1}) to humidified hydrogen (3 % H_2O, 2.42 L h^{-1}). Air was introduced to the cathode side at 10.88 L h^{-1} rate. The cells were reduced in about 3 hours. For the long term stability test on sample 2, the flux of oxygen was increased to 21.77 L h^{-1} and hydrogen to 7.77 L h^{-1} (fuel utilization of about 7.6 %). The cell current was fixed at 1.4 A.

Electrochemical measurements were conducted using Solartron 1255/FRA system. The current–voltage (*IV*) characteristic of the cell was measured using linear sweep amperometry at a scan rate of 12.5 mA/s from OCV (1.09 V) to 0.6 V. The impedance of the cell was recorded in the range of 100 kHz down to 0.1 Hz under open circuit voltage (OCV) or under load condition. The difference between sample 1 and sample 2 is the diameter of the gold grid current collector: a diameter of 1.6 cm is used for sample 1 and 3.7 cm for sample 2 (Figure 2-13b, 13c). The areas of the current collection were thus ($\pi \cdot r^2$) ~ 2.01 and 10.75 cm^2 for sample 1 and sample 2, respectively.

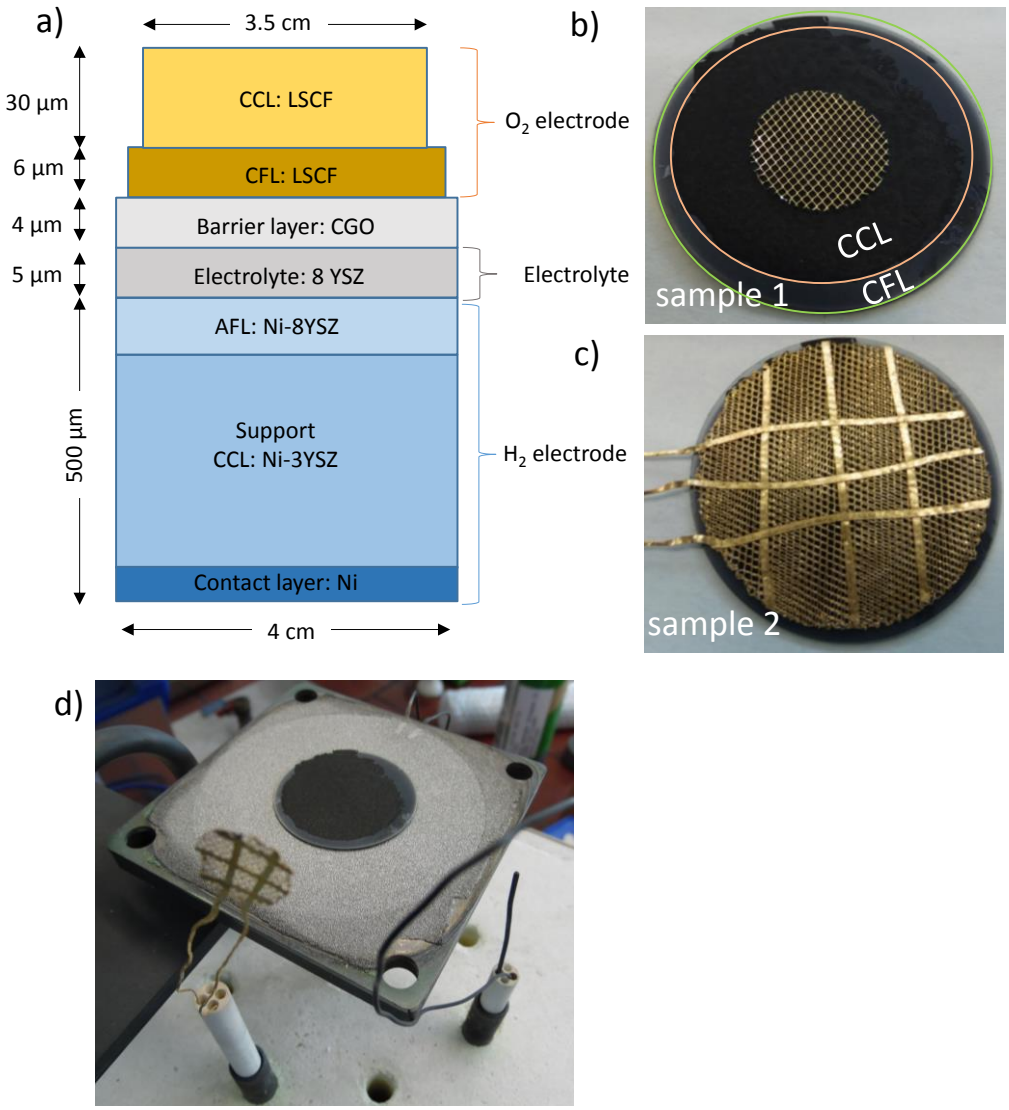

Figure 2-13 a) Schematic representation of the cell structure. A circular grid of b) 1.6 cm and c) 3.7 cm in diameter of Au are used in sample 1 and sample 2, respectively. d) The experimental test set-up.

2.6 Summary

The details of the experimental techniques employed in this work have been described in this chapter. Specific details about the experimental set-ups and equipment were given at the end of each respective section.

All these techniques give complementary information on the cathode films, linking crystallographic and chemical properties at the nanometer scale to microstructure at the micrometer scale.

3 INFLUENCE OF MICROSTRUCTURE, COMPOSITION AND SINTERING TEMPERATURE ON THE ELECTRODE PERFORMANCE

Chapter 3 starts with a comparison of cathode resistance of LSCF in two type of microstructures. The microstructures are controlled by varying ESD deposition parameters. Then, various LSCF/CGO compositions are studied by SEM, TEM, XRD, and EIS to see the effect of microstructure evolution on electrode performance. Only pure LSCF and 60:40 vol. % LSCF/CGO are chosen for reconstruction by FIB/SEM technique. The 60:40 vol. % composite composition is selected to study the effect of sintering temperature on electrode performance. The grain growths are monitored by SEM and XRD, and possible consequences are discussed with respect to initial ESD deposition parameters and electrode polarization resistances.

3.1 Introduction

As introduced in Section 1.7.4, the studies conducted by Marinha *et al.* and Sar *et al.* have contributed to the understanding of ORR in LSCF cathodes. Marinha *et al.* [85] identified the three cathode processes of pure LSCF which are charge transfer process at the LSCF/CGO interface, a diffusion process within the volume of LSCF coupled with oxygen transfer at the LSCF/gas interface. They emphasized the importance of electrode/gas phase surface area and current collecting layer (CCL). Sar *et al.* focused only on the coral-type microstructure (the highest surface area microstructure) and deposited homogeneous and graded 60:40 vol. % LSCF/CGO composite films [86,87]. They did not see any improvement with the variations of composite composition. The microstructural characterization of the films was done by 3D synchrotron tomography [164]. In average a 0.7 μm^{-1} specific surface area was calculated in the composite coral-type microstructures. This is approximately twenty times lower than the pure coral-type LSCF films reported by Marinha *et al.* (15.9 μm^{-1}) [83]. Such differences can only be attributed to the densification of the film with the addition of CGO particles in the composite film. Nevertheless, a direct comparison of electrode performances between Marinha and Sar cannot be made since the films of Marinha were deposited in a static substrate holder while Sar used a moving holder, which resulted in different microstructures. Moreover, as mentioned earlier, both authors used different electrolyte materials.

As a continuation, this work will bring a complementary knowledge on the influence of the electrode microstructure, the composition and sintering temperature on the performance. The chapter starts with the comparison of LSCF films in coral vs columnar type microstructures. Next, the effect of various concentrations of LSCF/CGO columnar films are shown and discussed. Following that, a parametric study on the sintering temperature from 800 to 1100 °C is conducted on both coral and columnar type composite films (60:40 vol. % LSCF/CGO). All ESD films are topped with 30 μm thick CCL of the same LSCF composition for electrochemical impedance measurements.

3.2 The effect of microstructure on the pure LSCF electrode performance

Although studied by Marinha *et al*., pure LSCF films in coral and columnar-type microstructures (~5-6 μm) were deposited once more for comparison purposes, and sintered in air at 800 °C rather than 900 °C. The two particular microstructures of columnar and coral-types have been fabricated according to the procedure given in references [83,87] (see Figure 3-1). Other than the sintering temperature, Marinha *et al.* used a static spray deposition, while in this study, the substrate holder was automated in *x-y* direction to get more homogeneous film in thickness. The porous structure of the films presents a hierarchical character: large interconnected space between the coral and columnar blocks at the macro-scale and fine porous structure within the blocks at the nano-scale. The large openings are mentioned as macro-pore channels in the rest of the thesis. Significant differences in the width of the coral and columnar geometries are visible by comparing both work. While the width of the columnar blocks increase, the cauliflower shaped coral features get smaller in this study. It is particularly easier to compare the columnar-type microstructure. The width of the columns in this study are about two fold higher (10-15 μm in this study and 4-5 μm in Marinha *et al*.'s). The microstructural parameters of pure LSCF films in columnar microstructure investigated by 3D FIB/SEM technique are also compared [83,165]. The specific surface in this study is two to three fold higher (19 ± 6 μm^{-1}, Table 3-1) in comparison to Marinha *et al*.'s columnar LSCF film (8.63 μm^{-1}).

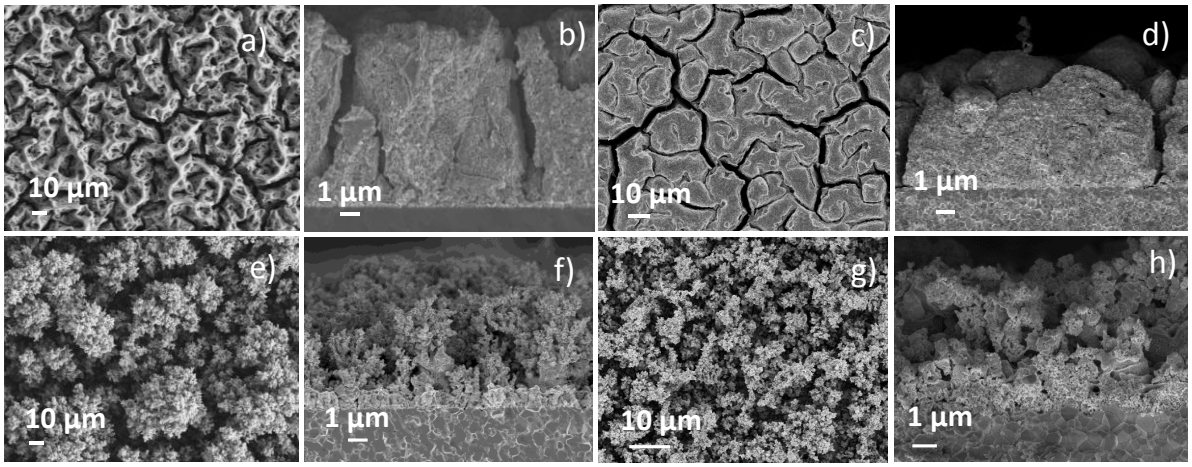

Figure 3-1 Top and cross section views of columnar (a, b) and coral LSCF (e, f) by Marinha *et al*. [83] and columnar (c, d) and coral (g, h) LSCF in this study. The SEM images were taken before depositing CCL.

As shown in Figure 3-2, the lowest values of ASR_{pol} are recorded for columnar microstructures rather than the coral ones. In comparison to previously reported data on LSCF cathodes with similar processing conditions (columnar type microstructure deposited by ESD technique), the polarization resistance of 100 LSCF in this work is approximately two times lower than that of Marinha *et al.* [91] and close to those determined by Hsu *et al*. at 600 °C [72]. In the first place, one can relate this result to the sintering temperature; 900 °C for 2 h (Marinha *et al*.) and 800 °C for 2 h (Hsu *et al*. and this study). Low sintering temperature helps to keep nano-sized features of the microstructure which might have a significant impact on electrode kinetics. However, it is important to note that the microstructure, particularly the width of the columns in the columnar-type microstructure in this study is 2-3 fold larger than Marinha *et al*'s. This results in different specific surface area (surface area per volume) and thus to a significant change in activation energies. While an average of 1.40 eV is calculated for all LSCF films, the columnar LSCF of Marinha *et al*. is 1.72 eV. As shown in Appendix E, the higher specific surface area also refers to a higher amount of porosity and active sites. Depending on the percolation limit, the effective transport parameters vary largely with the amount of porosity, especially at low temperatures. According to the model that was developed in this thesis (Chapter 5) the activation energy of a 1 µm wide column is calculated to be 1.55 eV while that of 10 µm wide columns are 1.38 eV. This illustrates the effect of the size of the columns. Nonetheless, the

model assumes ideal current collection. At this point, one cannot exclude the current constriction effects as a function of width of the columns.

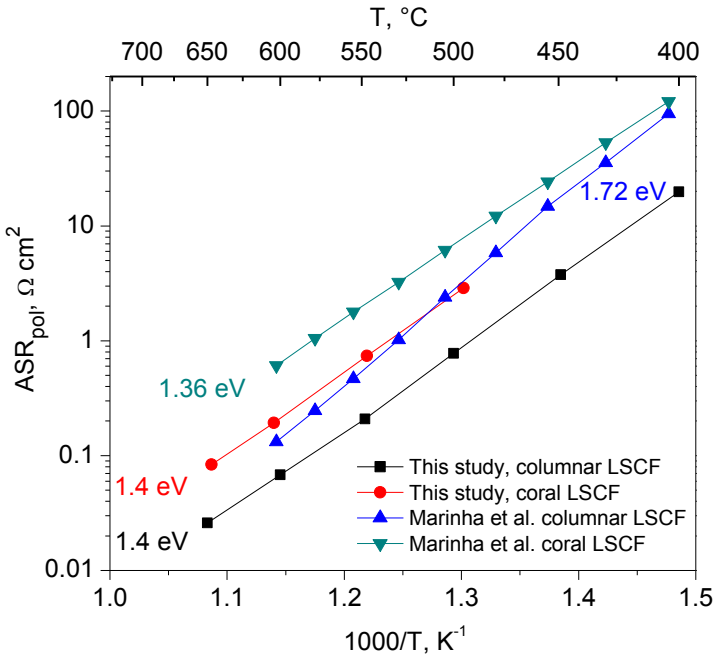

Figure 3-2 Arrhenius plot of ASR_{pol} compared for coral and columnar 100 LSCF films in this study and Marinha *et al.*'s [83].

Next, to further decrease the ASR and the activation energy, we studied the effect of various concentrations of CGO in LSCF in columnar microstructure.

3.3 The effect of CGO addition in LSCF electrode in columnar-type microstructure

The strategy to improve the ORR in the cathode relies both on the cathode material choice and on the micro/nanostructure design of the cathode [5,40,166]. The introduction of ionic transport extends the ORR path from triple phase boundary (tpb) points to the gas-MIEC double-phase boundary (dpb), thus providing optimal kinetics [167]. Also, it has been demonstrated that the addition of a second phase with high ionic conductivity in the MIEC matrix, typically the same as the electrolyte material, allows the electrode performance to be drastically improved [52–

58] (see section 1.7.3). All these studies pointed to the conclusion that CGO addition leads to a lowering of the area specific resistance (ASR). However a rational guideline for choosing the optimal CGO content, in relation with other important microstructural parameters (e.g. porosity, surface area), is still missing.

In this work, we choose to focus on columnar microstructure to investigate the influence of CGO addition. Four compositions have been prepared with 0, 25, 40 and 60 vol. % CGO in LSCF. Figure 3-3 shows the SEM images of three films with 0, 25 and 40 vol. % CGO in LSCF. The 60 vol. % CGO film could not be imaged by SEM due to bad adherence to the electrolyte. It is apparent from the top views that all films have similar macro porous width of 1-2 μm (Figure 3-3a, 3b and 3c). 9-10 μm high and 10-15 μm wide columns are observed in 100 LSCF films. The columns in the composites seem lower down to 7-8 μm high and the width of the columns increase to 20-30 μm wide (Figure 3-3d, 3e and 3f). Microstructures differ markedly at the nano-scale. 100 LSCF film exhibits larger grains (> 50 nm) compared to the composite films (< 50 nm). The significant amount of porosity in pure LSCF gradually disappears with the addition of CGO (Figure 3-3g, 3h and 3i). Regardless of the electrode composition, a good adhesion between electrode and electrolyte is achieved up to 40 vol. % CGO after sintering at 800 °C for 2h in air. The SEM micrographs were characterized by image analysis tools (ImageJ, http://rsbweb.nih.gov/ij/) and macro-pore channels between the columns were calculated to occupy approximately 15 % of the total volume.

Figure 3-4a, 4b shows the micro/nanostructural characterization of 100 LSCF and 60:40 vol. % LSCF/CGO by 3D FIB/SEM tomography. From these images, smaller volumes (Figure 3-4c, 4d) were extracted within a column to assess the internal porosity and specific open surface area. The "open" porosity and surface area (i.e. reachable by the gas outside) are quantified since they are pertinent for the ORRs. Still, the amount of closed porosity is smaller than 1 % for both films. The total open porosity is thus the sum of nano-porosity inside the columns and macro-porosity in between the columns. 100 LSCF exhibits homogeneously distributed small pores of ~75 nm, large specific surface area ($19 \pm 6\ \mu m^{-1}$), and high internal nano-porosity (22 ± 7 %), as indicated in Table 3-1. The specific surface area of 100 LSCF in this study is 2-4 fold higher than that of films with similar composition but different microstructures [43,157,160,164,168]. By contrast, the composite film exhibits a bimodal pore-size distribution, which consists of fine porosity (< 0.1 μm) close to the electrolyte interface and large micron sized porosity (> 0.5 μm) dispersed homogeneously in the upper layer of the cathode volume

(Figure 3-5). Figure 3-4e reveals the porosity distribution in the volume of the composite cathode. The internal nano-porosity in the composite is mainly located in the first 1.5 µm distance from the electrode/electrolyte interface and corresponds to 20 ± 3 % of porosity within that volume. The large micron sized porosity observed above this thickness is more likely the extensions of macro-pore channels. Thus, the upper layer of the composite can be considered dense.

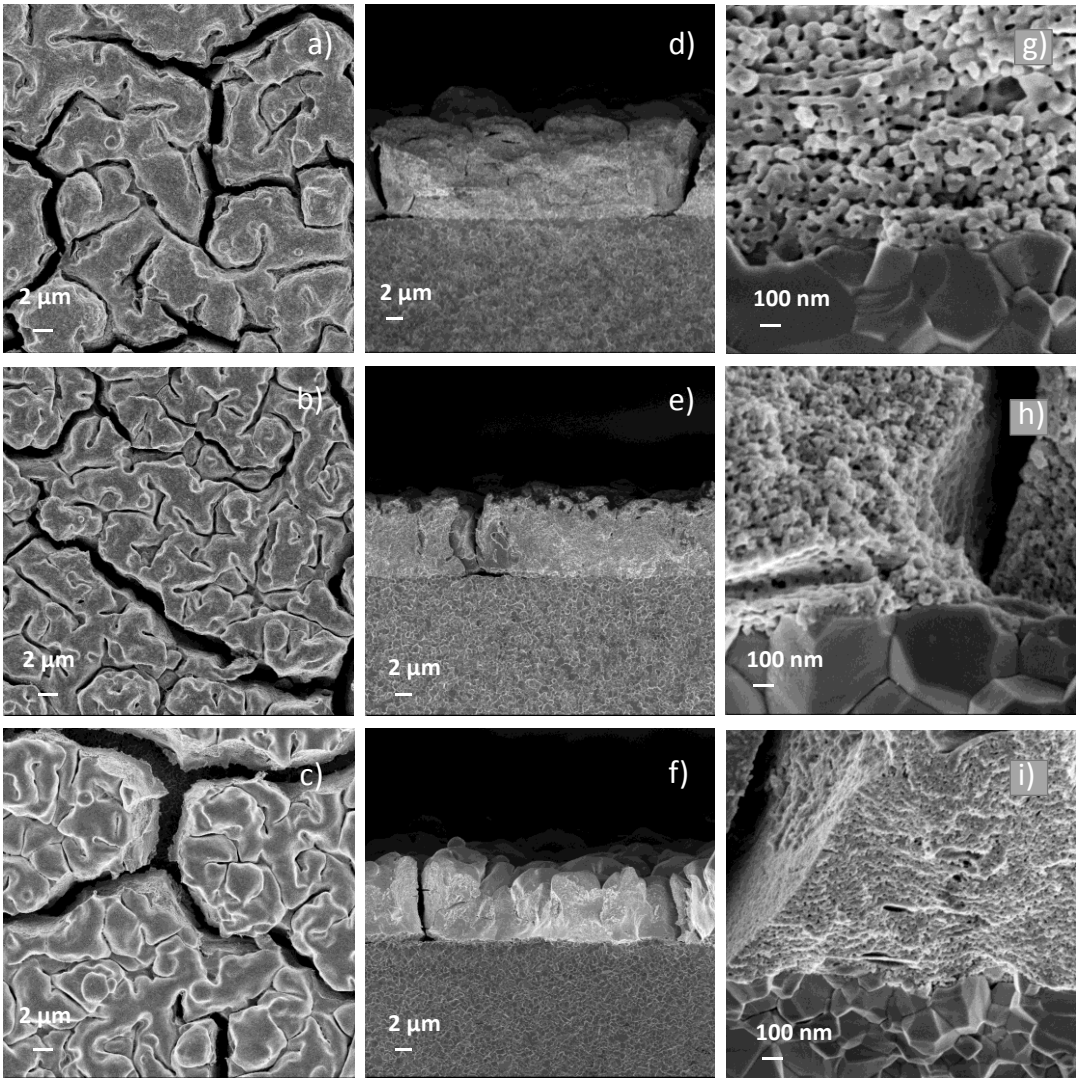

Figure 3-3 Top and cross-section SEM images of a, d, g) 100 LSCF, b, e, h) 75:25 LSCF/CGO and c, f, i) 60:40 LSCF/CGO composite films, sintered at 800 °C for 2 h in air.

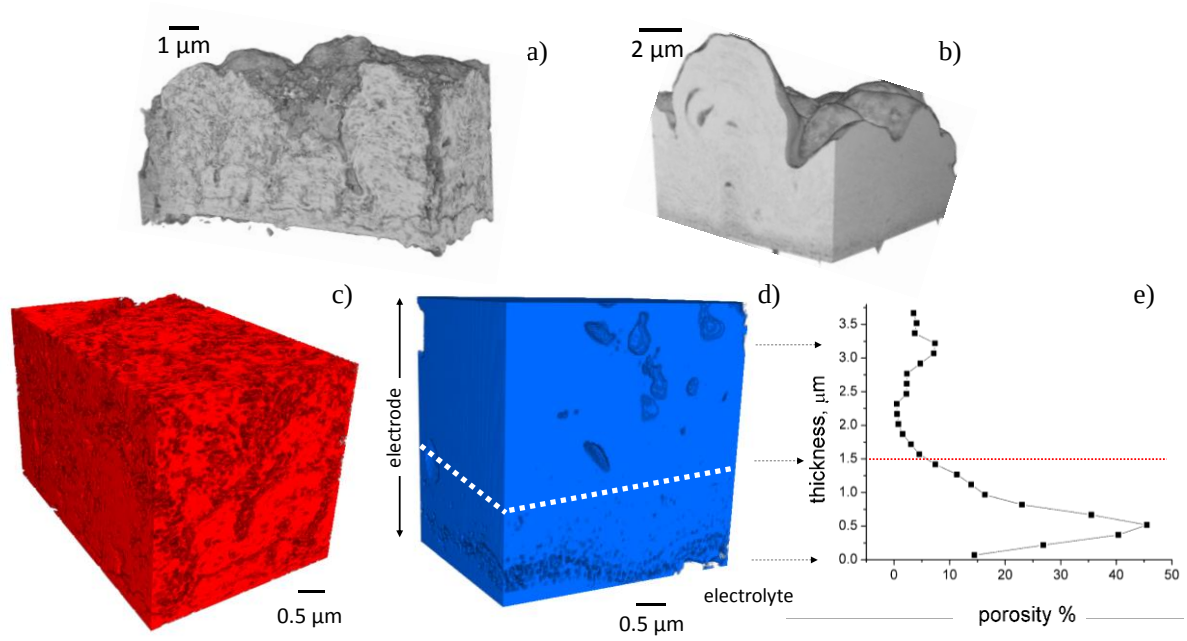

Figure 3-4. 3D reconstructed images by FIB/SEM technique of a) 100 LSCF and b) 60:40 LSCF/CGO composite. The micro/nanostructural parameters were extracted from a small region of the volume in a) and b). 100 LSCF is the reconstruction of volume in c) and 60:40 LSCF/CGO composite is the reconstruction of volume in d); the white dotted line indicates the separation between the highly porous lower portion (0-1.5 µm) and the relatively dense upper portion (1.5-3.76 µm) in the composite. e) The distribution of porosity amount as a function of the distance from the electrode-electrolyte interface for the composite.

Table 3-1. Parameters calculated by analyzing the reconstructed 3D FIB/SEM images. ε (porosity), and a (specific surface area) are calculated for three threshold values to provide an evaluation of the uncertainty [43]. For each parameter two values are given for the composite corresponding to: 0-1.5 µm thickness and 1.5-3.76 µm thickness.

ESD films	Thickness range, µm	Porosity, ε, %	Sp. Surf. Area, a, μm^{-1}	Tortuosity, τ
100 LSCF	0 - 4.35	22 ± 7	19 ± 6	1.50 ± 0.2
60:40 LSCF/CGO	0 - 1.50	20 ± 3	8 ± 4	2.1 ± 1.1
	1.5 - 3.76	4.0 ± 0.1	0.55 ± 0.05	0.44 ± 0.02

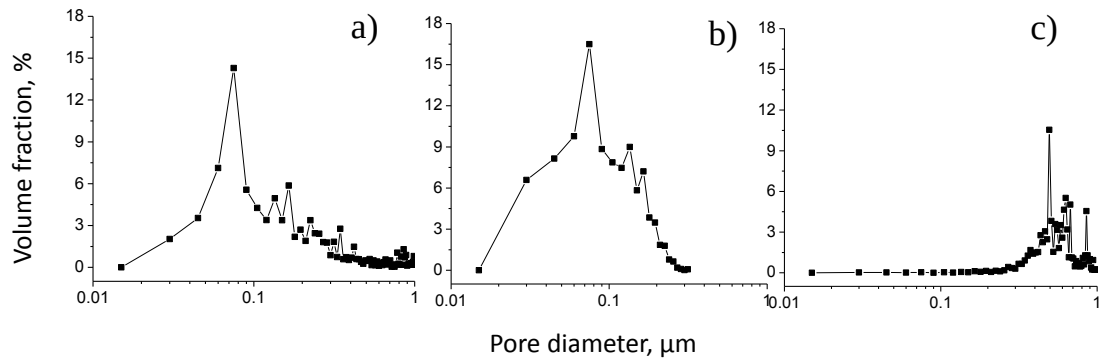

Figure 3-5 Pore size distribution of a) LSCF in the whole volume, b) 60:40 LSCF/CGO composite in the first 1.5 µm distance from electrode/electrolyte interface and c) above 1.5µm distance. Note: The distribution of pore sizes in the cathode volume was calculated in z direction (away from electrode/electrolyte interface) by ImageJ tool. Since the pores are heterogeneously distributed in the composite, two layers are separately calculated.

The crystal structure of 100 LSCF, 75:25 and 60:40 LSCF/CGO composite films was characterized by powder X-ray diffraction. The methodology described in Appendix A was applied on the diffractograms as shown in Figure 3-6**.** The refinement of the peaks shows good signal to noise ratio, indicating that LSCF and/or CGO phases were successfully obtained. The experimental results (in red) and the calculated results (in black) are consistent and the confidence factors R_{wp} and R_p are very close to the expected experimental factor, R_{exp} (χ^2 <5) (Table 3-2).

X-ray diffraction from the CGO electrolyte (blue) in all diffractograms showed distinct and sharp peaks with cubic lattice parameter of 5.419(1) Å in agreement with the reported CGO structure (Ref. JCPDS card 75-0161). The diffraction peaks of 100 LSCF were indexed to a perovskite unit cell with R$\bar{3}$c space group (No 167). The cell parameters of a = 5.498(1) Å, c = 13.480(4) Å calculated by refinement are in agreement with the values given in the JCPDS card number 48-0124. In the diffraction pattern of the composite film (blue), the main peaks of LSCF overlap with those of CGO. Still, distinct peaks, which clearly originate from rhombohedral phase of LSCF and from the cubic phase of CGO, are observed. The space group of LSCF remained R$\bar{3}$c, with a slight decrease in cell parameter a from 5.498(1) to 5.493(2) Å and a marked decrease in c parameter from 13.480(4) to 13.447(0) Å. The space group of CGO in the film remained Fm$\bar{3}$m (No 225) as well, with a systematic shift of all its peaks to lower

two-theta angles. This resulted in a larger cubic cell parameter of 5.442(2) Å in comparison to reported CGO structure (Ref. JCPDS card 75-0161). The cell parameters refinement with the addition of CGO may indicate a structural transformation. This can be explained by the inter-diffusion of the larger radius cations, La^{3+} and Sr^{2+}, from the LSCF phase to the CGO phase [149,169–171]. However, it has been shown that this inter-diffusion is not detrimental in terms of electrical conductivity or oxygen exchange behavior [149,170].

Table 3-2 The peak indexing study for the films with various concentrations of CGO.

Samples	LSCF		CGO	Reliability Factors		
	a (Å)	c (Å)	a (Å)	R_{Bragg}	R_{wp}	χ^2
100 LSCF	5.498(1)	13.480(4)	-	5.68	7.44	1.47
75:25 LSCF/CGO	5.502(8)	13.474(1)	5.445(9)	5.35	7.05	1.18
60:40 LSCF/CGO	5.493(2)	13.447(0)	5.442(2)	5.17	6.96	1.18

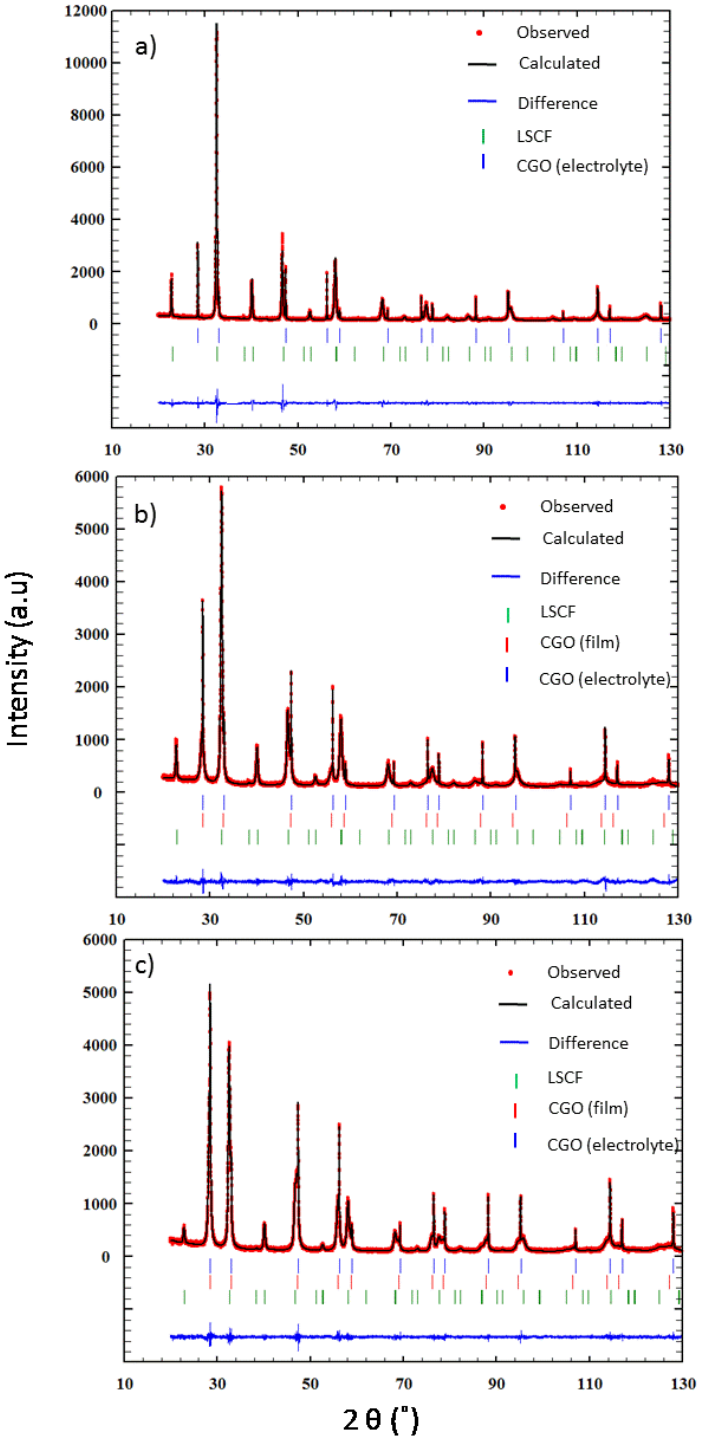

Figure 3-6 The Fullprof refinement of a) 100 LSCF b) 75:25 LSCF/CGO and c) 60:40 LSCF/CGO film sintered at 800 °C for 2 h. The experimental data in the diffractograms are in red, the calculated data from LeBail method are in black and their differences are in blue.

The 60:40 composite film sintered at 800 °C was scratched from the electrolyte support and characterized by high resolution transmission electron microscopy (HRTEM). Different zones were analyzed as shown in Figure 3-7. Diffraction patterns confirmed two crystalline phases; LSCF and CGO. The arrow-marked grain boundaries do not yield any evidence for amorphous grain-boundary phases.

Grain sizes in the films were determined by analyzing 75 to 100 different grains showing distinct Bragg contrast on plane-view TEM images for 100 LSCF and 60:40 composite, respectively. The composite exhibits small grains (25 ± 10 nm) with a narrow size distribution (LSCF grains are slightly larger than CGO), while 100 LSCF contains larger grains (50 ± 40 nm) with broader size distribution. In accordance with the literature, the addition of a second phase into LSCF suppresses the growth of the LSCF particles [56,172,173].

The elemental mapping by STEM-EDX revealed homogeneous distribution of each element in the crystallites as shown in Figure 3-8. The single grains in the center were identified as LSCF phase. Finally, the electrode/electrolyte interface was analyzed by TEM. Cross-section samples were prepared by the tripod polishing method using diamond lapping films to achieve sample thickness of about 10 μm. Low-angle argon ion beam milling was used for final perforation. Different zones were identified by electron diffraction as shown in Figure 3-9. The images taken in the bright field mode confirm the formation of nano-crystallites of both phases with uniform grain sizes and the absence of particle agglomeration, partial sintering or excessive growth of any phase. However, complete identification of the composition in single grains close to the interface was not possible since several small nanometer-sized grains were included within 100 nm-thick TEM specimen.

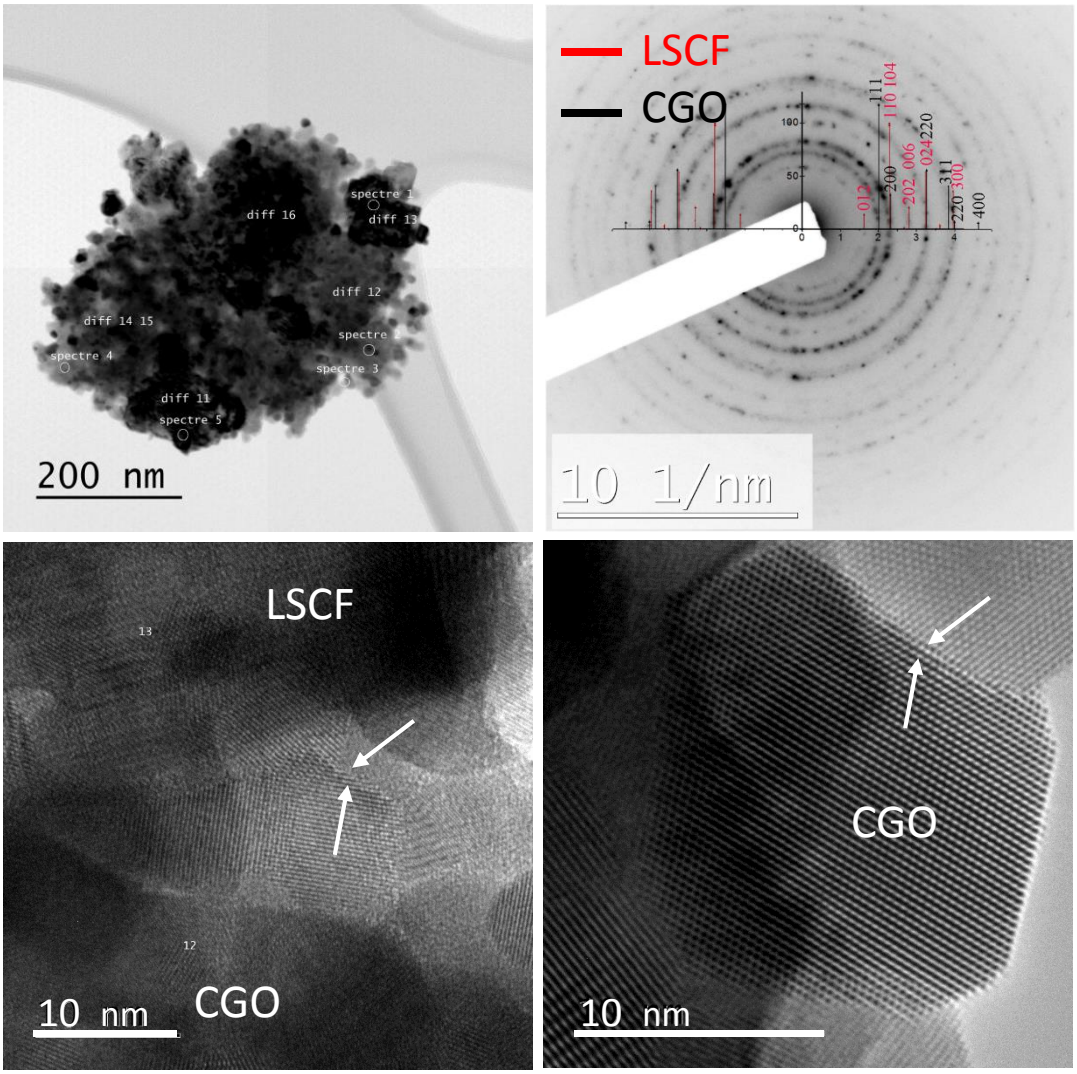

Figure 3-7 HRTEM electron diffractograms of the 60:40 composite film sintered at 800 °C. The arrows mark the grain boundaries.

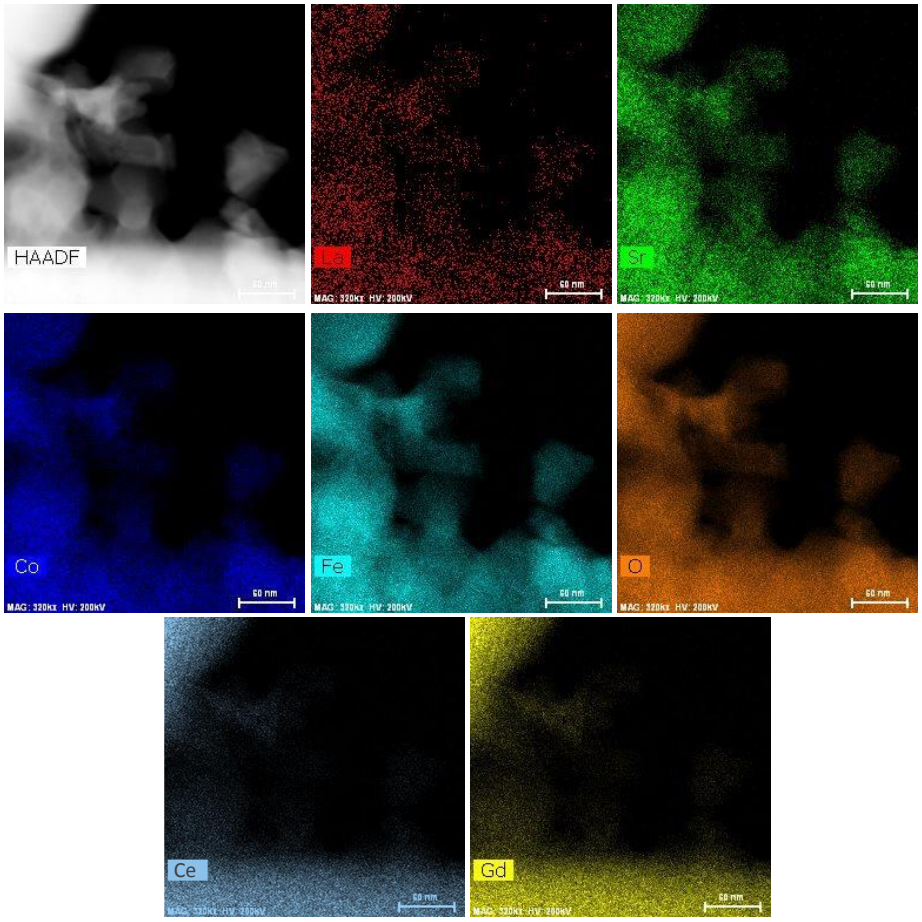

Figure 3-8 Elemental mapping by STEM EDX of the 60:40 composite film scratched from the deposited cell. Scale bars indicate 60 nm.

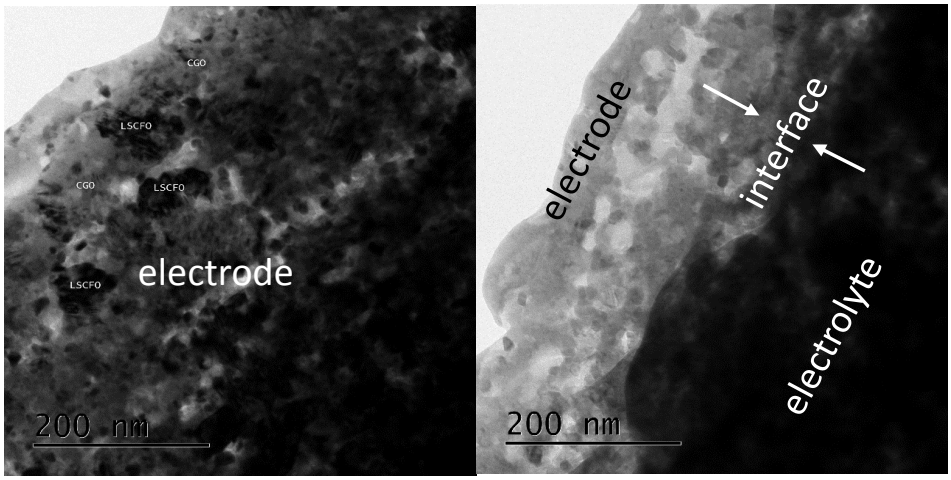

Figure 3-9 Cross-section TEM bright-field images of the 60:40 LSCF/CGO composite film on CGO sintered at 800 °C.

Figure 3-10 shows the Nyquist impedance plots of 100 LSCF, 75:25 LSCF/CGO and 60:40 LSCF/CGO composite films deposited symmetrically and measured at 500 and 600 °C in ambient air. One or two contributions to cathode resistance (ASR_1 and ASR_2) are observed depending on the temperature. At 500 °C, the overall cathode resistance is governed solely by ASR_1. The plots at 600 °C show at least two elementary contributions which are deconvoluted into polarization losses associated with the electrochemical reactions, ASR_1 and the gas diffusion in the pores or the stagnant gas layer at the electrode surface, ASR_2. The first is found more relevant for the fine microstructure of LSCF and LSCF/CGO composite films [174,175]. The fitting of such small impedances is problematic when considerable inductive effects or very high series resistances of the electrolyte exist. This is the case for all impedance spectra measured above 600 °C (Figure 3-10b, 10d and 10f).

The impedance spectra up to 500 °C have been fitted with the equivalent circuit, L-R_s-R_{G_f} // C where L represents the inductance of the wire, R_s accounts for the series resistance of the electrolyte and R_{G_f} symbolizes the resistance of fractal Gerischer element and is in parallel with a capacitance, C (Figure 2-10). The serial resistance, R_s, arising mainly from the ionic conductivity of the electrolyte, was routinely compared with the theoretical resistance calculated from the ionic conductivity of CGO and the geometry of the symmetric cells in order to verify that no electronic leak currents have influenced the measurements. For instance, at 600 °C, conductivity values between 0.017 ± 0.001 S cm^{-1} have been measured for all samples which compare well with the literature [176].

Typically, the Gerischer impedance presents 45 ˚ slope at high frequencies on a Nyquist plot, and a CPE-like response at low frequencies. In the case of a non-ideal form of the impedance, an *n-parameter* is introduced to obtain the so-called fractal Gerischer impedance equation [177] (see Appendices B). The fitted *n* values are both 0.9 for 100 LSCF and 75:25 composite, and 0.8 for the 60:40 composite. A lower *n* value indicates a more distorted spectra.

The value of the capacitance allows electrochemical processes to be assigned to charge transfer (current collector/MIEC and MIEC/electrolyte) and/or to non-charge transfer processes (solid state transport and oxygen surface exchange). A slight deformation at the high frequency part (a charge-transfer resistance of the electrode-electrolyte interface is too small for a good fit by an R//CPE circuit at high frequency) is accounted by a capacitance in parallel to the Gerischer element and is attributed to the faradaic charge transfer impedance. Similar values on the order of 0.4-0.6 mF cm^{-2} were reported previously for LSCF contacted with CGO electrolytes

[83,178,179]. However, these values are too large for an interfacial double layer capacitance. While it improves the fits, the exact nature of this capacitance remains as an open question. Baumann *et al*. speculated on the possible stoichiometric changes at the LSCF (electrode) / CGO (electrolyte) interface during the measurements [179]. The capacitance values for ASR_1 on the other hand are found to be of the order of 10^{-3}-10^{-2} F cm^{-2}, indicating that the reaction is rather involved on a larger fraction of the cathode. This so-called *chemical capacitance*, C_{chem} depends also on the utilization length, L_δ (Eq. 3-1) describing the depth of the cathode within which the oxygen reduction takes place ($L_\delta \approx \sqrt{D_o / k_o}$).

$$C_{chem} = \frac{2F^2(1-\varepsilon)c_v L_\delta}{\gamma RT} \qquad 3\text{-}1$$

with *F*, *R*, *T* being the Faraday's constant, ideal gas constant and temperature, respectively. ε is the fractal porosity. Thermodynamic factor γ relates the differential changes in oxygen partial pressure to the oxygen stoichiometry in the MIEC c_v (Appendix C, Eq. A-12). Kawada *et al*. [180] measured chemical capacitances as high as 0.1-1 F cm^{-2} on a 1.5 µm thin dense film of $(La_{0.6}Sr_{0.4})CoO_{3-\delta}$. Such values necessarily indicate that the bulk was involved in the transport of O^{2-} to the electrode/electrolyte interface. Our calculated capacitance is about two to three orders of magnitude lower which imply a utilization length smaller than 1 µm. This is in agreement with the mean particle size of the ESD cathodes.

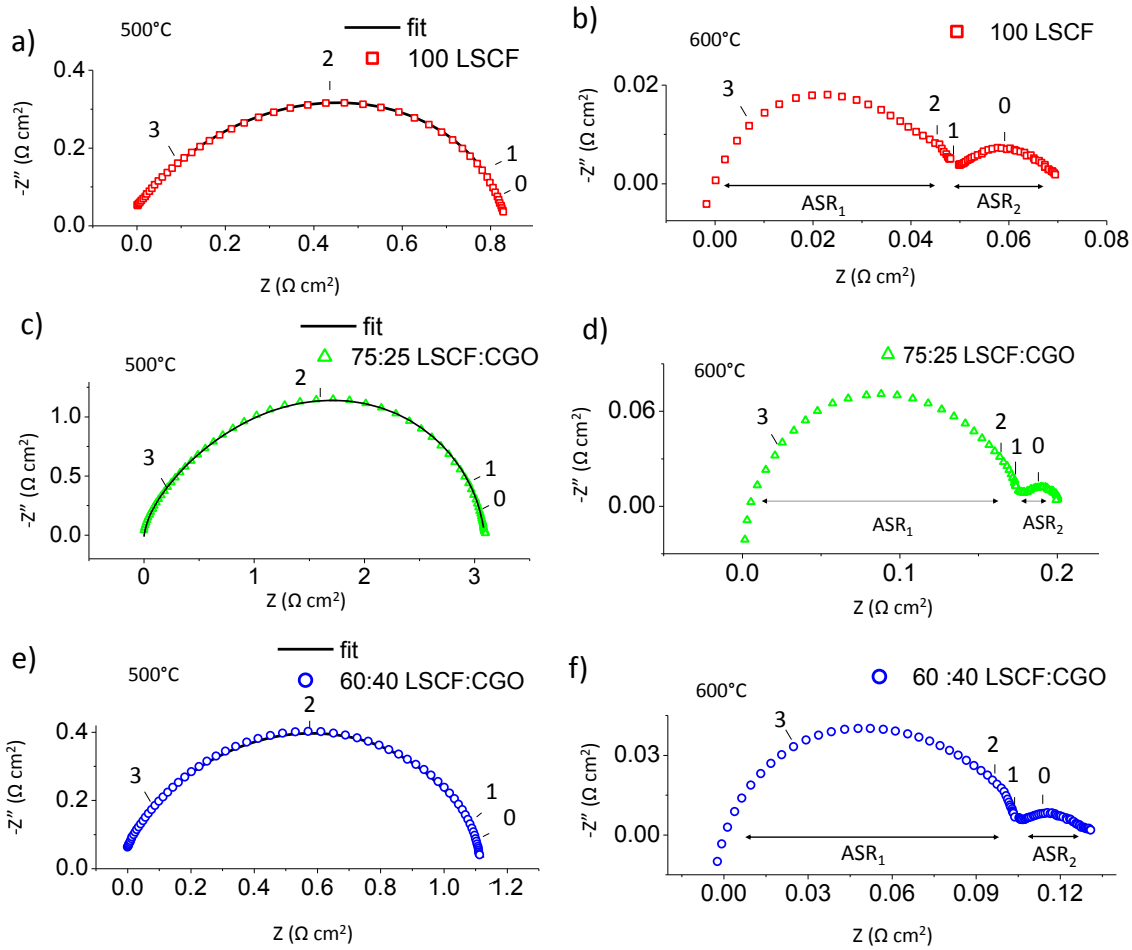

Figure 3-10 Nyquist impedance plots measured at OCV of a-b) 100 LSCF film c-d) 75:25 LSCF/CGO and e, f) 60:40 LSCF/CGO at 600 and 500 °C, respectively. The numbers on the diagram indicate the corresponding frequency in log scale. The ohmic resistance of the electrolyte is subtracted from all data for comparison purposes.

The transport parameters of oxygen (D_o and k_o) are shown in (Figure 3-11). They are calculated from the impedance spectra of pure LSCF film between 400 °C and 600 °C (see Appendix B). The values calculated for D_o are within the range reported in the literature, with an activation energy of 1.9 eV [53,181–184]. Regardless of the measurement technique, similar D_o values suggest that solid state diffusion is an intrinsic property governed solely by the composition of the material [182]. On the other hand, significant differences in k_o values were detected. We report k_o values that are significantly higher than in ref. [182] with a similar activation energy (1.4 eV in this study). Differences in surface composition related to preparation and deposition techniques are speculated [182].

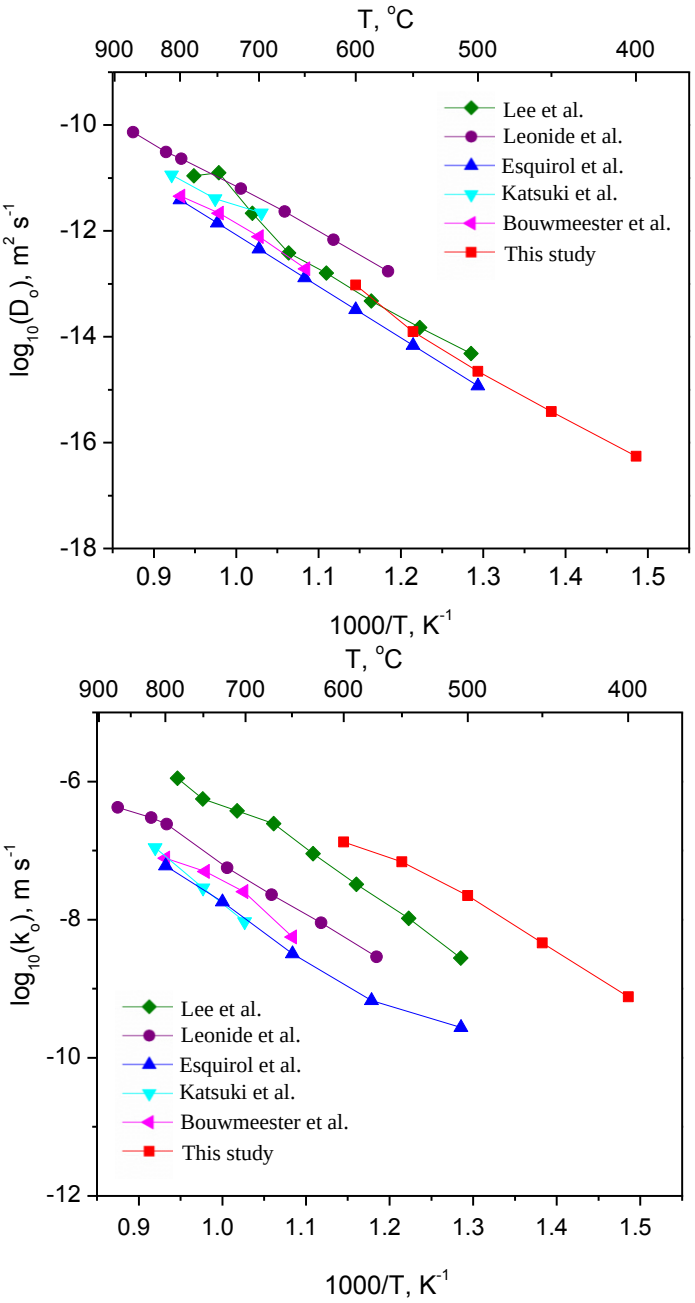

Figure 3-11. Oxygen self-diffusion and surface exchange coefficients calculated from electrochemical impedance data and comparison with literature data measured by different methods [53,181–184].

The temperature dependence of the total polarization losses, ASR_{pol} (sum of ASR_1 and ASR_2) is shown in Figure 3-12, indicating a linear behavior in the Arrhenius plot. Activation energies have been calculated from the corresponding slopes. The activation energies of the 75:25 composite were found the same as pure LSCF, while it decreased in the 60:40 and 40:60

LSCF/CGO composite. The decrease from 1.50 eV down to 1.30 eV is in agreement with previously reported results for CGO compositions higher than 30 vol. % [52–54,86,175,178,185]. However, the polarization resistance of 100 LSCF is lower than the composites at all temperatures higher than 450 °C. This is an intriguing result which had not been reported previously. We can only speculate on the consequence of the disappearance of a large amount of porosity in the upper portion and smaller specific surface area on the lower portion of the composite film. However, it is not possible to quantitatively analyze the electrode performance of hierarchical microstructures with existing 1D models. In Chapter 5, the influence of CGO and specific surface area on the ASR of columnar microstructures is discussed in detail based on a 3D FEM model.

It is worth noting that the polarization resistance of 100 LSCF is equal to 0.07 Ω cm^2 and 0.02 Ω cm^2 at 600 and 650 °C, respectively. To the best of our knowledge, it represents one of the lowest values measured for LSCF in 6428 composition. The very fine microstructure and high surface area of the cathode may well be the reason for such reduced ASR values [72,91].

Among the composites prepared in this work, the most promising results in terms of lower activation energy and ASR values were observed with 40 vol. % CGO. Since further film characterization with 60 vol. % CGO was not possible due to adherence problem on the interface, we selected 40 vol. % CGO for sintering study.

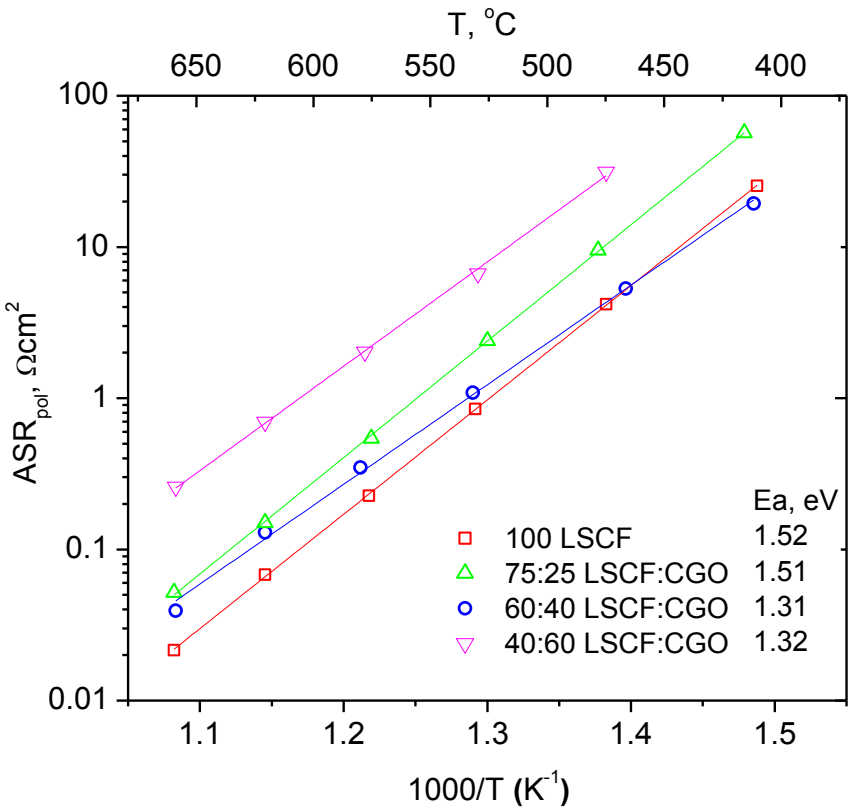

Figure 3-12 Arrhenius plot of ASR_{pol} for 100 LSCF and 25, 40, 60 vol. % LSCF/CGO composite films measured by EIS between 400-650 °C in OCV.

3.4 The effect of sintering temperature on 60:40 LSCF/CGO film performance

Another way of tailoring the microstructure and the ORR kinetics is by controlling the pore and the particle size through sintering temperature. Although high sintering temperature is preferable for good necking between particles, mechanical strength improvement, better adherence between electrode/electrolyte interface [56] and for an enhanced electronic conductivity of the ceramic materials [66], significant densification and pronounced grain growth may decrease the activity of the electrode due to decrease in surface area. It was shown that particle sizes of both phases in the composite films should remain as small as possible to attain a high TPB length [49,186]. Thus, some concessions are needed in order to find an optimum microstructure for desired application. An in-depth study of sintering in air was performed in order to improve the microstructural characteristics of CFL. For this, 60:40 vol. %

LSCF/CGO composite films in both coral and columnar microstructures were deposited by ESD and sintered for 2 h in ambient air at 800, 900, 1000 and 1100 °C, with heating and cooling rates at 2 °C min^{-1}. After the sintering of CFL, ~ 30 μm thick CCL was deposited for electrochemical measurements. The zoomed SEM images of the CFL are shown in Figure 3-13. In general, columnar-type films are denser than the coral-type films regardless of the sintering temperature. This is related to initial deposition parameters for ESD (Table 2-1). As explained in 2.1.2.2, the boiling point of the solvent mixture, the temperature of the substrate and the needle-substrate distance influence the solvent evaporation during flight and therefore the droplet size. The size of the droplet at the impact on the substrate is smaller in the coral-type microstructure. This phenomenon has a significant influence on morphology, texture, surface topography and hence the growth of grain size as a function of sintering temperature. The grain sizes in the coral films are slightly lower than the columnar films at sintering temperatures of 800 and 900 °C (both are well below 100 nm). Above 1000 °C, the columnar films suffer from excessive growth of LSCF phase (~ 150-200 nm) compared to CGO phase (~50 nm). In the meanwhile, the coral films keep their grain sizes well below 100 nm at all sintering temperatures.

The percolation and the distribution of both phases were visually examined by SEM micrographs in backscattered electron mode (Figure 3-14). A good contrast in between the phases was obtained in relation to the atomic numbers (the phase containing heavy rare earth elements like Ce and Gd appear much brighter). The whole film surface was scanned in backscattered electron mode and both phases were found well distributed all over the film. In close inspection, there is also a good dispersion, suggesting a rather good percolation of each phase.

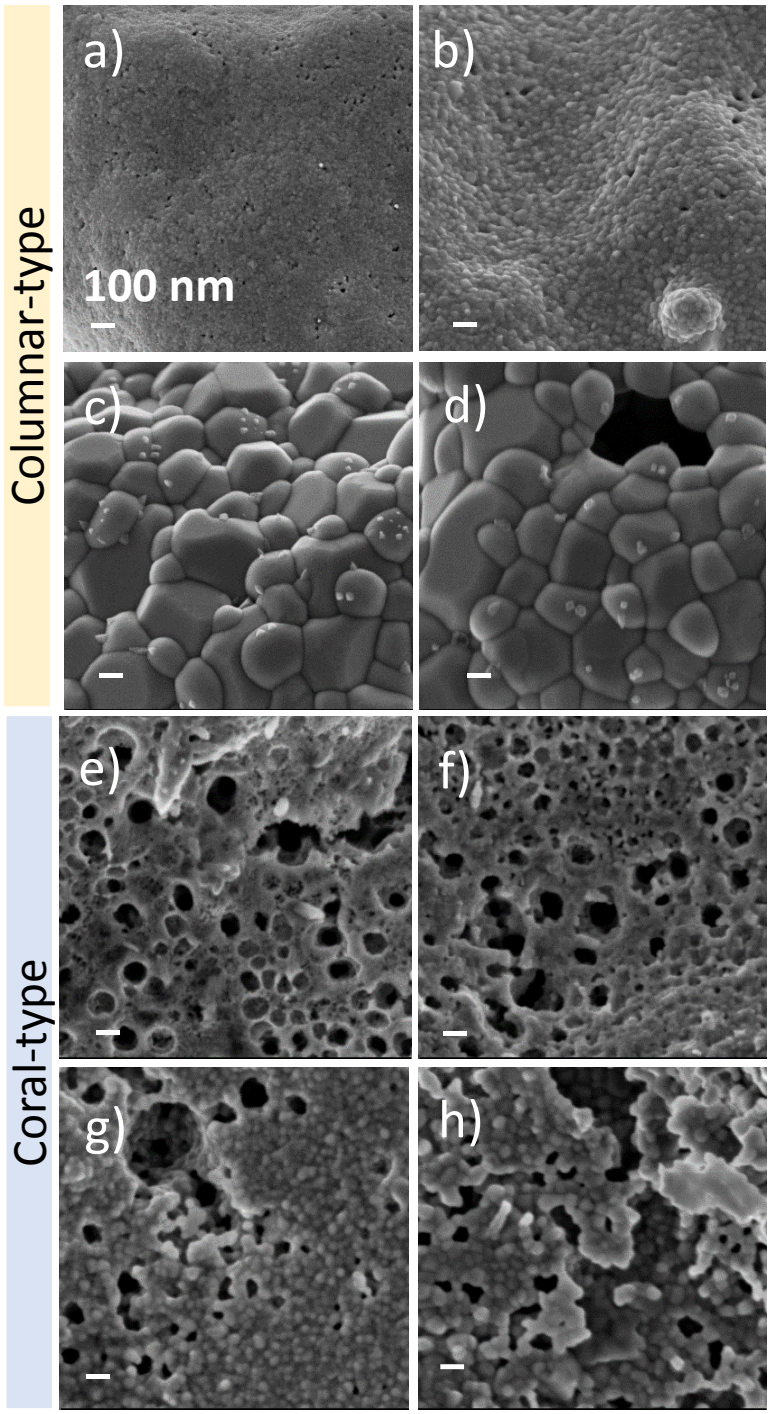

Figure 3-13 Sintering of 60:40 vol. % LSCF/CGO films in air for 2 h at 800 °C, 900 °C, 1000 °C and 1100 °C of a) to d) columnar-type films, e) to h) coral type films. The grains observable on c) and d) are the nano sized Pd deposited prior to SEM imaging to increase the conductivity of the films.

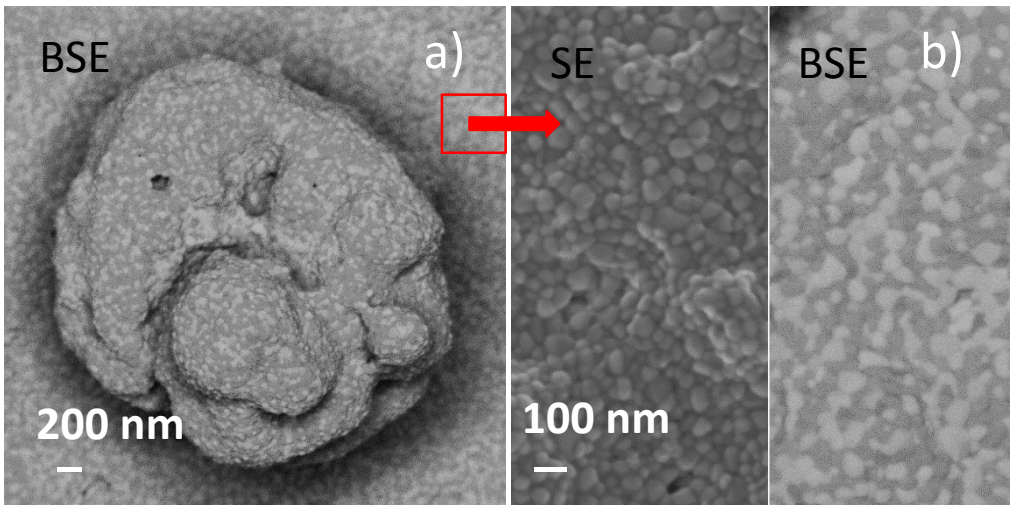

Figure 3-14 Top view of 60:40 LSCF/CGO composite films in coral microstructure imaged by backscattered electron detector. Sample is sintered in air for 2 h at 1000 °C. The light and dark grey colors represent CGO and LSCF phases, respectively.

In terms of adherence, the columnar films sintered at lower temperatures such as 800 °C appear to have good contact at the electrode/electrolyte interface, contrary to the one sintered at 1000 °C as shown in Figure 3-15a, 15b. Above 1000 °C, the films start to delaminate on the corners of macro-pore channels. This could be related to chemical expansion, phase transition and/or mismatch of thermal expansion coefficients (TEC). Li *et al*. reported that the TEC mismatch of 50:50 wt. % LSCF/CGO composite film on CGO electrolyte increases from 700 °C to 1000 °C [187]. This is particularly important at the interface of electrode (LSCF/CGO) and solid electrolyte (CGO). The adherence of coral microstructures on the electrolyte seem relatively better than columnar ones (Figure 3-15c, 15d). Such delamination are not observed at the interface at high sintering temperatures. All coral films present a thin dense layer of ~ 300 nm at the interface (Figure 3-15d), which seem to resist better to the high temperature heat treatment.

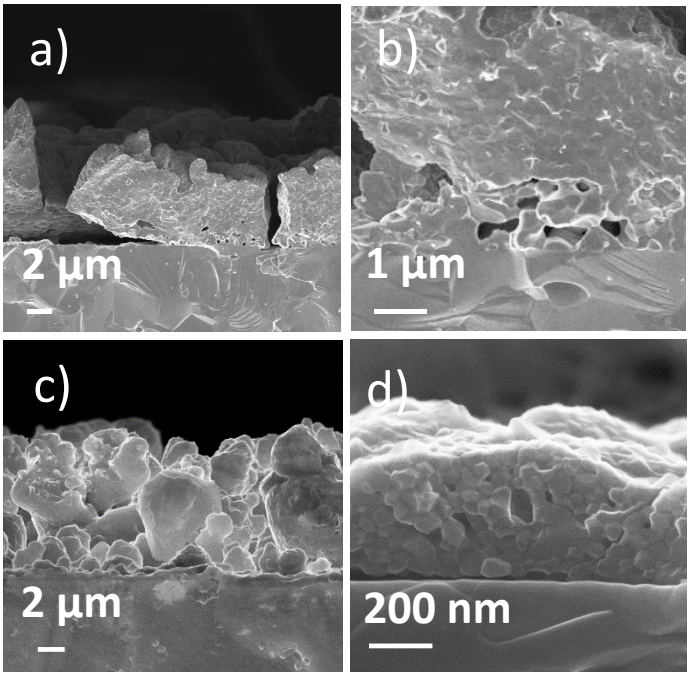

Figure 3-15 The cross section view of a), b) columnar and c), d) coral 60:40 vol. % LSCF/CGO composite films sintered in air for 2 h at 1000 °C.

The crystal structures of both microstructures sintered at 800 °C, 900 °C, 1000 °C and 1100 °C are characterized by powder X-ray diffraction (Figure 3-16). In all films, three phases (LSCF, CGO originating from the ESD coating and from the substrate) were identified. The diffraction peaks of LSCF in the columnar films sintered at 800 °C are indexed to a perovskite unit cell with $R\bar{3}c$ space group (No 167) with refined cell parameters of a = 5.488(9) Å, c = 13.401(5) Å. With increasing sintering temperature to 1100 °C, the lattice parameters of LSCF slightly increase to a=5.507(2) Å, c = 13.451(8) Å. Similar tendency is observed in the coral films with sintering temperature, all of which are in agreement with the values given in the PDF card no 04-017-2448. X-ray diffraction from the CGO electrolyte (substrate) in all diffractograms show distinct and sharp peaks of cubic unit cell ($Fm\bar{3}m$, No 225) with lattice parameter of 5.419(1) Å, agreeing well with the reported PDF card no 04-002-6160. The zoomed-in peaks in Figure 3-16 show the highest intensity peak (111) of CGO from the coating (indicated as G) and the electrolyte substrate (indicated as E). All the peaks of CGO coating slightly shift towards low two theta angles at low sintering temperatures (a=5.4587 Å) and this is more significant in the coral films. This indicates a combination of tensile and compressive stresses which frustrates the crystal and shifts it to higher lattice parameters. Under sintering, the lattice relaxes back to the reference CGO lattice positions (a=5.4159 Å), with all its peaks get sharper and increase in

intensity. Thus, the coating crystals have identical lattice parameters as the electrolyte with increasing temperature [188]. This result disproves our former speculations on the inter-diffusion of elements from LSCF to CGO. This is because this kind of peak shifts would not return back to reference positions with increasing sintering temperature.

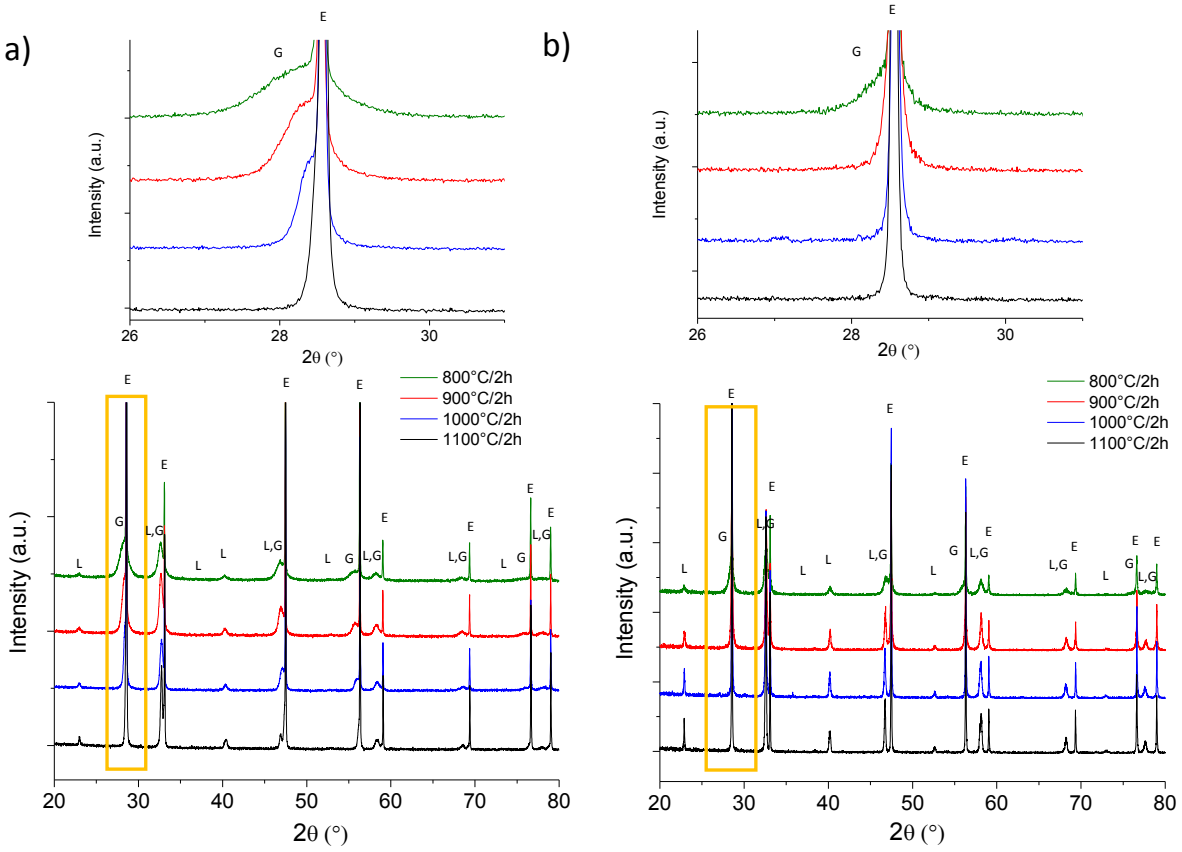

Figure 3-16 The XRD patterns of LSCF/CGO composite films in a) columnar and b) coral type films sintered in air for 2 h at 800 °C, 900 °C, 1000 °C and 1100 °C. The letter L represents LSCF, G represents CGO in the coating and E represents the electrolyte (CGO).

The electrochemical properties of double layer 60:40 vol. % LSCF/CGO composite films in two different microstructures (i.e. coral and columnar) were investigated by EIS after sintering from 800 to 1100 °C. The temperature dependence of the total cathode polarization resistances, ASR_{pol}, from 400 to 650 °C for both microstructures are shown in Figure 3-17. The films sintered at 800 °C and 900 °C show similar values in terms of ASR (0.13 ± 0.02 Ω cm^2 at 600 °C) and activation energy regardless of the microstructure. The lowest ASR values at 600 °C reported for similar CGO compositions in the literature are 0.17 Ω cm^2 by Leng et al.

[57], 0.19 Ω cm^2 by Wang et al. [58], 0.33 Ω cm^2 by Murray et al. [189] and 0.38 Ω cm^2 by Lee et al. The low ASRs obtained in this work are probably due to microstructures of high surface area resulting from small scale grains and porosity. Moreover, double layer cathode configuration (CFL-CCL) have been shown to help lowering the ASR. The enhancement in ORR is suggested to be related to more active surface provided by the thicker film with better current collecting [46,72,91,185].

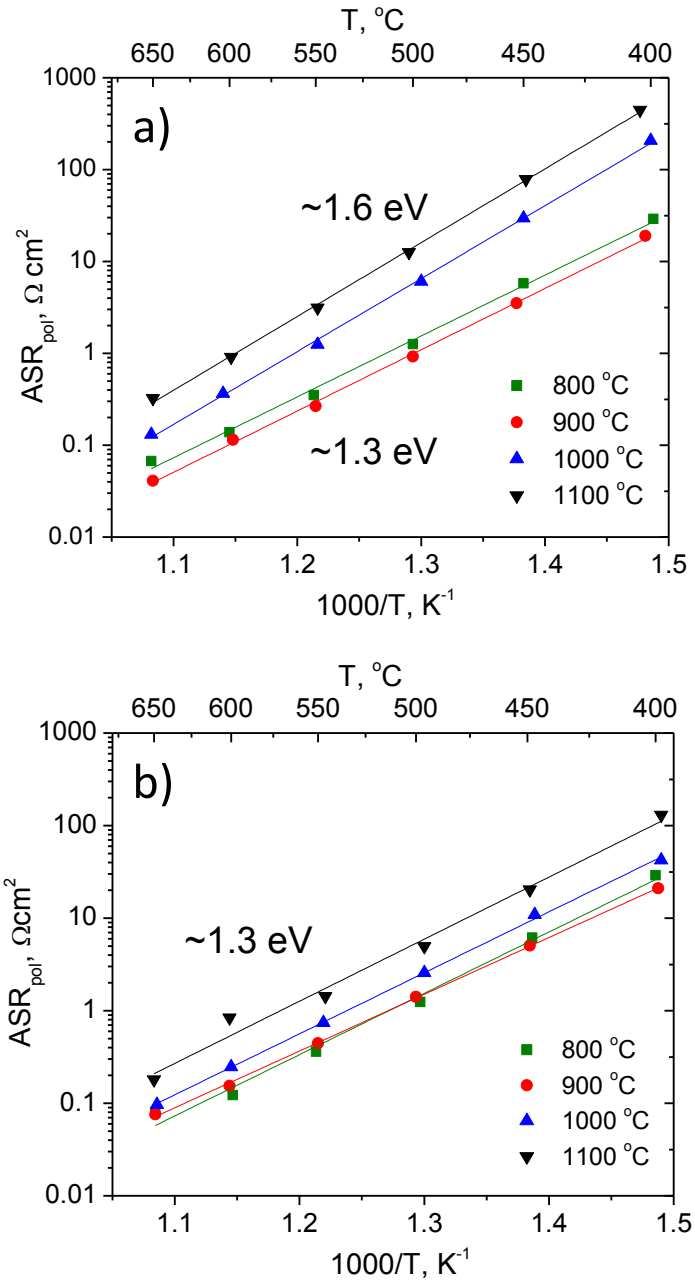

Figure 3-17 The Arrhenius plots of ASR for a) columnar b) coral 60:40 vol. % LSCF/CGO films sintered in air for 2 h at 800 °C, 900 °C, 1000 °C and 1100 °C.

The linear behavior in Arrhenius plot indicates similar ORR phenomena for all films. The activation energy values calculated from the slopes are approximately 1.3 eV, except for the columnar films sintered above 1000 °C (~1.6 eV), all of which are in agreement with previously reported results for CGO compositions higher than 30 wt. % [52–54]. Increasing the sintering temperature results in increased ASR for both microstructures, but this is more significant in the columnar films sintered above 1000 °C.

The impedance spectra are composed of several processes which contribute to the total ASR. They are deconvoluted into different semicircles in the complex impedance plane plots. For each case, a corresponding equivalent circuit is proposed and the identified loss mechanisms are assigned to electrochemical processes. Figure 3-18 and Figure 3-19 show the impedance spectra measured at 450 °C and 650 °C in the form of Nyquist and Bode plots of symmetrical cells of both microstructures sintered between 800 and 1100 °C. Fitting was done using different combinations of equivalent circuits composed of an inductance, L, a series resistance including the ohmic losses originating from electrolyte, R_s, a Gerischer element R_G, (or a fractal Gerischer element R_{G_f}) and/or R//CPE elements (a resistor in parallel with a constant phase element). The configurations are shown in the inset of figures. The serial resistance R_s arising mainly from the ionic conductivity of the electrolyte was routinely compared with the theoretical resistance calculated from the ionic conductivity of CGO and the geometry of the symmetric cells in order to verify that no electronic leak currents have influenced the measurements. For instance, at 600 °C, conductivity values of 0.017 ± 0.001 S cm^{-1} have been measured for all samples which compare well with the literature [176]. This indicates that sufficiently good contact between electrode and electrolyte can be achieved with ESD technique at sintering temperatures as low as 800 °C.

At 450 °C, two semicircles could be observed in the impedance plots of coral films: the high frequency semicircle (f_{summit} at 10 kHz), which is denoted as P_1 (P abbreviation stands for process) and a more resistive low frequency semicircle (f_{summit} at 1-4 Hz) as P_2. P_1 is observed as a separate arc for coral type microstructure at low operating temperatures. P_2 is observed in the impedance spectra of both films sintered at 800 and 900 °C, whereas above 1000 °C another process denoted as P_3 appears only on the columnar films at the lower frequency end with f_{summit} at 0.2 Hz. Within experimental accuracy, the apex frequencies of P_2 of columnar films are comparable to those of coral (f_{summit} at 2.5-15 Hz). In any case, the summit frequency of P_2 decreases with increasing sintering temperature [190].

At 650 °C, a separate semicircle at low frequencies (f_{summit} at 1 Hz) is identified and denoted as P_4, whereas the high frequency semicircle (f_{summit} at 100-300 Hz) is associated to P_2. Similarly, another process is observed only in the columnar films sintered above 1000 °C and assigned to P_3.

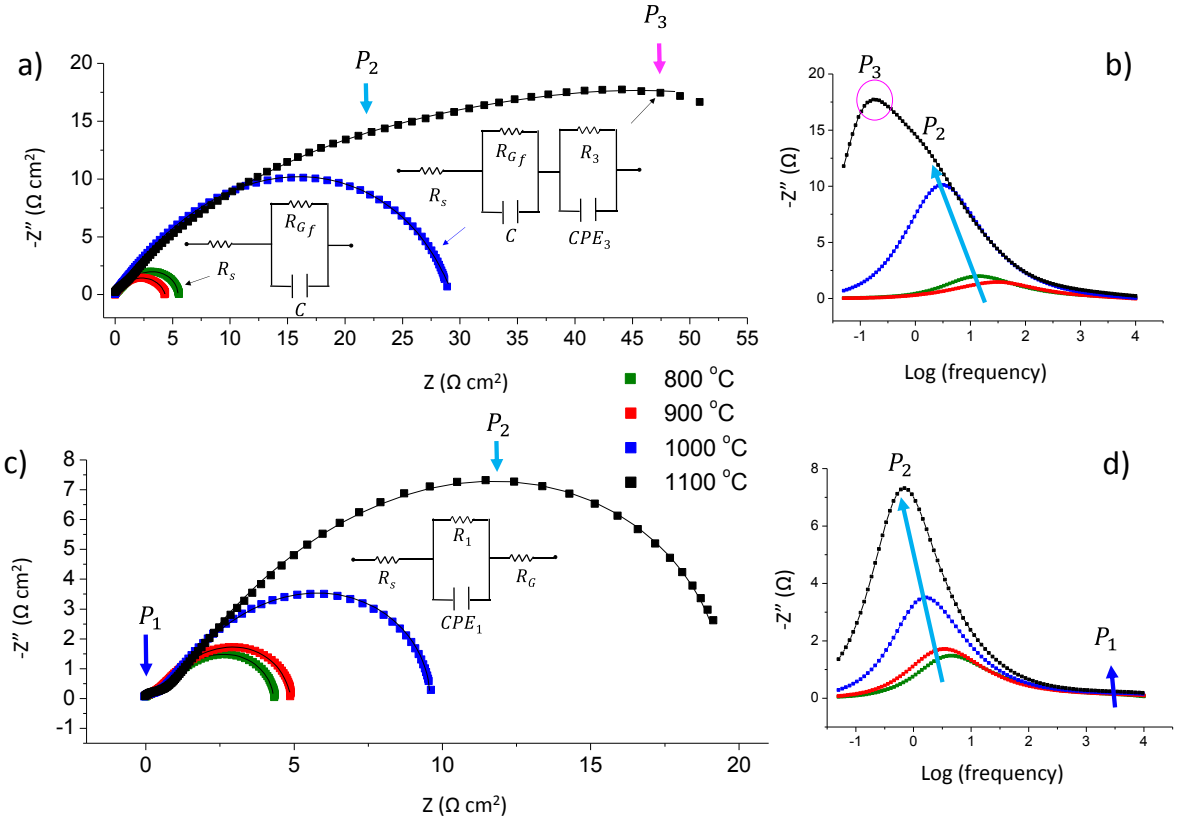

Figure 3-18 Nyquist and Bode plots of symmetrical cells measured at 450 °C of a), b) columnar and c), d) coral microstructures sintered in air for 2h at 800 °C, 900 °C, 1000 °C and 1100 °C. The fits to the spectra are indicated in black line. The series resistance was omitted for comparison purposes. The columnar films sintered at 800 and 900 °C were fitted with R_s -R_{G_f} // C circuit, while R//CPE element has been connected in series at low frequency for the films sintered at 1000 and 1100 °C as: R_s - R_{G_f} // C - R_2 // CPE_2. All the coral films were fitted with R_s - R_1 // CPE_1 - R_G.

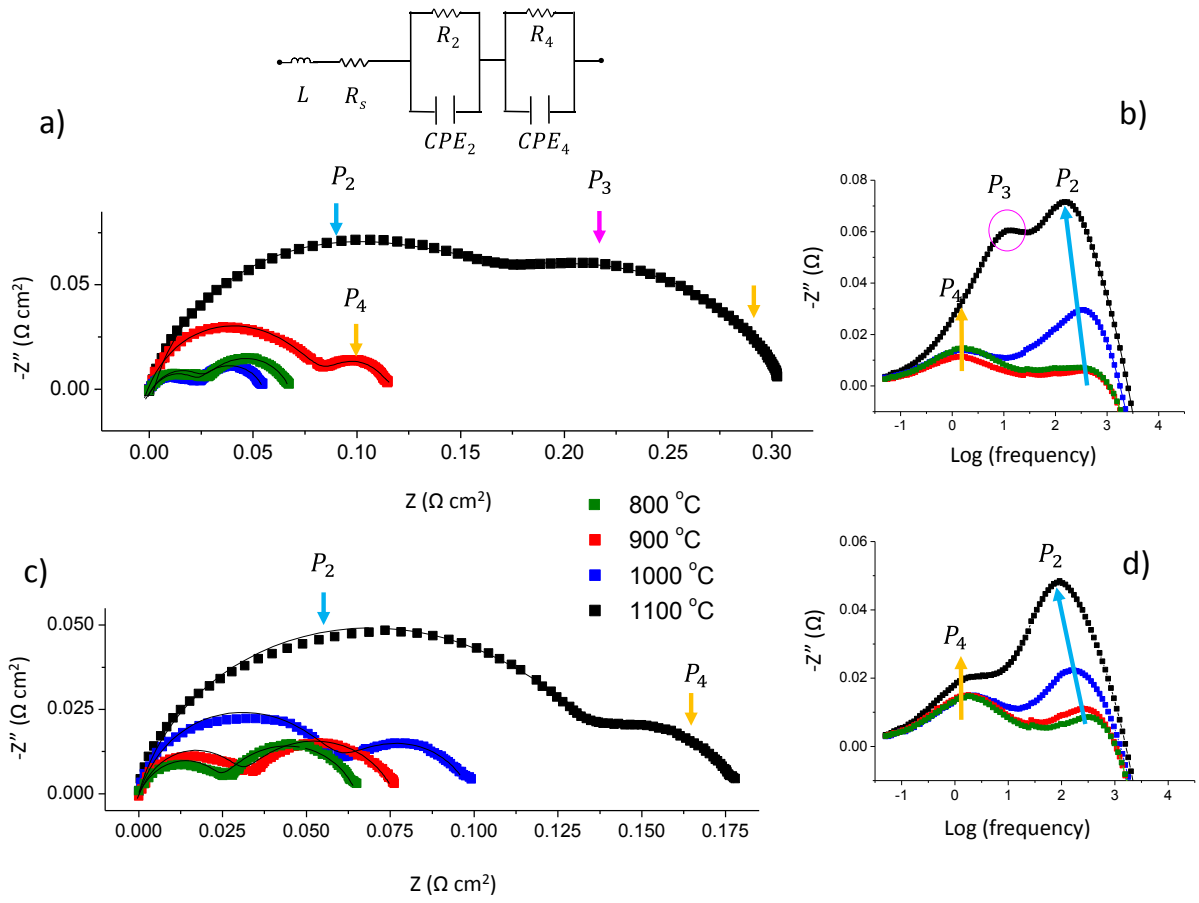

Figure 3-19 Nyquist and Bode plots of symmetrical cells measured at 650 °C of a), b) columnar-type and c), d) coral-type films sintered in air for 2h at 800 °C, 900 °C, 1000 °C and 1100 °C. The fits to the spectra are indicated in black line. The series resistance was omitted for comparison purposes. All films were fitted with L - R_s - R_2 // CPE_2 -R_4 // CPE_4 circuit, except the columnar films sintered above 1000 °C: L -R_s - R_2 // CPE_2 -R_3 // CPE_3 - R_4 // CPE_4.

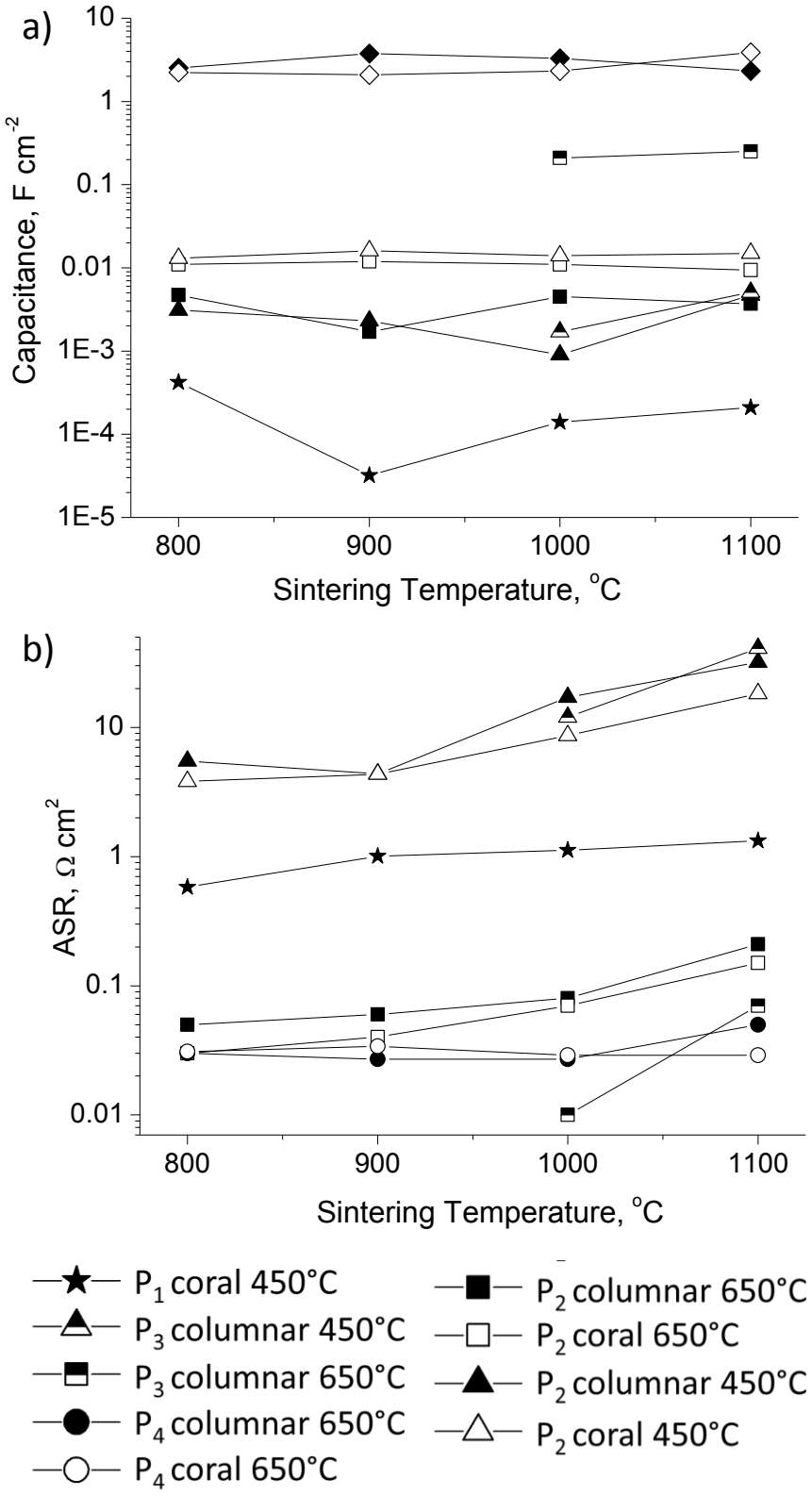

Figure 3-20 a) Capacitance and b) ASR values associated with P_1, P_2 , P_3 and P_4 processes versus sintering temperature for the two microstructures.

Figure 3-20 illustrates the dependence of capacitance and ASR values associated with P_1, P_2, P_3 and P_4 processes on sintering temperature for both microstructures. Capacitance is associated with changes of oxygen stoichiometry in the electrode occurring within a distance from the electrolyte. It can give fingerprints to whether or not the electrochemical processes are related to charge transfer (current collector/MIEC and MIEC/electrolyte) and/or to non-charge transfer processes (solid state transport and oxygen surface exchange). The observed capacitance values for P_1 in the coral films are found to be on the order of 10^{-5}-10^{-4} F cm^{-2}. In our previous work, the rate-limiting steps in dense, columnar and coral type LSCF electrodes contacted with CGO electrolyte were identified by analyzing the variation of resistance as a function of oxygen partial pressure and temperature [175]. The partial pressure had a slight dependence in temperature with an exponent value (n) of 0.1 for the dense film and 0.06 for the coral film ($R = c \cdot p_{O_2}^{-n}$, where R is resistance, c is a constant and n changes according to the limiting process), consistent with the values of an interfacial capacitance coupled to a charge transfer process [179]. The impedance plots of columnar films do not show a separate resistance associated with P_1 process suggesting that either the charge transfer is facile or convoluted within P_2. A slight deformation at the high frequency part of all impedance plots of columnar films is accounted for by a capacitance in parallel to a fractal Gerischer element (values around 0.2-0.5 mF cm^{-2}). As already discussed in the previous section, this suggests faradaic charge transfer impedance that is convoluted with P_2.

Large capacitances, so-called chemical capacitances (C_{chem}) depend on the cathode material and microstructure and generally ranges between 10^{-3} to 10 F cm^{-2} [92]. Since the capacitance values associated with the rest of the processes are a couple order of magnitude larger than double layer capacitances, it can be said that the limiting reaction steps are related to non-charge-transfer processes for both microstructures. P_2 is attributed to co-limited process of oxygen bulk diffusion and surface exchange reactions. The capacitance values associated with P_2 in coral type films are almost twice as high than columnar films at all sintering temperatures. Considering both microstructures having similar resistance values, capacitance and summit frequency are found to be directly related to each other according to: $RCf_{summit} = 1$. Following the relationship between summit frequency and characteristic time constant for a Gerischer impedance, $t_{chem}\ f_{summit} = \sqrt{3}/2\pi$, one can see that capacitance and time constants are reversely related to each other. Taking into account of the relationship between the time constant and the effective surface exchange coefficient, as specified in Appendix B; $a \cdot k_o \sim 1/t_{chem}$, it is found that the film with higher specific surface area will result in lower t_{chem} and

thus in higher capacitance values. Similar results have been reported by Marinha *et al*. with chemical capacitance values ranging between 4.0 ± 0.2 mF cm^{-2} for columnar-type LSCF films and 44 ± 12 mF cm^{-2} for coral-type LSCF films at 600 °C [83]. The capacitance associated to P_3 only observed in the columnar morphology was found to highly depend on the measuring temperature. Increasing temperature leads to almost two fold increase in the capacitance value. Similar trends in capacitance activation with temperature have been reported in the literature for LSCF [83] and $La_{1-x}Sr_xCo_{1-y}Ni_yO_{3-\delta}$ [191]. This is because the concentration of oxygen vacancies increases with temperature, giving rise to higher C_{chem}. Nevertheless, consistent with their capacitance values, P_3 can be associated with oxygen surface reactions, i.e. oxygen surface diffusion and dissociative adsorption, respectively [192,193]. Lastly, P_4, which is observed as a separate arc appeared in the impedance spectra above 550 °C for both microstructures, is associated to pore-gas diffusion and its resistance is temperature independent [165,174]. For all other processes, the resistance increases with sintering temperature. P_1 associated with charge transfer resistance increase with sintering temperature. For both microstructures, the resistance of P_2 remains the main limiting resistance at low measuring temperatures and increases with increasing sintering temperature. This is probably related to the reduction of specific surface area by densification of the film. The resistance associated with P_3 is as important as P_2 for columnar films sintered above 1000 °C and it is directly responsible for the increase in activation energy of the total ASR (1.3 eV to 1.6 eV, Figure 3-17a). These values are similar to the activation energy of pure LSCF [52,57,150,165,184], suggesting that the percolation of CGO is completely lost in these films and the ionic conduction is achieved only through LSCF particles.

3.5 Conclusion

Functional hierarchical nanostructured layers of well crystallized pure LSCF films were obtained in two different microstructures: coral and columnar. The latter was chosen for the characterization by FIB-SEM tomography after sintering at 800 °C for 2 h in air. In order to study the influence of CGO in the microstructure and electrochemistry, 0, 25, 40 and 60 vol. % CGO were sprayed together with LSCF to make composite films. Hierarchical films of columnar microstructures are composed of fine nano-porosity within the columns and large macro-pore channels in between the columns. The FIB/SEM tomography revealed heterogeneously distributed porosity within the 60:40 vol. % LSCF/CGO composite column in contrast to pure LSCF. Nevertheless, the composite film exhibited large nano-porosity (~20 % which is as high as pure LSCF) and specific surface area (~8 μm^{-1}) close to the electrode/electrolyte interface. While exceptionally low ASR values of 0.02 and 0.07 Ω cm^2 at 650 and 600 °C, respectively, were recorded for pure LSCF, the addition of CGO to this state-of-the-art cathode did not improve the electrochemical performance, in apparent contradiction with the common expectations. A possible explanation could lie in the modifications of the nanostructure, in particular the reduction of the specific surface area with the addition of CGO. This will be confirmed with the 3D-FEM modeling (Chapter 5). Further study on sintering temperature was conducted to optimize pore and grain sizes in 60:40 composite electrode in both coral and columnar microstructures. Due to different deposition parameters, the porosity and grain growth of the two microstructures were very different. The coral films had smaller grain sizes at all sintering temperatures. Furthermore, the grain growth of LSCF and CGO augmented non- uniformly in the columnar films sintered above 1000 °C. All the films sintered at 800 and 900 °C presented similar ASR and activation energy values regardless of the microstructure. Both microstructures sintered above 1000 °C showed increase in ASR, whereas the activation energies of the columnar films increased and resembled to that of pure LSCF. This is attributed to the disrupted CGO percolation due to excessive growth of LSCF phase

4 THE PERFORMANCE OF ARCHITECTURED DOUBLE LAYER LSCF CATHODE ON ANODE-SUPPORTED CELLS

Chapter 4 focuses on the optimization of the double layer cathode films of pure LSCF deposited by electrostatic spray deposition (ESD) technique as cathode functional layer (CFL) topped by LSCF deposited by screen printing (SP) technique as current collecting layer (CCL). The thicknesses of CFL and CCL are varied and current constriction effects are monitored by electrochemical impedance spectroscopy. Finally, the optimized double layer LSCF films are deposited on anode-supported fuel cells. The performance and long term durability of the complete cells are tested at 675 °C.

4.1 Introduction

The composition and the microstructure of the cathode films are among the key factors that define the length of the electrochemically active region (utilization length) within a porous electrode. The utilization length of the cathode, L_δ, can be calculated by the analytical expression derived by Adler *et al.* [92].

$$L_\delta = \sqrt{\frac{(1-\varepsilon)}{a\cdot\tau}\frac{D_o}{k_o}} \qquad 4\text{-}1$$

where ε, a and τ which are respectively the porosity, specific surface area and tortuosity, all of which can be calculated from image analysis of reconstruction data from FIB/SEM tomography. D_o and k_o are oxygen diffusion coefficient and oxygen surface exchange parameters. L_δ values are typically found in the range from 0.4 to 20 µm for mixed conductors with high rates of bulk ionic transport [194]. Oxygen partial pressure, temperature, and the surface area of the electrode have significant influence on L_δ. The microstructural parameters are calculated from reconstruction of images as shown in Table 3-1. The transport parameters are calculated from the fits of impedance data. Using Eq. 4-1, the utilization length of pure LSCF in this study was found on the order of 0.1 µm. As discussed thoroughly by Fleig and Adler, the 1D macrohomogeneous bulk transport assumption (Gerischer impedance) breaks down when the utilization length is on the same order or smaller than the particle size; $I_\delta \approx \sqrt{I_g D^q / k^q}$ (i.e I_g is the particle size) [194,195]. However, since fairly reasonable fits with Gerischer impedance were still obtained, we assume that the 1D macrohomogeneous approach is still applicable.

Giving the thickness of the ESD layer being more than a hundred times larger than the utilization length, it is reasonable to assume that only the ESD layer is electrochemically active. However, a number of studies have reported better performance with double layered electrodes (CFL-CCL) which are vastly thicker than the electrochemically active zone [46,72,91,92,97,185,196–200]. In order to explore the effect of microstructure and thickness on the electrode performance, LSCF films were deposited either as single layer by only SP (sintered at 800 °C/2h in air), by only ESD (sintered at 800 °C/2h in air) and as a double layer:

first by ESD (sintered at 800 °C/2h in air) followed by SP (as indicated in 2.1.2.3) for different CCL and CFL thicknesses.

4.2 The architecture of cathode films

4.2.1 Microstructural Characterization of the Films

Figure 4-1a, 1d and 1g shows the top and cross section views of the single layer film deposited by only SP. Apart from very few cracks (porosity) as observed from the top view, the film is generally quite flat on the surface. The thickness of the film is about 6 μm. Although, an average crystallite size of 28 nm is calculated by XRD peak broadening by Scherrer's formula, Figure 4-1g allows the observation of the agglomerates with an average particle size of 200 nm. Figure 4-1b, 1e and 1h exhibits the single layer film deposited by only ESD. The thickness of the film is also about 6 μm. The hierarchical porous character are highlighted with macro porosity separating the columns in Figure 4-1e, and nano porosity within the columns in Figure 4-1h. Figure 4-1c, 1f and 1i shows the double layer films coated by ESD and topped with SP. The thickness of the first layer (ESD) is about 6 μm, while the second layer (SP) is about 30 μm. The second layer provides a flatter surface than the first layer, thus improving the current collection by increasing the contact points between the surface and current collecting grid. The microstructural parameters of the ESD part of the double layer film were already introduced in Table 3-1. The microstructural parameters of the second layer by SP were calculated by 3D reconstruction of the images obtained by FIB/SEM tomography (Figure 4-2). A porosity amount of approximately 35 % and a specific surface area of 13 μm^{-1} were computed (Table 4-1).

Table 4-1 Microstructural parameters calculated by analyzing the reconstructed 3D FIB/SEM images. ε (porosity), and a (specific surface area) are calculated for three threshold values to provide an evaluation of the uncertainty [43].

SP films	Thickness range, μm	Porosity, ε, %	Sp. Surf. Area, a, μm^{-1}
100 LSCF	0 – 6.50	35 ± 4	13 ± 1

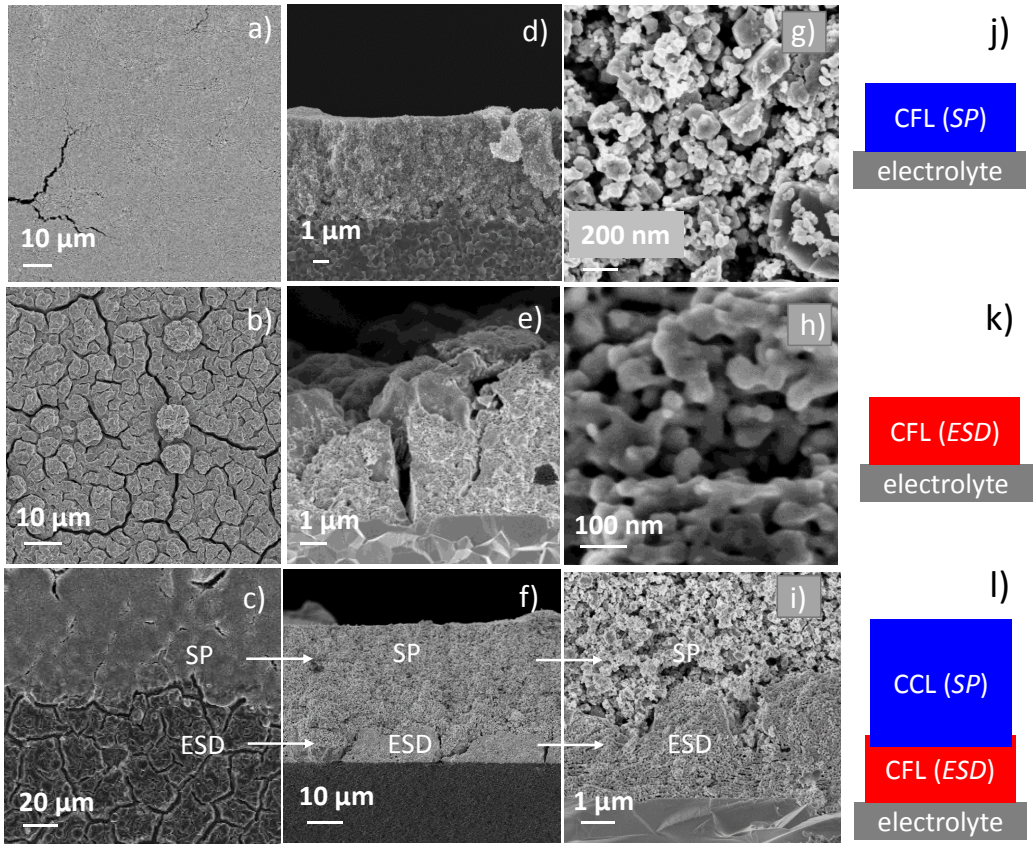

Figure 4-1 Top views of SEM images of single layer LSCF films of a) CFL (*SP*), b) CFL (*ESD*) and double layer film CFL-CCL (*ESD-SP*). Cross-sectional views of d) CFL (*SP*), e) CFL (*ESD*) and f) CFL-CCL (*ESD-SP*). g) h) and i) are the magnified images showing the porosity and particle sizes. j), k) and l) are the schematics of the three films.

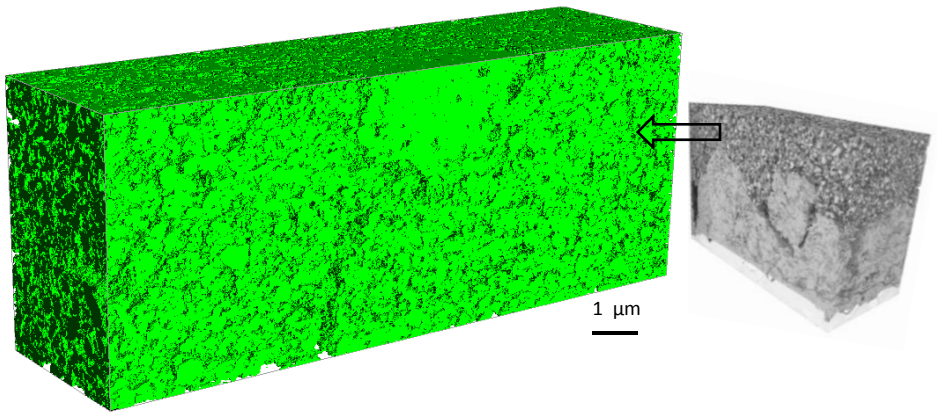

Figure 4-2 3D reconstruction of the CCL (SP) after FIB/SEM tomography.

4.2.2 Electrode Performance of by EIS

Figure 4-3 shows the Arrhenius plot of ASR_{pol} of single layer LSCF deposited by SP, referred to as CFL (*SP*), another single layer LSCF deposited by ESD, referred to as CFL (*ESD*) and the double layer LSCF deposited successively by ESD and SP, referred to as CFL-CCL (*ESD-SP*). The thickness of single layer films were equally 6 µm, while the bottom and top layers in the double layer film were 6 µm and 30 µm, respectively. The activation energies (~ 1.4 eV) were similar in all films. The striking result in comparing single layer films of CFL (*ESD*) and CFL (*SP*) is that about two orders of magnitude decrease in ASR_{pol} was obtained with CFL (*ESD*), while approximately 2.5 fold decrease was obtained with double layer CFL-CCL (*ESD-SP*) compared to single layer CFL (*ESD*).

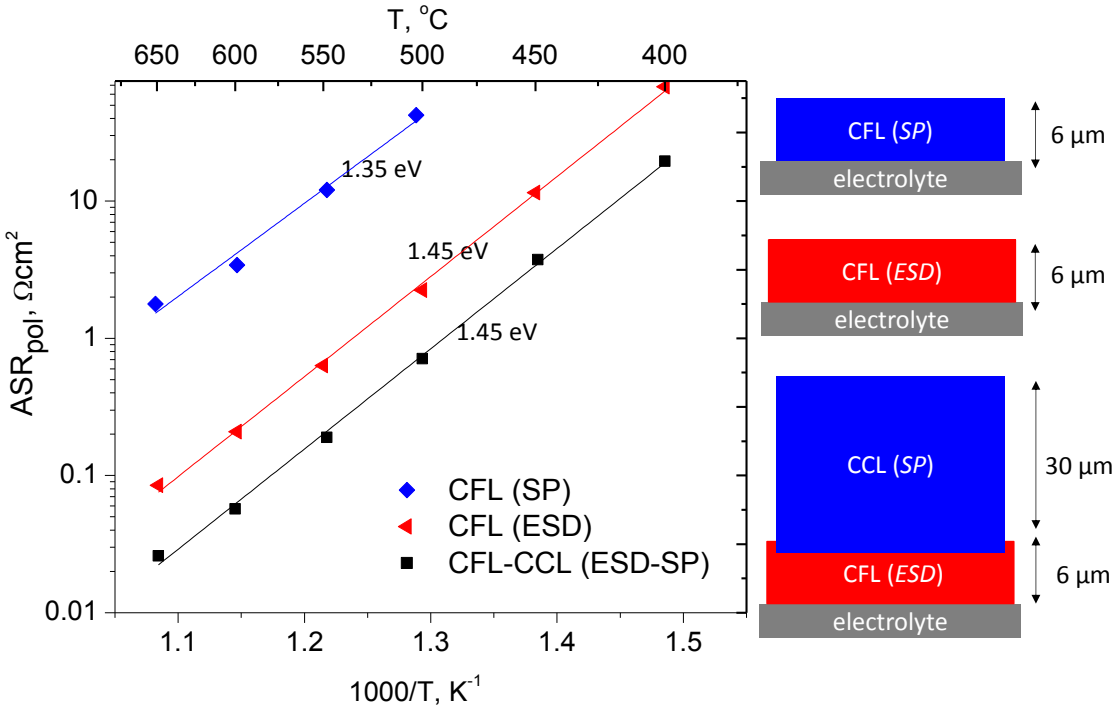

Figure 4-3 Arrhenius plot of ASRpol of CFL (*SP*), CFL (*ESD*) and CFL-CCL (*ESD-SP*) films.

4.2.2.1 CFL (*SP*)

The electrochemical characterization symmetrical cells of the screen printed film as CFL was performed by impedance spectroscopy at OCV from 400 to 650 °C in air.

Figure 4-4**,** shows the impedance spectra in the form of Nyquist plot. The series resistance of the electrolyte and polarization resistance of the cathode decrease with increasing temperature. Continuous shifts in the frequencies are demonstrated as a function of temperature. The impedance spectra at all temperatures were fitted with the equivalent circuit, *R*//*CPE* – *G*. The arc in the high frequency range can be associated to charge transfer resistance at the electrode/electrolyte interface with a capacitance value of the order of 1.5 10^{-5} F cm^{-2}, while the arc in the intermediate-to-low frequency range is related to the bulk diffusion and surface exchange processes in the porous electrode with a capacitance value of the order of 10^{-3} F cm^{-2} [175,179]. The charge transfer resistance is as high as 0.6 Ω cm^2 at 650 °C and 300 Ω cm^2 at 400 °C. CFL (*SP*). The decrease in resistance from CFL (*SP*) to CFL (*ESD*) can thus be equally attributed to improvement in charge transfer resistance at the interface and faster electrode kinetics related to nanostructured microstructure features. Indeed, the electrode/electrolyte interface has a predominant role in the charge transfer of oxygen ions. Hubert *et al.* recently reported only 55 % interfacial surface area coverage on the interface between screen printed LSCF on YSZ/CGO bilayer electrolyte [2]. In order to decrease the charge transfer resistance, the CFL (*SP*) should be sintered at temperatures higher than 1000 °C [50,201,202]. However, it should be kept in mind that increasing sintering temperature would increase the particle size, and lower the surface area, which in turn result in higher ASR values (Chapter 3).

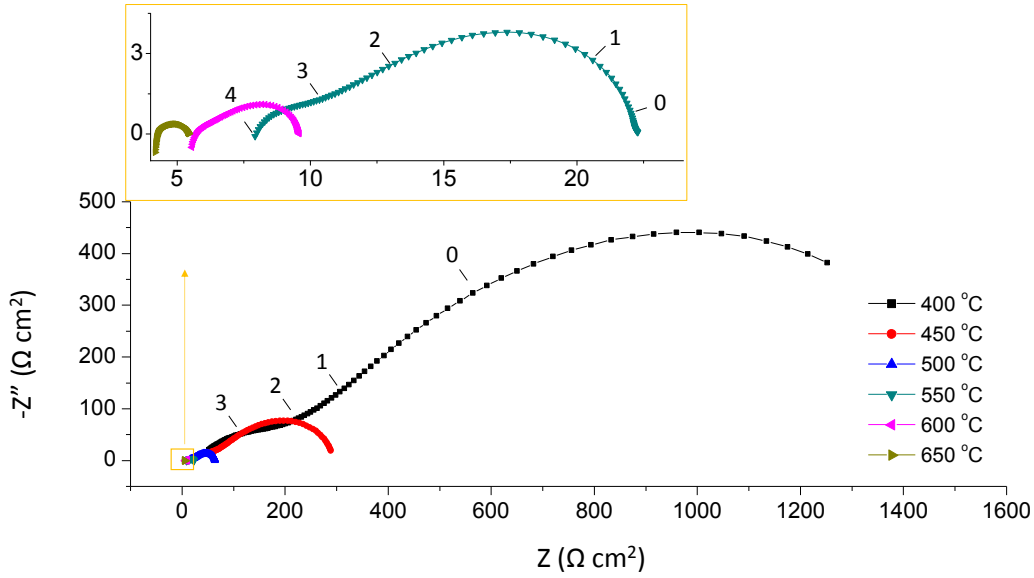

Figure 4-4 Nyquist plot of impedance spectra of screen printed CFL between 400-650 °C. The numbers on the diagrams indicate the logarithm of frequency.

4.2.2.2 CFL (*ESD*) and CFL-CCL (*ESD-SP*)

As for the comparison of impedances of single layer CFL (*ESD*) and CFL-CCL(*ESD-SP*), the following equivalent circuits are used as already illustrated in Figure 2-10; R_s - R_{G_f} // C between 400 °C and 500 °C and L - R_s - R_1 // CPE_1 - R_2 // CPE_2 at 550°C. Table 4-2 and Table 4-3 show the impedance fitting parameters for LSCF single and double layer films at 400-500 °C. The resistance and the characteristic time constants of the CFL-CCL (*ESD-SP*) film decreased more than twice compared to CFL (*ESD*) film. The capacitance of Gerischer element C_{chem} was calculated by the formula: $C_{chem} = t_{chem}/R_{G_f}$ (see Eq. A 6 in Appendix B). The capacitance value parallel to Gerischer element is in accordance with Baumann *et al.*'s reports and may be assigned to charge transfer processes at the electrode/electrolyte interface [179]. The fitting parameters at 550 °C with two R//CPE elements in series to each other are shown in Table 4-4. The high frequency processes fitted with R_1 // CPE_1 seem to be similar to Gerischer element. The calculated capacitances for C_1 can be associated to chemical capacitances. The capacitances associated with the low frequency arc obtained from the fitting are between 5 to 9 F cm $^{-2}$. Such large values are unlikely to be from any electrochemical process and are attributed to the gas phase diffusion process.

Table 4-2 Impedance fitting parameters of double layer CFL-CCL (*ESD-SP*) film at 400-500 °C.

T, °C	σ_{CGO}, S cm^{-1}	R_{G_f}, Ω	C_{chem}, mF cm^{-2}	C, mF cm^{-2}
400	0.35	25.0	1.65	0.259
450	0.64	4.74	2.27	0.345
500	1.04	0.98	7.92	0.545

Table 4-3 Impedance fitting parameters of single layer CFL (*ESD*) film at 400-500 °C.

T, °C	σ_{CGO}, S cm^{-1}	R_{G_f}, Ω	C_{chem}, mF cm^{-2}	C, mF cm^{-2}
400	0.25	65.8	0.87	0.345
450	0.48	11.0	1.75	0.296
500	0.83	2.11	2.52	0.367

Table 4-4 Impedance fitting parameters of a) CFL (*ESD*) and b) CFL-CCL (*ESD-SP*) films at 550 °C.

	σ_{CGO}, S cm^{-1}	R_1, Ω	C_1, mF cm^{-2}	R_2, Ω	C_2, F cm^{-2}
a)	1.48	0.25	1.83	0.020	5
b)	1.24	0.54	1.39	0.015	9

For a further discussion, the Nyquist and Bode plots are shown in Figure 4-5 and Figure 4-6, respectively. Nyquist plots are in general very similar, except a more inclined high frequency region in the double layer CFL-CCL films above 500 °C. Moreover, only one arc is observed up to 500 °C in both films. A second arc at the summit frequency around 1 Hz appears only above 550 °C.

The Bode-type plots show the existing of two arcs that are probably overlapped at high to medium frequency range (Figure 4-6). The peak maxima at 550-650 °C (green arrows) do not correspond to the same phenomena of those at 400-500 °C. In fact, the process that dominates the cathode resistance at 400-500 °C (blue arrow) can also be evidenced by the shoulder and asymmetry of the peaks in between 10-100 Hz at 550-600 °C. There is also the peak at about 1 Hz that is related to pore-gas diffusion that can only be observed above 550 °C. Comparing the plots of the two films, the summit frequencies are shifted to higher frequencies when double layer film is used [80]. The summit frequency and the resistance are related to the thermodynamic properties, surface kinetic and transport properties of the material (Appendix B). As has been shown earlier, the utilization length stays in the first couple of hundred

nanometers in the ESD layer, where the microstructure is assumed to be the same in both films. The enhancement in ORR may therefore be related to more active surface provided by the thicker film with better current collecting.

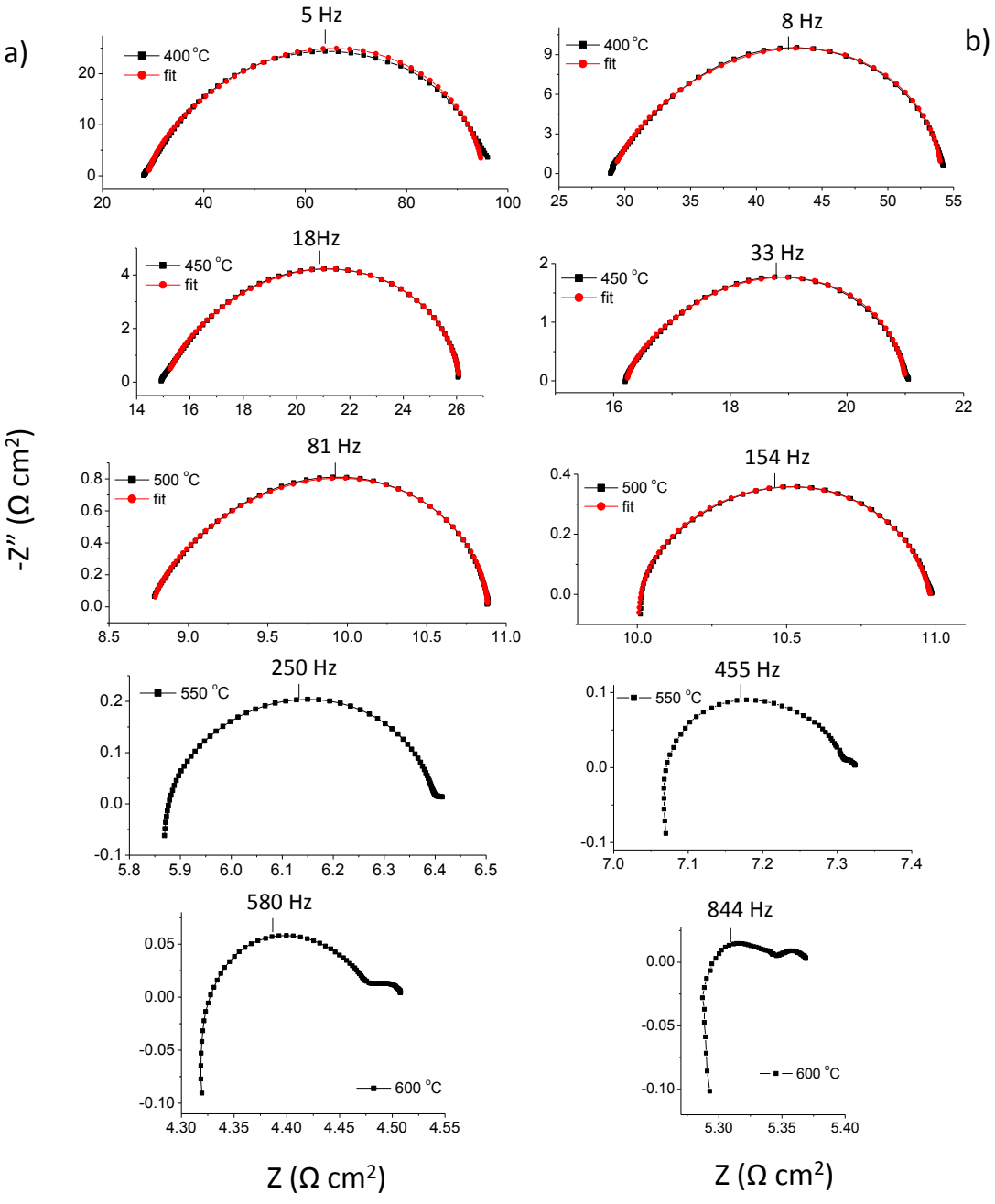

Figure 4-5 Nyquist plots of LSCF in a) single layer CFL (*ESD*) b) double layer CFL-CCL (*ESD-SP*) films from 400-600 °C. The thickness of the electrolyte used in the measurements of double layer film was 1.65 mm while it was 1.45 mm in the single layer film.

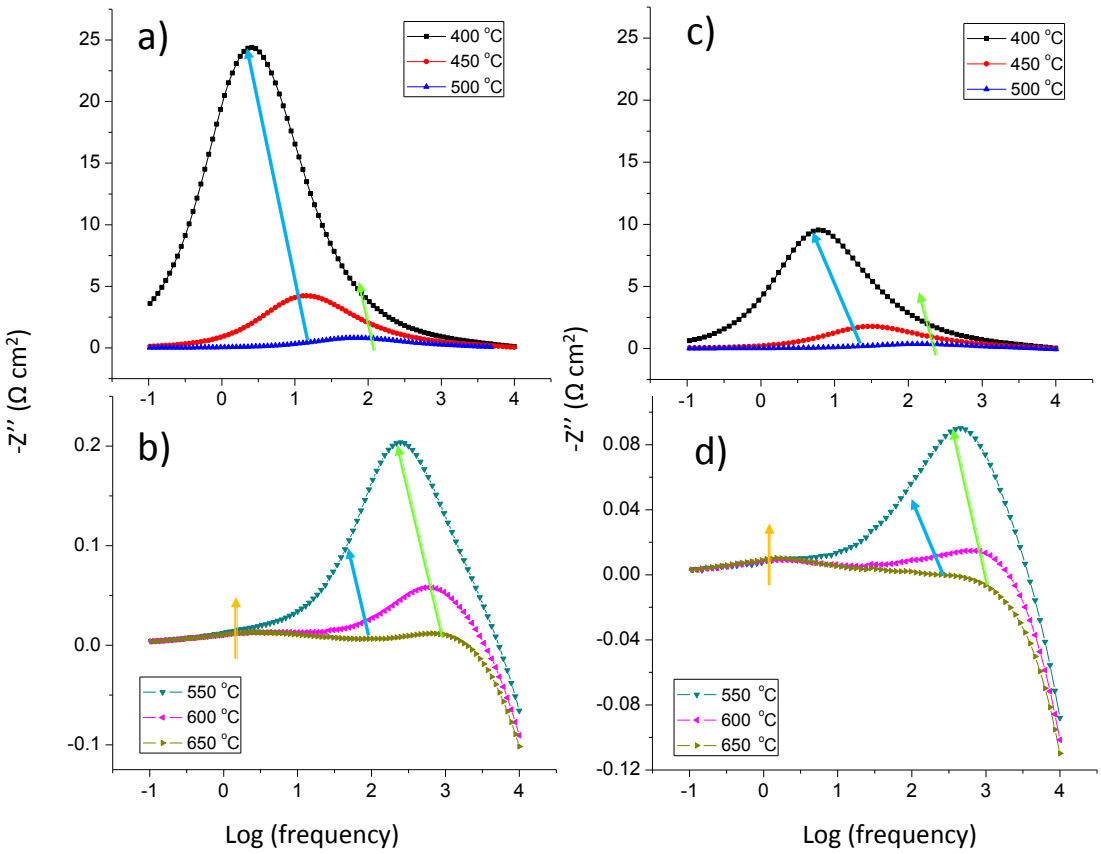

Figure 4-6 The Bode plots for a, b) CFL (*ESD*) film c, d) CFL-CCL film between 400-650 °C. Arrows indicate the three possible elementary electrode processes.

One of the factors contributing to the power loss is the ohmic resistance of the cell, which includes electrolyte resistance, electrode material resistance and the interface resistance due to non-optimized contact and current collection. It has a very strong dependence on the thickness of each cell component and the contact geometry between the electrode/electrolyte and the electrode/CCL. In the next two sections, the influence of CCL and CFL thicknesses on the performance of double layer films will be discussed.

4.3 The influence of CCL thickness on the performance of double layer electrode

Comparing the ASR in relation to the thicknesses of single layer CFL (*ESD*) and double layer CFL-CCL (*ESD-SP*) films provides more information on the effect of current collection. While the thickness of the CFL in the double layer films was kept fixed at 6 µm, the thickness of the CCL was varied from 20 to 50 µm (Figure 4-7). A sudden decrease in ASR_{pol} was obtained by adding the 20 µm thick CCL on the single layer film. Further decrease occurred when the CCL thickness was increased to 30 µm. At this thickness, the ASR reach a limit. This leads to the conclusion that in-plane conductivity in the CFL-CCL (6 µm -30µm) film is optimized [196].

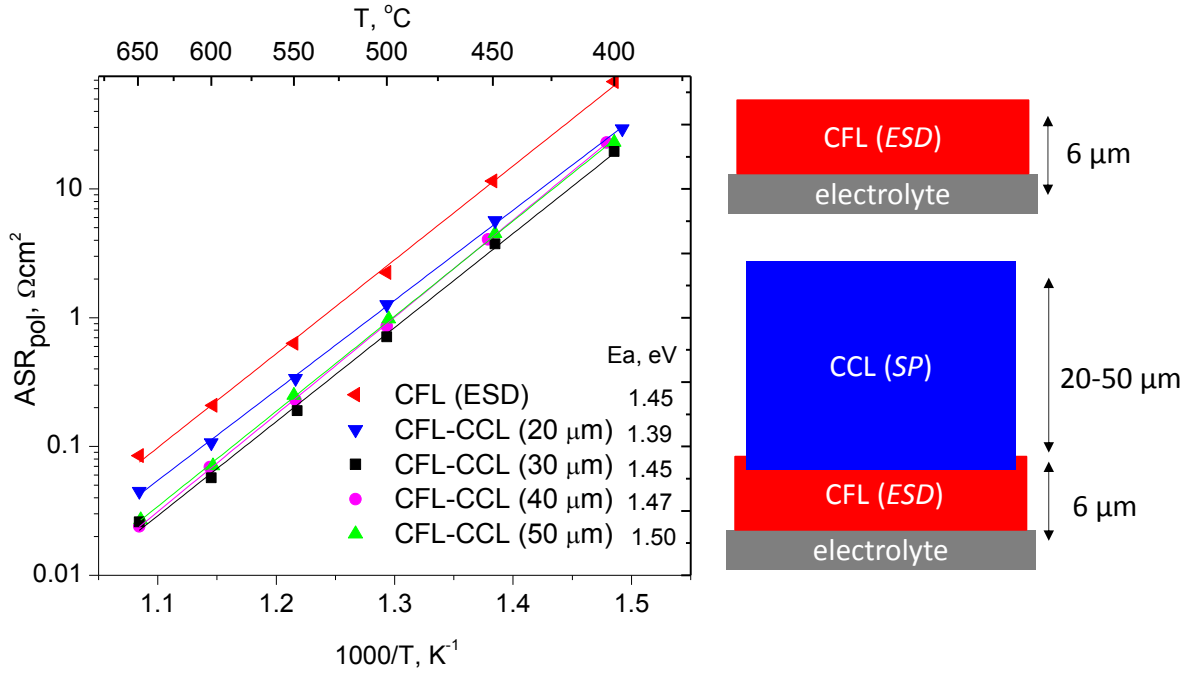

Figure 4-7 Arrhenius plot of ASRpol of CFL (*SP*), CFL (*ESD*) and CFL-CCL (*ESD-SP*) films.

Similar conclusions have been reached pointing at a minimum thickness related to the contact points to fully utilize the total surface area of the interface [46]. The electrode performance of single and double layer electrodes was studied by Jung *et al.* [198] and Kenney *et al.* [200]. Jung *et al.* achieved a power density as high as 1.5 W cm^{-2} at 750 °C with double layer electrodes in comparison to 0.9 W cm^{-2} with single layer electrodes, demonstrating the current constriction effects. They attributed this improvement to a simultaneous decrease in ohmic and

polarization resistance on the thicker cathode. Kenney *et al*. reported a 13.7 % increase on the average current density when the thickness of the CCL was increased from 5 to 15 μm on top of 15 μm thick CFL [200]. More detailed work by Kenjo *et al*. illustrated the local variations of the electrochemical activity due to non-uniform contact on the electrode/electrolyte interface as shown in Figure 4-8 [203]. Accordingly, within the vicinity of the interface (δ distance), the current lines are concentrated to the contact points and expands with increasing distance. If the electrolyte is sufficiently thick, the current lines reach to uniformity.

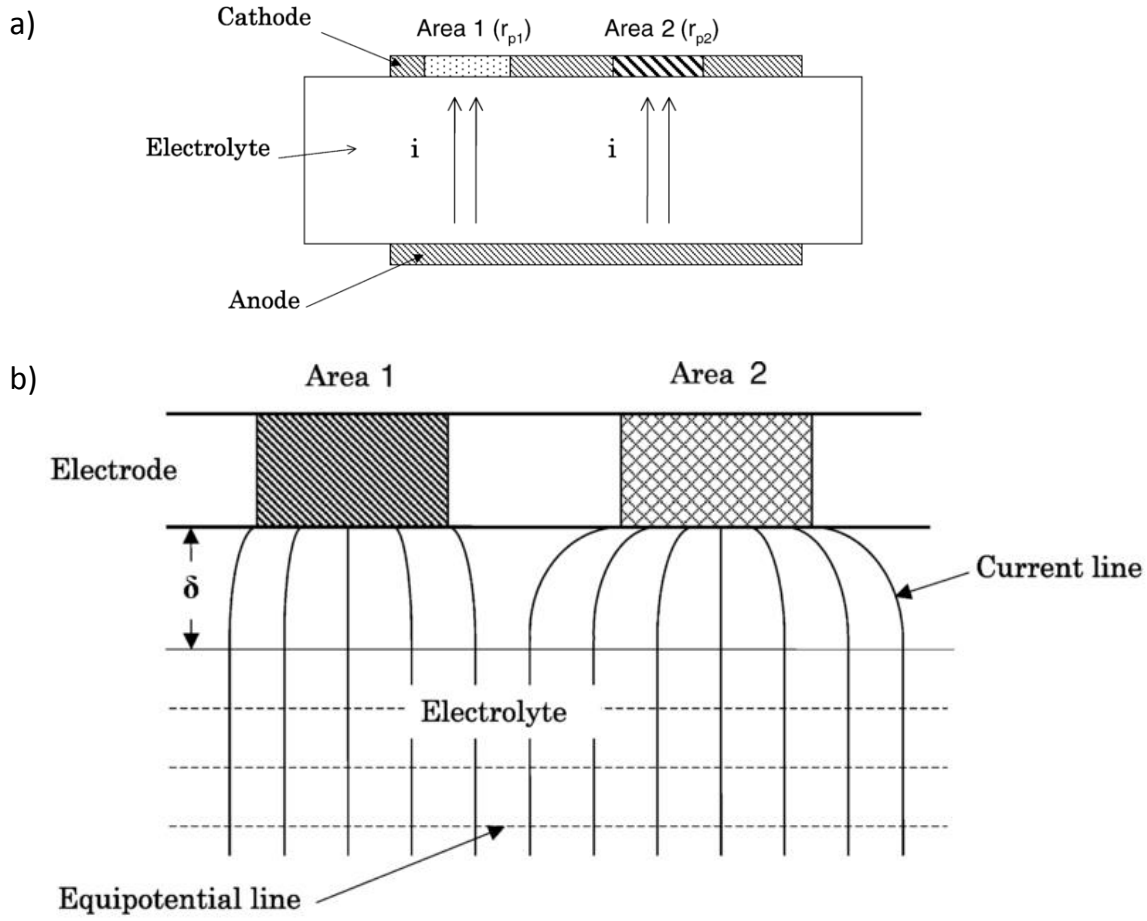

Figure 4-8 a) Scheme of a non-uniform electrode with two different local polarization resistances, r_{p1} and r_{p2}, respectively. b) Current distribution in the vicinity of the electrode/electrolyte interface. The current density is uniform outside the δ thickness, but shrinks inside this region due to discrete contacts [203].

In order to evaluate the current collection in our films, the conductivity of the CGO electrolyte was calculated for each film that is in contact with the electrolyte on a symmetrical cell. The

conductivity is an intrinsic property of the material. Nevertheless, a lower value would point out a bad contact and/or inhomogeneous current distribution. Figure 4-9 shows the Arrhenius plot of the conductivity of CGO electrolyte contacted with LSCF single layer CFL (*ESD*) film and the various thicknesses of double layer CFL-CCL films. A progressive decrease of σ_{CGO} from double layer CFL-CCL film to single layer CFL film is observed with respect to the literature [23]. Thicknesses above 30 μm thick CCL, the values are similar and constant. This indicates a good in-plane conductivity in the electrode, and that the whole electrode/electrolyte interface area is used [204]. This is also verified by calculating the effective thickness of the electrolyte by the following Eq. 4-2:

$$R_{elyt} = \frac{L}{\sigma_{CGO}} \qquad 4\text{-}2$$

where L is the effective thickness of the electrolyte, σ_{CGO} is the intrinsic ionic conductivity of the electrolyte and R_{elyt} is the resistance of the electrolyte. For single layer CFL (*ESD*) film, the resistance of the electrolyte at 600 °C was measured as 8.7 Ω cm^2. Assuming 0.02 S cm^{-1} as the conductivity value of CGO (600 °C) [23] one can deduce the effective thickness of the electrolyte as 0.174 cm. This value is greater than the actual thickness of the electrolyte which is 0.145 cm. On the other hand, for double layer CFL-CCL (6 μm -30 μm) film, the resistance of the electrolyte, R_{elyt} at 600 °C was measured as 8.08 Ω cm^2. In this case, L is equal to 0.16 cm, which is the same value as the actual electrolyte thickness (0.16 cm). The deviation in the effective thickness of the electrolyte was attributed to the discrete contacts of electrode and electrolyte as defined by Tannenberger *et al*. [205], and current constriction resistance as defined by Fleig and Maier [206]. It can be concluded that there is no current constriction when at least 30 μm CCL is topped on the 6 μm thick CFL layer.

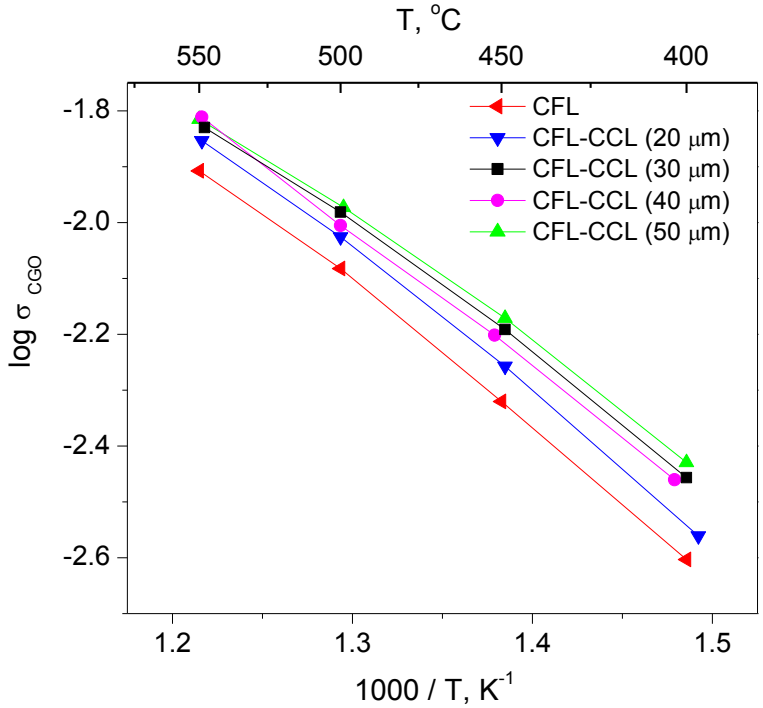

Figure 4-9 The Arrhenius plot of the ionic conductivity of CGO electrolyte contacted with single layer CFL (*ESD*) and double layer CFL-CCL (*ESD-SP*) films.

4.4 The influence of CFL thickness on the performance of double layer electrode

Films with various CFL thicknesses were obtained by controlling the time of ESD deposition from 20', 40', 1h, 1h45', 3h and 4h30' to study the influence of the CFL thickness on the double layer electrode performance. Figure 4-10 shows the average thicknesses of the films ranging between 0.5 and 18 μm. The macro-pore channels appeared after the film reached 5 μm in height. The surfaces of the microstructures are also flatter at the same time. The width of the macro-pore channels increased with increasing deposition time. 18 μm thick-film highly detached near the macro-pores, thus it was not considered for further characterization by impedance spectroscopy. All films seem to keep similar porosity inside the columns, however it is difficult to judge their amount from SEM images. It is noteworthy to mention that all the CFL (*ESD*) films were topped with 30 μm thick CCL (*SP*) before the electrochemical characterization by impedance spectroscopy because this thickness represents an optimum of electrical performances (Figure 4-3).

Figure 4-11 shows the Arrhenius plot of ASR_{pol}, for double layer CFL-CCL (*ESD-SP*) LSCF electrodes containing varying CFL thickness from 0.5 to 9.5 μm topped with 30 μm thick CCL. We can extract two sets of results as a function of CFL thickness. Two LSCF films containing thin CFL of 0.5 to 2.5 μm thick, show higher activation energy (~1.55 eV) than the electrodes with thicker CFL thickness > 5 μm (~1.45 eV) which have similar ASR_{pol} at any temperature. In the literature, activation energies were reported to vary between 1.23 and 1.69 eV for LSCF (electrode)/CGO (electrolyte) [54–57,69,178,202]. This large range of values can be explained by differences arising during fabrication, such as impurities in the starting materials, the deposition technique, the sintering temperature. Since all the films were fabricated in the same way in this study, this argument can be eliminated. Further arguments could be related to the differences in microstructure and current constriction effects. The lack of macro-pore channels in thin films or the different amount of nano porosity could be the differences in microstructure compared to other films. To investigate the current constriction effects, the ionic conductivity of CGO electrolyte was calculated as shown in Eq. 4-2. The film with the smallest thickness (0.5 μm) showed the lowest electrolyte conductivity, while all the others had similar values, in agreement with the literature [23]. It means that the minimum thickness necessary for homogeneous current distribution was reached already at an average thickness of 2.5 μm. Given the fact that the CGO conductivity values remain similar regardless of the appearance of the macro-pore channels, e.g. for thickness ranging from 2.5 to 4.4 μm, the current collection problems due to macro-pore channels can be disregarded. Comparing Figure 4-11 and Figure 4-12, one can also conclude that both the difference in microstructure and current collection are responsible for higher ASR_{pol} for 0.5 μm thick film, while only the difference in microstructure is responsible for the performance result of 2.5 μm thick film.

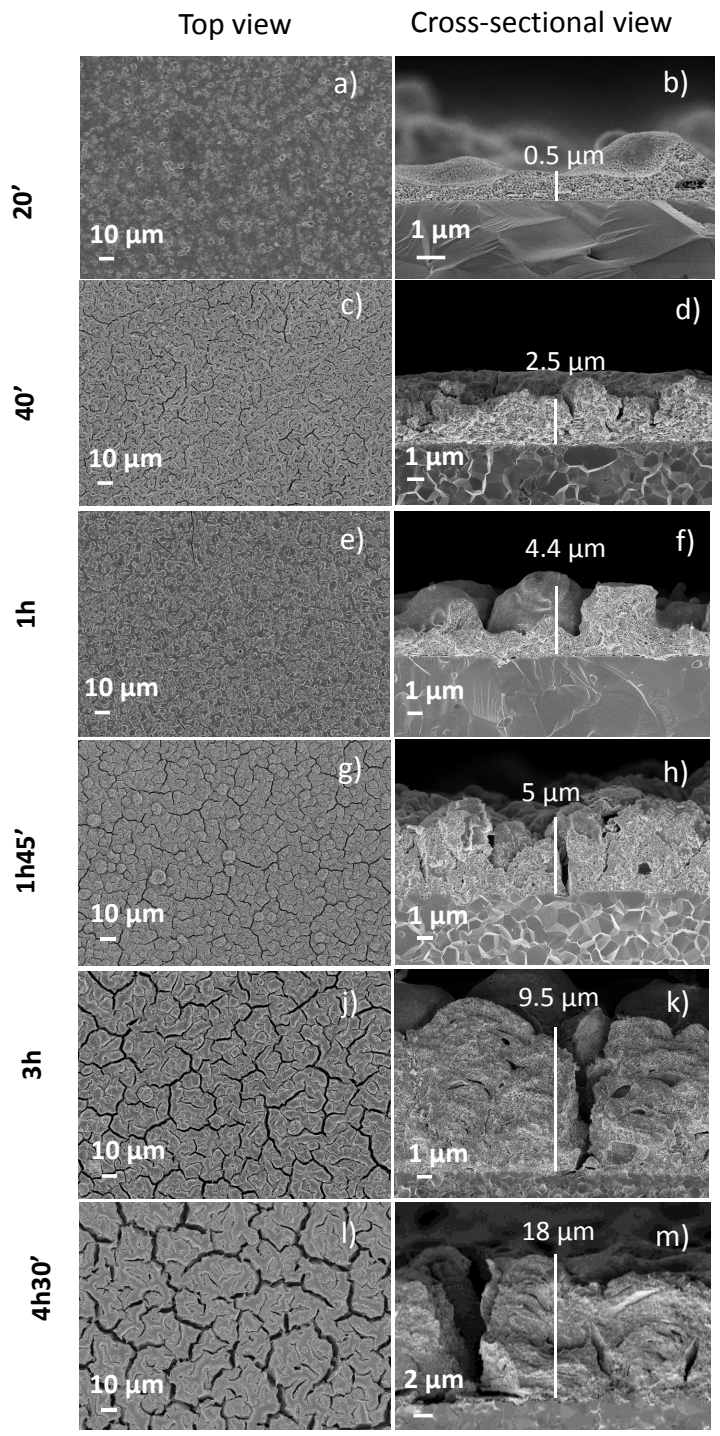

Figure 4-10 The CFL thickness was varied by changing the time of deposition by ESD from 20', 40', 1h, 1h45', 3h to 4h30'

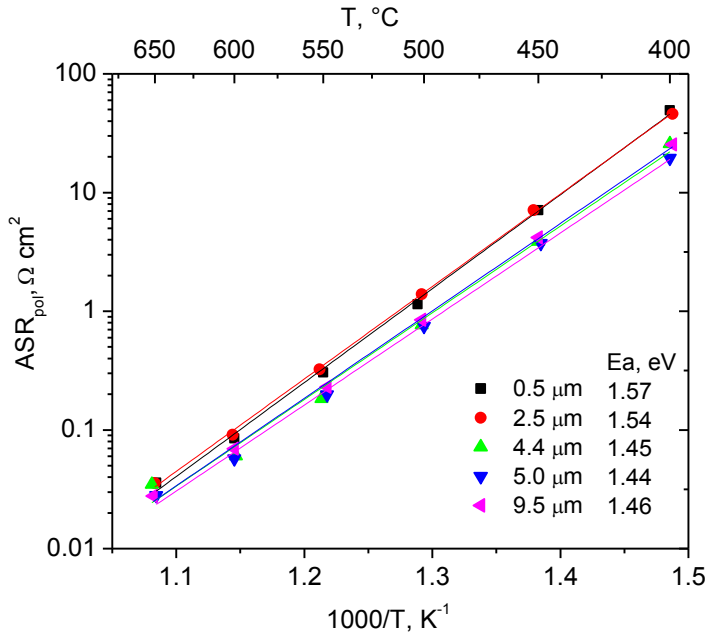

Figure 4-11 Arrhenius plot of ASRpol for varying thickness of CFL, while 30 μm thick CCL was kept fixed above CFL.

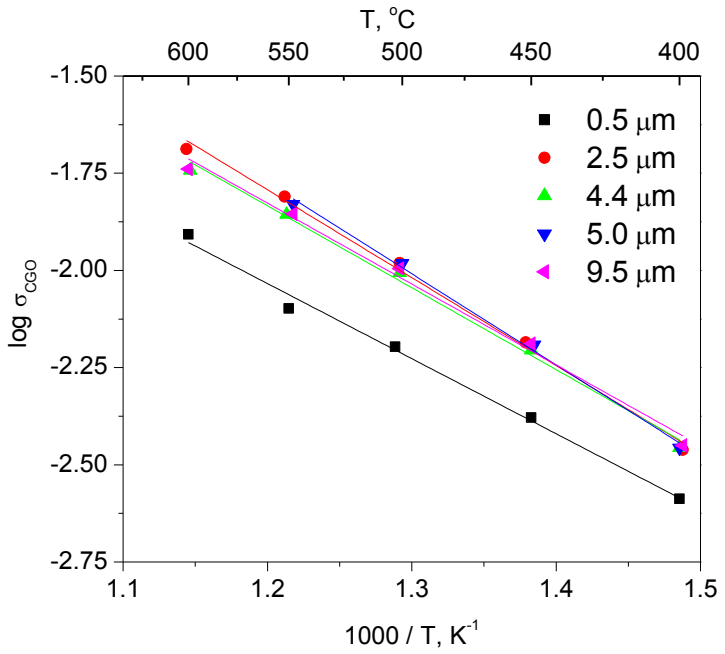

Figure 4-12 The conductivity of CGO electrolyte in contact with varying thicknesses of LSCF deposited by ESD.

4.5 Aging of the selected double layer LSCF cathode in symmetrical cell

The selected double layer LSCF cathode CFL-CCL (6 µm -30 µm) is deposited on both sides of CGO electrolyte as a symmetrical cell. The aging study has been performed at 600 °C for 800 h in air by impedance spectroscopy with 20 mV excitation amplitude in OCV conditions (Figure 4-13a). Five measurements were carried out after 1 h, 24 h, 200 h, 300 h and finally at 800 h. From 1 h to 24 h, the impedance did not vary in resistance magnitude or frequency distribution. The series resistance of the electrolyte decreased slightly, which could be either related to an enhanced contact of the cathode on the electrolyte, or it could simply be a slight variation in the temperature during impedance measurements. However, this trend has continued in the opposite sense along the time. Indeed, the series resistance of the electrolyte increased by about 5 % at the end of 800 h. Millar *et al.* had reported an aging study over 1500 h on LSM/YSZ (CFL) topped with $LaNi_{0.6}Fe_{0.4}O_{3-\delta}$, as CCL [207]. They found a drop of 41 % in the series resistance of the sample without CCL, while an increase of 28 % with CCL. After a close examination of the films by SEM, they observed chemical interaction on the interface of CFL and CCL. The commercial LSCF powder used in the SP layer in this study may include some small amount of impurity phases. These impurities might migrate and agglomerate to form insulating phases similar to Millar *et al.*'s observations. Moreover, elemental compositional variations at the electrode/electrolyte interface might also be responsible for the increase in series resistance. Further evaluation is necessary by STEM EDX mapping.

An 86 % increase in the total polarization resistance of the electrode was determined from the impedance spectra after 800 h. The Arrhenius plot of polarization resistance (Figure 4-13c) shows that the polarization resistance decreased slightly during the first 24 h, but then increased substantially at a longer time. The Bode plot shows a broad frequency distributions with three maxima at about 1000, 50 and 1 Hz. Although the resistance of all three processes increased with time, the biggest evolution is observed with the appearance of the 'hidden shoulder' (middle frequency) between 10-100 Hz (Figure 4-13b). As discussed earlier, this process corresponds to the same phenomenon with the maxima of the impedance at 400-500 °C, all of which are fitted with a Gerischer impedance. This process is thus attributed to a co-limited situation of diffusion and surface exchange in the porous cathode.

Comparing the SEM images of the sample before and after 800 h of aging in Figure 4-14, some decrease in porosity is observed in both layers. The smaller porosity and surface area and difficulties in supplying the oxygen into the active thickness may lead to such increase in total resistance.

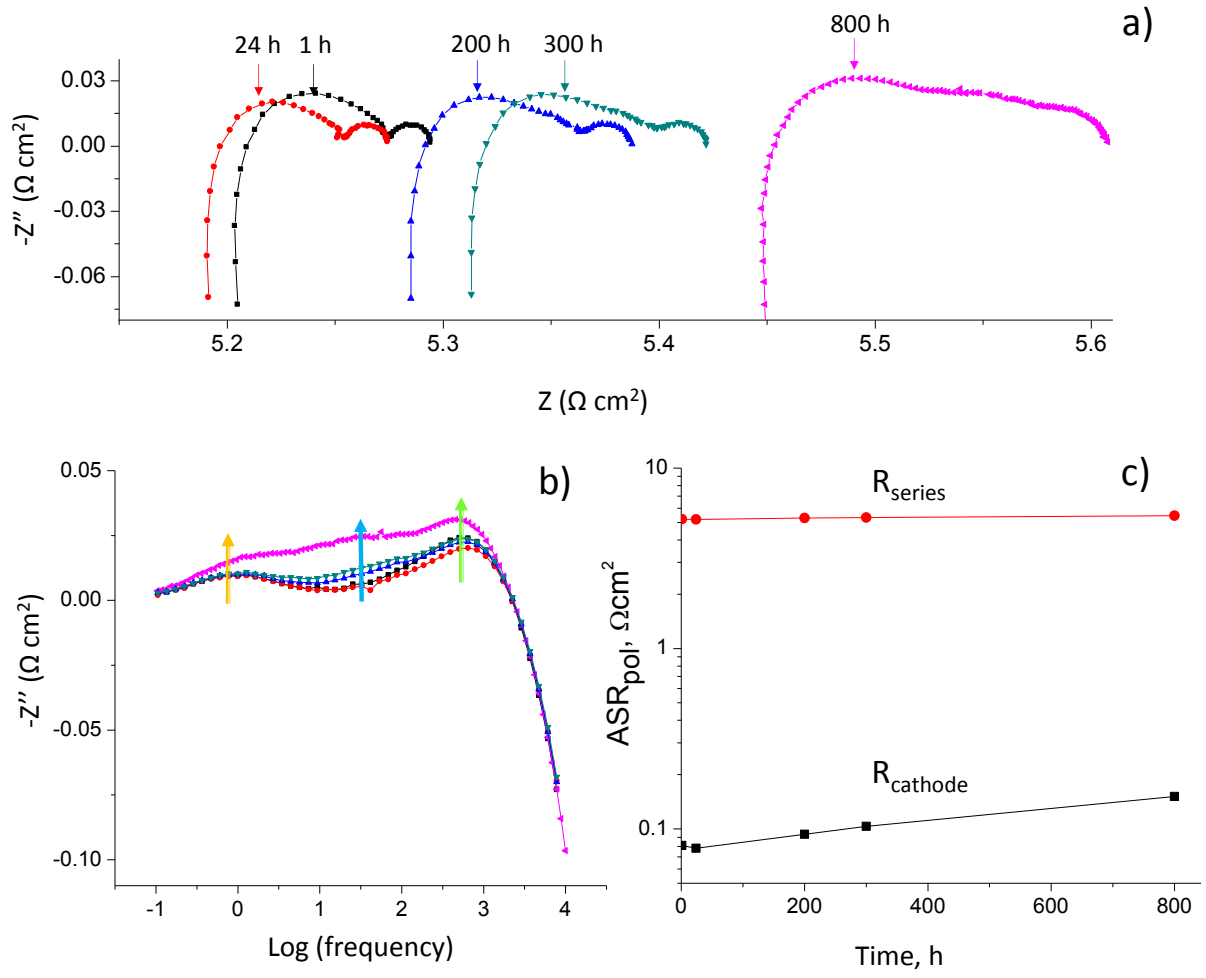

Figure 4-13 a) The Nyquist plot and b) The Bode plot of aging study of a symmetrical cell of CFL-CCL (6 µm -30 µm) cathode film measured at 600 °C in OCV. c) The change in cathode resistance and series resistance with respect to aging.

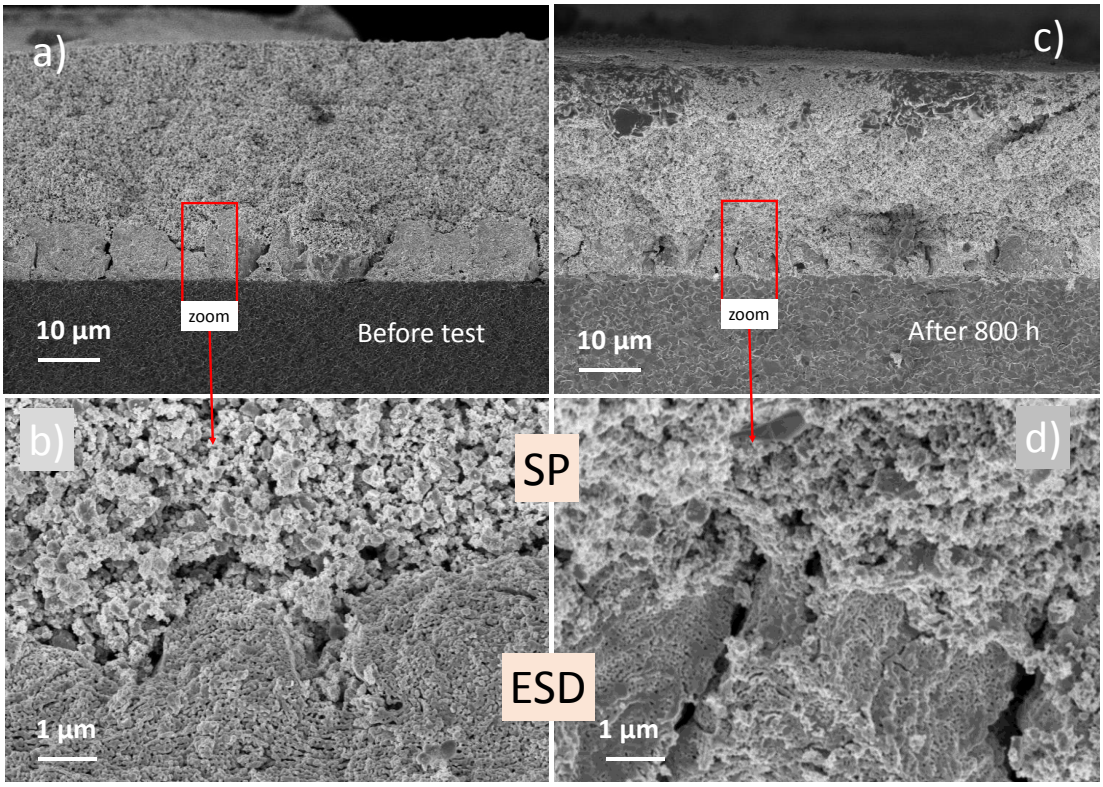

Figure 4-14 The cross sectional views of two samples a) and b) before the aging, c) and d) after 800 h of aging.

4.6 Integration of state-of-the-art double layer LSCF cathode on anode-supported SOFC

The details of the cell structure, materials and experimental setup have been described in Chapter 2. Figure 4-15 shows the cross section view of the cell focusing on the optimized double layer CFL-CCL cathode microstructure, together with the bilayer electrolyte and AFL before testing.

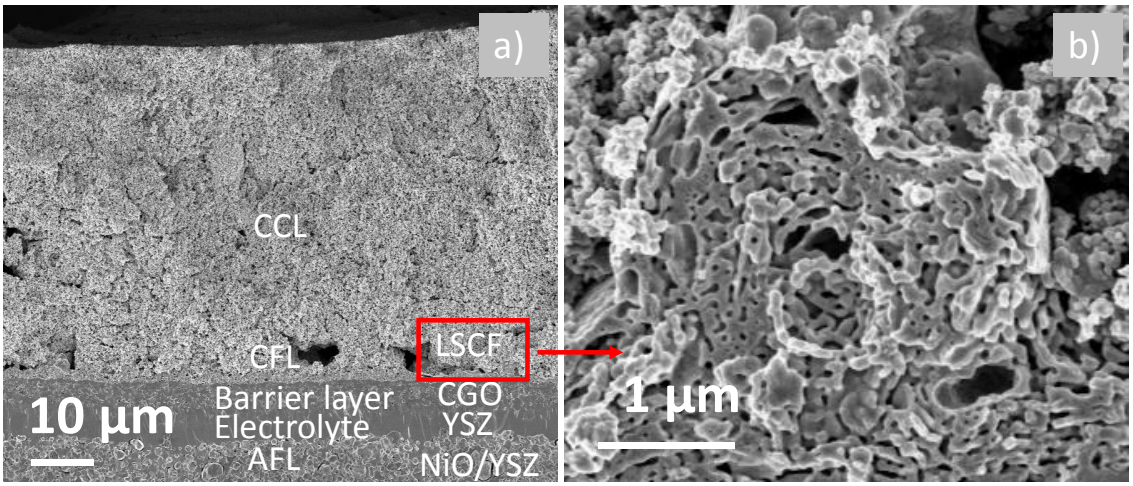

Figure 4-15 Cross section view of the full fuel cell before tests showing LSCF (CFL-CCL), CGO (barrier layer), 8YSZ (electrolyte) and NiO/8YSZ (AFL), b) zoom in the LSCF (CFL).

4.6.1 Performance Test of Complete Cell

Figure 4-16 shows the polarization curve of two identical samples, sample 1 and sample 2 (the diameter of current collecting grid is 3.7 cm for sample 1 and 1.6 cm for sample 2) measured at 675 °C. The maximum power density of sample 1 was obtained at 400 mW cm^{-2} and of sample 2 at 150 mW cm^{-2}.

The open-circuit voltage (OCV) of the bilayer YSZ/CGO electrolyte in this study was found sufficiently close to pure YSZ values predicted by the Nernst equation (~ 1.11 V at 650 °C [208]). This indicates a crack-free, gas tight electrolyte. CGO electrolyte was successfully

protected from getting reduced by the hydrogen gas on the anode side thanks to the dense YSZ film [209–211].

4.6.2 Loss processes

Figure 4-17 shows the impedance spectra of sample 1 measured at OCV and 0.7 V. The total resistance of 1.25 Ω cm^2 at OCV decreases to 0.65 Ω cm^2 at 0.7V. Three arcs observed with summit frequencies at 10 kHz, 100 Hz and 1 Hz are similar in both case. The cathode films measured at OCV showed also three arcs (Figure 4-13a), the first arc with a summit at 1 kHz was assigned to charge transfer resistance, the second arc to cathodic reactions between 10-100 Hz and the third arc with a summit at 1 Hz to pore-gas diffusion. Thus, in the full fuel cell, the cathode response is expected in the middle to low frequencies, in good agreement with the literature [210,212,213].

Three arcs with summit frequencies at 0.1–10 Hz, 10 Hz–1 kHz and 1–50 kHz have previously been ascribed to Ni/YSZ anode in a three-electrode setup [214–216]. Primdahl *et al*. assigned the low frequency responses (0.1-10 Hz) to gas conversion [215] and middle frequency responses (10 Hz-1 kHz) to gas diffusion [216]. Thus, middle and low frequency arcs represent both anode and cathode part. The high-frequency arc has been found in a number of Ni/YSZ anodes [212–214,217]. Charge-transfer reaction and ionic transport within the anode functional layer have been proposed for this arc.

The ohmic resistance of the electrolyte is another source of loss processes. The resistance of the bilayer electrolyte of sample 1 is about 0.2 Ω cm^2 at 675 °C. Table 4-5 summarizes the cell performances, OCVs, ohmic and polarization losses of various Ni-YSZ/YSZ or Ni-YSZ/YSZ-CGO bilayer electrolytes with LSCF, LSCF/CGO or LSC cathode films. The max power density in this work is mostly in accordance with the literature in comparison to similar thicknesses of electrolytes [45,138,209,211,218–226]. However, Oh *et al*. [227] and Noh *et al.* [228] have shown power densities much higher than the other works (Table 4-5) with 1300 and 2048 mW cm^{-2} at 650 °C, respectively. They obtained such results by decreasing the thickness of the electrolyte to few hundreds of nanometers. Both authors achieved to decrease the ohmic resistances to values as low as 0.037 and 0.038 Ω cm^2 and the polarization resistances to 0.22 and 0.23 Ω cm^2 at 650 °C, respectively.

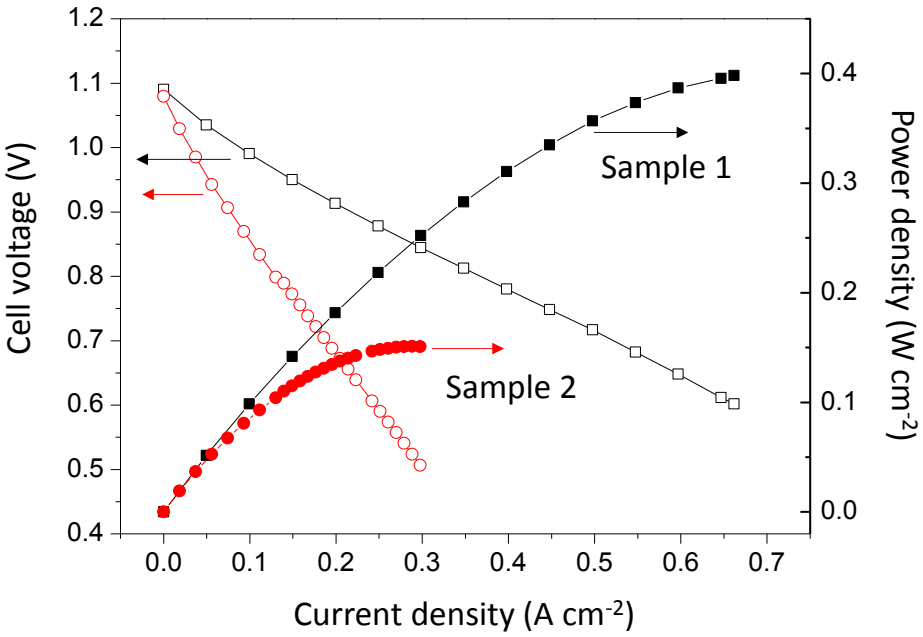

Figure 4-16 Cell performance of sample 1 and sample 2 at 675 °C.

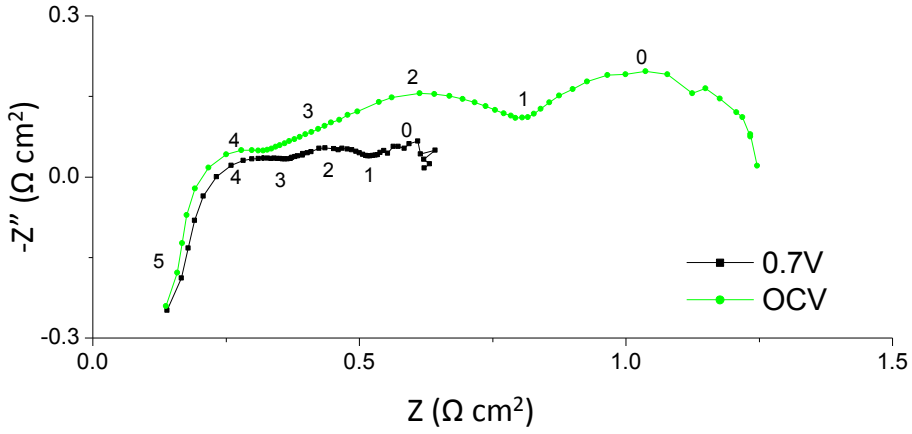

Figure 4-17 Nyquist impedance plot of sample 1 at OCV and at 0.7 V at 675 °C. The numbers in the diagram corresponds to logarithm of frequencies.

4.6.3 Long term stability test of the complete cell

The testing temperature for sample 1 was increased subsequently from 675 °C to 725 °C, then to 822 °C. A very fast degradation of the cell was observed. For this reason, the tests on sample 1 was ended and the aging was performed on sample 2. The cell current was fixed at 1.4 A. The degradation rate was found from the slope of the linear fit to the cell voltage data. After approximately 700 h of operation, the total potential degradation was 114 mV kh^{-1} or 13.85 % kh^{-1} compared to initial value (Figure 4-18). Sar *et al.* reported very similar values on LSCF/CGO composite films on YSZ/Ni-YSZ anode supported cell [229]. Similar to the present study, Stevenson *et al*. investigated the cell degradation of LSCF cathode on H.C Starck anode supported cells. They reported a 16 % kh^{-1} decrease from 400 to 1000 h of operation.

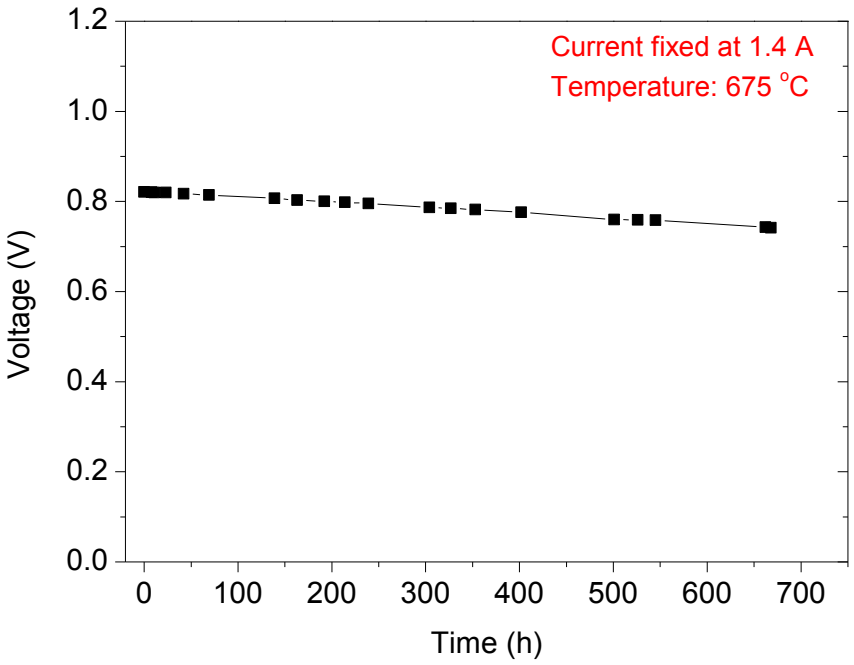

Figure 4-18 Degradation of sample 2 at 675 °C, current is fixed at 1.4 A.

Table 4-5 Summary of performance results with cells with Ni-YSZ(anode)/YSZ(electrolyte) and Ni-YSZ(anode)/YSZ-CGO(bilayer electrolyte).

Cathode	Electrolyte	Anode	Max. Power density (mW cm^{-2})	OCV (V)	R_{ohm} (Ω cm^2)	R_p (Ω cm^2)	Refs.
$La_{0.6}Sr_{0.4}Co_{0.2}Fe_{0.8}O_{3-\delta}$	8YSZ (16 μm)	Ni-YSZ	180 at 700 °C	~1.08 at 700 °C	0.38 at 700 °C	0.85 at 700 °C	[226]
$La_{0.58}Sr_{0.4}Co_{0.2}Fe_{0.8}O_{3-\delta}$	8YSZ (10 μm) CGO (0.5 μm)	Ni-YSZ	420 at 650 °C 770 at 700 °C	1.1			[225]
$La_{0.58}Sr_{0.4}CoO_{3-\delta}$ / $Ce_{0.9}Gd_{0.1}O_{2-\delta}$	8YSZ (1 μm) CGO (6 μm)	Ni-YSZ	301 at 700 °C	1.05 at 700 °C			[224]
$La_{0.58}Sr_{0.4}Co_{0.2}Fe_{0.8}O_{3-\delta}$	8YSZ $Ce_{0.8}Gd_{0.2}O_{2-\delta}$ (7 μm)	Ni-YSZ	~ 370 at 650°C at 0.7 V ~ 620 at 700°C at 0.7 V			~ 0.5 at 650 °C	[138]
$La_{0.6}Sr_{0.4}Co_{0.2}Fe_{0.8}O_{3-\delta}$	8YSZ (0.4 μm) $Ce_{0.9}Y_{0.1}O_{2-\delta}$(0.8 μm)	Ni-YSZ	760 at 770°C	1.01 at 770 °C			[223]
$La_{0.6}Sr_{0.4}Co_{0.2}Fe_{0.8}O_{3-\delta}$	8YSZ (10 μm) $Ce_{0.8}Gd_{0.2}O_{2-\delta}$ (2-3 μm)	Ni-YSZ	80 at 650 °C		~ 0.8 at 650 °C	~ 10 at 650 °C	[222]
$La_{0.6}Sr_{0.4}Co_{0.2}Fe_{0.8}O_{3-\delta}$	8YSZ (20 μm)	Ni-YSZ	470 at 800 °C	0.96 at 800 °C	0.12 at 800 °C	0.58 at 800 °C	[211]
$La_{0.6}Sr_{0.4}Co_{0.2}Fe_{0.8}O_{3-\delta}$ / $Ce_{0.9}Gd_{0.1}O_{2-\delta}$	8YSZ (15 μm) CGO (3-5 μm)	Ni-YSZ	479 at 650 °C 704 at 700 °C	~1.10 at 700 °C	1.57 at 650 °C 1.34 at 700 °C	0.47 at 650 °C 0.37 at 700 °C	[221]
$La_{0.6}Sr_{0.4}Co_{0.2}Fe_{0.8}O_{3-\delta}$	8YSZ (16 μm)	Ni-YSZ	507 at 650 °C 1014 at 700 °C	~1.05 at 700 °C	0.2 at 650 °C 0.12 at 700 °C		[45]
$La_{0.6}Sr_{0.4}Co_{0.2}Fe_{0.8}O_{3-\delta}$ / $Ce_{0.9}Gd_{0.1}O_{2-\delta}$	8YSZ (3 μm) CGO (7 μm)	Ni-YSZ	409 at 700 °C	~1.08 at 700 °C			[209]
$La_{0.6}Sr_{0.4}Co_{0.2}Fe_{0.8}O_{3-\delta}$	8YSZ (15 μm) CGO (7 μm)	Ni-YSZ	~300 at 680 °C	~1.10 at 680 °C			[220]
$La_{0.6}Sr_{0.4}CoO_{3-\delta}$	8YSZ (1 μm) CGO (200 nm)	Ni-YSZ	2048 at 650 °C	0.75 at 650 °C	0.037 at 650 °C	0.22 at 650 °C	[228]
$La_{0.6}Sr_{0.4}Co_{0.2}Fe_{0.8}O_{3-\delta}$ / $Ce_{0.9}Gd_{0.1}O_{2-\delta}$	8YSZ (14 μm) CGO (2-3 μm)	Ni-YSZ	631 at 750 °C	1.168 at 850 °C	0.174 at 850 °C	0.4 at 700 °C	[219]
$La_{0.6}Sr_{0.4}Co_{0.2}Fe_{0.8}O_{3-\delta}$ / $Ce_{0.9}Gd_{0.1}O_{2-\delta}$	8YSZ (100 nm) CGO (400 nm)	Ni-YSZ	1300 at 650 °C	>1.0 at 650 °C	0.038 at 650 °C	0.23 at 650 °C	[227]
$La_{0.58}Sr_{0.4}Co_{0.2}Fe_{0.8}O_{3-\delta}$	8YSZ (7-10 μm) $Ce_{0.8}Gd_{0.2}O_{2-\delta}$ (7 μm)	Ni-YSZ	~ 336 at 650°C at 0.7 V			~ 0.5 at 650 °C	[218]

The possible degradation mechanisms in each compartment were reviewed in detail in Chapter 1. Microstructural evolution in time is among the main degradation causes in SOFC electrodes. The microstructures of each compartment were viewed by SEM before and after durability test. Figure 4-19 focuses mainly on the cathode and bilayer electrolyte. In comparison to Figure 4-15, the cathode microstructure keeps the porosity intact in both CFL and CCL after 700 h of durability test. Nevertheless, it is worth reminding that the experimental conditions are very different in two cases; in the first case, the degradation was monitored in OCV and in stagnant air, whereas in this case under constant oxygen gas flow and 0.8 V cathodic polarization. The CGO layer also seems quite porous, which is not desirable for a barrier layer. First of all, the total ionic conductivity decreases with increasing porosity. Secondly, a porous layer fails in stopping the diffusion of Sr, which may lead to the formation $SrZrO_3$ at the CGO/YSZ interface [163]. In any case no delamination of the cathode or cracking of electrolyte was observed along the interfaces. Figure 4-20 focuses on the microstructures of AFL and anode CCL. The porosity especially in the AFL (~ 10 μm) seem to significantly increase after the test. This behavior has been observed in the literature and attributed to the volume changes from NiO to Ni after anode reduction [230–232]. The decrease of nickel particle size and reorganization of the phases upon reduction is illustrated in Figure 4-21 [233]. The reduction is accommodated by the increased porosity within the structure without shrinkage. However, percolating nickel network can be broken at a critical porosity amount. Previously, a 40 % decrease in percolation connectivity of Ni phase has been observed, while almost no change has been observed for YSZ phase in a self-made anode upon reduction [234]. The decrease in percolation degree causes decrease in bulk conductivity and therefore to loss in power density. Similar observations have been reported in the literature [132,235,236].

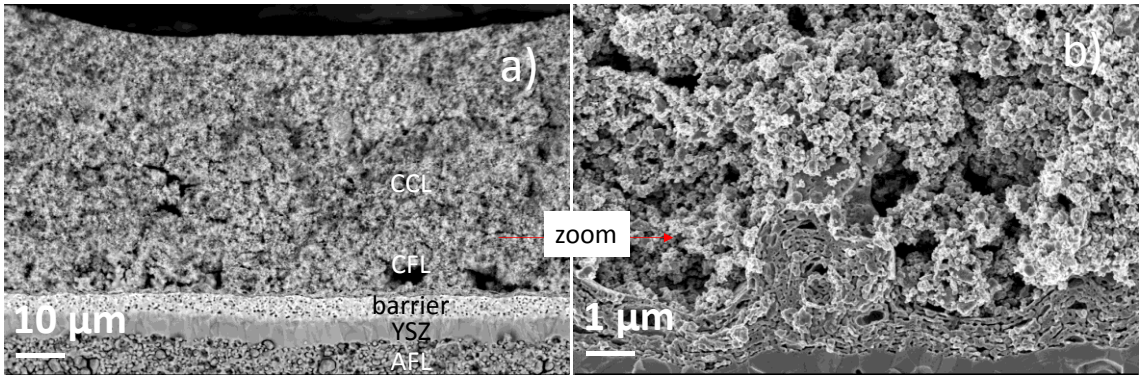

Figure 4-19 a) Cross section view of sample 2 after 700 h of durability test taken in backscattered electron mode. b) Zoom in the CFL-CCL region.

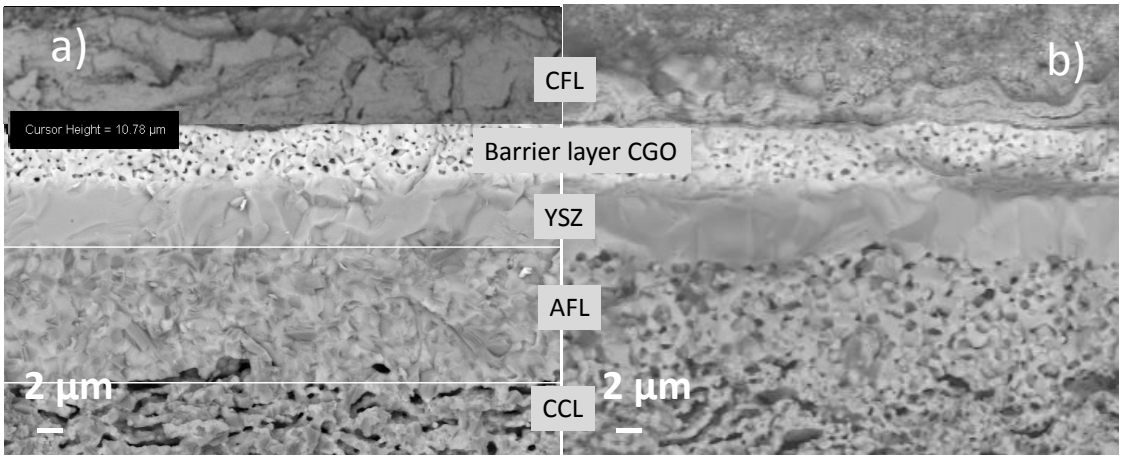

Figure 4-20 Cross section views measured with backscattered electron detector, a) sample before test, b) sample 2 after 700 h of durability test.

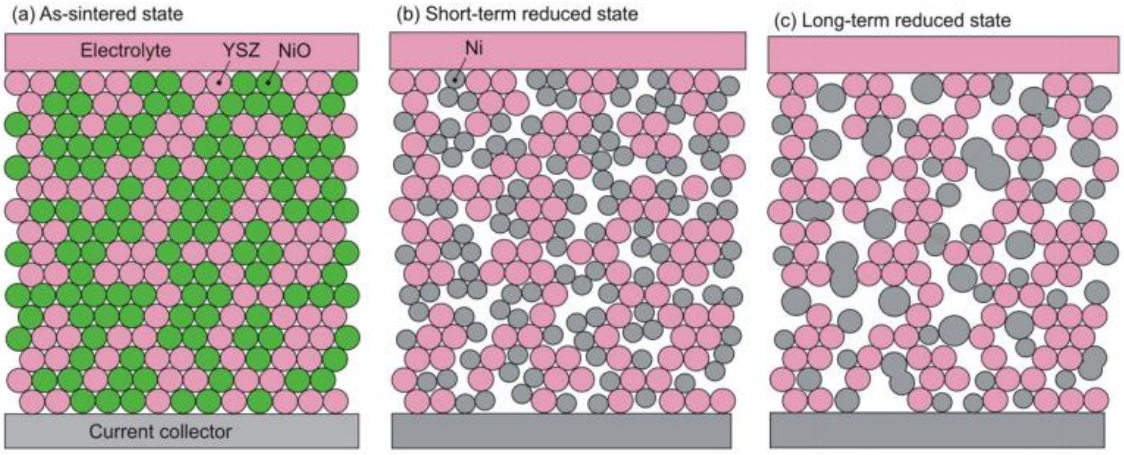

Figure 4-21 Schematics illustrating the microstructural changes upon reduction of anode material NiO/YSZ a) as sintered state, b) short-term reduced state and c) long-term reduced state. Reprinted from [233]. The reduced nickel particles are represented with gray color.

4.7 Conclusion

The functional layers of LSCF films prepared by ESD, SP and successive depositions of ESD and SP were compared by electrochemical impedance spectroscopy. Films deposited by ESD have fine details in the cathode microstructure showing increased surface area at the electrode/gas interface as well as good adherence at the electrode/electrolyte interface. Therefore, the utilization length in these films stay within a couple hundred nanometers from the electrode/electrolyte interface. Nevertheless, a certain cathode thickness (~5-6 μm CFL by ESD and ~30 μm CCL by SP in double layer cathode film) is necessary for an optimized cathode performance. Below these values, current constriction problems arise and increase the total ASR. Finally, the optimized LSCF CFL-CCL double layer films were deposited on anode supported cells. A buffer layer of CGO is deposited by ESD above YSZ prior to cathode films. A peak power density of 0.4 W cm^{-2} was obtained at 675 °C. The total potential degradation after 700 h was measured as 114 mV kh^{-1}, 13.85 % kh^{-1} compared to initial value. These results confirm the fact that degradation is a very important problem to be accounted for. More research on the cell design, microstructure and working conditions is necessary in order to reach more reasonable degradation rates.

5 RATIONAL DESIGN OF CATHODE MICROSTRUCTURES BY 3D FEM MODELLING

Chapter 5 presents two 3D FEM models taking into account the hierarchical nature of the cathode microstructure. The governing equations are introduced for both models. Model 1 is based on cubic particles that was previously reported in the literature for homogeneous pure LSCF microstructures. The model equations are taken from the references and adapted to our 60:40 LSCF/CGO composite film microstructure. Following model 1, a new 3D FEM model is proposed (model 2) that still takes into account the hierarchical microstructures and also enables simulations of larger macro features that is usually very demanding in terms of computation. The real microstructural parameters obtained from FIB/SEM technique are included in model 2 and the results are discussed in relation with the experimental data.

5.1 Introduction

Theoretical calculations and models are essential tools to understand the relations between performance and pertinent microstructural parameters and to suggest novel ways to optimize these parameters. Numerous aspects of parameter-performance relationships have been discussed theoretically, from 1D physicochemical models [50,89,92] to highly detailed elementary reaction kinetics [102,237] by means of several modeling tools (e.g., finite element method, resistor network analyses, analytical calculations). Other modelling approaches incorporating 2D or 3D finite element method (FEM) into a representative geometry [96,114,238] or into real microstructures extracted from 3D imaging have also been proposed [99,115,239].

As mentioned in Chapter 1, pioneer work on the analytical solution to ASR has been presented by Adler, Lane and Steele (ALS) [92]. The model takes a macro-homogeneous approach, neglecting potential heterogeneities in the spatial distribution of the different phases. The ALS model considers bulk path for oxygen ion diffusion and surface exchange reaction at the MIEC/gas surface within a homogenized medium. This model can also be expressed in terms of equivalent circuits. For an infinitely thick electrode, the solution takes the form of a Gerischer-type impedance. Afterwards, Nielsen *et al*. considered MIEC/CGO composite electrodes and proposed an analytical expression that comprises effective transport properties [240]. Mortensen *et al*. took a similar approach to the ALS model and defined a 1D analytical expression describing the impedance of porous MIEC/CGO composite electrodes [50]. Their model includes vacancy transport coefficient, D_v, in both the MIEC and the CGO, and oxygen exchange at the MIEC/gas surface (Eq. 1-15, Chapter 1). They found that ASR could be decreased in the cases where the vacancy transport coefficient of ionically conducting phase was larger than the MIEC phase. While the simplicity of 1D models allows for elegant qualitative analyses [50,92,240], they neglect important heterogeneities in the cathode geometry. Only FEM models can potentially account for the heterogeneous nature of an electrode microstructure. This is the main rationale for turning to a full 3D-FEM approach. However, running a model with a mesh that represents both macro- and nano- scale porosity would be extremely challenging in terms of computation resources due to huge differences in

length. In order to tackle this issue, it has been chosen to explicitly mesh the macro-pores and to account for the nano-pores through a homogenization approach.

5.2 Which Geometry?

There are various model representations of the microstructure, material properties, electrode kinetics, and transport phenomena. Kreller *et al*. modelled the electrode performance using three different geometry as illustrated in Figure 5-1: a) volume-averaged microstructure in 1 dimension, b) representative "pseudo-particles" which have size and arrangement chosen to match some sub-set of average microstructural properties (porosity, surface area etc.) and c) actual 3D microstructure obtained from FIB/SEM or synchrotron tomography [99]. Comparing the modelling results of the three geometries, sufficiently accurate estimation of the electrode performance in terms of polarization resistance is obtained by all three models. However, the first approach begins to fail as the size of the active region (utilization length) becomes competitive with (or smaller) than the microstructural features. The second approach is capable of predicting most of the features of the linear impedance of a real microstructure but fails in the true distribution of the frequency. The third approach is rather successful in predicting ASR and peak frequencies but also highly costly in terms of computation.

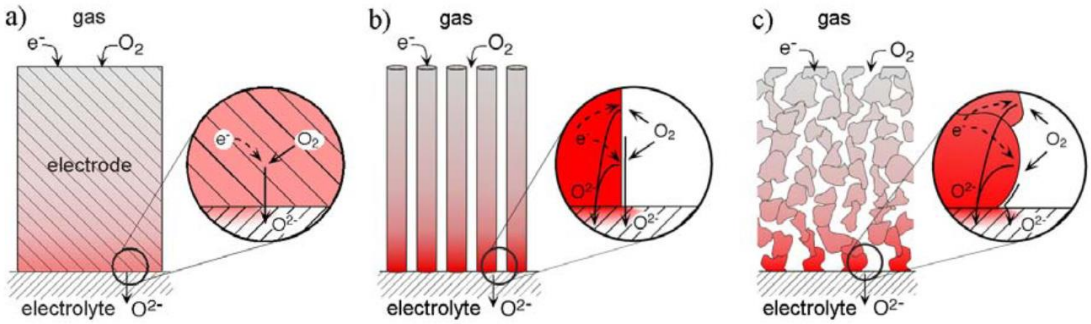

Figure 5-1 Various approximations of the microstructure commonly employed in microkinetic modeling of porous SOFC electrodes: a) macrohomogeneous approach; b) pseudo particles; c) explicit 3D geometry based on an image sample of the microstructure. Reprinted from [99].

It is therefore vital to choose among the three models considering beforehand what aspects of microstructure-performance relationship we are interested in. As introduced in previous chapters, ESD cathodes have a very distinct geometry with hierarchical porosity; macro pore channels in between columnar-like blocks and nano-porosity within those blocks. It has been shown that while macro-pore channels facilitate mass transport, nano porous networks enhance electrochemical reactions in the SOFC electrodes [8]. Nevertheless, hierarchical porosity should be well tailored according to the percolation of electronic and ionic phases. All these factors play a key role on the polarization resistance of an electrode [9–11]. The main objective of this chapter is therefore to use a geometry representative of hierarchical structure of ESD cathodes. In this configuration, the void filled with gas phase between two columns corresponds to macro-pore channels, while the void inside the column corresponds to nano-porosity. Kreller *et al*. have shown that a pseudo-particle model already gives a very good estimation of the ASR of the cathode. Thus, in order to save CPU time, a rectangular cuboid geometry which resembles to columnar-type microstructure has been modelled.

Two modelling approaches with microstructures similar to experimentally deposited films were taken for the simulation of LSCF and LSCF/CGO composite films (Figure 5-2). In model 1, a previously described 3D FEM model implemented for homogeneous porous MIEC cathodes on CGO electrolyte system is adopted [16,17]. The microstructure is designated by randomly distributed LSCF cubes and pore cubes, while the electrolyte is composed of a single dense cube. To extend this approach to a composite system, a fraction of the cubes are assigned to CGO (the same as electrolyte) in the cathode compartment. The choice of the size of the cubes is flexible (nm to μm). However, in order to represent a microstructure similar to the experimental one, cube size should be about 100 nm. Assuming 100 nm cube size, 10^6 cubes would be required to fill the columnar block size (10x10x10 μm^3), with each cube to be meshed with at least a few finite elements. Such a computation would be very challenging in today's technology, and has proven impossible with the available workstation at SIMaP laboratory. That is why, a compromise is required between the particle size and the columnar-like block size. The cube size was selected to be 400 nm in this study. Taking advantage of symmetry boundaries (only a quarter of the microstructure is simulated), the columnar-like blocks with similar dimensions to real films were simulated.

In model 2, a columnar-like block is represented by a single cube. The real microstructural parameters such as porosity and specific surface area calculated from FIB/SEM tomography

are used as input parameters. The effective transport parameters are included depending on the porosity and phase fraction. This model is therefore a combination of finite element and homogenization approaches. Thanks to the homogenization approach, one simulation takes a few minutes on a standard Linux workstation (6-core Intel Xeon X5660 processor, RAM 24Go). Model 1, largely inspired from the literature, was helpful to get started with FEM modelling of SOFC cathodes and then to validate model 2. Model 2 has been developed to answer the problems of model size and the hierarchical nature of ESD cathodes.

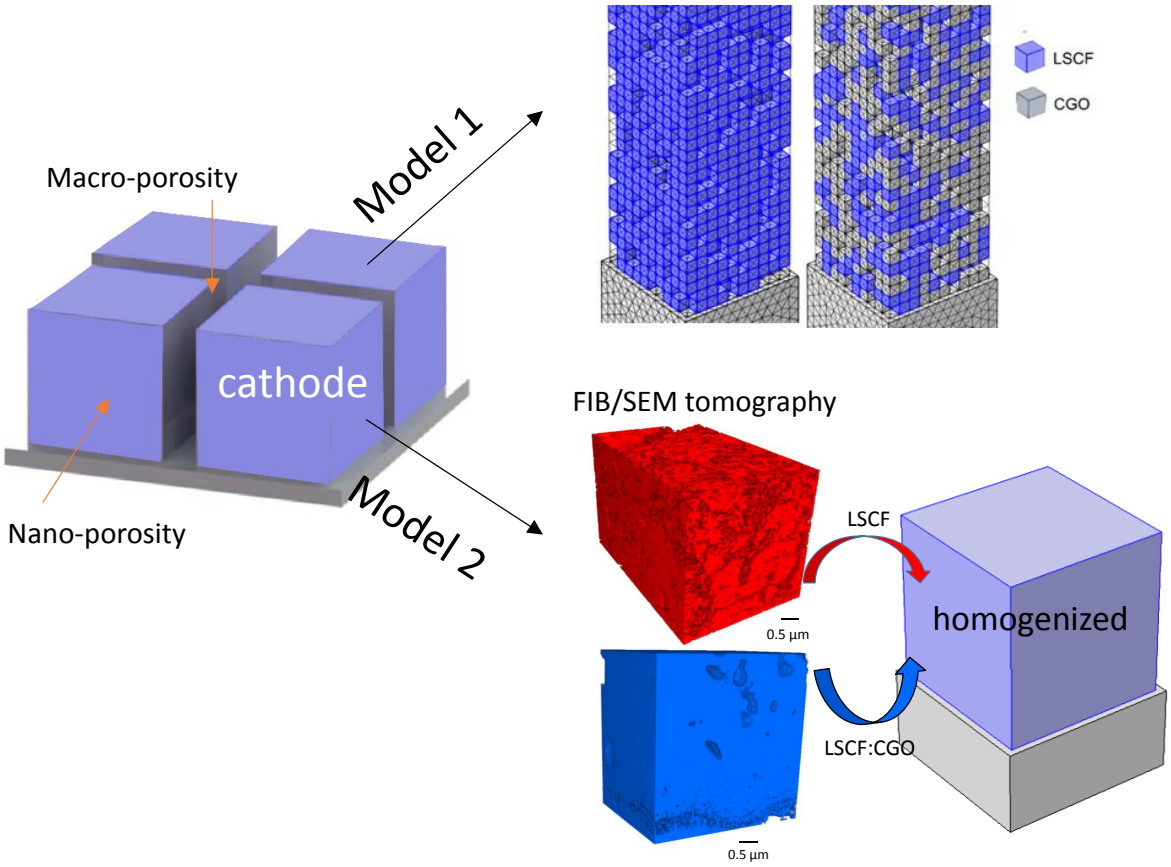

Figure 5-2 The two models (geometries) that have been studied in this thesis.

5.3 Simulations and assumptions

A previously described 3D FEM model for single phase MIEC cathode on CGO electrolyte [100,114,115,238,241] is adopted. This model is based on the approach initially proposed by Ruger *et al*. [114] who modelled the system in two domains, the cathode and the electrolyte. In the cathode domain, Fick's laws for the diffusion of O^{2-} ions and mass conservation are solved. In the electrolyte domain, Ohm's law and conservation of ionic current are solved. The two resulting partial differential equations are coupled by a charge transfer equation at the cathode/electrolyte interface. Appropriate boundary conditions account for the surface exchange on the surface of the cathode column. The model includes the following processes as illustrated in Figure 5-3:

1) Surface exchange process at the surface of LSCF in defined boundaries,

2) Bulk diffusion of reduced oxygen ions within the LSCF lattice,

3) Charge transfer at the LSCF (electrode) / CGO (electrolyte) and LSCF (electrode) / CGO (electrode) interfaces,

4) Ionic conduction in CGO (electrode and electrolyte).

The procedures, mesh convergence and boundary conditions for model 1 can be found in Appendix D. COMSOL Multiphysics FEM software was used to solve the two coupled partial differential equations governing bulk O^{2-} diffusion within LSCF and CGO ionic conduction. A number of assumptions were made in the model. The model is applicable to any mixed oxide conductor in which the only charge compensating defect is the oxygen anion vacancy. The MIEC is assumed to have infinite electronic conductivity but finite ionic conductivity. Thus, it is only the transport of ionic current that contributes to the total resistance. Moreover, any interfacial resistance between the current collector/electrode and counter electrode is neglected together with the polarization resistance at the counter electrode. As a result, the applied voltage distributes entirely across the electrode and causes a flux of oxide ions through the electrolyte. In addition, the partial pressure of oxygen gas is assumed to be uniform everywhere. It means that the porosity enables sufficient oxygen gas diffusion, i.e. the mass transport loss

can be neglected. These assumptions imply that the behavior of each geometry is representative of the electrode as a whole. Finally, a DC voltage (100 mV) between the current collector and the reversible counter electrode on the other side is applied under steady state conditions and the polarization resistance of the cathode is calculated. The output of the model is the polarization resistance.

5.4 3D FEM: Model 1

As discussed in the previous section, addition of an ionic conducting second phase (CGO) to LSCF, to enhance the electrode performance by extending the active thickness, gives rise to significant changes in the volume-specific surface area, porosity fraction within the column, tortuosity and the particle size. It is of great importance to quantify the influence of these microstructural properties to achieve fine-tuning of the electrode performance for future SOFC cathodes. Figure 5-3 illustrates the processes accounted for by model 1 for a composite cathode. Illustrations on the boundary conditions are given in Appendix D.

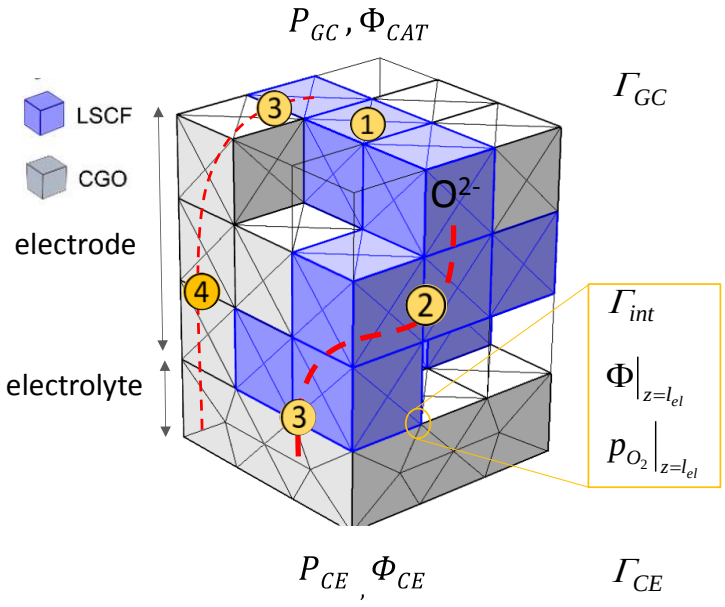

Figure 5-3 Illustration of the processes in the FEM model for a composite cathode. GC refers to Gas (oxygen) partial pressure at the Cathode, CE at the Counter Electrode and int refers to interface.

5.4.1 Governing equations

5.4.1.1 Cathode domain

The electronic conductivity of the MIEC is assumed to be very high. Thus, the gradient of the electrochemical potential of electronic charge carriers in the MIEC is almost vanishing. In this case, the ionic current in the MIEC corresponds to the total current of the electrode. The flux of oxygen ions $\vec{j}_O$ is calculated by Fick's first law of diffusion in the steady state.

$$\vec{j}_O = -D^{\delta}\vec{\nabla}c_o \qquad 5\text{-}1$$

The flux of oxygen vacancies is related to the gradient in oxygen concentration, c_O. At steady state, no change in vacancy concentration occurs and so the continuity equation holds:

$$\nabla(\vec{j}_o) = 0 \qquad 5\text{-}2$$

Eq. 5-1 and Eq. 5-2 were solved in the bulk of the MIEC for $\vec{\nabla}c_o$ at steady state.

Oxygen is exchanged through the boundary faces between gas phase and mixed conducting material. This process is described empirically by the fluxes calculated by the variation of the concentration from an equilibrium condition $(c_{o,eq})$ of the form:

$$\vec{j}_o.\vec{n} = k^{\delta,MIEC}(c_{o,eq} - c_o) \qquad 5\text{-}3$$

where $\vec{n}$ is the unit normal vector to the surface.

5.4.1.2 Electrolyte domain

The ionic current density in the electrolyte is governed by Ohm's law:

$$\vec{j}_{curr} = -\sigma_{ic}\vec{\nabla}\phi \qquad 5\text{-}4$$

Where σ_{ic} is the ionic conductivity and ϕ is the electrical potential.

The ionic current conservation law applies as:

$$\nabla(\vec{j}_{curr}) = 0 \qquad 5\text{-}5$$

Non-coupling boundary conditions are used on Γ_{CE}: an ideal reversible counter electrode (CE) with a constant potential is considered, i.e. $\phi = 0$.

5.4.1.3 Charge transfer and coupling boundary conditions

Nernst equation is calculated between the current collector and the counter electrode;

$$\Phi_{CAT} - \Phi_{CE} = \frac{RT}{2F}\ln\left(\sqrt{\frac{p_{GC}}{p_{CE}}}\right) - \eta_{model} \qquad 5\text{-}6$$

where $p_{GC} = 0.21$ bar and $p_{CE} = 10^{-23}$ bar are the partial pressure of O_2 in the gas channel and at the counter electrode, respectively. Φ_{CAT} is the potential applied on the cathode which is assumed to be constant due to large electronic conductivity. η_{model} , the total voltage loss of the model, is fixed at 0.1V [115].

The Nernst equation is applied at the cathode/electrolyte interface:

$$\Phi_{CAT} - \Phi\big|_{z=l_{el}} = \frac{RT}{2F}\ln\left(\sqrt{\frac{p_{O_2}\big|_{z=l_{el}}}{p_{CE}}}\right) - \eta_{\mathrm{CT}} \qquad 5\text{-}7$$

where $\Phi\big|_{z=l_{el}}$ is the potential in the electrolyte computed at the cathode/electrolyte interface ($z = l_{el}$). $p_{O_2}\big|_{z=l_{el}}$ is the equilibrium partial pressure of oxygen ions in the cathode calculated from the computed oxygen concentration using Eq. A-8 and Eq A-9 in Appendix C.

η_{CT} (CT refers to charge transfer) can be obtained using Eq. 5-6 and Eq. 5-7 as function of the input parameters and of the computed scalar fields c_o and Φ. A very small charge transfer resistance ASR_{CT} = 10^{-4} Ω cm^2 is used to calculate the corresponding charge transfer current $j_{CT} = \eta_{CT} / ASR_{CT}$.

The following boundary conditions are imposed at the electrolyte/cathode interface Γ_{int}:

$\vec{j}_o.\vec{n} = j_{CT} / 2F$ on the cathode side and $\vec{j}_{curr}.\vec{n} = j_{CT}$ on the electrolyte side to ensure the coupling between the two domains.

5.4.1.4 Calculation of the ASR

The resolution of Eq. 5-1, 5-2, 5-4 and 5-5 with appropriate boundary conditions is performed using FE analysis. The current *I* flowing through the system is deduced by integration of $\vec{j}_{curr}$ and the *ASR* is calculated as follows:

$$ASR_{CAT} = \frac{\eta_{\text{model}}}{I} - \frac{l_{el}}{\sigma_{ic}} \qquad 5\text{-}8$$

5.4.2 Model 1: Results and discussion

Two columnar microstructures representing pure LSCF and composite 60:40 vol. % LSCF/CGO films were generated (Figure 5-4a, 4b). Based on SEM image analysis tools (ImageJ), 15 % macro-porosity arising from the macro-pore channels was added in the electrode layer (Chapter 3). Thus, surface exchange around the macro-pore channels was activated. Making use of the symmetry, only a quarter of 8 *x* 8 *x* 4 μm^3 columns were generated as shown in Figure 5-4c. Moreover, 22 ± 7 % internal porosity was homogeneously distributed in the simulations of pure LSCF, while 20 ± 3 % internal porosity was introduced in the first 1.5 μm thickness of the composite geometry. For the composite, 40 % of the remaining cubes were assigned to CGO phase to represent 60:40 vol. % LSCF/CGO composite (Figure 5-4b). The selection of the particle (cube) size was not straightforward. If one wants to represent the dimensions of the columnar blocks similar to experiments (as high as 10 by 10 μm), one has to

choose the size of the individual particles (cube) on the order of a couple of hundred nanometers. Otherwise, the FEM model does not converge to a solution in a reasonable time (limits of CPU). On the other hand, if one wants to simulate particle sizes similar to the films, a concession has to be made in the width and height of the columnar block. For example, particle sizes smaller than 100 nm can be simulated only for columnar block equal or smaller than 1 x 1 x 10 μm^3. However, this can highly influence the results, since the surface area to volume ratio becomes significant on the ORRs when the width of the column is relatively narrow (Appendix E). In such a case, the ASR will be highly underestimated. Taking all these facts into account, we choose the following compromise: 400 nm sized cubes were built for both films in 8 x 8 x 4 μm^3 columnar block using symmetries.

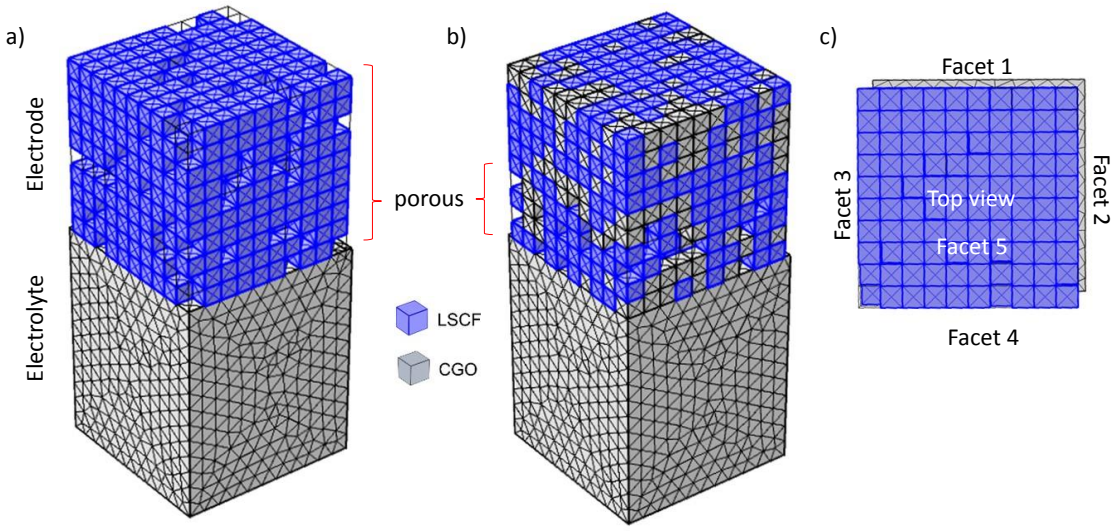

Figure 5-4 Columnar microstructures including 15% macro-pore channels. a) 100 vol. % LSCF with 22 % internal porosity b) 60:40 vol. % LSCF/CGO composite film with 20 % internal porosity in the 1.6 µm distance from the electrode/electrolyte interface. c) Top view, Repeat unit with numbered interfaces. Due to symmetry, no current flows across the Facet 3 and 4.

The specific surface area of LSCF (the geometry of Figure 5-4a) is 2.7 ± 0.4 μm^{-1}. Compared to the real values of *a* as noted in Table 3-1 (19 ± 6 μm^{-1}), 5 to 10 fold of difference can be observed. Still, the model calculates a much better performance for the composite in terms of ASR at all temperatures (Figure 5-5). This discrepancy compared to experimental observations (Section 3.3) may be due to the fact that it was not possible to reproduce the actual specific

surface area (computational limitations). Nevertheless, the activation energies estimated from the Arrhenius plot are in agreement with the experimental values. These results, in partial contradiction with experiment, have led us to design model 2 that accounts for the hierarchical features with larger differences in scale, i.e. similar to the actual cathodes.

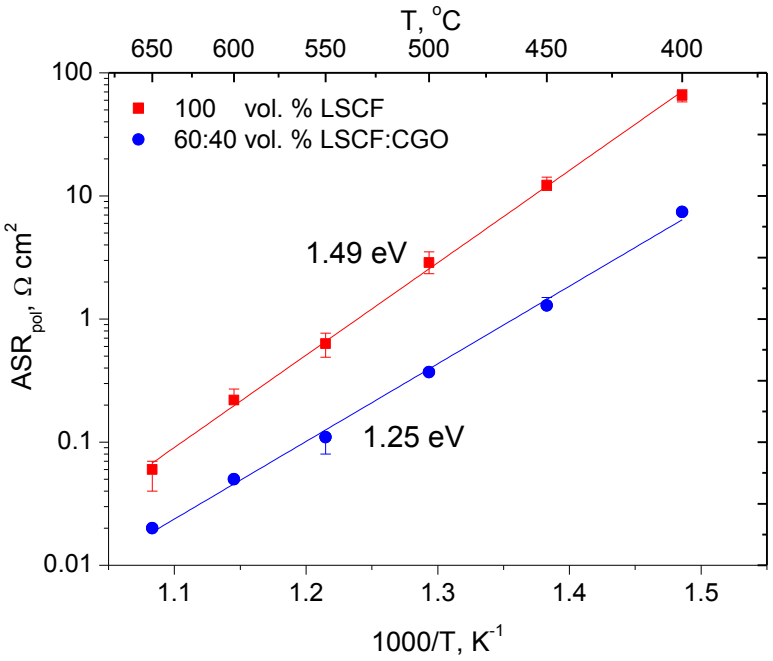

Figure 5-5 Arrhenius plot of ASR calculated by the model 1 for ε = 22 ± 7 % for 100 LSCF and ε = 20 ± 3 % in the first 1.5 µm and dense above it for the 60:40 composite.

5.5 3D FEM: Model 2

Similar assumptions as in model 1 were taken. Figure 5-6 sums up the approach taken in model 2. As shown in Figure 5-6a, the actual columnar structure is described by cuboid pillars. The macro-porosity (~ 15 %) is taken into account by using periodic boundary conditions as illustrated in Figure 5-6c. The internal nano-porosity within the column is accounted by homogenization approach. A source-term is used to model the contribution of the specific surface inside the column. The effective transport coefficients and the source term are computed using effective medium approximations. The bulk diffusion coefficients of pure LSCF and pure CGO, as well as the surface exchange coefficient of LSCF were extracted from

the EIS measurements (all parameters used in the model can be found in Appendix D). Highly controlled, regular and/or complex solid oxide structures are being achieved with the advancement of fabrication techniques and technologies [63]. With the homogenization approach, microstructures with interesting structural features and/or heterogeneities can be modelled without compromising the CPU time.

3D simulations of columnar-type films have been conducted on a 10 x 10 x 10 μm^3 geometry for both 100 LSCF and 60:40 LSCF/CGO films. For the composite cathode, the column domain is split into two domains representative of the lower and upper portions of the film: a porous microstructure is assumed on the first 1.5 µm distance from the electrolyte/electrode interface, whereas it is considered dense above, in accordance with the 3D FIB-SEM observations (Figure 5-6b).

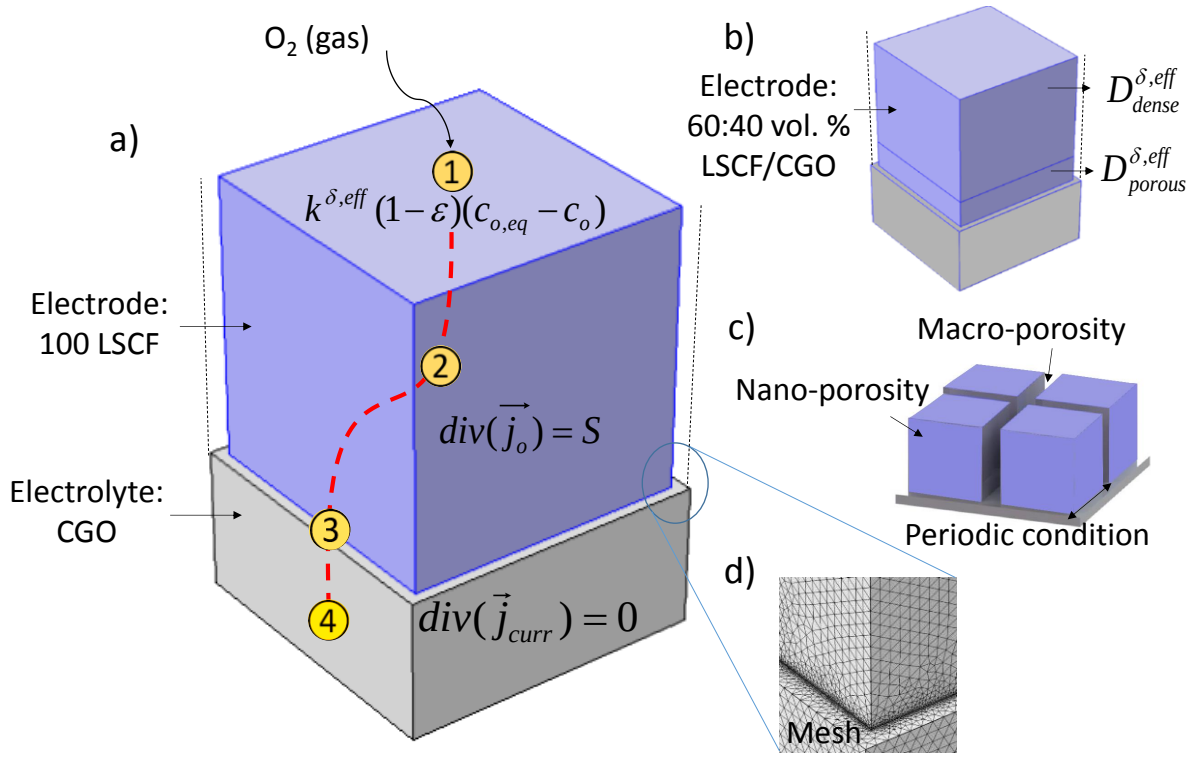

Figure 5-6 a) Schematics of the 3D FEM model in pure LSCF. (1) Surface exchange process at the surface of LSCF. $k^{\delta,eff}$ *(1-ε)* $(c_{o,eq} - c_o)$ is the incoming oxygen flux where $k^{\delta,eff}$, c_o and $c_{o,eq}$ are surface exchange coefficient of MIEC for a given MIEC volume fraction, oxygen concentration and equilibrium oxygen concentration, respectively. (2) Homogenization of the surface exchange within the column in a source term S and bulk diffusion of the reduced

oxygen ions in the lattice. $\vec{j}_o$ is the flux of oxygen ions (3) Charge transfer at the interface. (4) Ionic conduction in the electrolyte. $\vec{j}_{curr}$ is the ionic current. b) Schematics of 3D FEM model for LSCF/CGO composite illustrating the porous and dense layers. c) A representative pattern of periodic conditions. d) Mesh refinement close to the electrode/electrolyte interface (region of high gradients).

5.5.1 Governing Equations

5.5.1.1 Cathode domain

Similar to model 1, the flux of oxygen ions $\vec{j}_o$ is calculated by Fick's first law of diffusion in the steady state (Eq. 5-1): The surface exchange contribution due to internal nano-porosity within the column or a part of the column is taken into account via a source term S. The mass conservation equation that accounts for the source term is then:

$$\nabla(\vec{j}_o) = S \qquad 5\text{-}9$$

where,

$$S = k^{\delta,eff} \cdot a \cdot (c_{o,eq} - c_o) \qquad 5\text{-}10$$

$k^{\delta,eff}$ is the effective surface exchange coefficient that is a function of the MIEC volume fraction. The current density across the surface of the cathode is given by:

$$\vec{j}_o.\vec{n} = k^{\delta,eff}(1-\varepsilon)(c_{o,eq} - c_o) \ \ on\ \Gamma_{GC} \qquad 5\text{-}11$$

where $\vec{n}$ is the unit normal vector to the surface.

5.5.1.1.1 Cathode domain homogenization

For a composite and/or porous cathode column, the bulk and surface material properties D^{δ} and k^{δ} are homogenized using the effective medium approximation proposed by Wu *et al*. [242] for the bulk and a rule of mixture for the surface.

Bulk:

The model proposed by Wu *et al*. [242] and employed by Dusastre *et al*. [52] in the context of porous composite cathodes is used. The effective diffusion $D^{\delta,eff}$ of a three phase MIEC / ionic conductor (IC) / pores composite in 3D is given by the following expression:

$$\frac{D^{\delta,eff}-D^{\delta,MIEC}}{2D^{\delta,eff}+D^{\delta,MIEC}} f_v^{MIEC} + \frac{D^{\delta,eff}-D^{\delta,IC}}{2D^{\delta,eff}+D^{\delta,IC}} f_v^{IC} + \frac{1}{2}(1-f_v^{MIEC}-f_v^{IC}) = 0 \qquad 5\text{-}12$$

where $D^{\delta,MIEC}$, $D^{\delta,IC}$, f_v^{MIEC}, f_v^{IC} are the diffusion coefficients and the volume fractions of MIEC and ionically conducting phases, respectively.

Surface:

Assuming that only the MIEC material surface contributes to the oxygen exchange in a composite column, the effective exchange coefficient for a homogenized column is given by:

$$k^{\delta,eff} = k^{\delta,MIEC} \cdot f_v^{MIEC} \qquad 5\text{-}13$$

The equations in electrolyte domain, charge transfer equations in the interface and the calculation of ASR are the same as model 1.

5.5.2 Model 2: Results and Discussion

Figure 5-7a shows the Arrhenius plot of ASR calculated from the model. The model parameters of the specific surface area *a*, and the porosity *ε,* were directly taken from the reconstructed 3D

FIB/SEM images (Table 3-1). Calculated activation energies of 1.5 eV for pure LSCF and 1.4 eV for the composite suggest that the parameters used in the FEM model defining the kinetics (chemical transport parameters, D^{δ} and k^{δ}, concentration of oxygen, c_o) are reasonable. Inspection of Figure 3-12 and Figure 5-7a, shows that our FEM model realistically captures the intriguing behavior of only a slight performance improvement in the composite at low temperatures. This can be attributed to two combined effects. The first is related to the decrease of the specific surface area brought by the addition of CGO, eventually leading to larger ASR values at high temperatures. The second is related to an insufficient amount of CGO for ensuring a percolating network for such porosity amount close to the electrode/electrolyte interface (~20 % porosity). More precisely, the modification of the slope is directly related to the effective diffusion coefficient of the composite.

Figure 5-7b shows the effective diffusion coefficient of LSCF/CGO composite cathode calculated from pure LSCF and pure CGO diffusion coefficients. The amount of porosity as well as the amount of CGO governs the effective diffusion coefficient. In particular, a drastic decrease of effective diffusion coefficient is observed for 40 % CGO, by increasing the porosity from 0 to 20 % (activation energy increases from 0.61 to 1.53 eV) at temperatures lower than 500 °C. At higher temperatures, the difference in diffusion coefficients between LSCF and CGO becomes smaller, thus decreasing the relative effect of porosity.

To further illustrate the importance of CGO percolation, the effective diffusion coefficient has been calculated for different amounts of CGO at 400, 500 and 650 °C as shown in Figure 5-7c. A jump in the $D^{\delta,eff}$ value signifies that CGO percolation is reached at that particular temperature and CGO amount. At 400 °C, percolation can be achieved for 40 % CGO for a dense film (0 % porosity). In contrast, it can be reached with at least 50 % CGO for a 20 % porous film. Thus, for 40 % of CGO and 20 % porosity, the activation energy of the effective diffusion (1.53 eV) gets closer to the value of pure LSCF (1.81 eV), which in turn, increases the ASR of the composite at low temperatures.

A model considering a homogeneously distributed porosity would miss this effect of a locally larger porosity and would not capture the experimentally observed trends. Indeed, an activation energy of 1.07 eV is obtained when using values of porosity and specific surface area averaged over the whole cathode thickness (a = 3 μm^{-1}, ε = 7 %, Figure 5-8a). Such a value is far from the experimental results (1.3 eV). The high amount of porosity, located near the interface, decreases the $D^{\delta,eff}$ by impeding the percolation of the CGO phase. On the other hand, the

porosity is imperative to provide free surface for the oxygen exchange. Slightly increasing the amount of CGO, while keeping a high porosity should improve performances.

Assuming that the LSCF/CGO microstructural parameters are similar to those of pure LSCF (e.g. a = 19 μm^{-1}, ε = 22 % for both), an offset of the ASR to lower values can be attained due to an increase in specific surface area (Figure 5-8b). However, the slope of the curve remains similar to pure LSCF, making this kind of microstructure and composition interesting only at high temperatures. Thus, achieving a high performing cathode at low temperatures via the addition of a second ionically conducting phase to an existing optimized MIEC cathode is a very challenging task for the following reasons:

1) The addition of CGO drastically influences microstructural parameters, including grain size, pore volume fraction, pore size and specific surface area. While a large amount of porosity is generally beneficial in a pure MIEC cathode, it can be detrimental for a composite cathode, especially at low temperatures. A fine tuning of porosity is thus required.
2) A high amount of CGO may break the percolation of the MIEC network. Here also a fine tuning of the composition in relation with the microstructure is required.

It is also important not to disrupt the percolation network of the MIEC phase (electronic percolation). The dependence of the effective electronic conductivity as a function of CGO and porosity amounts can be calculated [52].

Figure 5-7d indicates that, for a 20 % porosity, the maximum amount of CGO that can be introduced in LSCF before breaking the percolation path of LSCF is close to 60 %.

To demonstrate the intricate relationship between the amount of porosity and of CGO in a composite film, 49 runs were conducted from 0 to 60 % of porosity and 0 to 60 % CGO in LSCF (Figure 5-9). Assuming cylindrical interconnected pores, the specific surface area is computed as a function of porosity and pore radius, r:

$$a = \frac{2*\varepsilon}{r} \qquad 5\text{-}14$$

For a pore diameter of approximately 60 nm, a good estimation of surface area and porosity was obtained in comparison to the experimentally observed values. Accordingly, the peak

performance with lowest resistance (~ 0.15 Ω cm^2) can be obtained for 20 % porosity and 60 % CGO at 500 °C. In the model, gas diffusion and electronic percolation of LSCF are not taking into account for the ASR calculation. Thus, below 10 % porosity and above 50 % porosity, we consider that the ASR is highly underestimated. Nevertheless, the estimation of the model is in accordance with the literature [54,57,58].

Figure 5-9 indicates that approaching 60 vol. % CGO would be beneficial. As explained in Chapter 3, we have attempted to deposit an ESD film with 40:60 LSCF/CGO with a similar columnar microstructure using the same deposition parameters. However, a good adhesion to the electrolyte could not be obtained. The present composite columnar film is the closest to the optimal value that can be fabricated by ESD technique. Nevertheless this FEM model offers the possibility to design new cathode materials and microstructures for numerous types of deposition techniques. Moreover, it is a readily adaptable tool to examine numerous structured ceramic frameworks from one-dimensional nanostructures (e.g. nanotubes, nanowires) to complex hierarchical morphologies (e.g. infiltrated cathodes, 3D printed regular scaffolds) that can be engineered beforehand.

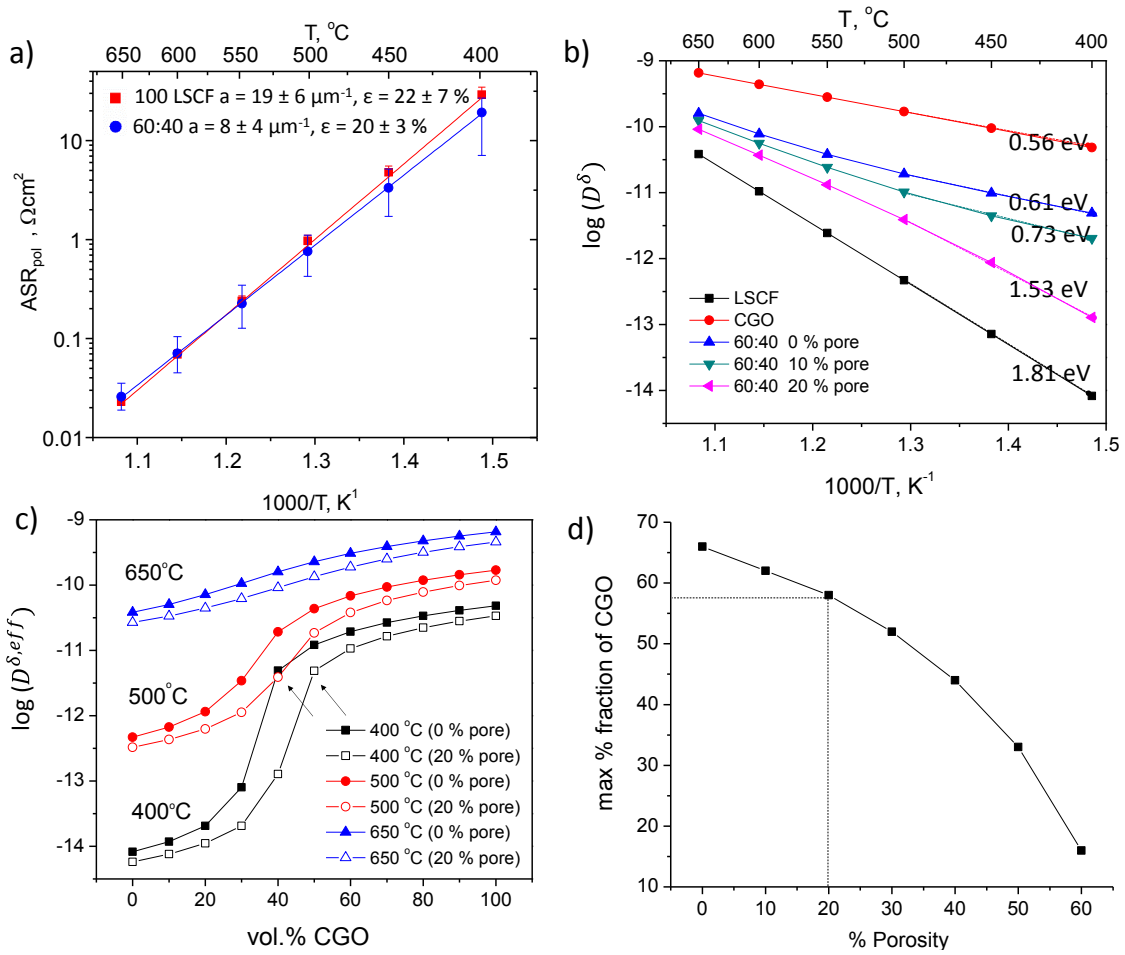

Figure 5-7 a) Arrhenius plot of ASR calculated by the model for a = 19 ± 6 µm^{-1}, ε = 22 ± 7 % for 100 LSCF and a = 8 ± 4 µm^{-1}, ε = 20 ± 3 % in the first 1.5 µm for the 60:40 composite. b) Effective diffusion coefficient of 60:40 composite for 0, 10 and 20 % porosity calculated from diffusion coefficients of pure components. The activation energy is calculated for T below 500 ˚C. c) The effect of porosity on the percolation limit of CGO. d) Maximum amount of CGO that can be added in LSCF without losing LSCF percolation.

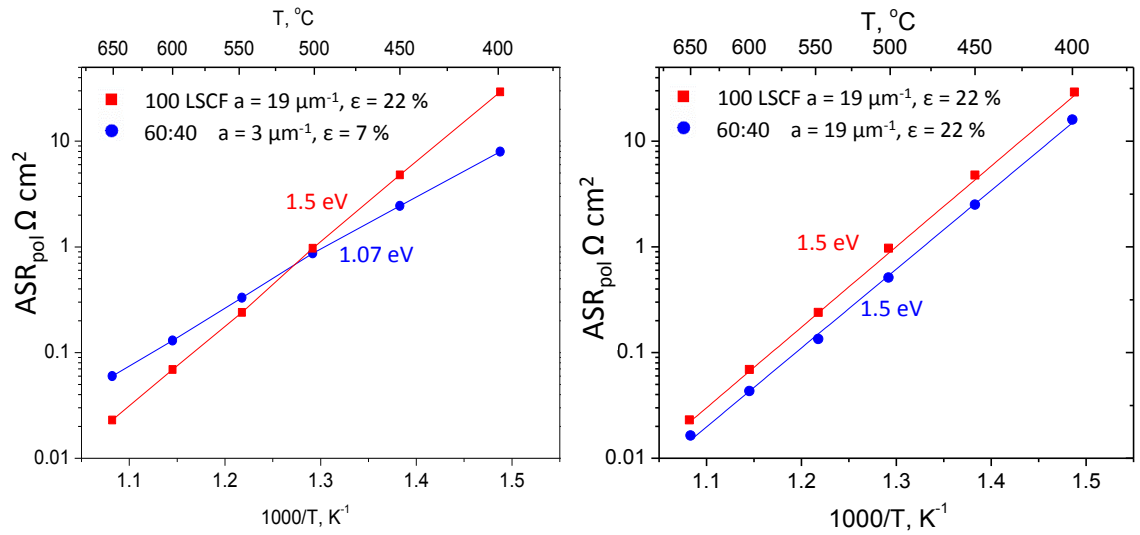

Figure 5-8. Arrhenius plot of ASR calculated by the model for a) a = 19 μm^{-1}, ε = 22 % for 100 LSCF and homogeneously distributed porosity in the reconstructed volume of 60:40 LSCF/CGO composite film with a = 3 μm^{-1}, ε = 7 %, b) assuming composite film had the same microstructural parameters as that of 100 LSCF.

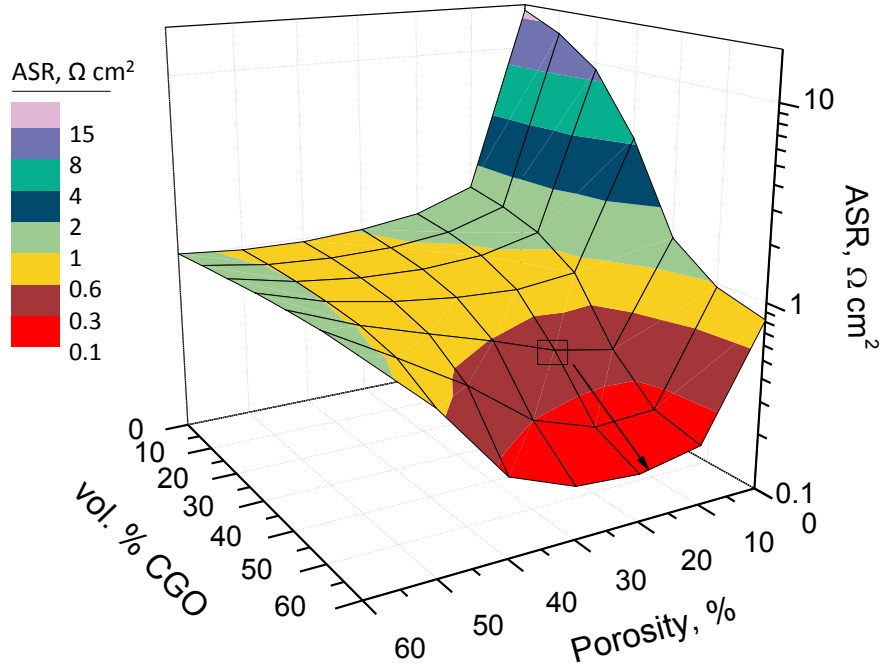

Figure 5-9. Optimization of the composite cathode at 500 °C for 60 nm pore size: ASR vs vol. % of CGO and porosity. The square represents the optimized CGO and porosity contents for the ESD composite films.

5.6 Conclusion

In order to find an optimal CGO content and porosity, two 3D FEM models accounting for the hierarchical nature of the microstructures for pure and composite films were developed for the first time. Indeed, existing 1D continuum models are not appropriate for describing hierarchical microstructures. These two models enable the calculation of ASR of periodic columnar structures similar to experimentally observed ESD cathodes with hierarchical porosity.

The ‘cube model’ is a continuation of previously reported work in the literature. Hierarchical microstructures and composite LSCF/CGO films were successfully demonstrated. However, it is limited to smaller geometries if small particle (cube) sizes are used.

Similarly, model 2 describes columnar microstructures. Inside the columns, all the transport and microstructure related parameters are homogenized using a source term. In this way, real microstructure parameters conformal to 3D reconstruction of real images are simulated. This approach concerns the modelling of all the macro structures with interesting structural features and/or heterogeneities without compromising the CPU time. It gets particularly interesting with the rapid advancement of fabrication techniques and technologies where highly controlled, regular and/or complex solid oxide structures are achieved. With model 2, a very good agreement has been found between the experimental and simulated ASR values at all investigated temperatures. The model shows the importance of local morphological heterogeneities. Finally, the intricate relationship between the amount of porosity and the ionically conducting second phase (CGO) in the MIEC (LSCF) is revealed. For the given transport parameters, the model estimates the peak performance for 20 % porosity and 60 vol. % CGO in LSCF at 500 °C

CONCLUSIONS AND PERSPECTIVES

1. Conclusions

Functional hierarchical nanostructured layers of well crystallized $La_{0.6}Sr_{0.4}Co_{0.2}Fe_{0.8}O_{3-\delta}$ (LSCF) and various compositions of LSCF/ $Ce_{0.9}Gd_{0.1}O_{2-\delta}$ (CGO) composite films have been examined to operate in intermediate temperature ranges (400-700 °C). To decrease the Area Specific Resistance (ASR) of the cathode films, two cases were examined in terms of microstructure evolution.

In the first case, pure LSCF films on CGO substrate were deposited by ESD equipped with a substrate holder moving in *x-y* directions. Different morphologies in coral and columnar-types were compared with similar films obtained by static ESD. The microstructure of the columnar-type film is affected the most. Big differences in the width of the corresponding columns results in dramatic differences in the activation energies. The influence of macro-porosity in the overall specific surface area in the narrow columns is big. However, narrow columns show higher resistances at low temperatures. This could simply be related to increased constriction effects and/or to lower effective diffusion coefficient at low operating temperatures. Nevertheless, in the new experimental design, exceptionally low ASR values of 0.02 and 0.07 Ω cm^2 at 650 and 600 °C, respectively are recorded for pure LSCF in columnar-type microstructure.

In the second case, the composition of the columnar films is varied by adding 25, 40 and 60 vol. % CGO in LSCF. The addition of CGO to this state-of-the-art cathode was previously reported to improve the electrochemical performance especially at low operating temperatures. The composite is usually preferred over pure films due to its higher total ionic conductivity at low operating temperatures. As expected, the activation energy of the composites of 40 and 60 vol. % CGO (1.3 eV) are less than pure LSCF (1.5 eV). However, the ASR of the composites at high operating temperatures is found to be considerably higher than pure LSCF, whereas the gain in ASR at low temperatures is not that obvious. While attempts to explain such behavior by 1D analytical models incorporating microstructure and transport parameters work quite well for pure LSCF, it fails for the composite. Indeed, 3D reconstructed images reveal heterogeneous distribution of nano-porosity in the 60:40 LSCF/CGO composite. The addition of CGO drastically influences the microstructure, including particle size, pore volume fraction, pore size and distribution as well as the specific surface area. The inner porosity is located in

the 1.5 μm distance from the electrode/electrolyte interface. The size of the porosity in the composite is larger than pure LSCF, thus the specific surface area ($8 \pm 4\ \mu m^{-1}$) is two-three fold of magnitude smaller than that of pure LSCF ($19 \pm 6\ \mu m^{-1}$) (Table 3-1). Nevertheless, these are still amongst the highest specific surface area values achieved for SOFC cathodes.

60:40 vol. % LSCF/CGO composite film in coral and columnar type microstructures are chosen to study the effect of grain sizes and pores in various sintering temperatures. Despite the coarser surfaces, better necking between particles and better adherence on the electrode/electrolyte interface are expected with increasing sintering temperature. However, the breadth of processing parameters and environmental conditions that can affect the optimal microstructure is vast. Therefore, it is difficult to reach a consensus as to which sintering temperature is optimal. All the films sintered from 800 to 1100 °C were characterized by SEM, XRD and EIS. SEM images reveal a significant difference in grain growth in two microstructures, especially at T >1000 °C. The LSCF grains in columnar films sintered above 1000 °C show much faster grain growth compared to CGO grains, which leads to approximately three times larger LSCF grains. On the other hand, the grain sizes increase in a similar rate in all coral films. At all sintering temperatures, the coral films are more porous with smaller grain sizes compared to the columnar ones. This is attributed to the initial ESD deposition conditions. In terms of electrochemical response, although the films of both microstructures sintered at 800 to 900 °C for 2 h in air give similar and lower ASR values, the limiting cathode processes are different. Above 1000 °C, the increase in ASR and therefore the activation energy in columnar films are attributed to the disrupted CGO percolation due to excessive growth of LSCF phase. According to these results, high sintering temperature does not improve the cathode performance. Therefore, it is concluded that the optimal sintering temperature for ESD cathodes should be kept well below 900 °C. The pure LSCF columnar films sintered at 800 °C were hence chosen for the performance tests on NiO/Ni-YSZ anode supported fuel cells (4 cm in diameter).

Before the tests, further optimization on the thickness of the double layer LSCF films was performed on symmetrical cells of smaller scale (1.6 cm in diameter). The double layer films (CFL-CCL) are composed of successive depositions of ESD and SP films. The SP layer is varied from 20 to 50 μm in 10 μm steps, while the ESD layer is kept fixed at 6 μm. On the other hand, the ESD layer is varied from 0.5 μm to 18 μm while the thickness of SP layer is kept fixed at 30 μm. It was shown that the electrode processes remain similar regardless of the thickness. This is in agreement with the estimated utilization length which is only a few

hundred nanometers from the electrode/electrolyte interface. Hence, the utilization length is always within ESD layer. The ASR of the cathode and series resistance of the electrolyte were monitored in the Nyquist impedance plot. The ionic conductivity of the CGO electrolyte contacted with various thicknesses of LSCF double layer films was compared with the theoretical values. Since it is an intrinsic property, a lower value signifies problems in the current collecting. It is shown that ASR and series resistance are not influenced by the film thicknesses above 4.4 μm thick ESD and 30 μm thick SP double layer films. Below these values, the current collection problems are evidenced. The CFL-CCL films with optimized thicknesses were deposited on larger NiO/Ni-YSZ anode supported cells. A dense barrier layer of CGO was deposited by ESD and sintered prior to the cathode film depositions. Two cells of the same kind are studied for electrochemical measurements at 675 °C. The first sample shows a maximum power density around 0.4 W cm^{-2}, while the second sample reaches only up to 0.15 W cm^{-2}. Nevertheless, these values are in good agreement to the previous reports on LSCF films deposited on Ni/Ni-YSZ anode supported cells. The durability tests up to 700 h performed on sample 2 show total potential degradation of 114 mV kh^{-1} or 13.85 % kh^{-1} compared to initial value. The degradation issues need to be studied further if these materials are to be used as cathode materials in SOFCs.

Two 3D FEM models were developed taking into account the hierarchical nature of the cathode microstructure. The macro-pore channels and columnar blocks are modelled. The first model was taken from the literature and adapted in the heterogeneous composite columnar microstructure. However, due to big computational requirements, simulations of the cathode with particle/pore sizes and width of the columns similar to the real microstructures are not possible. Although the trend in activation energy similar to experimental results are obtained, model 1 computes much better ASR performance for the 60:40 vol. % LSCF/CGO composite at all measuring temperatures. Following model 1, a new 3D FEM model was proposed (model 2) that would still take into account the hierarchical microstructures and would also enable simulations of larger macro features. This was possible by combining finite element method and homogenization approach in the cathode domain similar to 1D continuum approaches. For the composite film with an inhomogeneous distribution of porosity within the thickness, two cathode domains are defined: porous near the electrolyte and dense above 1.5 μm thickness. Thanks to the homogenization approach, the exact values of porosity and specific surface area (from FIB/SEM) are introduced in the model.

The major findings of the modelling are:

1) While a large amount of porosity is generally beneficial in a pure MIEC cathode, it could be detrimental for a composite cathode, especially at low temperatures. It is because the effective diffusion coefficient of the LSCF/CGO composite cathode decreases as the operating temperature is reduced. A fine tuning of porosity is thus required.
2) A high amount of CGO may break the percolation of the MIEC network. Here also a fine tuning of the composition in relation with the microstructure is required.
3) For the given transport and microstructural parameters, assuming similar grain sizes of LSCF and CGO, the FEM model estimated the peak performance for 20 % porosity and 60 vol. % CGO in LSCF at 500 °C. However, 40:60 LSCF/CGO film in columnar microstructure had adherence problems on the electrolyte surface. Nevertheless, 60:40 LSCF/CGO composite film was already close to the optimal value predicted by the model.

2. Perspectives

The fabrication of cathodes by ESD open doors for the optimization of electrodes for SOFCs. Although the deposition of LSCF by ESD dates back to 2008 in LEPMI, there remains number of aspects regarding the microstructure control with respect to initial deposition parameters and sintering temperature treatments.

It has been shown that even a slight change in the configuration in experimental set-up (static or a moving substrate holders in ESD, Section 3.2) results in a great change in the microstructure of LSCF, i.e. columnar width and specific surface area, hence the performance of the electrode. However, the correlated effects of pore gas diffusion and current collecting with respect to the size of the columnar width and macro-pore channels are not yet explored. These can be studied by electrochemical impedance spectroscopy and modelling.

In the full cell configuration, it is required to optimize the thickness and the density of the electrolyte, since the YSZ/CGO bilayer electrolyte was quite thick (~9 μm), and the CGO barrier layer was porous. This probably has caused further performance lost. One can propose to deposit CGO as a thinner and denser layer by ESD using shorter deposition time. An

adjustment of ESD parameters has to be performed in order to deposit the films on substrates with different scales. This is not simple; some trials are necessary to get similar microstructures.

The degradation phenomena of the full cell after long term operation is not studied in detail during this thesis. The changes in the cathode microstructure before and after long term tests can be determined by FIB/SEM technique. According to the observations in Chapter 4, anode and electrolyte compartments seem to suffer more than the cathode from long term tests. This needs to be verified by both impedance spectroscopy and FIB/SEM tomography. On a further note, STEM-EDX elemental mapping analyses at the interfaces before and after long term tests must also be undertaken in order to see if new phases have formed due to inter-diffusion of elements.

As for the FEM simulations, a time dependent impedance model is developed based on our stationary model 2 as shown in Figure 1. At the moment, the high frequency part of the impedance spectrum for pure LSCF deviates from 45° Gerischer character. This might be due to very small utilization length in LSCF film. Accordingly, better meshing at the interface might be necessary. The simulations of the composites seem rather good, since the utilization length is much larger than pure LSCF, and the meshing at the interface does not cause problems. With this method, the evolution of impedance spectra as a function of microstructural parameters and composition can be simulated and compared to the experimental data. This might also be useful for the simulations for long-term degradation tests.

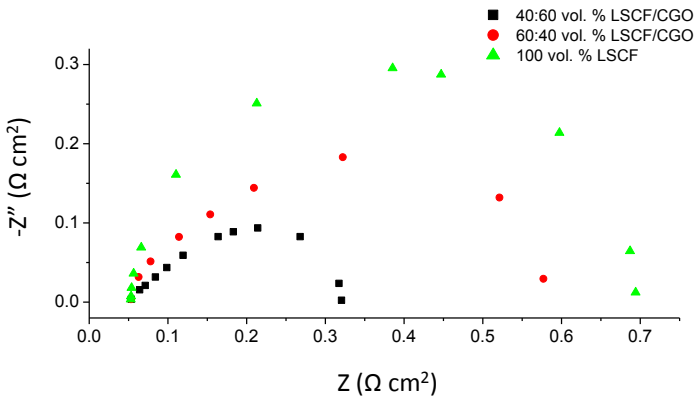

Figure 1. Simulated Nyquist impedance spectrum at 500 °C for 100 LSCF and 60:40 LSCF/CGO composite measured at 600 °C, similar microstructural parameters are used as in Chapter 5.

Throughout this thesis, we have shown that the LSCF/CGO composites is not better than pure LSCF due to densification in the microstructure. For this reason, new materials or composites should be considered. It has been shown in our laboratory that the architectural design at the interfaces of $Ln_2NiO_{4+\delta}$ (Ln: La, Pr) deposited by ESD on CGO electrolytes can substantially decrease the ASR from 0.12 Ω cm^2 at 700 °C [243] down to 0.02 Ω cm^2 [244]. In this design, a porous layer of CGO is deposited on dense electrolyte by SP technique and sintered prior to LnNO deposition by ESD. This LnNO ESD film partially penetrates into the first CGO porous film leading to a denser CGO–LnNO composite base-layer (Figure 2). To the best of our knowledge, this composite sub-layer plays a main role in obtaining the best electrochemical properties of nickelates available in the literature. These preliminary results are very promising and further compositions and characterizations are necessary.

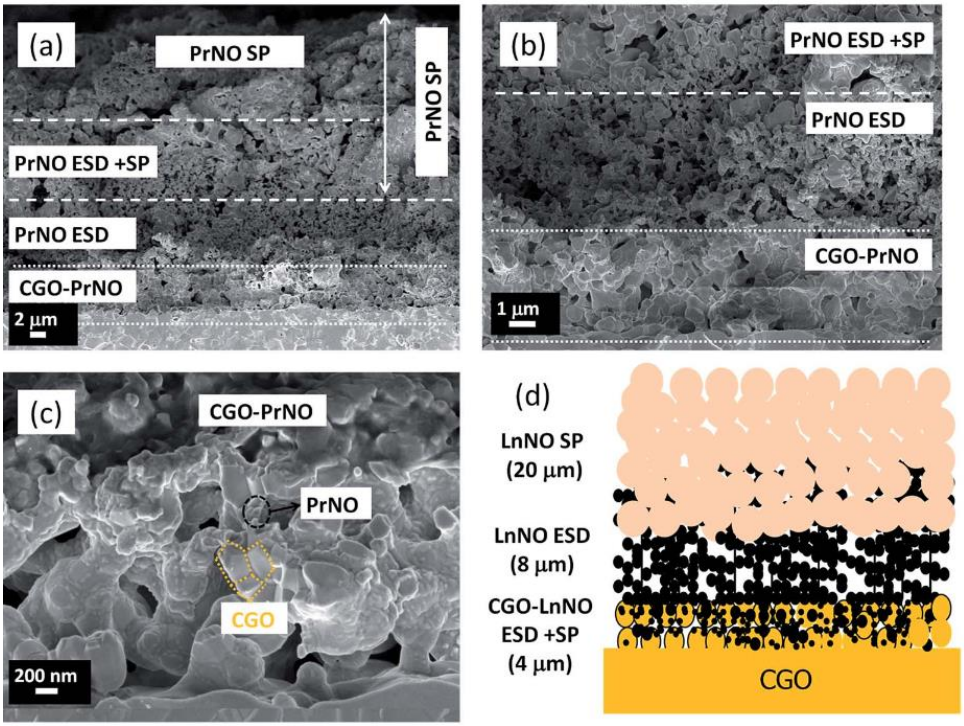

Figure 2. SEM micrographs of $Ln_2NiO_{4+\delta}$ films a), b) cross-section c) CGO–PrNO sub-layer on the CGO electrolyte d) schematic of the triple layer design. Reprinted from [244].

APPENDICES

Appendix A

Refinements of diffraction patterns by LeBail method. The FullProf software developed by Juan Rodriguez-Carvajal was used to perform the refinement profile and structure of the resulting diffraction patterns [245]. The refinement profile with cell constraint was achieved by exploiting the method of Le Bail [246]. The Pseudo-Voigt function was used to refine only the angular positions to determine the lattice parameters (a, b, c) and the profile of the lines.
By a set of successive iterations, calculated diffractograms are obtained, which has to be consistent with the best experimental diffractograms. The value of the quality of fitting is given according to the difference between the calculated and the experimental data. Several confidence factors are calculated to account for the quality of the refinement. These factors are designated by R_{Bragg}, R_p, and $R_{\omega p}$ and R_{exp} (in %) and χ^2:

- The R_{Bragg} factor reflects the quality of the structural model for each phase φ regardless of peak profile. It is defined by the formula:

$$R_B = \frac{\sum_i |I_{ko} - I_{kc}|}{\sum_i I_{ko}} \qquad A\,1$$

where I_{ko} represents the integrated intensity observed at the i^{th} reflection and I_{kc} the corresponding calculated intensity.

- The profile factors R_p and $R_{\omega p}$ characterizes the quality of the refinement as a whole, taking into account both the shape and the peak intensities as well as the background noise:

$$R_p = \frac{\sum_i |y_{io} - y_{ic}|}{\sum_i y_{io}} \qquad A\,2$$

$$R_{wp} = \left[\frac{\sum_i w_i (y_{io} - y_{ic})^2}{\sum_i w_i y_{io}^2} \right]^{\frac{1}{2}} \qquad A\,3$$

where y_{io} and y_{ic} represent the observed individual intensity and individual intensity calculated at each i^{th} step of the profile. w_i denotes the weight associated with the measured intensity.

- the minimum expected factor (taking into account the statistical experimental diagram):

$$R_{\exp} = \left[\frac{N - P + C}{\sum_i w_i y_{io}^2} \right]^{\frac{1}{2}} \qquad A\,4$$

where N is the number of measured points in the diagram, P the number of refined parameters and C the number of constraints.

From these last two factors ($R_{\omega p}$ and R_{exp}), it is possible to calculate a statistical parameter, called χ^2 which approaches unity when the model fits perfectly with experimental data: $\chi^2 = (R_{wp} / R_{exp})^2$.

Appendix B

Fractal Gerischer Impedance

The impedance plots shown throughout this thesis resemble a Gerischer impedance with a 45° characteristic slope at high frequencies. However, the impedance spectra were slightly depressed, indicating a non-ideal capacitive response. A depressed Gerischer-like impedance spectrum was also reported for the $(La_{1-x}Sr_x)CoO_{3-\delta}$ electrodes [247]. A third parameter is included, n, to account for the non-ideal fractal Gerischer. When the fractal Gerischer correction factor, *n*, is close to 1, the impedance spectrum takes the form of a normal Gerischer impedance with 45 ° slope at high frequency and when it is close to 0.5, it takes the form of a semicircle. This concept has been discussed in a paper by Boukamp *et al*. to which the reader is referred for further details [248].

$$Z(\omega) = \frac{R_{chem}}{\sqrt{1+(j\omega t_{chem})^n}} \qquad A\,5$$

where ω is the angular frequency and R_{chem} and t_{chem} are the characteristic resistance and time constant, respectively. First t_{chem} is calculated using the formula of $t_{chem} \cdot \omega_{max} = \sqrt{3}/2\pi$ where ω_{max} is the maximum frequency in the impedance plot. The parameter, *n*, was found in between 0.8 and 0.9 in all the fittings.

Calculation of Transport Parameters from Gerischer impedance:

The oxygen surface exchange coefficient, k_o (cm s^{-1}), and bulk diffusion coefficient D_o (cm^2 s^{-1}) are calculated from the Gerischer impedance [240] according to:

$$k_o = \frac{c_v}{c_o}\frac{1}{a\,\gamma}\frac{1}{t_{chem}} \qquad A\,6$$

$$D_o = \left(\frac{RT}{4F^2}\right)^2 \left(\frac{\tau}{(1-\varepsilon)aR^2 k_o C_o^2}\right) \qquad A\,7$$

The parameters ε, a, and τ were taken from Table 3-1.

Appendix C

Properties of LSCF

In mixed-conducting materials such as LSCF, the oxygen vacancies in the perovskite structure interact with the oxygen gas in the surrounding atmosphere. An oxygen equilibrium concentration c_o is reached depending on the oxygen partial pressure in the atmosphere. The rate of exchange of oxygen on the surface is determined by the exchange coefficient k^{δ}. An equilibrium is reach between the oxygen ions at the surface and in the bulk by a diffusion process. How fast this balance can be achieved is dependent on the chemical solid diffusion coefficient D^{δ}. Since the electronic conductivity is orders of magnitude higher than the ionic conductivity in the considered mixed conducting materials, these three material parameters are critical to the performance of a cathode.

The oxygen ion concentration of the mixed conductive material in equilibrium with the partial pressure of oxygen in the surrounding atmosphere is a temperature-dependent function. The models considered in this thesis assume constant homogeneous temperature distribution. Therefore, the relationship between the oxygen ion equilibrium concentration and oxygen partial pressure must be determined for all observed temperatures. In general, no direct method other than the (expensive) neutron diffraction exists for the measurement of oxygen ion concentration. The non-stoichiometry of oxygen, δ and the lattice constants of the unit cell are combined to determine the equilibrium oxygen ion concentration.

$$c_o = \frac{3-\delta}{\delta} \cdot c_v = \frac{3-\delta}{\delta} \cdot \frac{3}{V \cdot N_A} \qquad A\,8$$

Where V is the volume of the unit cell, N_A is the Avogadro's number and c_v is the concentration of oxygen ion lattice sites. There are available non-stoichiometry δ data of oxygen in the lattice measured by X-ray diffraction, thermogravimetry and solid electrolyte coulometry for various temperature, ambient oxygen partial pressure and composition range [181,249]. The following equation holds for the oxygen non-stoichiometry data of δ and $\log(p_{O2})$ plot [181].

$$c_O\left(T, P_{O_2}\right) = \alpha(T) * log\left(P_{O_2}\right) + \beta(T) \qquad A\,9$$

where α and β parameters are the slope and intercept of the c_o and log(p_{O2}) graph. c_v values above 600 °C are taken from ref. [115] and extrapolated to room temperature. c_o is calculated using Eq. 8-8 and Eq. 8-9.

The effective transport parameters are important parameters for the performance of a MIEC cathode. The intrinsic values cannot be measured directly, therefore effective measurable quantities are quantified, but the result is highly dependent on the experimental technique applied. There are typically three experimental method: tracer diffusion (indicated with a suffix *), chemical diffusion (indicated with a suffix δ) and electrical conductance (indicated with a suffix q)[250]. The material parameters determined by means of various types of experiments can be converted into each other (Figure - A 1). Tracer and electrical measurements give similar values for the surface exchange rate constant in case of a mixed conductor with predominant electronic conductivity:

$$k^* \sim k^q \text{ and } D^* \sim D^q \qquad A\ 10$$

while those obtained from “chemical” experiments (D^δ and k^δ) are substantially higher than tracer parameters [250]:

$$k^\delta = \gamma \cdot k^* \text{ and } D^\delta = \gamma \cdot D^* \qquad A\ 11$$

The thermodynamic enhancement factor, γ, relates the differential changes in oxygen partial pressure to the oxygen stoichiometry of the perovskite [182].

$$\gamma\left(T, P_{O_2}\right) = \frac{1}{2}\left|\frac{\partial\, lnP_{O_2}}{\partial\, ln\, c_v}\right| = \frac{1}{2}\left|\frac{\partial\, lnP_{O_2}}{\partial\, ln\, \delta}\right| \qquad A\ 12$$

$$\gamma\left(T, P_{O_2}\right) = \frac{1}{2} ln(10)\left(logP_{O_2} + \frac{\beta(T)}{\alpha(T)}\right) \qquad A\ 13$$

Tracer diffusivity for oxygen (D^*) includes the possibility for oxygen ions to jump back to their original lattice sites, which is energetically favorable, after their first jump. Therefore, D^* is usually lower than intrinsic values, and they are correlated by a factor called the correlation factor (f_o), which is close to unity (0.69 for MIEC [251]). Assuming $D^* = D_o \cdot f_o$ and $k^* \cong k_o$ [182]

$$D^\delta = \frac{D^*}{f_o} \cdot \frac{c_o}{c_v} \cdot \gamma \text{ and } k^\delta = k_o \cdot \frac{c_o}{c_v} \cdot \gamma \qquad A\ 14$$

A strong relationship has been found between *D* and *k*, which was interpreted as an indication that oxygen vacancies also play an important role for the surface exchange process [252].

The correlation between diffusion coefficients measured by different techniques:

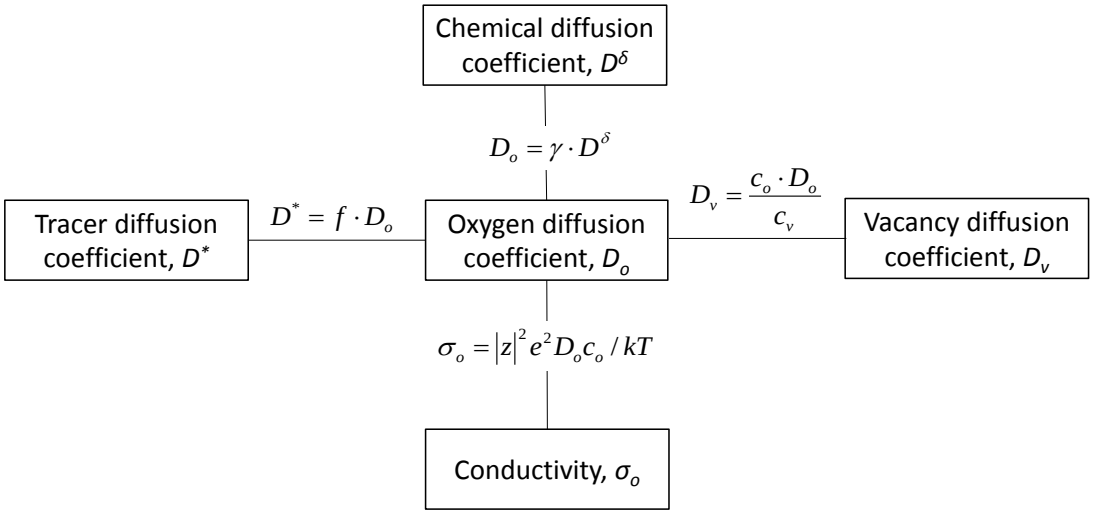

Figure - A 1 Scheme showing how the diffusion coefficients measured by different techniques are related to each other. Reprinted from [253].

Appendix D

Procedure

The commercial software COMSOL Multiphysics 4.4 is used for the FEM modelling. As a measure for the electrode performance, the area specific resistance ASR is calculated as a function of material parameters and microstructure characteristics. The standard procedure for COMSOL is to construct a geometry by using built-in CAD tools. All of the steps were integrated into a single main MATLAB function consisting of a mix of calls to COMSOL commands and standard MATLAB code to generate the appropriate assignment of geometric features to a given domain (electronic conductor, ionic conductor or pore). Once a geometry is constructed, physics and boundary conditions may be applied to the sub-volumes, surfaces, edges, and vertices. COMSOL equations and boundary conditions were applied automatically by custom script on the basis of this feature identification. Finally, the finite element problem was meshed, assembled and solved with COMSOL routines.

Automated feature assignment

Due to the number and complexity of geometric features and couplings, we developed a subroutine to automatically assign appropriate domain to geometric features and apply the appropriate physics. Automation with a script ensures rapid execution of the simulation and inclusion of all important features, as opposed to manual assignment which is very slow and prone to errors. The first part of the script identifies the various geometric sub-features and tracks them with MATLAB arrays. The appropriate boundary conditions, rate equations, and other features were assigned after identification.

Mesh convergence

The accuracy of the results depends on the size of the finite elements defined by the mesh. Therefore, an optimized mesh should be used within a reasonable computational time. The mesh was generated by COMSOL Multiphysics. A parametric mesh convergence study was conducted prior to the simulations for both model as shown in Figure - A 2**Error! Reference**

source not found.. First, a periodic geometry of 10 *x* 10 *x* 80 cubes (cube size: 50 nm) is generated in model 1 with randomly distributed 30 % of porosity. ASR is calculated for different mesh values (degree of freedom). In order to conduct the same study, the microstructure and transport parameters of model 1 were homogenized in the same volume (0.5 *x* 0.5 *x* 4 μm^3) and were integrated in model 2. The results are compared to 1D ALS model for verification. From coarse to fine mesh, model 2 easily converge to a value close to the one predicted by ALS model. We choose to work with a 'normal' mesh refine at the electrolyte cathode interface (max element size set to 10/300 microns at this interface, Figure 5-6d). This mesh show less than 1 % difference with the finest mesh was taken as an approximation to the actual solution. On the other hand, the convergence of model 1 was not complete, even with a fine mesh. Interestingly, model 1 calculates an ASR similar to that of model 2 and 1D ALS model with a coarse mesh. This was also encountered by Rüger *et al*. [114] and Häffelin *et al*. [100] with their 3D cube model. The reason behind it remains unclear.

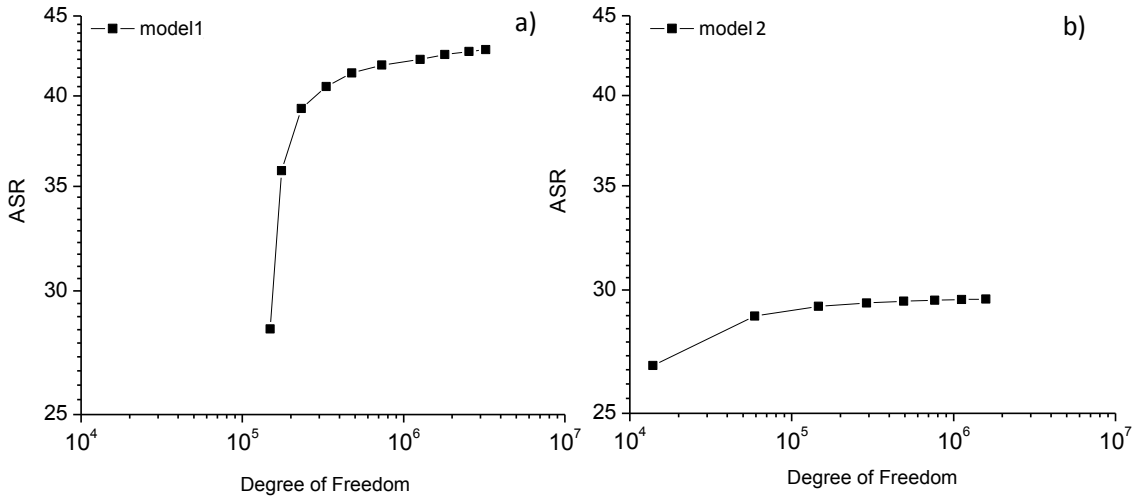

Figure - A 2 The mesh convergence study in model 1 a) and model 2 b). The same microstructure parameters are chosen for both models. The ASR calculated by 1D ALS model for this microstructure is 29 Ω cm^2.

Boundary conditions for model 1:

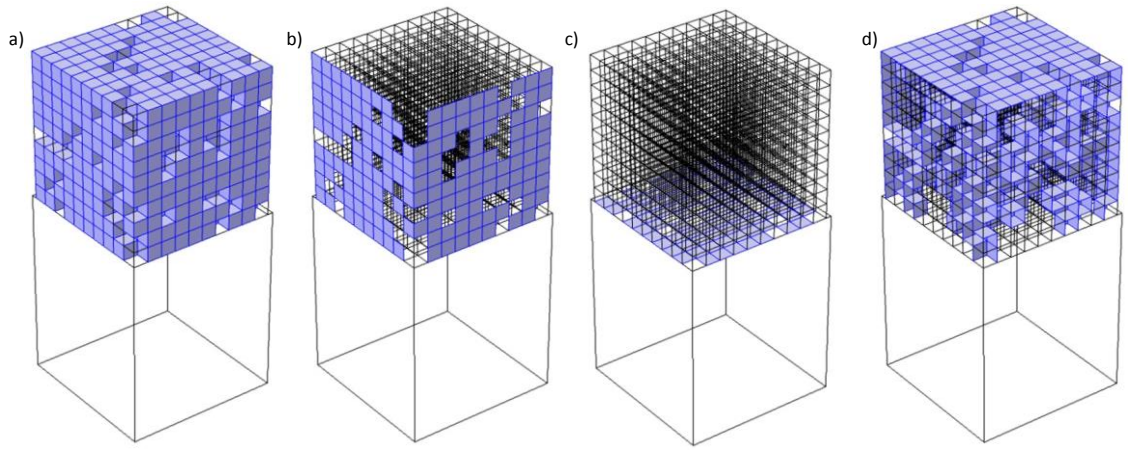

Figure - A 3 a) Cubes activated for Fick's 1st law of diffusion b) No flux zone for diffusion, indicating symmetrical situation. c) Charge transfer at the electrode electrolyte interface, coupling of two physics: transport of diluted species (cathode) and electric current (electrolyte) d) oxygen exchange boundary sites

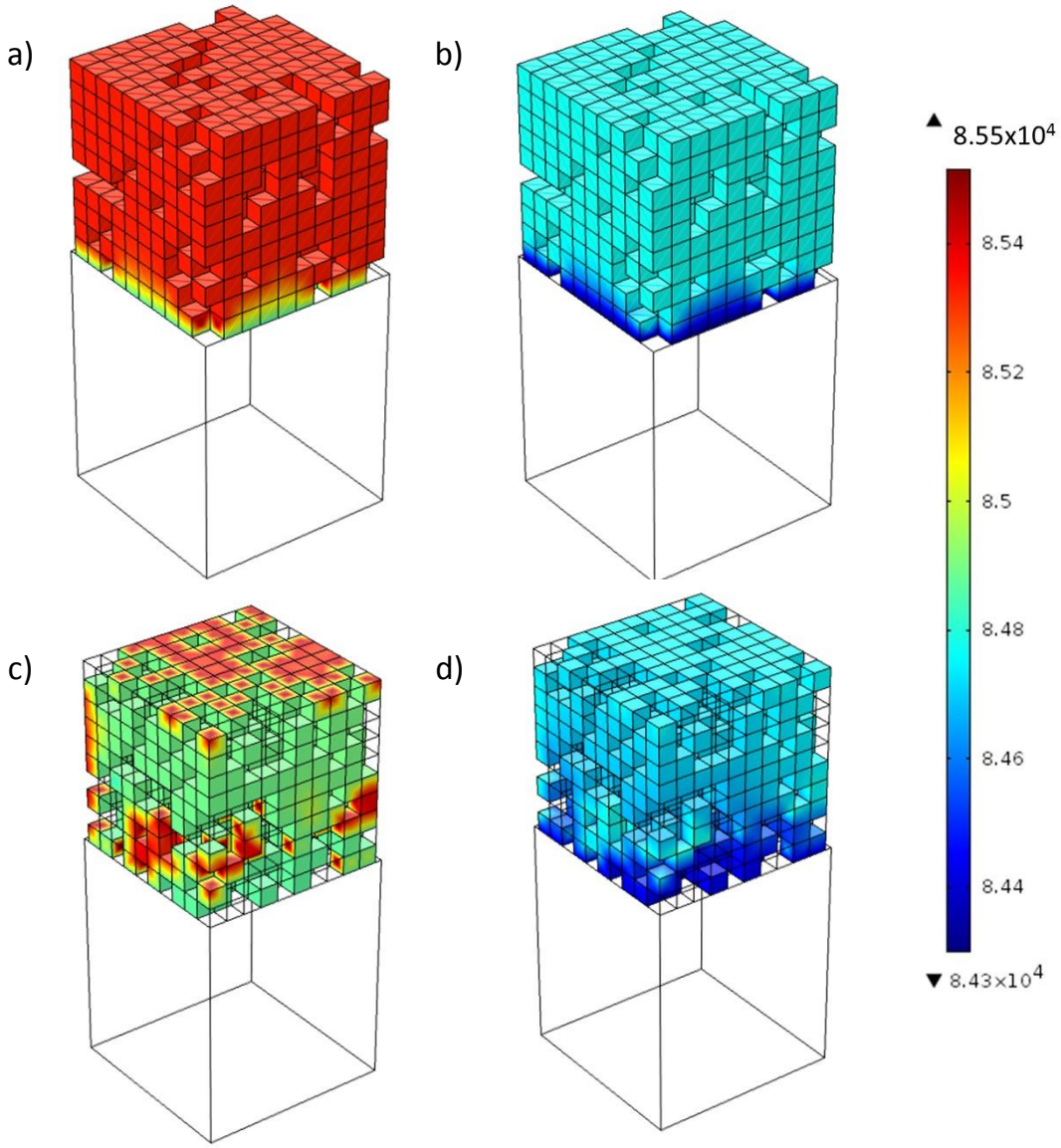

Figure - A 4 Concentration gradient profile for pure LSCF calculated at a) 400 °C and b) 650 °C. 60:40 LSCF/CGO composite calculated at c) 400 °C and d) 650 °C.

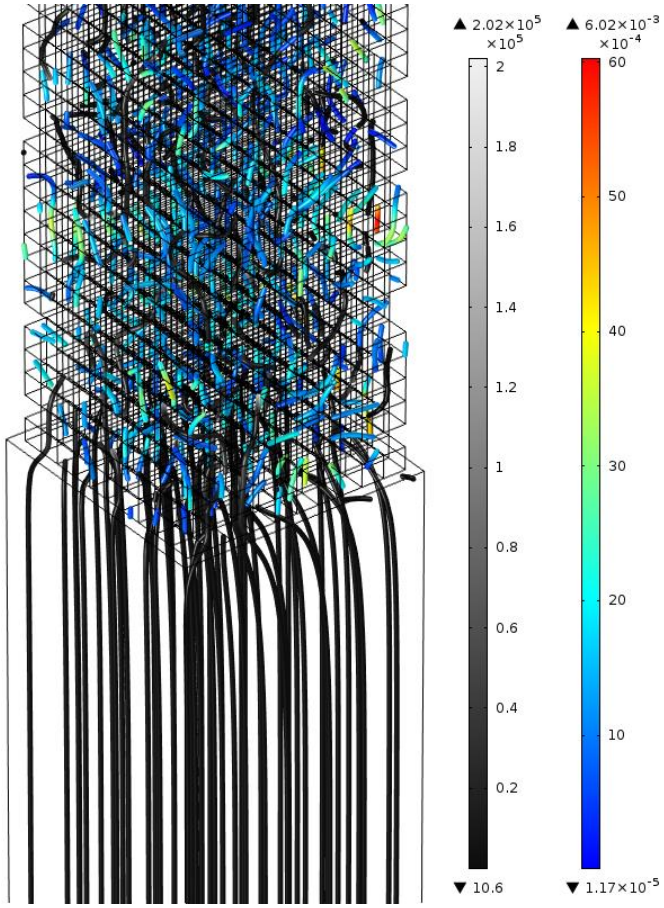

Figure - A 5 The current lines in composite electrode showing the coupling of ionic (colorful) and electronic current (grey)

Validation of Model 1

The proposed 3D FEM model is validated in comparison to the well-established 1D ALS model [92] which assumes a macrohomogeneous geometry and a pure MIEC material. Next, this 3D FEM model was simulated on columnar microstructure to calculate the ASR of pure LSCF and LSCF/CGO composite. In this work, a model geometry consisting of randomly distributed cubes of pure MIEC (LSCF) and pore phase on top of the dense electrolyte (CGO) have been generated as depicted in Figure - A 6. Each cube represent LSCF particles and the voids represent the porosity. The total geometry of the cathode consists of 10 × 10 × 25 cubes in which the length of a cube edge is 400 nm. The required geometrical parameters were computed on 10 numerically generated cubes with 30 % porosity. The averaged values were 1.3 for tortuosity and 2.98 μm^{-1} for the specific surface area. The parameters used in both models can be found in Table- A 1.Error! Reference source not found.

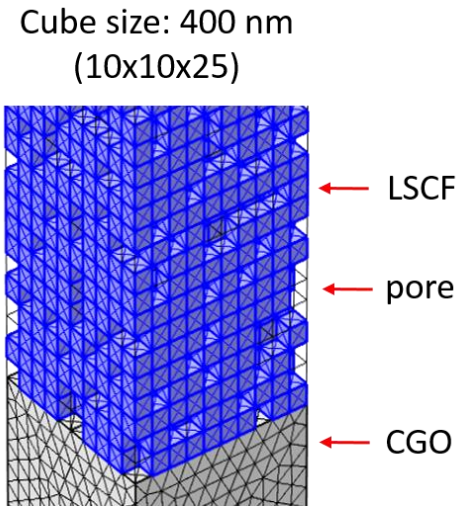

Figure - A 6. A macrohomogeneous porous MIEC cathode (LSCF) on CGO electrolyte.

Table- A1. Parameters used in the ALS and 3D FEM model.

T., ˚C	c_v, mol.m^{-3}	c_o, mol.m^{-3}	γ	a(T)	b(T)	D^{δ}, m^2·s^{-1}	k^{δ}, m·s^{-1}
550	85506	85075	448.33	218.47	85221	1.03E-15	4.71E-07
600	85399	84937	410.00	238.08	85097	4.49E-15	1.04E-06
650	85152	84773	378.75	257.69	84947	1.66E-14	2.10E-06

The comparison of ASR calculated by these two models can be found in Table- A 2. The results are in good agreement and thus validating the 3D FEM model.

Table- A 2 Comparison of ASR of 100 LSCF between 550-650 ˚C by 1D ALS Model and 3D FEM Model 1.

Model type	650˚C	600˚C	550˚C
1D ALS	0.040	0.111	0.353
3D FEM model	0.041±0.003	0.121±0.007	0.393±0.020

Model 1 is published in ECS Transactions [241] before we obtained real microstructural parameters from FIB/SEM tomography. A 30 % internal porosity is assumed for pure LSCF while completely dense structure for the 60:40 composite (Figure A 7). The results are as follows:

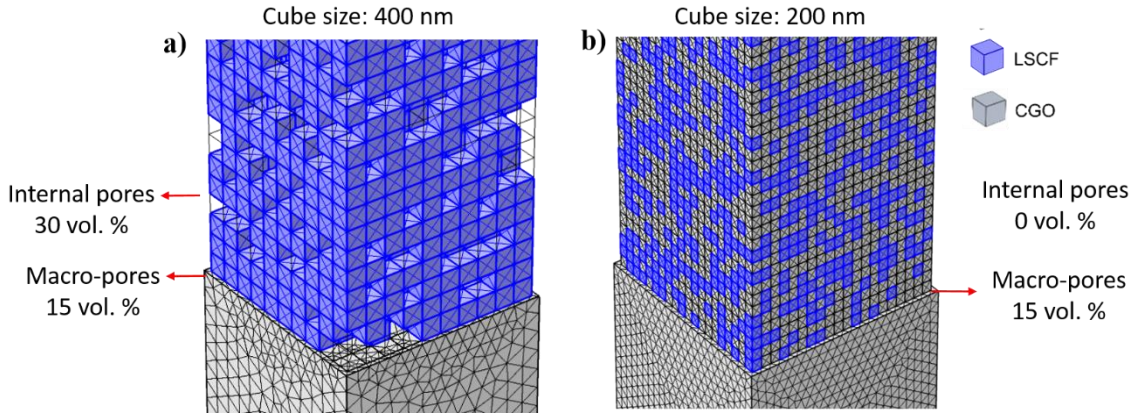

Figure - A 7 Columnar microstructures including 15% macro-pore channels. a) 100 vol. % LSCF with 30 vol. % internal porosity b) 60:40 vol. % LSCF/CGO composite without any porosity within the column. The figures represent only a quarter of the total geometry.

Table- A 3 Average ASR between 550-650 ˚C obtained from 3D FEM model 1

Sample	650˚C	600˚C	550˚C
100 LSCF	0.04	0.13	0.43
60:40 LSCF/CGO	0.05	0.09	0.19

Error! Reference source not found. shows the results of the 3D FEM simulations for 100 LSCF and 60:40 LSCF/CGO in model 1. ASR of the composite is slightly higher than that of pure LSCF at 650 °C revealing that the composite may not be beneficial at high temperatures due to the microstructural evolution related to CGO addition. However, in contradiction with our experimental observations, the model shows superior performance for the composite already at temperatures lower than 600 °C. Still, the correct trend is captured: as in the experiment, the ASR increases slower (smaller activation energy) for the composite as the operation temperature decreases. The observed overestimation of ASR for pure LSCF sample may be related to the selection of the particle/pore size (400 nm in model) leading to an underestimation of the specific surface area.

Validation of Model 2

The model has been validated in comparison to 1D ALS model as shown in Figure - A 8**.**

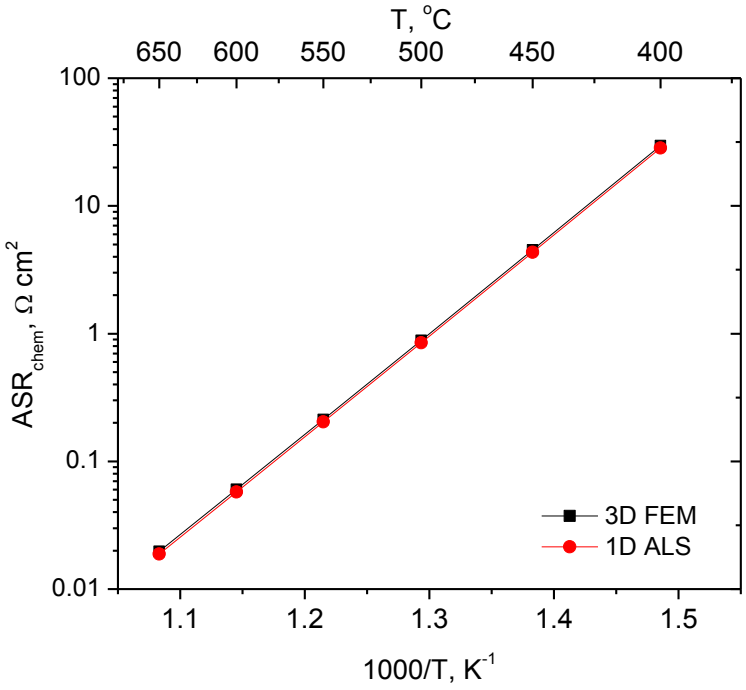

Figure - A 8 Comparison of the full 3D FEM model and the 1D ALS model [92] for a 4 µm thick macrohomogeneous cathode (i.e. without macro-pore channels) for a = 25 µm-1 and ε = 29 %.

Table- A 4 The parameters used in the model 2.

T., °C	$c_{v,}$ mol.m^{-3}	c_o, mol.m^{-3}	γ	α	β	D^{δ}, m^2·s^{-1}	k^{δ}, m·s^{-1}
400	85659	85330	615.39	159.64	85437	$3.30\cdot10^{-14}$	$5.01\cdot10^{-7}$
450	85633	85271	547.00	179.25	85392	$2.26\cdot10^{-13}$	$2.49\cdot10^{-6}$
500	85588	85156	493.19	198.86	85320	$1.21\cdot10^{-12}$	$1.00\cdot10^{-5}$
550	85506	85075	448.33	218.47	85221	$5.23\cdot10^{-12}$	$3.40\cdot10^{-5}$
600	85399	84937	410.00	238.08	85097	$1.91\cdot10^{-11}$	$9.99\cdot10^{-5}$
650	85152	84773	378.75	257.69	84947	$6.06\cdot10^{-11}$	$2.60\cdot10^{-4}$

Appendix E

The influence of columnar width on activation energy

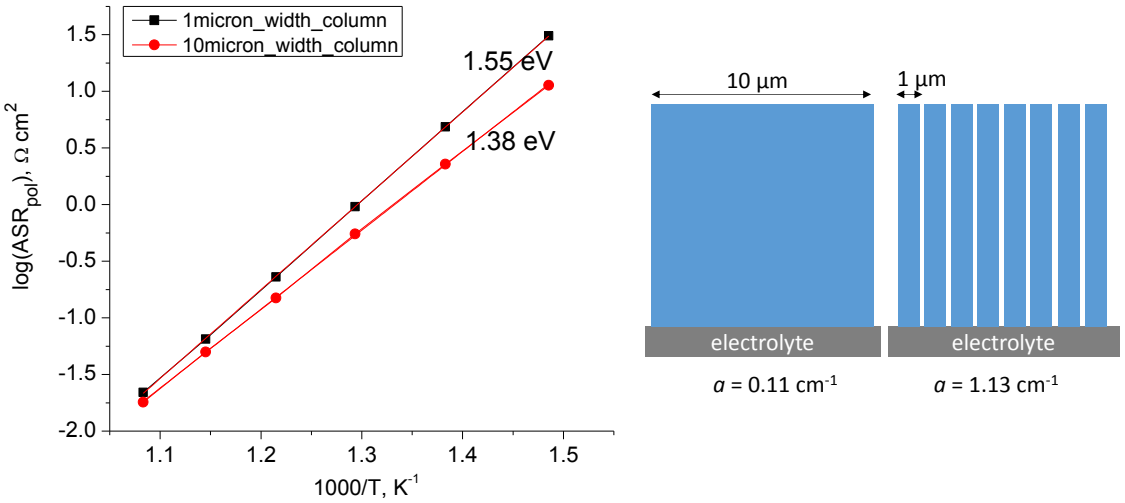

Figure - A 9 The significance of macro-pore channels calculated by columnar geometry in FEM model.

As shown in Figure - A 9, the importance of macro pore channels can be observed by comparing two columnar microstructures with different widths. The activation energy and the resistances are calculated for these two columnar microstructures. Assuming 15 vol. % macro-pore channels without any porosity inside the columns, it is found that the specific surface area of 1 µm wide columns are about ten times higher than that of 10 µm columns. This results in great change in resistance and activation energy in the Arrhenius plot. This can be explained by the influence of porosity in effective diffusion coefficients, especially at T < 500 °C.

REFERENCES

[1] O. Yamamoto, Solid oxide fuel cells: fundamental aspects and prospects, Electrochim. Acta. 45 (2000) 2423–2435.

[2] M. Hubert, J. Laurencin, P. Cloetens, J. da Silva, F. Lefebvre-Joud, P. Bleuet, A. Nakajo, E. Siebert, Role of Microstructure on Electrode Operating Mechanisms for Mixed Ionic Electronic Conductors: From Synhcrotron-Based 3D Reconstruction to Electrochemical Modeling, Solid State Ionics. 294 (2016) 90–107.

[3] F. Zhao, A. V. Virkar, Dependence of polarization in anode-supported solid oxide fuel cells on various cell parameters, J. Power Sources. 141 (2005) 79–95.

[4] A. Aguadero, L. Fawcett, S. Taub, R. Woolley, K.-T. Wu, N. Xu, J.A. Kilner, S.J. Skinner, Materials development for intermediate-temperature solid oxide electrochemical devices, J. Mater. Sci. 47 (2012) 3925–3948.

[5] P.R. Shearing, D.J.L. Brett, N.P. Brandon, Towards intelligent engineering of SOFC electrodes: a review of advanced microstructural characterisation techniques, Int. Mater. Rev. 55 (2010) 347–363.

[6] M.-H. Sun, S.-Z. Huang, L.-H. Chen, Y. Li, X.-Y. Yang, Z.-Y. Yuan, B.-L. Su, Applications of hierarchically structured porous materials from energy storage and conversion, catalysis, photocatalysis, adsorption, separation, and sensing to biomedicine, Chem. Soc. Rev. 45 (2016) 3479–3563.

[7] A.Z. Lichtner, D. Jauffrès, C.L. Martin, R.K. Bordia, Processing of Hierarchical and Anisotropic Porosity LSM-YSZ Composites, J. Am. Ceram. Soc. 96 (2013) 2745–2753.

[8] Y. Chen, Y. Lin, Y. Zhang, S. Wang, D. Su, Z. Yang, M. Han, F. Chen, Low temperature solid oxide fuel cells with hierarchically porous cathode nano-network, Nano Energy. 8 (2014) 25–33.

[9] L. Dieterle, P. Bockstaller, D. Gerthsen, J. Hayd, E. Ivers-Tiffée, U. Guntow, Microstructure of Nanoscaled La0.6Sr0.4CoO3-δ Cathodes for Intermediate-Temperature Solid Oxide Fuel Cells, Adv. Energy Mater. 1 (2011) 249–258.

[10] L.C.R. Schneider, C.L. Martin, Y. Bultel, L. Dessemond, D. Bouvard, Percolation effects in functionally graded SOFC electrodes, Electrochim. Acta. 52 (2007) 3190–3198.

[11] N. Hildenbrand, P. Nammensma, D.H.A. Blank, H.J.M. Bouwmeester, B.A. Boukamp, Influence of configuration and microstructure on performance of La2NiO4+δ intermediate-temperature solid oxide fuel cells cathodes, J. Power Sources. 238 (2013) 442–453.

[12] S.P.S. Badwal, Zirconia-based solid electrolytes: microstructure, stability and ionic conductivity, Solid State Ionics. 52 (1992) 23–32.

[13] J.A. Kilner, C.D. Waters, The effects of dopant cation-oxygen vacancy complexes on the anion transport properties of non-stoichiometric fluorite oxides, Solid State Ionics. 6 (1982) 253–259.

[14] F. Tietz, Thermal expansion of SOFC materials, Ionics (Kiel). 5 (1999) 129–139.

[15] A. Nakajo, J. Kuebler, A. Faes, U.F. Vogt, H.J. Schindler, L.K. Chiang, S. Modena, J. Van Herle, T. Hocker, Compilation of mechanical properties for the structural analysis of solid oxide fuel cell stacks. Constitutive materials of anode-supported cells, Ceram. Int. 38 (2012) 3907–3927.

[16] J.W. Fergus, Electrolytes for solid oxide fuel cells, J. Power Sources. 162 (2006) 30–40.

[17] Y. Arachi, H. Sakai, O. Yamamoto, Y. Takeda, N. Imanishai, Electrical conductivity of the ZrO2 – Ln2O3 (Ln = lanthanides) system, Solid State Ionics. 121 (1999) 133–139.

[18] M.G. Chourashiya, J.Y. Patil, S.H. Pawar, L.D. Jadhav, Studies on structural,

morphological and electrical properties of Ce1-xGdxO2-(x/2), Mater. Chem. Phys. 109 (2008) 39–44.

[19] S. Zha, C. Xia, G. Meng, Effect of Gd (Sm) doping on properties of ceria electrolyte for solid oxide fuel cells, J. Power Sources. 115 (2003) 44–48.

[20] Z. Tianshu, P. Hing, H. Huang, J. Kilner, Ionic conductivity in the CeO2–Gd2O3 system (0.05≤Gd/Ce≤0.4) prepared by oxalate coprecipitation, Solid State Ionics. 148 (2002) 567.

[21] V. V. Ivanov, V.R. Khrustov, Y.A. Kotov, A.I. Medvedev, A.M. Murzakaev, S.N. Shkerin, A. V. Nikonov, Conductivity and structure features of Ce1-xGdxO2-δ solid electrolytes fabricated by compaction and sintering of weakly agglomerated nanopowders, J. Eur. Ceram. Soc. 27 (2007) 1041–1046.

[22] Y.P. Fu, Y.S. Chang, S.B. Wen, Microwave-induced combustion synthesis and electrical conductivity of Ce1-xGdxO2-1/2x ceramics, Mater. Res. Bull. 41 (2006) 2260–2267.

[23] B.C.H. Steele, Appraisal of Ce1-yGdyO2-y/2 electrolytes for IT-SOFC operation at 500C, Solid State Ionics. 129 (2000) 95–110.

[24] V. V Kharton, F.M. Figueiredo, N. L, E.N. Naumovic, A. V Kovalevsky, A.A. Yaremchenko, A.P. Viskup, A. Carneiro, F.M. Marques, J.D. Frade, Ceria-based materials for solid oxide fuel cells, J. Mater. Sci. 36 (2001) 1105–1117.

[25] N. Jordan, W. Assenmacher, S. Uhlenbruck, V.A.C. Haanappel, H.P. Buchkremer, D. Stover, W. Mader, Ce0.8Gd0.2O2-δ protecting layers manufactured by physical vapor deposition for IT-SOFC, Solid State Ionics. 179 (2008) 919–923.

[26] J.-J. Choi, D.-S. Park, B.-G. Seong, H.-Y. Bae, Low-temperature preparation of dense (Gd,Ce)O2−δ–Gd2O3 composite buffer layer by aerosol deposition for YSZ electrolyte-based SOFC, Int. J. Hydrogen Energy. 37 (2012) 9809–9815.

[27] T. Ishihara, Development of New Fast Oxide Ion Conductor and Application for Intermediate Temperature Solid Oxide Fuel Cells, Bull. Chem. Soc. Jpn. 79 (2006) 1155–1166.

[28] H. Yahiro, Electrical properties and reducibilities of ceria-rare earth oxide systems and

their application to solid oxide fuel cell, Solid State Ionics. 36 (1989) 71–75.

[29] M. Mogensen, N.M. Sammes, G.A. Tompsett, Physical, chemical and electrochemical properties of pure and doped ceria, Solid State Ionics. 129 (2000) 63–94.

[30] B. Dalslet, P. Blennow, P.V. Hendriksen, N. Bonanos, D. Lybye, M. Mogensen, Assessment of doped ceria as electrolyte, J. Solid State Electrochem. 10 (2006) 547–561.

[31] T. Inoue, T. Setoguchi, K. Eguchi, H. Arai, Study of a Solid Oxide Fuel-Cell with a Ceria-Based Solid Electrolyte, Solid State Ionics. 35 (1989) 285–291.

[32] S. Uhlenbruck, N. Jordan, J.M. Serra, H.P. Buchkremer, D. Stöver, Application of electrolyte layers for solid oxide fuel cells by electron beam evaporation, Solid State Ionics. 181 (2010) 447–452.

[33] J. Stevenson, T.R. Armstrong, L.R. Pederson, J. Li, C.A. Lewinsohn, S. Baskaran, Effect of A-site cation nonstoichiometry on the properties of doped lanthanum gallate, Solid State Ionics. 113–115 (1998) 571–583.

[34] K. Yamaji, T. Horita, M. Ishikawa, N. Sakai, H. Yokokawa, Chemical stability of the La0.9Sr0.1Ga0.8Mg0.2O2.85 electrolyte in a reducing atmosphere, Solid State Ionics. 121 (1999) 217–224.

[35] S. Atkinson, S. Barnett, R.J. Gorte, J.T.S. Irvine, A.J. McEvoy, M. Mogensen, S.C. Singhal, J.M. Vohs, Advanced anodes for high-temperature fuel cells., Nat. Mater. 3 (2004) 17–27.

[36] R.N. Basu, Materials for Solid Oxide Fuel Cells, in: S. Basu (Ed.), Recent Trends Fuel Cell Sci. Technol., Anamaya Publishers, New Delhi, India, 2010: pp. 660–674.

[37] A. Chroneos, B. Yildiz, A. Tarancón, D. Parfitt, J.A. Kilner, Oxygen diffusion in solid oxide fuel cell cathode and electrolyte materials: mechanistic insights from atomistic simulations, Energy Environ. Sci. 4 (2011) 2774.

[38] L.W. Tai, M.M. Nasrallah, H.U. Anderson, D.M. Sparlin, S.R. Sehlin, Structure and electrical properties of La1-xSxCo1-yFeyO3. Part 2. The system La1-xSrxCo0.2Fe0.803, Solid State Ionics. 76 (1995) 273–283.

[39] A. Petric, P. Huang, F. Tietz, Evaluation of La-Sr-Co-Fe-O perovskites for solid oxide

fuel cells and gas separation membranes, Solid State Ionics. 135 (2000) 719–725.

[40] Z. Gao, L.V. Mogni, E.C. Miller, J.G. Railsback, S.A. Barnett, A Perspective On Low-Temperature Solid Oxide Fuel Cells, Energy Environ. Sci. 9 (2016) 1602–1644.

[41] S.J. Cooper, M. Kishimoto, F. Tariq, R.S. Bradley, A.J. Marquis, N.P. Brandon, J.A. Kilner, P.R. Shearing, Microstructural Analysis of an LSCF Cathode Using In Situ Tomography and Simulation, ECS Trans. 57 (2013) 2671–2678.

[42] J. Laurencin, R. Quey, G. Delette, H. Suhonen, P. Cloetens, P. Bleuet, Characterisation of Solid Oxide Fuel Cell Ni–8YSZ substrate by synchrotron X-ray nano-tomography: from 3D reconstruction to microstructure quantification, J. Power Sources. 198 (2012) 182–189.

[43] J. Joos, T. Carraro, A. Weber, E. Ivers-Tiffée, Reconstruction of porous electrodes by FIB/SEM for detailed microstructure modeling, J. Power Sources. 196 (2011) 7302–7307.

[44] J.R. Wilson, W. Kobsiriphat, R. Mendoza, H.Y. Chen, J.M. Hiller, D.J. Miller, K. Thornton, P.W. Voorhees, S. Adler, S.A. Barnett, Three-dimensional reconstruction of a solid-oxide fuel-cell anode., Nat. Mater. 5 (2006) 541–4.

[45] Z. Lei, Q. Zhu, L. Zhao, Low temperature processing of interlayer-free La0.6Sr0.4Co0.2Fe0.8O3-δ cathodes for intermediate temperature solid oxide fuel cells, J. Power Sources. 161 (2006) 1169–1175.

[46] V.A.C. Haanappel, J. Mertens, D. Rutenbeck, C. Tropartz, W. Herzhof, D. Sebold, F. Tietz, Optimisation of processing and microstructural parameters of LSM cathodes to improve the electrochemical performance of anode-supported SOFCs, J. Power Sources. 141 (2005) 216–226.

[47] B. Völker, R.M. McMeeking, Impact of particle size ratio and volume fraction on effective material parameters and performance in solid oxide fuel cell electrodes, J. Power Sources. 215 (2012) 199–215.

[48] R. Suwanwarangkul, E. Croiset, M.W. Fowler, P.L. Douglas, E. Entchev, M.A. Douglas, Performance comparison of Fick's, dusty-gas and Stefan–Maxwell models to predict the concentration overpotential of a SOFC anode, J. Power Sources. 122 (2003) 9–18.

[49] B. Kenney, M. Valdmanis, C. Baker, J.G.G. Pharoah, K. Karan, Computation of TPB length, surface area and pore size from numerical reconstruction of composite solid oxide fuel cell electrodes, J. Power Sources. 189 (2009) 1051–1059.

[50] J.E. Mortensen, M. Søgaard, T. Jacobsen, Analytical, 1-Dimensional Impedance Model of a Composite Solid Oxide Fuel Cell Cathode, J. Electrochem. Soc. 161 (2014) F161–F175.

[51] B. Fan, J. Yan, X. Yan, The ionic conductivity, thermal expansion behavior, and chemical compatibility of La0.54Sr0.44Co0.2Fe0.8O3-δ as SOFC cathode material, Solid State Sci. 13 (2011) 1835–1839.

[52] V. Dusastre, J.A. Kilner, Optimization of composite cathodes for intermediate temperature SOFC applications, Solid State Ionics. 126 (1999) 163–174.

[53] A. Esquirol, J. Kilner, N. Brandon, Oxygen transport in La0.6Sr0.4Co0.2Fe0.8O3-δ/Ce0.8Ge0.2O2-x composite cathode for IT-SOFCs, Solid State Ionics. 175 (2004) 63–67.

[54] E. Perry Murray, M.J. Sever, S.A. Barnett, Electrochemical performance of (La,Sr)(Co,Fe)O3 –(Ce,Gd)O3 composite cathodes, Solid State Ionics. 148 (2002) 27–34.

[55] D. Beckel, U. Muecke, T. Gyger, G. Florey, A. Infortuna, L. Gauckler, Electrochemical performance of LSCF based thin film cathodes prepared by spray pyrolysis, Solid State Ionics. 178 (2007) 407–415.

[56] H.J. Hwang, J.-W.J.W. Moon, S. Lee, E.A. Lee, Electrochemical performance of LSCF-based composite cathodes for intermediate temperature SOFCs, J. Power Sources. 145 (2005) 243–248.

[57] Y. Leng, S. Chan, Q. Liu, Development of LSCF–GDC composite cathodes for low-temperature solid oxide fuel cells with thin film GDC electrolyte, Int. J. Hydrogen Energy. 33 (2008) 3808–3817.

[58] W. Wang, M. Mogensen, High-performance lanthanum-ferrite-based cathode for SOFC, Solid State Ionics. 176 (2005) 457–462.

[59] D. Marinha, C. Rossignol, E. Djurado, Influence of electrospraying parameters on the

microstructure of La0.6Sr0.4Co0.2F0.8O3−δ films for SOFCs, J. Solid State Chem. 182 (2009) 1742–1748.

[60] S. Guo, H. Wu, F. Puleo, L. Liotta, B-Site Metal (Pd, Pt, Ag, Cu, Zn, Ni) Promoted La1−xSrxCo1−yFeyO3–δ PerovskiACte Oxides as Cathodes for IT-SOFCs, Catalysts. 5 (2015) 366–391.

[61] J. Moon, H. Hwang, M. Awano, K. Maeda, Preparation of NiO – YSZ tubular support with radially aligned pore channels, Mater. Lett. 57 (2003) 1428–1434.

[62] R.E. Williford, L. a. Chick, G.D. Maupin, S.P. Simner, J.W. Stevenson, Diffusion Limitations in the Porous Anodes of SOFCs, J. Electrochem. Soc. Electrochem. Soc. 150 (2003) A1067.

[63] J.C. Ruiz-Morales, D. Marrero-López, M. Gálvez-Sánchez, J. Canales-Vázquez, C. Savaniu, S.N. Savvin, Engineering of materials for solid oxide fuel cells and other energy and environmental applications, Energy Environ. Sci. 3 (2010) 1670–1681.

[64] A.Z. Lichtner, D. Jauffrès, D. Roussel, F. Charlot, C.L. Martin, R.K. Bordia, Dispersion, connectivity and tortuosity of hierarchical porosity composite SOFC cathodes prepared by freeze-casting, J. Eur. Ceram. Soc. 35 (2015) 585–595.

[65] T. Li, Z. Wu, K. Li, Single-step fabrication and characterisations of triple-layer ceramic hollow fibres for micro-tubular solid oxide fuel cells (SOFCs), J. Memb. Sci. 449 (2014) 1–8.

[66] N. Droushiotis, A. Torabi, M.H.D. Othman, T.H. Etsell, G.H. Kelsall, Effects of lanthanum strontium cobalt ferrite (LSCF) cathode properties on hollow fibre micro-tubular SOFC performances, J. Appl. Electrochem. 42 (2012) 517–526.

[67] M. Lejeune, T. Chartier, C. Dossou-Yovo, R. Noguera, Ink-jet printing of ceramic micro-pillar arrays, J. Eur. Ceram. Soc. 29 (2009) 905–911.

[68] C.-C. Yu, J.D. Baek, C.-H. Su, L. Fan, J. Wei, Y.-C. Liao, P.-C. Su, Inkjet-printed Porous Silver Thin Film as a Cathode for Low-Temperature Solid Oxide Fuel Cell, ACS Appl. Mater. Interfaces. 8 (2016) 10343.

[69] C.S. Hsu, B.H. Hwang, Microstructure and Properties of the La0.6Sr0.4Co0.2Fe0.8O3 Cathodes Prepared by Electrostatic-Assisted Ultrasonic Spray Pyrolysis Method, J.

Electrochem. Soc. 153 (2006) A1478.

[70] A. Jaworek, A.T. Sobczyk, Electrospraying route to nanotechnology: An overview, J. Electrostat. 66 (2008) 197–219.

[71] M. Beidaghi, Z. Wang, L. Gu, C. Wang, Electrostatic spray deposition of graphene nanoplatelets for high-power thin-film supercapacitor electrodes, J. Solid State Electrochem. 16 (2012) 3341–3348.

[72] C.-S. Hsu, B.-H. Hwang, Y. Xie, X. Zhang, Enhancement of Solid Oxide Fuel Cell Performance by La0.6Sr0.4Co0.2Fe0.83−δ Double-Layer Cathode, J. Electrochem. Soc. 155 (2008) B1240–B1243.

[73] T. Kim, A. Canlier, G. Kim, J. Choi, M. Park, S. Min, J. Han, Electrostatic Spray Deposition of Highly Transparent Silver Nanowire Electrode on Flexible Substrate Electrostatic Spray Deposition of Highly Transparent Silver Nanowire Electrode on Flexible Substrate, Appl. Mater. Interfaces. 5 (2013) 788–794.

[74] H. Yoon, J.H. Woo, Y.M. Ra, S.S. Yoon, H.Y. Kim, S. Ahn, J.H. Yun, J. Gwak, K. Yoon, S.C. James, Electrostatic Spray Deposition of Copper–Indium Thin Films, Aerosol Sci. Technol. 45 (2011) 1448–1455.

[75] C.H. Chen, E.M. Kelder, M.J.G. Jak, J. Schoonman, Electrostatic spray deposition of thin layers of cathode materials for lithium battery, Solid State Ionics. 86–88 (1996) 1301–1306.

[76] J. Schoonman, Nanostructured materials in solid state ionics, Solid State Ionics. 135 (2000) 5–19.

[77] I. Taniguchi, R.C. van Landschoot, J. Schoonman, Electrostatic spray deposition of Gd0.1Ce0.9O1.95 and La0.9Sr0.1Ga0.8Mg0.2O2.87 thin films, Solid State Ionics. 160 (2003) 271–279.

[78] G. Constantin, C. Rossignol, J.P. Barnes, E. Djurado, Interface stability of thin, dense CGO film coating on YSZ for solid oxide fuel cells, Solid State Ionics. 235 (2013) 36–41.

[79] D. Marinha, L. Dessemond, E. Djurado, Comprehensive Review of Current Developments in IT-SOFCs, Curr. Inorg. Chem. 3 (2013) 2–22.

[80] R.K. Sharma, M. Burriel, L. Dessemond, V. Martin, J.-M. Bassat, E. Djurado, An innovative architectural design to enhance the electrochemical performance of La2NiO4+δ cathodes for solid oxide fuel cell applications, J. Power Sources. 316 (2016) 17–28.

[81] R. Neagu, D. Perednis, A. Princivalle, E. Djurado, Influence of the process parameters on the ESD synthesis of thin film YSZ electrolytes, Solid State Ionics. 177 (2006) 1981–1984.

[82] R.K. Sharma, M. Burriel, L. Dessemond, J. Bassat, E. Djurado, La n+1 Ni n O 3n+1 (n =2 and 3) phases and composites for solid oxide fuel cell cathodes : Facile synthesis and electrochemical properties, J. Power Sources. 325 (2016) 337–345.

[83] D. Marinha, L. Dessemond, J.S. Cronin, J.R. Wilson, S.A. Barnett, E. Djurado, Microstructural 3D Reconstruction and Performance Evaluation of LSCF Cathodes Obtained by Electrostatic Spray Deposition, Chem. Mater. 23 (2011) 5340–5348.

[84] E. Djurado, A. Salaün, G. Mignardi, A. Rolle, M. Burriel, S. Daviero-Minaud, R.N. Vannier, Electrostatic spray deposition of Ca3Co4O9+δ layers to be used as cathode materials for IT-SOFC, Solid State Ionics. 286 (2016) 102–110.

[85] D. Marinha, PhD Thesis, Institute Polytechnique de Grenoble, 2010.

[86] J. Sar, PhD Thesis, Interfaces et durabilité d'électrodes avancées pour l'énergie (IT-SOFC et SOEC), Universite Grenoble Alpes, 2014.

[87] J. Sar, F. Charlot, A. Almeida, L. Dessemond, E. Djurado, Coral Microstructure of Graded CGO/LSCF Oxygen Electrode by Electrostatic Spray Deposition for Energy (IT-SOFC, SOEC), Fuel Cells. 14 (2014) 357–363.

[88] N.T. Hart, N.P. Brandon, M.J. Day, N. Lapena-Rey, Functionally graded composite cathodes for solid oxide fuel cells, J. Power Sources. 106 (2002) 42–50.

[89] J. Deseure, Y. Bultel, L.C.R. Schneider, L. Dessemond, C. Martin, Micromodeling of Functionally Graded SOFC Cathodes, J. Electrochem. Soc. 154 (2007) B1012–B1016.

[90] M. Liu, W. Zhinglin, Significance of interfaces in solid-state cells with porous electrodes of mixed ionic–electronic conductors, Solid State Ionics. 107 (1998) 105–110.

[91] D. Marinha, J. Hayd, L. Dessemond, E. Ivers-Tiffée, E. Djurado, Performance of

(La,Sr)(Co,Fe)O3−x double-layer cathode films for intermediate temperature solid oxide fuel cell, J. Power Sources. 196 (2011) 5084–5090.

[92] S. Adler, J. Lane, B. Steele, Electrode Kinetics of Porous Mixed-Conducting Oxygen Electrodes, J. Electrochem. Soc. 143 (1996) 3554–3564.

[93] J. Deseure, L. Dessemond, Y. Bultel, E. Siebert, Modelling of a SOFC graded cathode, J. Eur. Ceram. Soc. 25 (2005) 2673–2676.

[94] J. Deseure, Y. Bultel, L. Dessemond, E. Siebert, P. Ozil, Modelling the porous cathode of a SOFC: Oxygen reduction mechanism effect, J. Appl. Electrochem. 37 (2007) 129–136.

[95] A. Abbaspour, K. Nandakumar, J. Luo, K.T. Chuang, A novel approach to study the structure versus performance relationship of SOFC electrodes, J. Power Sources. 161 (2006) 965–970.

[96] J. Fleig, On the width of the electrochemically active region in mixed conducting solid oxide fuel cell cathodes, J. Power Sources. 105 (2002) 228–238.

[97] A. Ali, X. Wen, K. Nandakumar, J. Luo, K.T. Chuang, Geometrical modeling of microstructure of solid oxide fuel cell composite electrodes, J. Power Sources. 185 (2008) 961–966.

[98] Q. Cai, C.S. Adjiman, N.P. Brandon, Modelling the 3D microstructure and performance of solid oxide fuel cell electrodes: Computational parameters, Electrochim. Acta. 56 (2011) 5804–5814.

[99] C. Kreller, M. Drake, S. Adler, H. Chen, Modeling SOFC cathodes based on 3-D representations of electrode microstructure, ECS Trans. 35 (2011) 815–822.

[100] A. Häffelin, J. Joos, M. Ender, A. Weber, E. Ivers-Tiffee, Time-Dependent 3D Impedance Model of Mixed-Conducting Solid Oxide Fuel Cell Cathodes, J. Electrochem. Soc. 160 (2013) F867–F876.

[101] S. Sunde, Simulations of composite electrodes in fuel cells, J. Electroceramics. 5 (2000) 153–182.

[102] V. Yurkiv, R. Costa, Z. Ilhan, A. Ansar, W.G. Bessler, Impedance of the Surface Double Layer of LSCF/CGO Composite Cathodes: An Elementary Kinetic Model, J.

Electrochem. Soc. 161 (2014) F480–F492.

[103] J.D. Nicholas, L. Wang, A. V Call, S.A. Barnett, Use of the Simple Infiltrated Microstructure Polarization Loss Estimation (SIMPLE) model to describe the performance of nano-composite solid oxide fuel cell cathodes., Phys. Chem. Chem. Phys. 14 (2012) 15379–92.

[104] M. Gong, R.S. Gemmen, D.S. Mebane, K. Gerdes, X. Liu, Simulation of Surface-Potential Driven ORR Kinetics on SOFC Cathode with Parallel Reaction Pathways, J. Electrochem. Soc. 161 (2014) F344–F353.

[105] A. Enrico, P. Costamagna, Model of infiltrated La1-xSrxCo1-yFeyO3-δ cathodes for intermediate temperature solid oxide fuel cells, J. Power Sources. 272 (2014) 1106–1121.

[106] A.M. Svensson, S. Sunde, K. Nisancioglu, Mathematical Modeling of Oxygen Exchange and Transport in Air-Perovskite-Yttria-Stabilized Zirconia Interface Regions. I. Reduction of Intermediately Adsorbed Oxygen, J. Electrochem. Soc. 145 (1998) 2719–2732.

[107] A.M. Svensson, S. Sunde, K. Nisancioglu, Mathematical Modeling of Oxygen Exchange and Transport in Air-Perovskite-Yttria-Stabilized Zirconia Interface Regions. II Direct exchange of Oxygen vacancies, J. Electrochem. Soc. 145 (1998) 1390–1400.

[108] G.W. Coffey, L.R. Pederson, P.C. Rieke, Competition Between Bulk and Surface Pathways in Mixed Ionic Electronic Conducting Oxygen Electrodes, J. Electrochem. Soc. 150 (2003) A1139.

[109] S.B. Adler, X.Y. Chen, J.R. Wilson, Mechanisms and rate laws for oxygen exchange on mixed-conducting oxide surfaces, J. Catal. 245 (2007) 91–109.

[110] J. Deseure, Y. Bultel, L. Dessemond, E. Siebert, Modelling of dc and ac responses of a planar mixed conducting oxygen electrode, Solid State Ionics. 176 (2005) 235–244.

[111] J. Fleig, R. Merkle, J. Maier, The p(O2) dependence of oxygen surface coverage and exchange current density of mixed conducting oxide electrodes: model considerations., Phys. Chem. Chem. Phys. 9 (2007) 2713–2723.

[112] L.C.R. Schneider, C.L. Martin, Y. Bultel, D. Bouvard, E. Siebert, Discrete modelling of the electrochemical performance of SOFC electrodes, Electrochim. Acta. 52 (2006)

314–324.

[113] D. Chen, Z. Lin, H. Zhu, R.J. Kee, Percolation theory to predict effective properties of solid oxide fuel-cell composite electrodes, J. Power Sources. 191 (2009) 240–252.

[114] B. Rüger, A. Weber, E. Ivers-Tiffée, 3D-Modelling and Performance Evaluation of Mixed Conducting (MIEC) Cathodes, ECS Trans. 7 (2007) 2065–2074.

[115] T. Carraro, J. Joos, B. Rüger, A. Weber, E. Ivers-Tiffée, 3D finite element model for reconstructed mixed-conducting cathodes: I. Performance quantification, Electrochim. Acta. 77 (2012) 315–323.

[116] B. Rüger, J. Joos, A. Weber, T. Carraro, E. Ivers-Tiffée, 3D Electrode Microstructure Reconstruction and Modelling, ECS Trans. 25 (2009) 1211–1220.

[117] H. Yokokawa, H. Tu, B. Iwanschitz, A. Mai, Fundamental mechanisms limiting solid oxide fuel cell durability, J. Power Sources. 182 (2008) 400–412.

[118] J. Kondoh, S. Kikuchi, Y. Tomii, Y. Ito, Effect of Aging on Yttria-Stabilizecl Zirconia I. A study of its Electrochemical Properties, J. Electrochem. Soc. 145 (1998) 1527–1536.

[119] J. Kondoh, S. Kikuchi, Y. Tomii, Y. Ito, Effect of Aging on Yttria-Stabilizecl Zirconia II. A study of the Effect of Microstructure on Conductivity, J. Electrochem. Soc. 145 (1998) 1536–1549.

[120] J. Kondoh, S. Kikuchi, Y. Tomii, Y. Ito, Effect of Aging on Yttria-Stabilizecl Zirconia III. A study of the Effect of Local Structures on Conductivity, J. Electrochem. Soc. 145 (1998) 1550–1560.

[121] F.T. Ciacchi, S.P.S. Badwal, The system Y2O3-Sc2O3-ZrO2: Phase stability and ionic conductivity studies, J. Eur. Ceram. Soc. 7 (1991) 197–206.

[122] O. Yamamoto, Y. Takeda, R. Kanno, K. Kohno, Electrical conductivity of tetragonal stabilized zirconia, J. Mater. Sci. 25 (1990) 2805–2808.

[123] S.P.S. Badwal, Yttria Tetragonal Zirconia Polycrystalline Electrolytes for Solid State Electrochemical Cells, Appl. Phys. A Solids Surfaces. 50 (1990) 449–462.

[124] C.C. Appel, N. Bonanos, A. Horsewell, S. Linderoth, Ageing behaviour of zirconia stabilized by yattria and manganase oxide, J. Mater. Sci. 36 (2001) 4493–4501.

[125] T.S. Zhang, J. Ma, L.B. Kong, P. Hing, S.H. Chan, J.A. Kilner, High-Temperature Aging Behavior of Gd-Doped Ceria, Electrochem. Solid-State Lett. 7 (2004) J13.

[126] T.S. Zhang, J. Ma, L.B. Kong, S.H. Chan, J.A. Kilner, Aging behavior and ionic conductivity of ceria-based ceramics: A comparative study, Solid State Ionics. 170 (2004) 209–217.

[127] A. Atkinson, Chemically-induced stresses in gadolinium-doped ceria solid oxide fuel cell electrolytes, Solid State Ionics. 95 (1997) 249–258.

[128] A. Tsoga, A. Naoumidis, D. Stöver, Total electrical conductivity and defect structure of ZrO2-CeO2-Y2O3-Gd2O3 solid solutions, Solid State Ionics. 135 (2000) 403–409.

[129] L. Li, O. Van Der Biest, P.L. Wang, J. Vleugels, W.W. Chen, S.G. Huang, Estimation of the phase diagram for the ZrO2–Y2O3–CeO2 system, J. Eur. Ceram. Soc. 21 (2001) 2903–2910.

[130] D. Fouquet, A.C. Müller, A. Weber, E. Ivers-Tiffée, Kinetics of oxidation and reduction of Ni/YSZ cermets, Ionics (Kiel). 9 (2003) 103–108.

[131] T. Iwata, Characterization of Ni-YSZ Anode Degradation for Substrate-Type Solid Oxide Fuel Cells, J. Electrochem. Soc. 143 (1996) 1521–1525.

[132] D. Simwonis, F. Tietz, D. Stover, Nickel coarsening in annealed Ni / 8YSZ anode substrates for solid oxide fuel cells, Solid State Ionics. 132 (2000) 241–251.

[133] A. Hagen, R. Barfod, P.V. Hendriksen, Y.-L. Liu, S. Ramousse, Degradation of Anode Supported SOFCs as a Function of Temperature and Current Load, J. Electrochem. Soc. 153 (2006) A1165–A1171.

[134] M. Gong, X. Liu, J. Trembly, C. Johnson, Sulfur-tolerant anode materials for solid oxide fuel cell application, J. Power Sources. 168 (2007) 289–298.

[135] Y. Matsuzaki, I. Yasuda, The poisoning effect of sulfur-containing impurity gas on a SOFC anode: Part I. Dependence on temperature, time, and impurity concentration, Solid State Ionics. 132 (2000) 261–269.

[136] K. T, C. Chung, P.H. Larsen, M. Mogensen, The Mechanism Behind Redox Instability of Anodes in High-Temperature SOFCs, J. Electrochem. Soc. 152 (2005) A2186.

[137] D. Waldbillig, A. Wood, D.G. Ivey, Electrochemical and microstructural characterization of the redox tolerance of solid oxide fuel cell anodes, J. Power Sources. 145 (2005) 206–215.

[138] A. Mai, V.A.C. Haanappel, S. Uhlenbruck, F. Tietz, D. Stöver, Ferrite-based perovskites as cathode materials for anode-supported solid oxide fuel cells: Part I. Variation of composition, Solid State Ionics. 176 (2005) 1341–1350.

[139] M. Shah, P.W. Voorhees, S.A. Barnett, Time-dependent performance changes in LSCF-infiltrated SOFC cathodes: The role of nano-particle coarsening, Solid State Ionics. 187 (2011) 64–67.

[140] M. Shah, G.A. Hughes, P.W. Voorhees, S.A. Barnett, Stability and Performance of LSCF-infiltrated SOFC cathodes: Effect of Nano-Particle Coarsening, ECS Trans. 35 (2011) 2045–2053.

[141] S.P. Simner, M.D. Anderson, M.H. Engelhard, J.W. Stevenson, Degradation Mechanisms of La–Sr–Co–Fe–O3 SOFC Cathodes, Electrochem. Solid-State Lett. 9 (2006) A478–A481.

[142] Y. Gong, R.L. Patel, X. Liang, D. Palacio, X. Song, J.B. Goodenough, K. Huang, Atomic Layer Deposition Functionalized Composite SOFC cathode LSCF-CGO: Enhanced Long-Term Stability, Chem. Mater. 25 (2013) 4224–4231.

[143] S. Uhlenbruck, T. Moskalewicz, N. Jordan, H.J. Penkalla, H.P. Buchkremer, Element interdiffusion at electrolyte-cathode interfaces in ceramic high-temperature fuel cells, Solid State Ionics. 180 (2009) 418–423.

[144] R. Knibbe, J. Hjelm, M. Menon, N. Pryds, M. Søgaard, H.J. Wang, K. Neufeld, Cathode-electrolyte interfaces with CGO barrier layers in SOFC, J. Am. Ceram. Soc. 93 (2010) 2877–2883.

[145] Y. Du, M. Yashima, T. Koura, M. Kakihana, M. Yoshimura, Measurement and calculations of the ZrO2-CeO2-LaO1.5 phase diagram, Calphad. 20 (1996) 95–108.

[146] A. Martinez-Amesti, A. Larranaga, L.M. Rodriguez-Martinez, A.T. Aguayo, J.L. Pizarro, M.L. No, A. Laresgoiti, M.I. Arriortua, Reactivity between La(Sr)FeO3 cathode, doped CeO2 interlayer and yttria-stabilized zirconia electrolyte for solid oxide fuel cell

applications, J. Power Sources. 185 (2008) 401–410.

[147] W.-R. Kiebach, W. Zhang, W. Zhang, M. Chen, K. Norrman, H.-J. Wang, J.R. Bowen, R. Barford, P.V. Hendriksen, Stability of LSCF/CGO cathodes during sintering and solid oxide fuel cell operation, J. Power Sources. 283 (2015) 151–161.

[148] F. Tonus, S.J. Skinner, In-situ neutron diffraction study of cathode/electrolyte interactions under electrical load and elevated temperature, Solid State Sci. 55 (2016) 88–92.

[149] J. Druce, J.A. Kilner, Composite Ceramic Membranes for Oxygen Separation in Carbon Capture and Storage Systems, ECS Trans. 16 (2009) 327–336.

[150] N. Ni, S.J. Cooper, R. Williams, N. Kemen, D.W. McComb, S.J. Skinner, Degradation of (La0.6Sr0.4)0.95(Co0.2Fe0.8)O3−δ Solid Oxide Fuel Cell Cathodes at the Nanometer Scale and below, ACS Appl. Mater. Interfaces. 8 (2016) 17360–17370.

[151] X. Chen, C. Jin, L. Zhao, L. Zhang, C. Guan, L. Wang, Y.F. Song, C.C. Wang, J.Q. Wang, S.P. Jiang, Study on the Cr deposition and poisoning phenomenon at (La0.6Sr0.4)(Co0.2Fe0.8)O3-δ electrode of solid oxide fuel cells by transmission X-ray microscopy, Int. J. Hydrogen Energy. 39 (2014) 15728–15734.

[152] A.M. Ganan-Calvo, J. Davila, A. Barrero, Current and droplet size in the electrospraying of liquids scaling laws, J. Aerosol Sci. 28 (1997) 249–275.

[153] D. Marinha, L. Dessemond, E. Djurado, Microstructure-Electrical Properties of Original LSCF Films Deposited by ESD for IT-SOFCs, ECS Trans. 28 (2010) 93–103.

[154] D.R. Lide, CRC Handbook of Chemistry and Physics, 88th ed., Lavosier, 2007.

[155] J. Rodríguez-Carvajal, Recent developments of the program FULLPROF, Comm. Powder Diffr. (IUCr). Newsl. 26 (2001) 12–19.

[156] Geodict User Guide, Porodic. Tutor. Doc. (2013).

[157] J. Joos, M. Ender, T. Carraro, A. Weber, E. Ivers-Tiffée, Representative volume element size for accurate solid oxide fuel cell cathode reconstructions from focused ion beam tomography data, Electrochim. Acta. 82 (2012) 268–276.

[158] Felix H. Kim, D. Penumadu, V.P. Schulz, A. Wiegmann, Pore Size Distribution and Soil

Water Suction Curve from Micro-tomography Measurements and Real 3-D Digital Microstructure of a Compacted Granular Media by Using Direct Numerical Simulation Technique, in: L. Laloui, A. Ferrari (Eds.), Multiphysical Test. Soils Shales, 2013: pp. 171–176.

[159] A. Wiegmann, A. Zemitis, EJ-HEAT: A Fast Explicit Jump Harmonic Averaging Solver for the Effective Heat Conductivity of Composite Materials, Berichte Des Fraunhofer ITWM. 94 (2006).

[160] K. Matsuzaki, N. Shikazono, N. Kasagi, Three-dimensional numerical analysis of mixed ionic and electronic conducting cathode reconstructed by focused ion beam scanning electron microscope, J. Power Sources. 196 (2011) 3073–3082.

[161] S. Georges, Etude de nouveaux conducteurs par ions O2- derives de La2Mo2O9, Universite du Maine, 2003.

[162] E. Lay-Grindler, J. Laurencin, J. Villanova, P. Cloetens, P. Bleuet, A. Mansuy, J. Mougin, G. Delette, Degradation study by 3D reconstruction of a nickel-yttria stabilized zirconia cathode after high temperature steamAC electrolysis operation, J. Power Sources. 269 (2014) 927–936.

[163] J. Szász, F. Wankmüller, V. Wilde, H. Störmer, D. Gerthsen, N.H. Menzler, E. Ivers-Tiffée, High-Performance Cathode/Electrolyte Interfaces for SOFC, ECS Trans. 68 (2015) 763–771.

[164] J. Sar, O. Celikbilek, J. Villanova, L. Dessemond, C.L. Martin, E. Djurado, Three dimensional analysis of Ce0.9Gd0.1O1.95–La0.6Sr0.4Co0.2Fe0.8O3−δ oxygen electrode for solid oxide cells, J. Eur. Ceram. Soc. 35 (2015) 2–10.

[165] Özden Çelikbilek, D. Jauffrès, E. Siebert, L. Dessemond, M. Burriel, C.L. Martin, E. Djurado, Rational design of hierarchically nanostructured electrodes for solid oxide fuel cells, J. Power Sources. 333 (2016) 72–82.

[166] J.A. Kilner, M. Burriel, Materials for Intermediate-Temperature Solid-Oxide Fuel Cells, Annu. Rev. Mater. Res. 44 (2014) 365–393.

[167] J. Fleig, J. Maier, The polarization of mixed conducting SOFC cathodes: Effects of surface reaction coefficient, ionic conductivity and geometry, J. Eur. Ceram. Soc. 24

(2004) 1343–1347.

[168] D. Gostovic, J.R. Smith, D.P. Kundinger, K.S. Jones, E.D. Wachsman, Three-Dimensional Reconstruction of Porous LSCF Cathodes, Electrochem. Solid-State Lett. 10 (2007) B214–B217.

[169] A.L. Shaula, V. V. Kharton, F.M.B. Marques, A. V. Kovalevsky, A.P. Viskup, E.N. Naumovich, Oxygen permeability of mixed-conducting composite membranes: effects of phase interaction, J. Solid State Electrochem. 10 (2005) 28–40.

[170] J. Druce, J.A. Kilner, Improvement of Oxygen Surface Exchange Kinetics for CGO with Surface Treatment, J. Electrochem. Soc. 161 (2013) F99–F104.

[171] M. Izuki, M.R. Brito, K. Yamaji, H. Kishimoto, D.H. Cho, T. Shimonosono, T. Horita, H. Yokokawa, Interfacial stability and cation diffusion across the LSCF/GDC interface, J. Power Sources. 196 (2011) 7232–7236.

[172] B.F. Angoua, E.B. Slamovich, Single solution spray pyrolysis of La0.6Sr0.4Co0.2Fe0.8O3−δ–Ce0.8Gd0.2O1.9 (LSCF–CGO) thin film cathodes, Solid State Ionics. 212 (2012) 10–17.

[173] J.H. Joo, G.S. Park, C.-Y. Yoo, J.H. Yu, Contribution of the surface exchange kinetics to the oxygen transport properties in Gd0.1Ce0.9O2−δ–La0.6Sr0.4Co0.2Fe0.8O3−δ dual-phase membrane, Solid State Ionics. 253 (2013) 64–69.

[174] S.P. Yoon, S.W. Nam, S.G. Kim, S.A. Hong, S.H. Hyun, Characteristics of cathodic polarization at Pt/YSZ interface without the effect of electrode microstructure, J. Power Sources. 115 (2003) 27–34.

[175] D. Marinha, L. Dessemond, E. Djurado, Electrochemical investigation of oxygen reduction reaction on La0.6Sr0.4Co0.2Fe0.8O3−δ cathodes deposited by Electrostatic Spray Deposition, J. Power Sources. 197 (2012) 80–87.

[176] B.C.H. Steele, Appraisal of Ce1-y GdyO2-y/2 electrolytes for IT-SOFC operation at 500C, Solid State Ionics. 129 (2000) 95–110.

[177] B.A. Boukamp, H.J.M. Bouwmeester, Interpretation of the Gerischer impedance in solid state ionics, Solid State Ionics. 157 (2003) 29–33.

[178] V.C. Kournoutis, F. Tietz, S. Bebelis, AC Impedance Characterisation of a

La0.8Sr0.2Co0.2Fe0.8O3-δ Electrode, Fuel Cells. 9 (2009) 852–860.

[179] F.S. Baumann, J. Fleig, H. Habermeier, J. Maier, Impedance spectroscopic study on well-defined (La,Sr)(Co,Fe)O3−δ model electrodes, Solid State Ionics. 177 (2006) 1071–1081.

[180] T. Kawada, J. Suzuki, M. Sase, A. Kaimai, K. Yashiro, Y. Nigara, J. Mizusaki, K. Kawamura, H. Yugami, Determination of Oxygen Vacancy Concentration in a Thin Film of La0.6Sr0.4CoO3−δ by an Electrochemical Method, J. Electrochem. Soc. 149 (2002) E252.

[181] H.J.M. Bouwmeester, M.W. Den Otter, B.A. Boukamp, Oxygen transport in La0.6Sr0.4Co1−yFeyO3−δ, J. Solid State Electrochem. 8 (2004) 599–605.

[182] S.-N. Lee, A. Atkinson, J.A. Kilner, Effect of Chromium on La0.6Sr0.4Co0.2Fe0.8O3-δ Solid Oxide Fuel Cell Cathodes, J. Electrochem. Soc. 160 (2013) F629–F635.

[183] M. Katsuki, S.S. Wang, M. Dokiya, T. Hashimoto, High temperature properties of La0.6Sr0.4Co0.8Fe0.2O3-δ oxygen nonstoichiometry and chemical diffusion constant, Solid State Ionics. 156 (2003) 453–461.

[184] A. Leonide, B. Rüger, A. Weber, W.A. Meulenberg, E. Ivers-Tiffée, Impedance Study of Alternative (La,Sr)FeO3−δ and (La,Sr)(Co,Fe)O3−δ MIEC Cathode Compositions, J. Electrochem. Soc. 157 (2010) B234.

[185] J. Bae, B.C.H. Steele, Properties of LSCF double layer cathodes on gadolinium-doped cerium oxide (CGO) electrolytes I Role of oxygen exchange and diffusion, Solid State Ionics. 106 (1998) 255–261.

[186] V.M. Janardhanan, V. Heuveline, O. Deutschmann, Three-phase boundary length in solid-oxide fuel cells: A mathematical model, J. Power Sources. 178 (2008) 368–372.

[187] N. Li, A. Verma, P. Singh, J.-H. Kim, Characterization of La0.58Sr0.4Co0.2Fe0.8O3−δ–Ce0.8Gd0.2O2 composite cathode for intermediate temperature solid oxide fuel cells, Ceram. Int. 39 (2013) 529–538.

[188] N. Light, O. Kesler, Air plasma sprayed Cu-Co-GDC anode coatings with various Co loadings, J. Power Sources. 233 (2013) 157–165.

[189] E.P. Murray, M.J. Sever, S.A. Barnett, Electrochemical performance of LSCF-CGO

composite cathodes, Solid State Ionics. 148 (2002) 27–34.

[190] M.J.Jørgensen, S.Primdahl, C.Bagger, M.Mogensen, Effect of sintering temperature on microstructure and performance of LSM-YSZ composite cathodes, Solid State Ionics. 139 (2001) 1–11.

[191] P. Hjalmarsson, M. Søgaard, M. Mogensen, Electrochemical behaviour of (La1−xSrx)sCo1−yNiyO3−δ as porous SOFC cathodes, Solid State Ionics. 180 (2009) 1395–1405.

[192] E. Fabbri, L. Bi, D. Pergolesi, E. Traversa, High-performance composite cathodes with tailored mixed conductivity for intermediate temperature solid oxide fuel cells using proton conducting electrolytes, Energy Environ. Sci. 4 (2011) 4984–4993.

[193] Y. Lu, C. Kreller, S. Adler, Measurement and Modeling of the Impedance Characteristics of Porous La1−xSrxCoO3−δ Electrodes, J. Electrochem. Soc. 156 (2009) B513.

[194] S. Adler, Factors governing oxygen reduction in solid oxide fuel cell cathodes., Chem. Rev. 104 (2004) 4791–843.

[195] J. Fleig, Solid Oxide Fuel Cell Cathodes: Polarization Mechanisms and Modeling of the Electrochemical Performance, Annu. Rev. Mater. Res. 33 (2003) 361–382.

[196] P. Holtappels, C. Bagger, Fabrication and performance of advanced multi-layer SOFC cathodes, J. Eur. Ceram. Soc. 22 (2002) 41–48.

[197] J. Hayd, L. Dieterle, U. Guntow, D. Gerthsen, E. Ivers-Tiffée, Nanoscaled La0.6Sr0.4CoO3-δ as intermediate temperature solid oxide fuel cell cathode: Microstructure and electrochemical performance, J. Power Sources. 196 (2011) 7263–7270.

[198] H.Y. Jung, W.S. Kim, S.H. Choi, H.C. Kim, J. Kim, H.W. Lee, J.H. Lee, Effect of cathode current-collecting layer on unit-cell performance of anode-supported solid oxide fuel cells, J. Power Sources. 155 (2006) 145–151.

[199] K. Sasaki, J.-P. Wurth, R. Gschwend, M. Godickemeier, L.J. Gauckler, Cathodic Polarization and Ohmic Resistance, J. Electrochem. Soc. 143 (1997) 530–543.

[200] B. Kenney, K. Karan, Engineering of microstructure and design of a planar porous

composite SOFC cathode: A numerical analysis, Solid State Ionics. 178 (2007) 297–306.

[201] S.-F. Wang, Y.-R. Wang, C.-T. Yeh, Y.-F. Hsu, S.-D. Chyou, W.-T. Lee, Effects of bi-layer La0.6Sr0.4Co0.2Fe0.8O3−δ-based cathodes on characteristics of intermediate temperature solid oxide fuel cells, J. Power Sources. 196 (2011) 977–987.

[202] X. Lou, S. Wang, Z. Liu, L. Yang, M. Liu, Improving La0.6Sr0.4Co0.2Fe0.8O3-δ cathode performance by infiltration of a Sm0.5Sr0.5CoO3-δ coating, Solid State Ionics. 180 (2009) 1285–1289.

[203] T. Kenjo, Y. Kanehira, Influence of the local variation of the polarization resistance on SOFC cathodes, Solid State Ionics. 148 (2002) 1–14.

[204] M. Brown, S. Primdahl, M. Mogensen, Structure / Performance Relations for Ni / Yttria-Stabilized Zirconia Anodes for Solid Oxide Fuel Cells, J. Electrochem. Soc. 147 (2000) 475–485.

[205] H.J. Tannenberger, H. Siegert, Fuel Cell Systems—II, B. S. Baker, Symposium Chairman, R.F. Gould, Washington DC, 1969.

[206] J. Fleig, J. Maier, The Influence of Current Constriction on the Impedance of Polarizable Electrodes, J. Electrochem. Soc. 144 (1997) L302.

[207] L. Millar, H. Taherparvar, N. Filkin, P. Slater, J. Yeomans, Interaction of (La1-xSrx)1-yMnO3-Zr1-zYzO2-d cathodes and LaNi0.6Fe0.4O3 current collecting layers for solid oxide fuel cell application, Solid State Ionics. 179 (2008) 732–739.

[208] G. Chiodelli, L. Malavasi, Electrochemical open circuit voltage (OCV) characterization of SOFC materials, Ionics (Kiel). 19 (2013) 1135–1144.

[209] Q.L. Liu, K.A. Khor, S.H. Chan, X.J. Chen, Anode-supported solid oxide fuel cell with yttria-stabilized zirconia/gadolinia-doped ceria bilalyer electrolyte prepared by wet ceramic co-sintering process, J. Power Sources. 162 (2006) 1036–1042.

[210] Z. Gao, V.Y. Zenou, D. Kennouche, L. Marks, S.A. Barnett, Solid oxide cells with zirconia/ceria Bi-Layer electrolytes fabricated by reduced temperature firing, J. Mater. Chem. A. 3 (2015) 9955–9964.

[211] H.J. Cho, G.M. Choi, Fabrication and characterization of Ni-supported solid oxide fuel

cell, Solid State Ionics. 180 (2009) 792–795.

[212] R. Barfod, A. Hagen, S. Ramousse, P. V. Hendriksen, M. Mogensen, Break Down of Losses in Thin Electrolyte SOFCs, Fuel Cells. 6 (2006) 141–145.

[213] A. Leonide, V. Sonn, A. Weber, E. Ivers-Tiffée, Evaluation and Modeling of the Cell Resistance in Anode-Supported Solid Oxide Fuel Cells, J. Electrochem. Soc. 155 (2008) B36–B41.

[214] S.H.S.H. Jensen, A. Hauch, P.V. Hendriksen, M. Mogensen, N. Bonanos, T. Jacobsen, A Method to Separate Process Contributions in Impedance Spectra by Variation of Test Conditions, J. Electrochem. Soc. 154 (2007) B1325.

[215] S. Primdahl, M. Mogensen, Gas Conversion Impedance: A Test Geometry Effect in Characterization of Solid Oxide Fuel Cell Anodes, J. Electrochem. Soc. 145 (1998) 2431.

[216] S. Primdahl, M. Mogensen, Gas Diffusion Impedance in Characterization of Solid Oxide Fuel Cell Anodes, J. Electrochem. Soc. 146 (1999) 2827.

[217] H. Zhu, A. Kromp, A. Leonide, E. Ivers-Tiffee, O. Deutschmann, R.J. Kee, A Model-Based Interpretation of the Influence of Anode Surface Chemistry on Solid Oxide Fuel Cell Electrochemical Impedance Spectra, J. Electrochem. Soc. 159 (2012) F255–F266.

[218] T. Van Gestel, F. Han, D. Sebold, H.P. Buchkremer, D. Stöver, Nano-structured solid oxide fuel cell design with superior power output at high and intermediate operation temperatures, Microsyst. Technol. 17 (2011) 233–242.

[219] D. Wang, J. Wang, C. He, Y. Tao, C. Xu, W.G. Wang, Preparation of a Gd0.1Ce0.9O2-δ interlayer for intermediate-temperature solid oxide fuel cells by spray coating, J. Alloys Compd. 505 (2010) 118–124.

[220] Y. Sakito, A. Hirano, N. Imanishi, Y. Takeda, O. Yamamoto, Y. Liu, Silver infiltrated La0.6Sr0.4Co0.2Fe0.8O3 cathodes for intermediate temperature solid oxide fuel cells, J. Power Sources. 182 (2008) 476–481.

[221] S.Y. Park, J.H. Ahn, C.W. Jeong, C.W. Na, R.H. Song, J.H. Lee, Ni-YSZ-supported tubular solid oxide fuel cells with GDC interlayer between YSZ electrolyte and LSCF cathode, Int. J. Hydrogen Energy. 39 (2014) 12894–12903.

[222] W.-H. Kim, H.-S. Song, J. Moon, H.-W. Lee, Intermediate temperature solid oxide fuel

cell using (La,Sr)(Co,Fe)O3-based cathodes, Solid State Ionics. 177 (2006) 3211–3216.

[223] D. Perednis, L.J. Gauckler, Solid oxide fuel cells with electrolytes prepared via spray pyrolysis, Solid State Ionics. 166 (2004) 229–239.

[224] S. Cho, Y. Kim, J.H. Kim, A. Manthiram, H. Wang, High power density thin film SOFCs with YSZ/GDC bilayer electrolyte, Electrochim. Acta. 56 (2011) 5472–5477.

[225] F. Han, R. Mücke, T. Van Gestel, A. Leonide, N.H. Menzler, H.P. Buchkremer, D. Stöver, Novel high-performance solid oxide fuel cells with bulk ionic conductance dominated thin-film electrolytes, J. Power Sources. 218 (2012) 157–162.

[226] J.H. Joo, G.M. Choi, Thick-film electrolyte (thickness <20μm)-supported solid oxide fuel cells, J. Power Sources. 180 (2008) 195–198.

[227] E.O. Oh, C.M. Whang, Y.R. Lee, S.Y. Park, D.H. Prasad, K.J. Yoon, J.W. Son, J.H. Lee, H.W. Lee, Extremely thin bilayer electrolyte for solid oxide fuel cells (SOFCs) fabricated by chemical solution deposition (CSD), Adv. Mater. 24 (2012) 3373–3377.

[228] H.S. Noh, K.J. Yoon, B.K. Kim, H.J. Je, H.W. Lee, J.H. Lee, J.W. Son, The potential and challenges of thin-film electrolyte and nanostructured electrode for yttria-stabilized zirconia-base anode-supported solid oxide fuel cells, J. Power Sources. 247 (2014) 105–111.

[229] J. Sar, J. Schefold, A. Brisse, E. Djurado, Durability test on coral Ce0.9Gd0.1O2-δ-La0.6Sr0.4Co0.2Fe0.8O3-δ with La0.6Sr0.4Co0.2Fe0.8O3-δ current collector working in SOFC and SOEC modes, Electrochim. Acta. 201 (2016) 57–69.

[230] K.T. Lee, N.J. Vito, M. Camaratta, H.S. Yoon, E. Wachsman, Effect of Ni-GDC AFL Composition on Performance of IT-SOFCs, ECS Trans. 28 (2010) 151–163.

[231] T.S. Li, W.G. Wang, H. Miao, T. Chen, C. Xu, Effect of reduction temperature on the electrochemical properties of a Ni/YSZ anode-supported solid oxide fuel cell, J. Alloys Compd. 495 (2010) 138–143.

[232] A. Faes, A. Hessler-Wyser, A. Zryd, J. Van Herle, A review of RedOx cycling of solid oxide fuel cells anode, Membranes (Basel). 2 (2012) 585–664.

[233] T. Klemensø, PhD Thesis, Relationships between structures and performance of SOFC anodes, Technical University of Denmark, 2006.

[234] Z. Jiao, N. Shikazono, N. Kasagi, Quantitative Characterization of SOFC Nickel-YSZ Anode Microstructure Degradation Based on Focused-Ion-Beam 3D-Reconstruction Technique, J. Electrochem. So. 159 (2012) B285–B291.

[235] R.M.C. Clemmer, S.F. Corbin, The influence of pore and Ni morphology on the electrical conductivity of porous Ni/YSZ composite anodes for use in solid oxide fuel cell applications, Solid State Ionics. 180 (2009) 721–730.

[236] M.H. Pihlatie, A. Kaiser, M. Mogensen, M. Chen, Electrical conductivity of Ni-YSZ composites: Degradation due to Ni particle growth, Solid State Ionics. 189 (2011) 82–90.

[237] J. Laurencin, M. Hubert, K. Couturier, T.L. Bihan, P. Cloetens, F. Lefebvre-Joud, E. Siebert, Reactive Mechanisms of LSCF Single-Phase and LSCF-CGO Composite Electrodes Operated in Anodic and Cathodic Polarisations, Electrochim. Acta. 174 (2015) 1299–1316.

[238] M. Søgaard, P.V. Hendriksen, T. Jacobsen, M. Mogensen, Modelling of the Polarization Resistance from Surface Exchange and Diffusion Coefficient Data, 7th Eur. SOFC Forum. B064 (2006).

[239] M.E. Lynch, D. Ding, W.M. Harris, J.J. Lombardo, G.J. Nelson, W.K.S.S. Chiu, M. Liu, Flexible multiphysics simulation of porous electrodes: Conformal to 3D reconstructed microstructures, Nano Energy. 2 (2013) 105–115.

[240] J. Nielsen, T. Jacobsen, M. Wandel, Impedance of porous IT-SOFC LSCF:CGO composite cathodes, Electrochim. Acta. 56 (2011) 7963–7974.

[241] Ö. Çelikbilek, D. Jauffrès, L. Dessemond, M. Burriel, C.L. Martin, E. Djurado, A Coupled Experimental/Numerical Approach for Tuning High-performing SOFC-Cathode, ECS Trans. 72 (2016) 81–92.

[242] Z. Wu, M. Liu, Modelling of ambipolar transport properties of composite mixed ionic-electronic conductors, Solid State Ionics. 93 (1996) 65–84.

[243] V. Vibhu, A. Rougier, J.C. Grenier, J.-M. Bassat, Mixed Nickelates Pr2-xLaxNiO4+δ Used as Cathodes in Metal Supported SOFCs, ECS Trans. 57 (2013) 2093–2100.

[244] R.K. Sharma, M. Burriel, L. Dessemond, J.-M. Bassat, E. Djurado, Design of interfaces

in efficient Ln 2 NiO 4+δ (Ln = La, Pr) cathode for SOFCs application, J. Mater. Chem. A. 4 (2016) 12451–12462.

[245] J. Rodríguez-Carvajal, FULLPROF: A Program for Rietveld Refinement and Pattern Matching Analysis, in: Abstr. Satell. Meet. Powder Diffr. XV Congr. IUCr, 1990: p. 127.

[246] A. Le Bail, Extracting structure factors from powder diffraction data by iterating, full pattern profile fitting, in: Proc. Int. Conf., NIST Special Publication, 1992: p. 846.

[247] S. Adler, Mechanism and kinetics of oxygen reduction on porous La1-xSrxCo3-δ electrodes, Solid State Ionics. 111 (1998) 125–134.

[248] B.A. Boukamp, M. Verbraeken, D.H.A. Blank, P. Holtappels, SOFC-anodes, proof for a finite-length type Gerischer impedance?, Solid State Ionics. 177 (2006) 2539–2541.

[249] D. Mantzavinos, A. Hartley, I.S. Metcalfe, M. Sahibzada, Oxygen stoichiometries in La1-xSrxCo1-yFeyO3-δ perovskites at reduced oxygen partial pressures, Solid State Ionics. 134 (2000) 103–109.

[250] J. Maier, On the correlation of macroscopic and microscopic rate constants in solid state chemistry, Solid State Ionics. 112 (1998) 197–228.

[251] T. Ishigaki, S. Yamauchi, K. Kishio, J. Mizusaki, K. Fueki, Diffusion of oxide ion vacancies in perovskite-type oxides, J. Solid State Chem. 73 (1988) 179–187.

[252] R.A. De Souza, J.A. Kilner, Oxygen transport in La1−xSrxMn1−yCoyO3±δ perovskites Part II. Oxygen surface exchange, Solid State Ionics. 126 (1999) 153–161.

[253] P. Hjalmarsson, Strontium and nickel substituted lanthanum cobaltite as cathode in Solid Oxide Fuel Cells, Riso National Laboratory for Sustainable Energy, Technical University of Denmark, 2008.

LIST OF TABLES

LIST OF FIGURES

LIST OF ABBREVIATIONS AND ACRONYMS

General	
IT-SOFC	Intermediate Temperature - Solid Oxide Fuel Cell
ORR	Oxygen Reduction Reaction
TEC	Thermal Expansion Coefficient
CFL	Cathode Functional Layer
AFL	Anode Functional Layer
CCL	Current Collecting Layer
TPB	Triple Phase Boundary
MIEC	Mixed Ionic-Electronic Conductor
IC	Ionic Conductor
1D ALS model	1 dimensional Adler Lane Steele model
Materials	
LSCF	$La_{0.6}Sr_{0.4}Co_{0.2}Fe_{0.8}O_{3-\delta}$
LSCF/CGO	$La_{0.6}Sr_{0.4}Co_{0.2}Fe_{0.8}O_{3-\delta}$ / $Ce_{0.9}Gd_{0.1}O_{2-\delta}$
YSZ	Yttrium doped Zirconia $(Y_2O_3)_{0.08}(ZrO_2)_{0.92}$
NiO	Nickel oxide
LSM	$(LaSr)MnO_3$
Techniques	
ESD	Electrostatic Spray Deposition
SP	Screen Printing
FIB/SEM	Focused Ion Beam / Scanning Electron Microscopy
SEM	Scanning Electron Microscope
XRD	X-ray Diffraction
TEM	Transmission Electron Microscope
EIS	Electrochemical Impedance Spectroscopy
3D FEM	Three Dimensional Finite Element Method
Impedance	
OCV	Open Circuit Voltage
AC	Alternating Current
DC	Direct Current
CPE	Constant Phase Element
ASR	Area Specific Resistance
ASR_{pol}	Area Specific Polarization Resistance
t_{chem}	Characteristic time constant
Modelling	
COMSOL Multiphysics	Finite Element Simulation Software
MATLAB	Numerical computing, programming language
CPU	Central Processing Unit
RVE	Representative Volume Element

SYMBOLS AND UNITS

U	V	Voltage
U_N	V	Nernst Voltage
U_C	V	Real output voltage
η_{ohm}	V	Ohmic overpotential
η_{act}	V	Activation overpotential
η_{conc}	V	Concentration overpotential
η_{ct}	V	Charge transfer overpotential
I	A	Current
j	A m^{-2}	Current Density
ASR	Ω m^2	Area Specific Resistance
α	K^{-1}	Thermal expansion coefficient
σ_{ic}	S m^{-1}	Ionic conductivity
σ_{ec}	S m^{-1}	Electronic conductivity
T	K	Temperature
ε		Fractional porosity
a	m^{-1}	Specific surface area
τ		Tortuosity factor
L_δ	m	Utilization length
c_o	mol m^{-3}	Concentration of oxygen ions
$c_{o,eq}$	mol m^{-3}	Oxygen partial pressure dependent equilibrium value of oxygen ion concentration
c_v	mol m^{-3}	Concentration of oxygen ion lattice sites
Do	m^2 s	Oxygen diffusion coefficient
D*	m^2 s	Oxygen tracer diffusion coefficient
D^δ	m^2 s	Oxygen chemical diffusion coefficient
k_o	m s	Surface oxygen exchange coefficient
k*	m s	Tracer surface oxygen exchange coefficient
k^δ	m s	Chemical surface oxygen exchange coefficient
p_{GC}	bar	Oxygen gas partial pressure at the cathode side
p_{CE}	bar	Oxygen gas partial pressure at the counter electrode side
η_{model}	V	Total voltage loss in the model
ϕ		Electrical potential applied in the cathode

R=8.314	J K^{-1} mol^{-1}	Gas constant
$F=9.649\cdot10^4$	C mol^{-1}	Faraday's constant
$e=1.602\cdot10^{-19}$	C	Elementary charge
$k=8.617\cdot10^{-5}$	eV K^{-1}	Boltzmann constant
$N_A=6.022\cdot10^{23}$	mol^{-1}	Avogadro's number

PUBLICATIONS AND COMMUNICATIONS

Peer-reviewed Articles

1. **Celikbilek O**., Siebert, E., Jauffres D., Martin C.L., Djurado E., *The effect of microstructure on the electrochemical performance of LSCF/GDC composite electrodes for IT-SOFCs,* in preparation
2. **Celikbilek O**., Dailly, J., Jauffres D., Martin C.L., Djurado E., *Optimization of double layer LSCF cathode film for IT/SOFC,* in preparation
3. **Celikbilek O**., Jauffres D., Siebert, E., Dessemond L., Burriel M., Martin C.L., Djurado E., *Rational Design of Hierarchically Nanostructured Electrodes for Solid Oxide Fuel Cells*, J. Power Sources. **333** (2016) 72–82.
4. Sar, J., **Celikbilek, O.**, Villanova, J., Dessemond, L., Martin, C., Djurado, E., *Three dimensional analysis of* $Ce_{0.9}Gd_{0.1}O_{1.95}$–$La_{0.6}Sr_{0.4}Co_{0.2}Fe_{0.8}O_{3-\delta}$ *oxygen electrode for solid oxide cells*, J. Eur. Ceram. Soc. **35,** 2–10 (2015).

Proceedings

5. **Celikbilek O**., Jauffres D., Burriel M., Dessemond L., Martin C.L., Djurado E., *A coupled experimental/numerical approach for tuning high-performing SOFC-cathode*, ECS Trans. **72** (2016) 81–92.
6. Sharma, R.K., **Celikbilek O**., Burriel M., Dessemond L., Bassat, J.M., Djurado E., *Electrochemical Performance and Chemical Stability of Architecturally Designed* $La_{2-X}Pr_xNiO_{4+\delta}$ *IT-SOFC Cathodes*, ECS Trans. **72** (2016) 1-8.
7. **Celikbilek O**., Jauffres D., Dessemond L., Burriel M., Martin C.L., Djurado E., *Effect of microstructural parameters on a performant SOFC cathode: Modelling vs Experiments*, Proceedings of 12th European SOFC Forum, **B1504** (2016)

International communications

1. **Celikbilek O**., Jauffres D., Siebert, E., Dessemond L., Burriel M., Martin C.L., Djurado E., *Effect of microstructural parameters on a performant SOFC cathode: Modelling vs Experiments*, EFCF, 12th European SOFC and SOE Forum, Lucerne, Switzerland, July 2016, (oral)**.**
2. **Celikbilek O**., Jauffres D., Siebert, E., Dessemond L., Burriel M., Martin C.L., Djurado E., *A coupled experimental/numerical approach for tuning high-performing SOFC-cathode*, ECS 229th Meeting, San Diego, United States, May-June 2016 (oral)**.**
3. **Celikbilek O**., Burriel M., Dessemond L., Martin C.L., Djurado E., *Towards architectured SOFC electrodes: A study of micro/nano-structural evolution*, 6th International Conference on Fundamentals and Development of Fuel Cells, FDFC, Toulouse, France, February 2015, (oral).
4. **Celikbilek O**., Burriel M., Djurado E., *Effect of sintering on the microstructural properties of a composite cathode for SOFC*, MAT4ENERGY Workshop, Grenoble, France, June 2014, (poster).
5. **Celikbilek O**., Burriel M., Dessemond L., Djurado E., *Composite cathodes towards improved performances for IT-SOFC,* Second International Workshop on Nano Materials for Energy Conversion, NMEC-2014, Vietnam, Nov. 2014, (poster).

National communications (France)

6. **Celikbilek O**., Jauffres D., Martin C.L., Workshop, Rational Design of Hierarchically Nanostructured Electrodes for Solid Oxide Fuel Cells, St Gobain, November 2016 (oral).
7. **Celikbilek O**., Jauffres D., Dessemond L., Burriel M., Martin C.L., Djurado E., *A coupled experimental/numerical approach for tuning high-performing SOFC-cathode,* Colloque Labex CEMAM, Grenoble, France, January 2016 (poster).
8. **Celikbilek O**., Jauffres D., Burriel M., Dessemond L., Martin C.L., Djurado E., *Microstructural control of electrochemical properties of innovative oxygen electrode for SOFCs: experimental vs modelling*, GdR-HySPàC-2015, Porticcio, France, October 2015 (oral).

9. **Celikbilek O**., Sharma, R., Burriel M., Dessemond L., Djurado E., *A study of micro/nano-structural evolution of a composite cathode for SOFC*, Congrès de la Société Chimique de France, SCF-2015, Lille, France, July 2015 (poster).
10. **Celikbilek O**., Jauffres D., Burriel M., Dessemond L., Martin C.L., Djurado E., *Composite cathodes towards improved performances for IT-SOFC*, Journée de Printemps de la section Rhône-Alpes de la Société Chimique de France, Lyon, France, June 2015, (poster).
11. **Celikbilek O**., Burriel M., Martin C.L., Djurado E., *Architectured electrodes for energy conversion: SOFCs, SOECs*, Colloque Labex CEMAM, Grenoble, France, July 2014, (poster).
12. **Celikbilek O**., Burriel M., Djurado E., *Micro/nano-structural evolution of a composite cathode for SOFC*, Journée de printemps Section Rhône-Alpes de la Société Chimique de France, Chambéry, France, June 2014, (poster).